Mechanisms of star formation quenching in local galaxies

Barbara Mazzilli Ciraulo

To cite this version:

Barbara Mazzilli Ciraulo. Mechanisms of star formation quenching in local galaxies. Astrophysics [astro-ph]. Université Paris sciences et lettres, 2022. English. NNT : 2022UPSLO002 . tel-03850840

HAL Id: tel-03850840
https://theses.hal.science/tel-03850840v1

Submitted on 14 Nov 2022

PSL
UNIVERSITÉ PARIS

THÈSE DE DOCTORAT
DE L'UNIVERSITÉ PSL

Préparée à l'Observatoire de Paris

Mécanismes éteignant la formation des étoiles au sein de galaxies proches

Soutenue par
Barbara Mazzilli Ciraulo
Le 21 janvier 2022

École doctorale n°127
Astronomie et Astrophysique d'Ile-de-France

Spécialité
Astronomie et Astrophysique

Composition du jury :

David Patton Professeur, Université Trent	*Rapporteur*
Francine Marleau Professeure associée, Université d'Innsbrück	*Rapporteure*
Susanne Aalto Professeure, Université de Chalmers	*Examinatrice*
Éric Emsellem Astronome, ESO	*Examinateur*
Hélène Sol Directrice de recherche, LUTH - Observatoire de Paris	*Présidente du jury*
Françoise Combes-Bottaro Professeure, LERMA - Observatoire de Paris	*Directrice de thèse*
Anne-Laure Melchior Maîtresse de conférence, LERMA - Observatoire de Paris	*Directrice de thèse*

MINES ParisTech | PSL

> "Science doesn't always go forwards. It's a bit like doing a Rubik's cube. You sometimes have to make more of a mess with a Rubik's cube before you can get it to go right."
>
> Jocelyn Bell

> "You will learn that you are so much more capable than you might imagine or even dream."
>
> Peggy Whitson

Résumé

Les données astronomiques deviennent de plus en plus précises et permettent d'affiner notre compréhension des processus qui régissent l'évolution des galaxies, mais nous ne disposons toujours pas d'un paradigme global pour expliquer certains mécanismes physiques, en particulier l'extinction de la formation stellaire. Le déclenchement et la régulation de cette extinction ne sont pas compris en détail étant donné les nombreux processus dont elle peut résulter et les différentes échelles de temps qui sont impliquées.

Le but de ce projet de thèse est d'étudier le contenu en gaz, l'activité de formation d'étoiles et son extinction dans les galaxies en utilisant les données spectroscopiques de l'étude SDSS-IV MaNGA, ainsi que des observations de gaz moléculaire et atomique. En outre, ce travail s'appuie sur l'étude de la cinématique du gaz ionisé, pour interpréter les profils des raies d'émission observés.

Tout d'abord, je décris l'échantillon de galaxies proches sur lequel j'ai décidé de me concentrer. Il s'agit de 29 galaxies qui présentent des caractéristiques cinématiques complexes dans leurs spectres dans le domaine visible. Dans la deuxième partie, je présente une analyse de cet échantillon en termes de paramètres structurels des galaxies et d'activité de formation d'étoiles. Je conclus que ces objets nous permettent d'échantillonner différentes phases de l'évolution des galaxies, qui résultent d'événements de fusions mineures. Dans la troisième partie, je détaille les résultats que j'ai obtenus en appliquant une procédure d'ajustement de spectres innovante aux données d'une galaxie MaNGA particulière. Cette approche permet de mettre en évidence une fusion mineure, impliquant deux galaxies le long de la ligne de visée, en décomposant les caractéristiques spectrales optiques, à la fois dans les raies d'émission du gaz et dans le continuum stellaire. Dans la quatrième partie, je me concentre sur l'analyse du contenu en gaz froid à travers des observations de gaz moléculaire et atomique. Je déduis les masses de gaz moléculaire ainsi qu'une relation de Kennicutt-Schmidt afin d'estimer l'efficacité de la formation d'étoiles des galaxies étudiées.

Abstract

Astronomical data become more and more precise and help the refining of our understanding of the processes that drive galaxy evolution, but we still do not have a global paradigm to explain some physical mechanisms. The triggering and regulation of star formation quenching are especially not understood in detail given the numerous processes that this quenching can be resulting from and the different timescales that are involved.

The aim of this thesis project is to study the gas content, star formation activity and quenching within galaxies using integral field spectroscopic data from the SDSS-IV MaNGA survey, as well as single-dish observations of molecular and atomic gas.

Firsly, I describe the sample of nearby galaxies that I decided to focus on. It consists of 29 nearby galaxies that show complex kinematic features in their optical spectra. It is drawn from the cross-identification between the MaNGA data release DR15 and a sample of more than 5000 galaxies that are mainly isolated but show an excess fraction of S0 and spirals with larger bulges, and exhibit a central excess star formation. In the second part, I present an analysis of this sample in terms of galaxy structural parameters and star formation activity. I conclude that these objects enable us to sample different phases of galaxy evolution, which result from minor-merger events. In the third part, I detail the results that I obtained by applying an innovative fitting procedure to the data from one peculiar MaNGA galaxy. This approach helps reveal a minor-merger event by disentangling the optical spectral features, both in the gas and stellar components. In the fourth part, I focus on the analysis of the cold gas content through molecular and atomic gas observations. I infer the molecular and atomic gas masses as well as a Kennicutt-Schmidt relation so as to estimate the star formation efficiency of the studied galaxies.

Remerciements

Je souhaite tout d'abord remercier Anne-Laure et Françoise de m'avoir donné l'opportunité de mener ce projet de thèse à l'Observatoire de Paris. Cette aventure aura été riche en enseignements, en rencontres, en discussions et je tâcherai de garder le meilleur de tout cela.
Merci Anne-Laure, pour le partage de tes innombrables idées, pour ton aide et tes corrections apportées lors de la rédaction des papiers, *abstracts* et autres *proposals*. Merci Françoise, d'avoir pris le temps de répondre à mes questions, toujours avec patience et enthousiasme. Merci de voir le côté positif des choses à chaque moment.

Mon aventure en astrophysique a commencé avant mon arrivée à Paris et je tiens donc à remercier notamment Bernd Vollmer et Andreea Petric de m'avoir fait et donné confiance. Merci aux colocs de Kinohou, Calum, Eduardo, Ismael, Jordan, Kai, Michaela. Nos aventures hawaïennes, que j'associe également à Jonathan et Mariya, sont gravées dans ma mémoire.

Un grand merci évidemment aux collègues du LERMA avec qui ce fut un plaisir de partager ces années. Je remercie l'équipe administrative pour leur dévouement, leur efficacité et leur disponibilité. Un merci particulier à Woihiba: merci de m'avoir soutenue, encouragée et fait rire même durant les moments difficiles. Tu es un vrai rayon de soleil. Un merci spécial à Tarikakan également, pour ta réactivité, ton enthousiasme pour nous aider.
Anaëlle, je te remercie pour nos discussions, ta volonté de m'aider, de m'enseigner ces concepts de dynamique des galaxies que tu maîtrises tellement mieux que moi. J'ai beaucoup appris grâce à toi. Merci également pour ton humour et ton soutien dans les moments sombres.
Ein großer Dank gilt dir Daniel für deine Zeit in der du viele meiner Fragen beantwortetest, in der wir uns über Programmierung unterhalten haben und gemeinsam die Fehler gesucht und behoben haben. Danke auch, dass du mich dazu gefördert hast, weiterhin Deutsch zu sprechen.
Aristide, il va être difficile de résumer nos 3 années passées ensemble dans le bureau 701. Entre un atelier sciure, jardinage, ou couture, tu as été là pour m'écouter, me motiver, me redonner confiance. Refaire le monde en ta compagnie et te défier lors de *blind-tests* ont été un vrai plaisir! Merci pour tout.

Bien entendu, je dois l'aboutissement de ce travail à de nombreuses personnes extérieures à l'Observatoire qui me sont chères. Merci Isabelle d'avoir proposé une relec-

ture anglophone et d'avoir consacré du temps à la correction de plusieurs parties de ce manuscrit.

Nina, William, c'est un honneur de vous avoir pour ami.e.s après près de 25 ans et c'est toujours un plaisir de passer des heures en votre compagnie.

Antoine, Lorraine, Marion, Raphaël vous m'accompagnez depuis tant d'années et m'avez toujours permis de garder le moral.

Clara, Delphine, Eva, Hélène, Laura, Lilyan, Maïlys, Mathilde, nos années strasbourgeoises sont de merveilleux souvenirs et j'espère qu'à l'avenir nous en écrirons d'aussi beaux tou.te.s ensemble. Vous m'avez connue dans tous mes états, sans jamais aucun jugement, merci. Alexis, Alice, j'ai été peu présente et j'espère que vous ne m'en tiendrez pas rigueur. Je suis fière de vous et suis heureuse de vous compter dans ma «famille» de coeur.

Bastien, il est difficile d'exprimer toute ma gratitude. Merci d'être sur la même longueur d'onde que moi, merci d'être indulgent, merci de croire en moi.

Louise, docteure en astrophysique que tu es, tu as été un véritable pilier dans cette aventure. Une source d'inspiration aussi. Je suis impatiente de partager le même bureau que toi, un jour.

François, je ne sais même pas par où commencer. Merci pour ton amour, merci d'avoir tout pris en charge pour que je puisse me concentrer sur mon travail. Merci d'avoir effectué moult tâches ingrates, à des heures impromptues, pour faire avancer mon travail. Merci de m'avoir montré avec patience que les montagnes se dressant devant moi n'étaient pas insurmontables.

Enfin, la réalisation de cette thèse est une victoire que je dois également attribuer à ma famille. Amalia et Mélina, nous sommes si différentes mais nous nous complétons si bien. Votre amour de sœurs a été un moteur pour moi. Elisa et Gabriel, vous m'avez apporté tant de bonheur en à peine quelques mois, rien qu'avec vos sourires. Merci à mes parents de m'avoir transmis ce goût d'apprendre, de m'avoir toujours encouragée à poursuivre mes rêves. Merci à mon papa, à qui j'aurais aimé pouvoir présenter cette thèse. Merci à ma maman, d'être une femme formidable. Merci d'avoir porté le monde sur tes épaules pour que je réussisse, d'avoir toujours trouvé les mots justes pour me donner des ailes.

Contents

List of Figures

List of Abbreviations

AGN	Active Galactic Nucleus. 15, 17–19, 39, 68, 104
APEX	Atacama Pathfinder Experiment. 23
BPT	Baldwin Phillips Terlevich. xi, 4, 17, 18
DECaLS	Dark Energy Camera Legacy survey. 22
DESI	Dark Energy Spectroscopic Instrument. xi, 22
EW	Equivalent width. 17, 18
FUV	Far UltraViolet. 20
FWHM	Full Width at Half Maximum. 30, 96
GALEX	Galaxy Evolution Explorer. xiii, 22, 23
GASS	GALEX Arecibo SDSS Survey. xi, 23
IFU	Integral Field Unit. xi, 30, 32
IMF	Initial Mass Function. xi, 12, 20
IR	InfraRed. 20
IRAM	Institut de RadioAstronomie Millimétrique. 23, 93, 94, 99, 104
ISM	InterStellar Medium. 10
LINER	Low Ionisation Nuclear Emission-line Region. 18
LOSVD	Line-Of-Sight Velocity Distribution. xii, 74–76

NRT	Nançay Radio Telescope. 106
PGs	Passive Galaxies. 18, 19
RCSED	Reference Catalog of Spectral Energy Distributions. xi, 22, 33
RGs	Retired Galaxies. 18, 19
SDSS	Sloan Digital Sky Survey. 4, 19, 21–23, 29, 30, 33, 69
SF	Star Forming. 18, 19
SFR	Star Formation Rate. 12–14, 20, 28, 29, 32, 69, 98
UKIDSS	UKIRT Deep Sky Survey. 22
UV	UltraViolet. 20
WHAN	WidtH of Hα versus NII. xi, 4, 18, 19
xCOLD	extended CO Legacy Database. xi, 23

Introduction

Dans ce chapitre introductif, j'aborde certains aspects essentiels de l'évolution des galaxies afin de motiver mon travail de thèse et de le situer dans un contexte général.

Propriétés générales des galaxies

La découverte de l'existence d'objets extragalactiques est une percée scientifique que l'on peut qualifier de récente, puisque l'astronome Edwin Hubble met en évidence la nature extragalactique de la galaxie d'Andromède (alors appelée nébuleuse) dans les années 1920. Il utilise pour cela la relation période-luminosité des étoiles variables Céphéïdes, calibrée par l'astronome Henrietta Swan Leavitt, et démontre que ces étoiles n'appartiennent pas à la Voie Lactée.
L'astronomie extragalactique s'est depuis développée et a fait d'énormes progrès en termes de couverture d'observation, de qualité des données et d'efficacité du traitement des données.

Morphologie

Une galaxie est un assemblage d'étoiles, de poussières et de gaz, tenus ensemble par la force gravitationnelle. Les galaxies peuvent avoir des morphologies très différentes. Edwin Hubble a établi la première classification (Hubble, 1936), divisant les galaxies en trois groupes principaux: les spirales, les elliptiques et les irrégulières (voir fig. 1.1). Cette classification a été précisée et complétée en incluant les barres, la forme des bras spiraux, ou encore le degré d'ellipticité (par ex. De Vaucouleurs, 1959).

Profils de luminosité de surface

Les galaxies elliptiques ont généralement un profil de luminosité de surface qui peut être bien ajusté par un profil dit de Sérsic, tel que défini par l'équation 1.1. L'indice de Sérsic, noté n, indique la concentration du profil: plus n est élevé, plus la luminosité est concentrée. La valeur $n = 1$ correspond à un profil exponentiel, adapté à la description de la distribution de luminosité du disque d'une galaxie spirale.

Distribution de couleurs

La couleur apparente est une propriété qui varie d'une galaxie à l'autre. Cette couleur est déterminée par l'âge et la masse des étoiles qui composent la galaxie; elle fournit donc d'importantes informations sur l'évolution de la galaxie observée. Plusieurs systèmes photométriques, basés sur l'utilisation de filtres, ont été définis pour décrire la couleur d'un objet céleste. Les systèmes $UBVRI$ et u, g, ri, z (similaire au système u', g', r', i', z') sont par exemple très répandus. La magnitude d'une galaxie dans une bande donnée correspond à la mesure de la luminosité de la galaxie dans cette bande. Une couleur est définie comme la différence entre deux magnitudes (par exemple $u - r$, $g - r$ ou $B - V$).

Le milieu interstellaire

Le milieu interstellaire (MIS) est constitué de poussières et de gaz. Son cycle est étroitement lié à l'évolution de la galaxie elle-même.

La poussière interstellaire

La poussière interstellaire est un ensemble de particules solides, de taille variable $(0,1 - 1\mu\,\mathrm{m})$. Les grains de poussière absorbent, dispersent, et ré-émettent à des longueurs d'onde plus grandes la lumière des étoiles. La poussière interstellaire est en ce sens responsable du rougissement du milieu interstellaire. Elle tient aussi un rôle important de catalyseur du processus de formation des molécules.

Le contenu en gaz

Le gaz ne représente qu'une fraction modeste de la masse d'une galaxie mais c'est un composant clé pour comprendre l'évolution des galaxies, puisqu'il est le réservoir de la formation d'étoiles. Le gaz interstellaire est principalement constitué d'hydrogène, d'hélium ($\sim$ 25%) et d'éléments plus lourds formés par fusion au cœur des étoiles.
Le gaz interstellaire est présent sous différentes phases, dont les propriétés de densité et d'ionisation sont différentes.

Activité et extinction de la formation d'étoiles dans les galaxies

Loi de formation stellaire

La formation d'étoiles a lieu dans les nuages moléculaires les plus denses. Les observations ont néanmoins démontré que ce processus est peu efficace (1-5% de la masse de gaz est convertie en masse stellaire). La loi de formation stellaire s'écrit comme une loi de puissance entre la densité surfacique du taux de formation stellaire Σ_{SFR} et la densité surfacique du gaz Σ_{gas}. Cette relation est appelée loi de Kennicutt-Schmidt (Schmidt, 1959; Kennicutt, Jr., 1998).

Bimodalité observée au sein des galaxies

Bimodalité de couleur

Les galaxies dans l'Univers Local suivent une distribution bimodale sur les diagrammes couleur-magnitude et couleur-masse. Deux principaux groupes sont observés: le «nuage bleu», constitué essentiellement de galaxies formant activement des étoiles, dominé par des galaxies spirales, et la «séquence» rouge, composée surtout de galaxies dites éteintes, qui ne forment plus d'étoile, majoritairement elliptiques. La zone située entre ces deux groupes est appelée la «vallée verte» (Salim, 2014).

Séquence principale de formation d'étoiles

Les observations montrent une forte corrélation entre le taux de formation stellaire, *i.e.* la masse d'étoiles formée par an, et la masse d'étoiles existante au sein d'une galaxie. Cette relation est dénommée «séquence principale de formation d'étoiles» et sa définition a été abondamment discutée dans différents travaux (par ex. Whitaker et al., 2012; Speagle et al., 2014; Renzini & Peng, 2015; Tomczak et al., 2016; Pearson et al., 2018).

Processus d'extinction

L'arrêt de la formation d'étoiles est communément appelé «extinction» et peut être la conséquence de divers mécanismes physiques, relatifs à l'environnement dans lequel évolue la galaxie ou bien aux propriétés internes de la galaxie elle-même. Ces différents processus sont intensément discutés dans l'optique de déterminer si l'un d'entre eux est prépondérant.

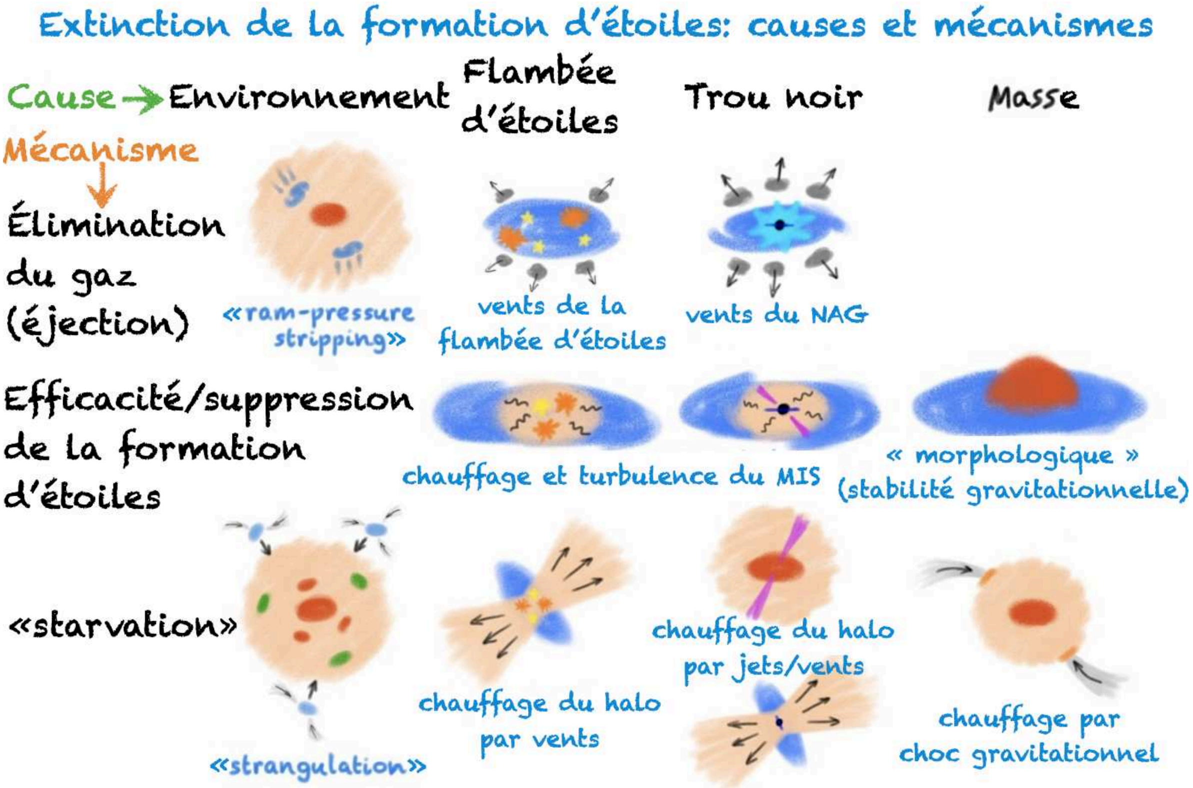

Figure (1) Représentations schématiques des causes possibles de l'extinction de la formation d'étoiles. Figure utilisée avec l'accord de Roberto Maiolino, traduite en français. [1]

Étude du milieu interstellaire par la spectroscopie

Raies de recombinaison

Le milieu interstellaire peut être étudié via l'observation des raies d'émission du gaz. Ces raies sont produites par les électrons qui passent d'un état d'énergie excité à un état plus faible. Les

---

[1] Illustration originale: https://www.robertomaiolino.net/projects/quench

raies de l'hydrogène sont largement étudiées. La figure ?? illustre les raies dites de Balmer, correspond aux émissions lors de la désexcitation de l'électron vers le niveau $n = 2$. D'autres transitions observées dans les galaxies sont les raies dites interdites, telles que [NII], [OIII] ou [SII].

Diagrammes de diagnostic d'excitation

L'ionisation responsable des raies d'émission observées peut être due à divers phénomènes. Le gaz peut être ionisé par les étoiles jeunes et chaudes dans les régions de formation stellaire, mais aussi par un noyau actif galactique (NAG). Différents diagrammes de diagnostic sont utilisés pour distinguer l'excitation due à la formation d'étoiles de celle dominée par une activité de type NAG. Les plus courants sont le diagramme BPT (Baldwin et al., 1981) et le diagramme WHAN (Cid Fernandes et al., 2011), respectivement décrits sur les figures 1.9 et 1.10.

Relevés astrophysiques

Une multitude de relevés astrophysiques existent et fournissent des données photométriques et spectroscopiques de dizaines de milliers de galaxies. Je fais usage de certaines d'entre elles dans le cadre de mon travail de thèse.

Le relevé SDSS a observé un tiers du ciel et a rendu publics des images et des spectres pour plus de trois millions d'objets astrophysiques. J'utilise certaines des données de la septième publication de données.

Le projet RCSED répertorie 800299 galaxies observées par SDSS et fournit des données à valeur ajoutée comme des observations complémentaires (GALEX et UKIDSS), mais aussi les résultats des ajustements de spectres (flux des raies d'émission) et des propriétés dérivées (obscuration, métallicité, etc).

Afin de comparer mes observations de gaz moléculaire à l'IRAM 30 m, j'utilise les données publiées par le relevé xCOLD GASS, un projet qui a observé l'émission CO de 532 galaxies proches.

Le pendant de ce projet pour le gaz atomique est le relevé xGASS, qui observe 1179 galaxies avec le télescope Arecibo.

De la nécessité de la spectroscopie intégrale de champ

La principale limitation des relevés spectroscopiques précédemment cités est qu'ils ne permettent pas une étude spatiale des propriétés physiques du gaz et des étoiles, puisqu'ils ne fournissent qu'un seul spectre par galaxie observée. La spectroscopie intégrale de champ est la technique permettant d'étudier le gaz et les étoiles en différents endroits de la galaxie observée. Elle repose sur la combinaison de l'imagerie et de la spectroscopie. Les données spectroscopiques sont finalement fournies sous forme de cubes de données avec deux dimensions spatiales (ascension droite et déclinaison) et une dimension spectrale (longueur d'onde ou fréquence).

Plan de la thèse

Ce travail de thèse s'appuie sur l'analyse de diverses données observationnelles de galaxies proches, afin d'étudier les mécanismes physiques responsables de la régulation et de l'extinction de la formation d'étoiles.
Le chapitre 2 présente la description du relevé MaNGA, ainsi que la sélection de l'échantillon de 29 galaxies proches sur lequel repose mon travail (échantillon DP/MaNGA).
Le chapitre 3 présente l'analyse des données MaNGA de ces 29 galaxies, afin de relier leurs propriétés morphologiques, structurelles et leur activité de formation stellaire.
Dans le chapitre 4, je décris la procédure innovante d'ajustement de spectres que j'ai appliquée à une galaxie de l'échantillon DP/MaNGA et qui m'a permis de mettre en évidence que ce système correspond en fait à une paire de galaxies en interaction.
Dans le chapitre 5, je m'intéresse au contenu en gaz froid des 29 galaxies DP/MaNGA.

1

Introduction

In this introductory chapter, I will cover some relevant aspects of galaxy evolution to motivate the scope of the work of my thesis.

1 Galaxy properties

The discovery of galaxies as external objects from the Milky Way is a breakthrough in science that can be qualified as recent, since their designation dates from the 1930s. Before that, the Great Debate, also named the Shapley-Curtis debate, opposed these two astronomers on the nature of quite diffuse objects visible in the sky, the so-called nebulae. The former argued that these objects were part of our Galaxy, while the latter claimed that they were distant, extended objects, corresponding to proper galaxies themselves. Eventually, Edwin Hubble measured the magnitudes of Cepheid variable stars within the Andromeda galaxy and by using the calibrated relationship between period and luminosity discovered and established by Henrietta Swan Leavitt (Leavitt & Pickering, 1912), he proved the distances to these stars and thus their extra-galactic nature.

For decades, extragalactic astronomy has developed and made tremendous progress in terms of observation coverage, data quality and data processing efficiency.

1.1 Morphology

All galaxies consist of huge conglomerations of stars, dust and gas whose cohesion is provided by the gravitational force, but they show a variety of morphology. Hubble established the first classification of galaxies entirely based on morphological appearance (Hubble, 1936). Galaxies were mainly sub-divided in three main groups: the spiral, the elliptical and the irregular galaxies. These types are represented by the famous Hubble's "tuning-fork" (see Fig. 1.1). Spiral galaxies encompass the normal spirals and the barred spirals (SB), and both of these groups have types Sa, Sb and Sc, which correspond to different evolutionary types: from a to c, the proportion of gas and young stars becomes larger. Elliptical galaxies do not show any extended disc but look like more or less flattened ellipsoids. They are classified using an index, between 0 and 7, depending on their ellipticity: this index is defined as $10\,\epsilon$ where ϵ is the galaxy ellipticity given by the major and minor axis (respectively denoted as a and b): $\epsilon = (a - b)/a$. The greater the index, the flatter the galaxy. Irregular galaxies do not exhibit any settled structure such as bulge, disc or spiral arms, but they do have an important gas content. S0 galaxies, also called lenticulars, are often considered as intermediate objects between ellipticals and spirals since they

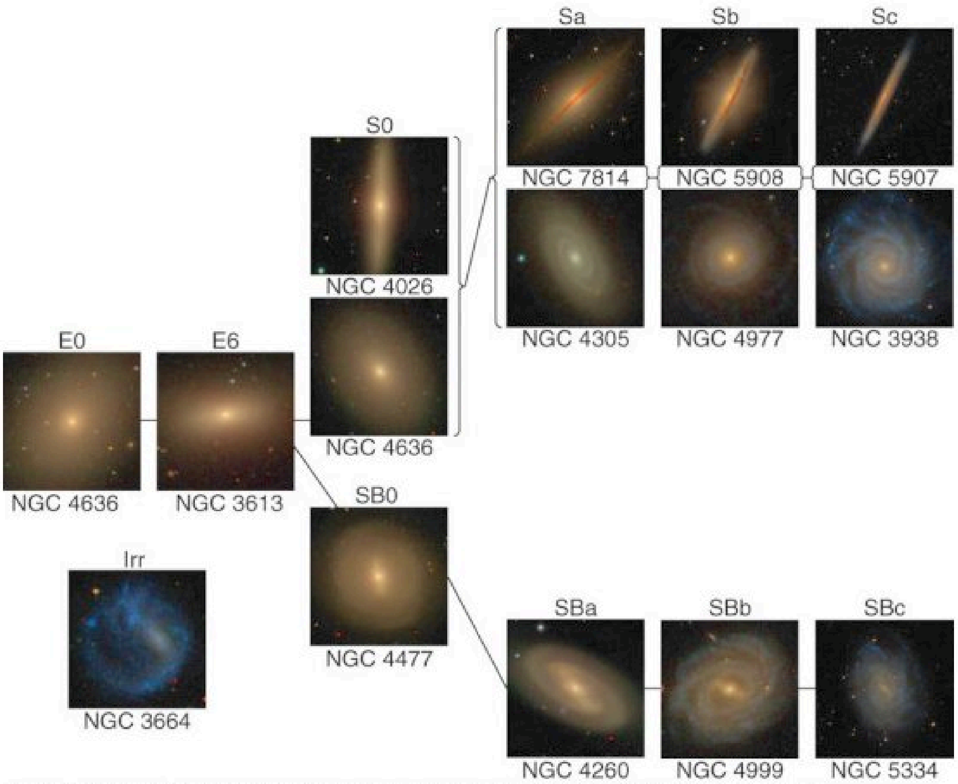

Astrophysical Research Consortium (ARC) and the Sloan Digital Sky Survey (SDSS) Collaboration, http://www.sdss.org, courtesy of Michael Blanton (NYU)

Figure (1.1) Hubble's tuning fork depicted with false-colour images from the Sloan Digital Sky Survey.

exhibit a prominent bulge and a disc, which does not contain a lot of gas and dust and does not show spiral-arm like structure though. De Vaucouleurs extended the Hubble classification (De Vaucouleurs, 1959) by complementing the scheme with structural components such as bars, rings and spiral arms. In his scheme, each class of galaxy has an assigned numerical value, defining its Hubble stage and named T. T lies in the range -6 to +10 with negative values for early-type galaxies and positive ones for late-type galaxies. In many current photometric catalogues, the galactic sources are listed with their assigned values, called T-type.

1.2 Surface brightness profiles

Spheroidal (or elliptical) galaxies have usually a surface brightness profile that can be well fitted by a Sérsic profile, also called $R^{1/n}$ profile:

$$I(R) = I_0 \exp\left[-\beta_n \left(\frac{R}{R_e}\right)^{1/n}\right] \tag{1.1}$$

where I_0 is the central surface brightness, n is the Sérsic index and R_e is the effective radius enclosing half of the total light. The greater the value of n, the more centrally concentrated the profile. The specific case of $n = 4$ is called the de Vaucouleurs profile and is used to describe elliptical galaxies. For $n = 1$, Eq. 1.1 corresponds to an exponential profile, that can be used to describe the light distribution of the disc of a spiral galaxy. The exponential profile is usually denoted as

$$I(R) = I_0 \exp\left(-\frac{R}{R_d}\right) \tag{1.2}$$

where R_d is the exponential scale length. So as to decompose the surface brightness of spiral galaxies between the bulge and the disc components, one uses a Sérsic and an exponential profile, respectively.

1.3 Colour distribution

Another property that obviously varies from galaxy to galaxy is the apparent colour. It is determined by the stars that populate the galaxy and given that the specific colour of a star depends on its age and mass, studying the photometry of a galaxy provides information about the stellar population and the evolution stage of this galaxy. Different photometric systems have been established to describe the colour of astronomical objects. These photometric systems rely on different filters, characterised by their central wavelength and their width.

A commonly-used system is the UBV system, initially introduced by Harold Jester Johnson. It is based on the respective ultraviolet, blue and visible magnitudes. This photometric system is completed by the Cousins RI system and one refers to $UBVRI$ Johnson-Cousins system when considering the combination of both. The Sloan Digital Sky Survey (York et al., 2000) considers u, g, r, i, z passbands, used at the 2.5m telescope at Apache Point Observatory, that are constructed to minimise overlaps and gaps between the filters (Fukugita et al., 1996); and imaging data have also been collected with the u', g', r', i', z' system, used at the 1m telescope at the United States Naval Observatory (USNO) (Smith et al., 2002). The latter system is very similar to the u, g, r, i, z system. The magnitude of a galaxy in a band is a measure of the luminosity of this object falling in the given band. A colour is defined as a difference between two magnitudes (for instance $g - r$ or $u - r$). Table 1.1 gathers the properties of the filters of $UBVRI$ and u, g, r, i, z systems and Fig. 1.2 shows the corresponding transmission curves.

	$UBVRI$			SDSS	
	λ_eff(Å)	$\Delta\lambda$(Å)		λ_eff(Å)	$\Delta\lambda$(Å)
U	3663	650	u	3551	581
B	4361	890	g	4686	1262
V	5448	840	r	6166	1149
R	6407	1580	i	7480	1237
I	7980	1540	z	8932	994

Table (1.1) Effective wavelengths and widths of the filters of the broad-band $UBVRI$ and u, g, r, i, z systems (Stoughton et al., 2002).

K-correction

The flux observed in a band $\Delta\lambda$ around a wavelength λ has been emitted in a band $\Delta\lambda' = \Delta\lambda/(1+z)$, where z is the redshift of the source. So as to compare the colours of two sources with different redshifts, the fluxes must be corrected, this is called the K-correction (Oke & Sandage, 1968). This quantity relates the apparent flux of the source received in a given photometric bandpass to its intrinsic flux emitted in the original bandpass. Let a source observed through a bandpass R, located at a luminosity distance D_L, and for which the absolute magnitude in the emitted bandpass E is to be determined. The K_{ER} correction is then defined by:

$$m_R = M_E + D_M + K_{ER} \tag{1.3}$$

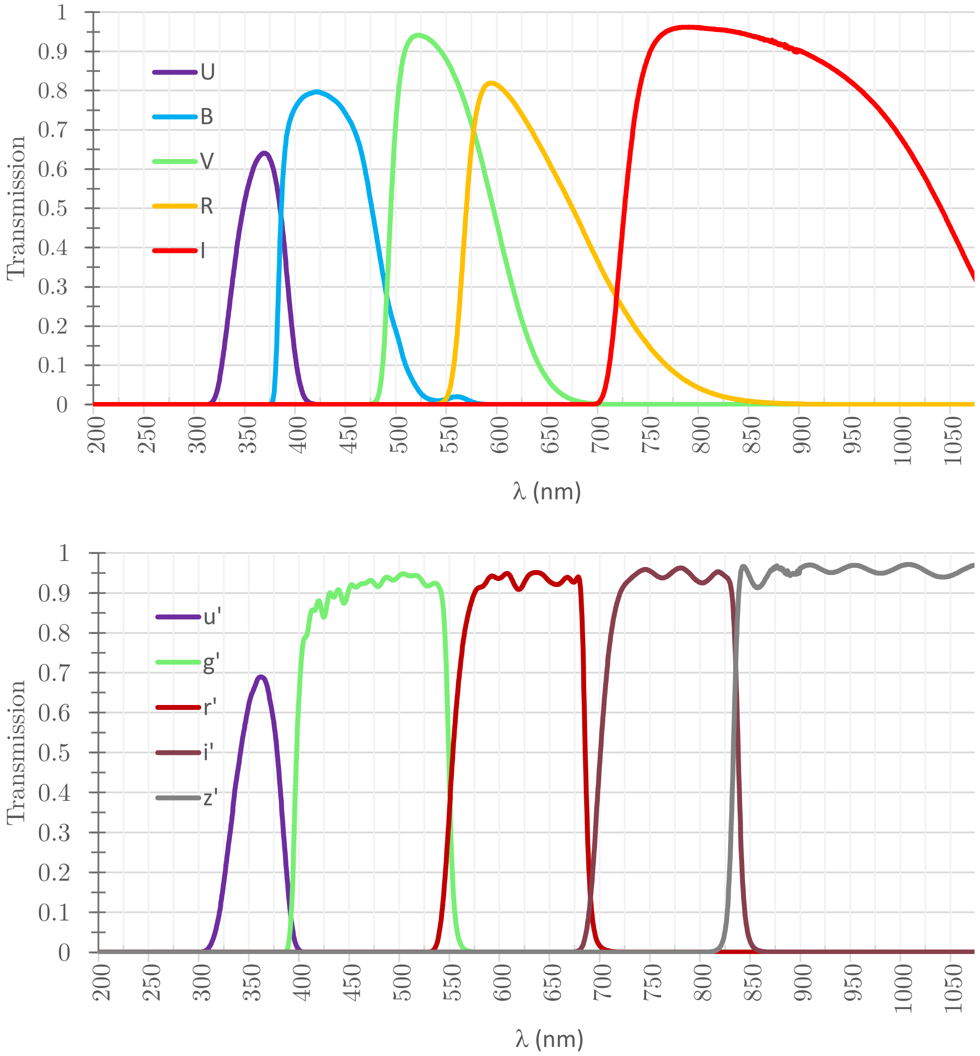

Figure (1.2) Normalised passbands of the Johnson-Cousins $UBVRI$ filters (**top panel**) and of the u', g', r, i', z' filters (**bottom panel**).

where the distance modulus D_M is defined by $D_M = 5\log_{10}\left[\frac{D_\mathrm{L}}{10\,\mathrm{pc}}\right]$.

Based on this formalism, Chilingarian et al. (2010) developed a K-correction estimate based on a minimal set of observables, namely an observed colour and the redshift of the source (see also Blanton & Roweis, 2007).

1.4 Interstellar medium content within galaxies

The interstellar medium (ISM) is made of dust and gas. Its life cycle is closely linked to the galaxy evolution: the gas is converted into stars, it may be ejected or stripped out through winds or interactions. Gas inflows from the intergalactic medium can also increase the amount of ISM.

1.4.1 Dust

Dust refers to solid particles, with a size in the range $0.01 - 1\mu$m, and formed of various elements such as silicate, carbon or iron, that are mixed with the interstellar gas. Dust grains absorb, scatter and re-emit at longer wavelengths the starlight and are in that way responsible for the reddening of the observed interstellar medium. Dust plays also an important role in gas evolution, as it catalyses the formation of molecules through atom adsorption on the grains.

1.4.2 Gas content

Whereas gas only represents a modest fraction of the total mass of the galaxy, which is dominated by the dark matter halo, it corresponds to the reservoir for star formation and therefore is a key component to depict galaxy evolution. Probing gas content, distribution and kinematics in galaxies requires the use of complementary data in multiple wavelength domains. The interstellar gas is principally composed of hydrogen, but also of about 25% of helium and other heavier elements in small amounts. It can be observed in different phases which are briefly described here below. Gas can be converted from a phase to another depending on the ionisation, temperature and on the potentially dissociative radiation of the region in which it evolves.

1.4.2.1 Neutral medium

It is predominantly composed of diffuse warm ($T \approx 10^{3.7}$K) and cloudy cold ($T \approx 10^2$K) atomic gas, namely HI. For galaxies with $z < 0.06$ (in order to achieve a sufficient sensitivity), the neutral content can be probed through the HI 21 cm line (see Sect. 4) observation.

1.4.2.2 Molecular gas

The cold gas refers to molecular gas (the most common being H_2, but other species such as CO, HCN are also present). It can be found in diffuse clouds ($n_{\rm H} \sim 100{\rm cm}^{-3}$) or in dense regions ($n_{\rm H} > 10^3{\rm cm}^{-3}$) that are heavily obscured. Star formation occurs in these gravitationally bound structures.

1.4.2.3 Ionised gas

Ionised gas itself can also be decomposed into two phases:

- The hottest one is called the coronal gas, so named because of its temperature and ionisation state that are comparable to the Sun corona, and corresponds to shock-heated gas with low density ($n_{\rm H} \sim 10^{-4}{\rm cm}^{-3}$). It is also referred to as the hot ionised medium.

- Last, the HII gas will be discussed at length in the course of the manuscript. This gas is photoionised by young, hot stars and can reach a temperature of $T = 10^4$K. It is distributed either in fairly low-density medium ($n_{\rm H} = 0.2{\rm cm}^{-3}$) or in dense regions ($n_{\rm H} = 10^4{\rm cm}^{-3}$), called HII regions.

Optical spectral features such as absorption and emission lines enable the source of the gas ionisation, the temperature and density of the medium to be determined.

2 Star formation activity and quenching in galaxies

2.1 Star formation law

As discussed in Sect. 1.4, the interstellar medium of galaxies is a multiphase environment. Star formation takes place in the densest regions of molecular clouds. Observations have nevertheless shown that its efficiency, defined as the fraction of gas mass converted into stellar mass, is relatively low (1-5% in local galaxies, Kennicutt & Evans, 2012), and increases with redshift (Tacconi et al., 2018). Based on observations, the star formation law is written as a power-law relation between the star formation rate (SFR) surface density, $\Sigma_{\rm SFR}$, and the gas surface density $\Sigma_{\rm gas}$:

$$\Sigma_{\rm SFR} = \Sigma_{\rm gas}^{N} \tag{1.4}$$

This relationship is called the Schmidt-Kennicutt law (Schmidt, 1959; Kennicutt, Jr., 1998). A slope $N = 1.4$ reproduces well the observational data (Kennicutt & Evans, 2012).

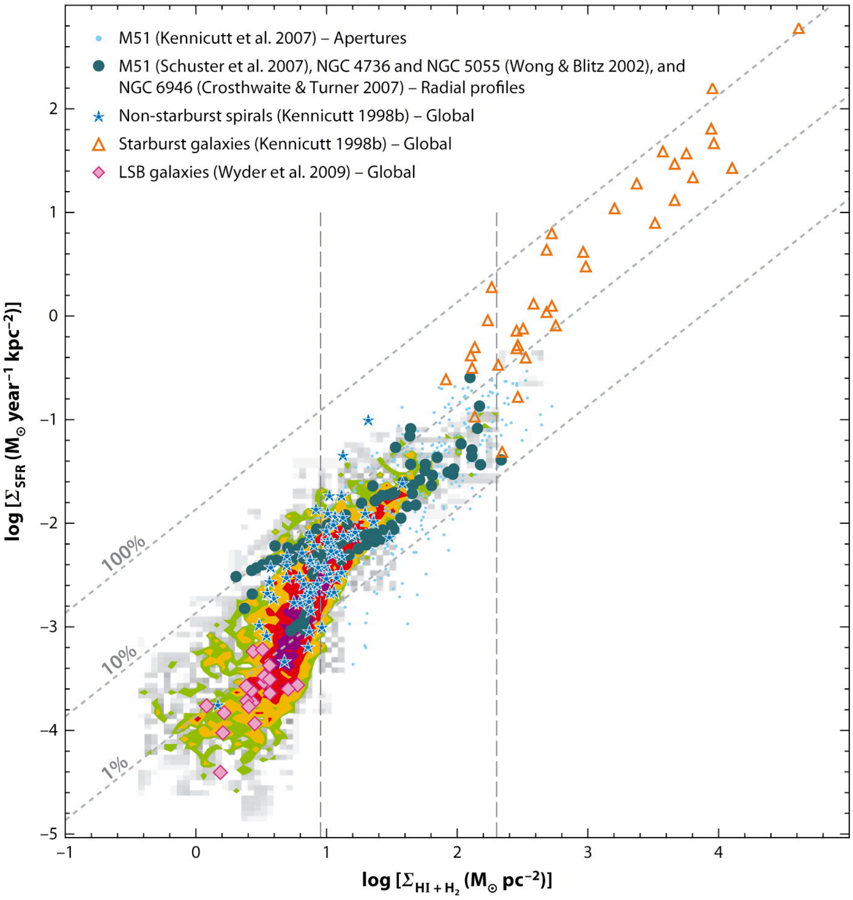

Figure (1.3) Relation between star-formation-rate density and cold (atomic and molecular) gas surface density for different datasets. The coloured contours denote the data from a sample of seven nearby galaxies at kpc-scale (Bigiel et al., 2008). The data points are colour-coded as shown in the legend. The grey dotted lines refer to the star formation law obtained with a constant star formation efficiency. The vertical dashed lines divide the plot, from left to right, into a low-density regime, an intermediate regime and a high-density regime. The first one corresponds to an inefficient star formation process, the second is typical of the central regions of normal spiral galaxies and the third is characteristic of starburst galaxies. Figure from Kennicutt & Evans (2012).

The initial mass function

The evolutionary path of a star is primarily determined by its mass. When studying the processes related to the triggering, the regulation and the termination of star formation, one has to rely on tools that make it possible to parametrise the masses of stars at their birth. Salpeter (1955) introduced the Initial Mass Function (IMF), $\phi(m)$, which gives the number of new born stars of a given mass, written as a power law:

$$\phi(m) = dN/dm \propto m^{-\alpha} \tag{1.5}$$

where N is the number of stars of mass m; and suggested $\alpha = -2.35$. His study excluded low-mass stars with $M_\star < 0.4 M_\odot$. More recently, larger amounts of data enabled alternatives to be explored and Kroupa (2001) proposed a broken power law, while Chabrier (2003) defined a lognormal distribution. Figure 1.4 displays the trends of some widely used IMFs.

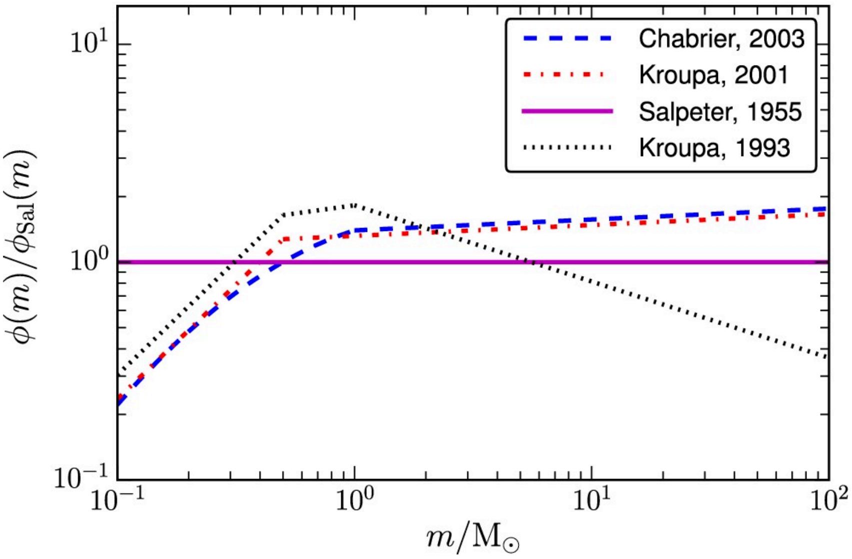

Figure (1.4) Trends of different IMFs. The IMFs are normalised with respect to the Salpeter parametrisation. Figure from Vincenzo et al. (2016).

2.2 Bimodality observed within galaxies

Colour bimodality

Large surveys from the last decades provided a huge quantity of data and enabled the physical properties of galaxies to be studied. It was thus observed that galaxies in the Local Universe show a bimodal distribution in the colour-magnitude and colour-mass diagrams (e.g. Strateva et al., 2001; Baldry et al., 2004; Wyder et al., 2007; Schawinski et al., 2014). Most of the galaxies are distributed in two sequences: a blue cloud, formed by active, star-forming galaxies, and a red sequence, encompassing quiescent objects. The region lying between these two groups is called green valley, and is thought to be an intermediate zone populated by transitional galaxies (Salim, 2014). The observed bimodality is clear in the colour-stellar mass diagram and colour-magnitude diagram (as shown in Fig. 1.5) as well as in the SFR-stellar mass diagram. Some authors studied this classification by using different diagrams, such as the $u-g$ versus $g-J$ diagram that makes possible to discriminate dusty red galaxies from the passive red ones (Schawinski et al., 2014). Williams et al. (2009) highlighted a bimodal distribution in the $U-V$-$V-J$ plane (UVJ diagram) out to z∼2. Galaxies belonging to the blue cloud are mostly late-type and irregular objects, while galaxies in the red sequence are principally early-type galaxies, even though some observations reveal nonetheless that some objects do not follow this trend (e.g. blue E-S0 galaxies found in the blue cloud, Kannappan et al., 2009).

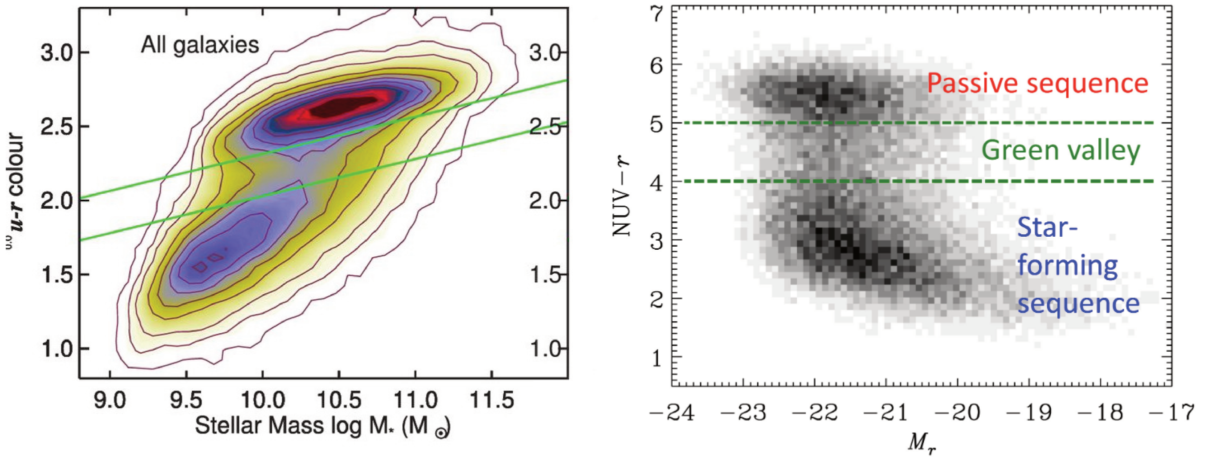

Figure (1.5) **Left panel:** $u - r$ colour-stellar mass diagram based on data products from the SDSS Data Release 7 (York et al., 2000; Abazajian et al., 2009). Contours show the linear density of galaxies and green lines display the location of the green valley, appearing as a "dip between bimodal colours". Adapted from Schawinski et al. (2014). **Right panel:** NUV-r colourvs. magnitude diagram based on the $z < 0.22$ GALEX/SDSS sample and data from Salim et al. (2007). Dashed green lines indicate the green valley, referred to as a "wide and relatively flat region lying between the peaks formed by star-forming and passive galaxies". From Salim (2014).

Star formation main sequence

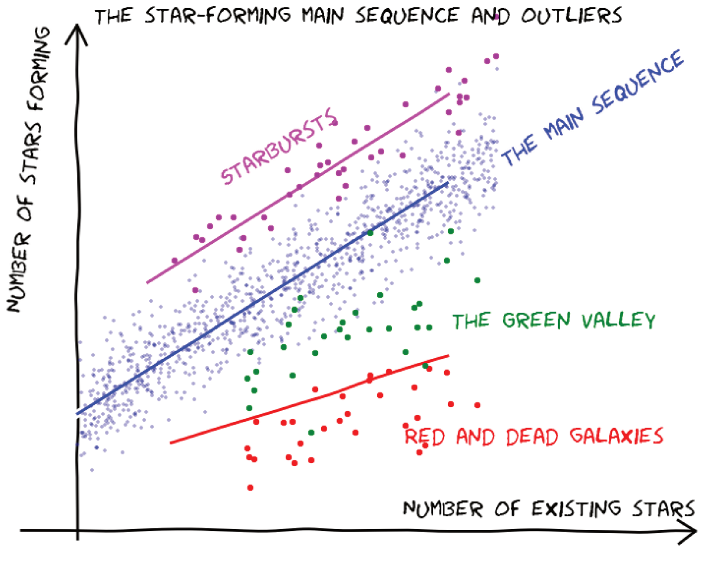

Figure (1.6) Schematic illustration of the star formation main sequence. A majority of galaxies appear to form stars at a rate that is proportional to the number of stars that they already have. Other galaxies do not follow this relation. Drawing from the CANDELS collaboration.

Galaxies in the Local Universe can be classified with respect to their star formation activity. Observational data revealed a strong correlation between the total mass of stars formed per year, the SFR, and the stellar mass, which has been discussed by different groups (e.g. Whitaker et al., 2012; Speagle et al., 2014; Renzini & Peng, 2015) and has since been defined as the star formation main sequence (or SFMS). Nonetheless, a complete consensus about its shape has not been found yet. Some studies such as Speagle et al. (2014) or Pearson et al. (2018) described the relation by a power law:

$$\log\left(\frac{\mathrm{SFR}}{M_{\odot}\mathrm{yr}^{-1}}\right) = \alpha \cdot \log\left(\frac{M_{\star}}{M_{\odot}}\right) + \beta \tag{1.6}$$

but other works support a turn-over of the relation -a shallower slope- at high masses ($\log(M_{\star}/M_{\odot}) \gtrapprox 10.5$, e.g. Tomczak et al., 2016).

2.3 Quenching processes

The termination of star formation is commonly referred to as quenching. It is crucial to probe the mechanisms that trigger and regulate this shutdown, being thus responsible for the transition of a galaxy from the blue star-forming cloud to the red quiescent sequence of the bimodal distribution discussed earlier. These processes are still strongly discussed nowadays and there is no consensus regarding what drives star formation quenching.

One quenching channel is related to the environment in which a galaxy evolves. Quenching can for instance be the result of ram-pressure stripping. A galaxy experiences this process when the intra-cluster gas in which it is moving transfers a dynamical pressure (a ram pressure) P_{ram} that exceeds the surface force that binds the interstellar medium to the disc of the galaxy under consideration. The gas is thus stripped out. Since surface densities decrease with respect to the distance from the galaxy centre, ram-pressure stripping is a process more efficient on the outer parts of the moving galaxy. Ram-pressure-stripping-induced HI-gas tails have been observationally detected (Chung et al., 2007), as well as ionised-gas tails (e.g. Smith et al., 2010; Boselli et al., 2016; Poggianti et al., 2016). Strangulation appears to be another important cause for star formation quenching, as it deprives the galaxy from gas through tidal forces. It affects the surrounding gas, which eventually can fuel the galactic reservoir by infalling and replenishing the interstellar medium, but that is not strongly bound to the galaxy and therefore more easily stripped off. Peng et al. (2015) qualified strangulation as “the primary mechanism for star formation quenching” through stellar metallicity observations.

The shutting down of star formation is not only an environment-related process, it can also be directly linked to the galaxy’s own evolution. Martig et al. (2009) proposed the concept of “morphological quenching” in which the gas content of the galaxy is not affected, but its gas becomes stabilised by a prominent bulge which prevents it from forming stars. The co-evolution of the Active Galactic Nucleus (AGN), present regardless of the morphology (Marleau et al., 2013), and its host galaxy is also a key question to address star formation quenching. On the one hand, the gas reservoir can be heated or even expelled by the release of the mechanical or radiative energy of the AGN to the medium (Heckman & Best, 2014), through outflows for instance (Cicone et al., 2014; Aalto et al., 2020). These processes can reduce or terminate star formation. It is referred to as *negative* feedback. On the other hand, the propagation of jet-driven shocks can precipitate gas cooling and trigger star formation (Best & Heckman, 2012; Ivison et al., 2012), which is called *positive* feedback. Mostly the AGN feedback is described as negative, as only a few objects show evidence of jet-induced star formation (e.g. Charmandaris et al., 2000) (see Combes, 2017, for a mini review).

3 Investigating the ISM through spectroscopy

3.1 Recombination lines

The ionised interstellar medium is traced through emission line observation. These emission lines are produced by electrons that drop down through the energy levels of the atom and their wavelengths depend on the energy difference between the levels.

Some of the strongest emission lines are the ones from hydrogen. Hydrogen gets ionised by photons with an energy above 13.6 eV. The detected line radiation arises from recombination of the electron from the excited state toward the ground state. The radiation is emitted at a wavelength defined by $\lambda = \frac{h\,c}{\Delta \mathrm{E}}$, where h is the Planck's constant, c the speed of light and ΔE the difference of energy between the two states. Measuring the relative intensities of hydrogen recombination lines (Hα, Hβ) can be used to evaluate the dust reddening on the line of sight. This method will be detailed in Sect. 3.3. Different cases of recombination can be distinguished: Case A: the region under consideration is optically thin to all emitted ionising photons, so each of them can escape; Case B: the region is optically thick, so the recombinations to ground state produce photons that are absorbed in their turn.

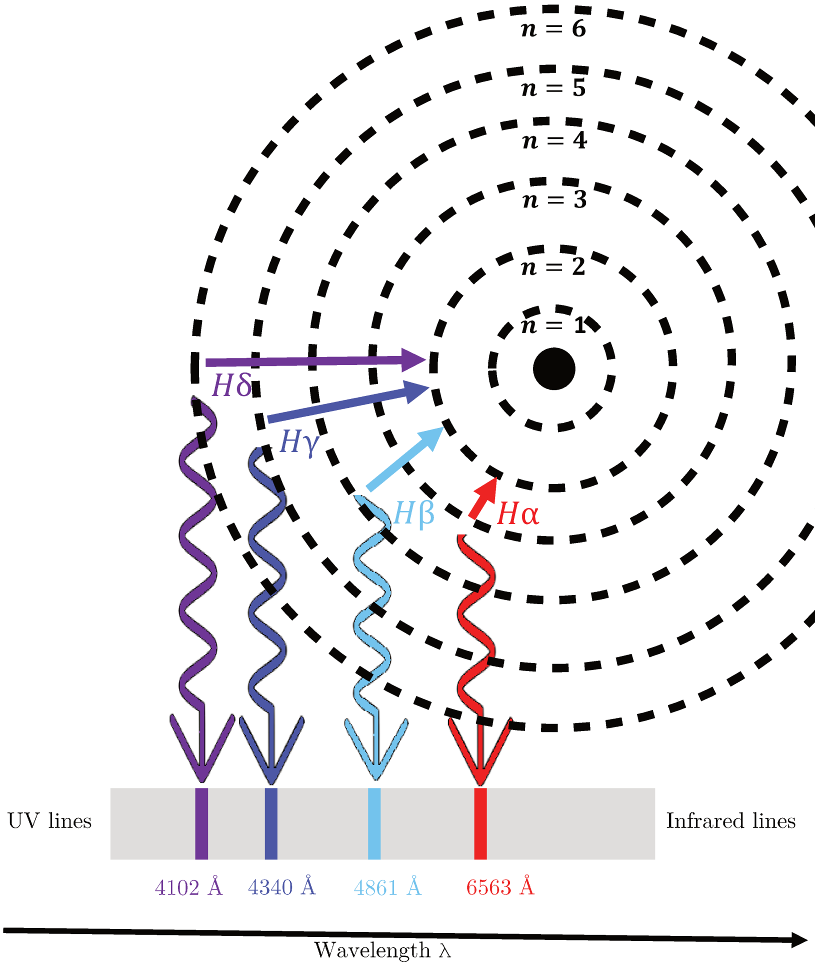

Figure (1.7) Schematic illustration of the Balmer lines. The dashed circles represent the energy levels at which the electron can get ionised. The coloured bands refer to the spectral lines resulting from the recombination processes.

- Other astrophysically important transitions are the forbidden lines of ions such as nitrogen, oxygen and sulfur, denoted [NII], [OIII] and [SII]. The interstellar space has indeed a very low density and thus collisions are rare and do not depopulate excited levels of energy, therefore forbidden transitions can happen.

Equivalent widths

As mentioned in the previous section, emission lines provide information about the region in which they were formed. But they are not the only spectral features that make possible to investigate the stellar content of a galaxy. The equivalent width (EW) provides a way to describe the relative strength of a line with respect to the continuous emission. It is defined as the width of a rectangular line profile whose height equals the continuum level and whose area is the same as the measured line. A schematic representation of the equivalent width of an emission line is displayed in Fig. 1.8.

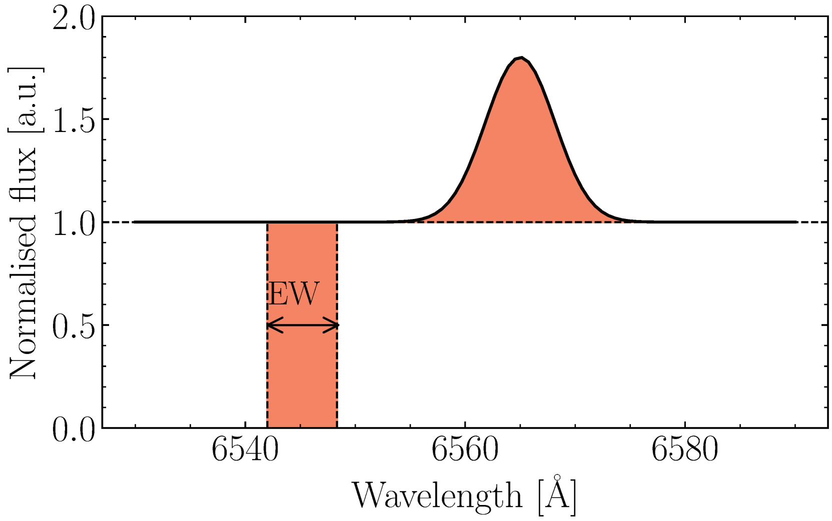

Figure (1.8) Illustration of the definition of the equivalent width (here of an emission line). The emission line has a given area (shown in light red below the Gaussian curve) which is equal to the area of the rectangle, whose width is the so-called equivalent width of the considered line.

3.2 Excitation diagnostic diagrams

Usually, the emission lines from HII regions dominate the line emission within galaxies. However, in some objects, the emission lines originate from an Active Galactic Nucleus (AGN). The galaxies where the emission lines from the AGN dominate the spectrum are called the Seyfert galaxies (Seyfert, 1943).

The objects where strong emission lines are observed but essentially from low-ionisation species are called LI(N)ERs: Low Ionisation (Nuclear) Emission Regions (Heckman, 1980). These galaxies have been extensively discussed.

- Baldwin et al. (1981) proposed a diagnostic diagram to distinguish star-forming galaxies from galaxies dominated by AGN by representing the ratios of some emission lines: [OIII]λ5008/Hβ vs. [NII]λ6585/Hα; [OIII]λ5008/Hβ vs. [SII]$\lambda\lambda$6718,6732/Hα and [OIII]λ5008/Hβ vs. [OI]λ6301/Hα. One refers to these plots as the BPT diagrams (an illustration is shown in Fig. 1.9). Since this diagnostic involves line ratios of close wavelengths, the effect of dust extinction on these line pairs is negligible.

Kewley et al. (2001) defined a demarcation line between the regions occupied by starbursts and objects with another excitation mechanism, in all three BPT diagrams, based on photoionisation modeling. Kauffmann et al. (2003) revised the demarcation by defining an empirical pure star formation line in the first diagnostic plot (representing [OIII]λ5008/Hβ vs. [NII]λ6585/Hα). Schawinski et al. (2007) established a new empirical Seyfert-LINER separation line.

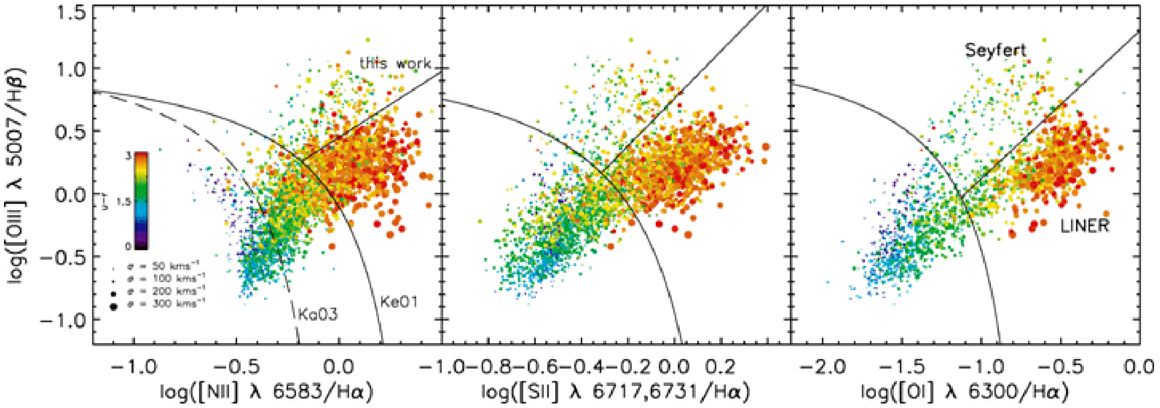

Figure (1.9) Figure from Schawinski et al. (2007). Three BPT diagrams, based on different emission line ratios. The empirical demarcation line between pure star formation and composite excitation is dashed. The solid curved line corresponds to the distinction between the excitation due to starbursts and that due to other mechanisms. The Seyfert-LI(N)ER line is labelled "this work" on the left panel.

- The emission lines [NII]λ6585 and Hα allow for a complementary classification of galaxies between star-forming and quenched ones. The Width of Hα versus NII (WHAN) diagram (Cid Fernandes et al., 2011, displayed in Fig. 1.10) provides a tool to discriminate galaxies hosting a weak AGN from "retired galaxies" belonging to the same classification in the BPT diagram. The so-called "retired galaxies" do not form stars but hot low-mass evolved stars ionise their gas. The classification criteria established by the authors are:
  - Star-Forming (SF) galaxies: $\log_{10}([\mathrm{NII}]/\mathrm{H}\alpha) < -0.4$ and EW(Hα) > 3Å;
  - strong AGN (sAGN): $\log_{10}([\mathrm{NII}]/\mathrm{H}\alpha) > -0.4$ and EW(Hα) > 6Å;
  - weak AGN (wAGN): $\log_{10}([\mathrm{NII}]/\mathrm{H}\alpha) > -0.4$ and $3 <$ EW(Hα) < 6Å;
  - Retired Galaxies (RGs): EW(Hα) < 3Å;
  - Passive Galaxies (PGs): EW(Hα) < 0.5Å and EW([NII]) < 0.5Å.

These last two categories encompass similar objects, but passive galaxies refer to galaxies that can be defined as "lineless".

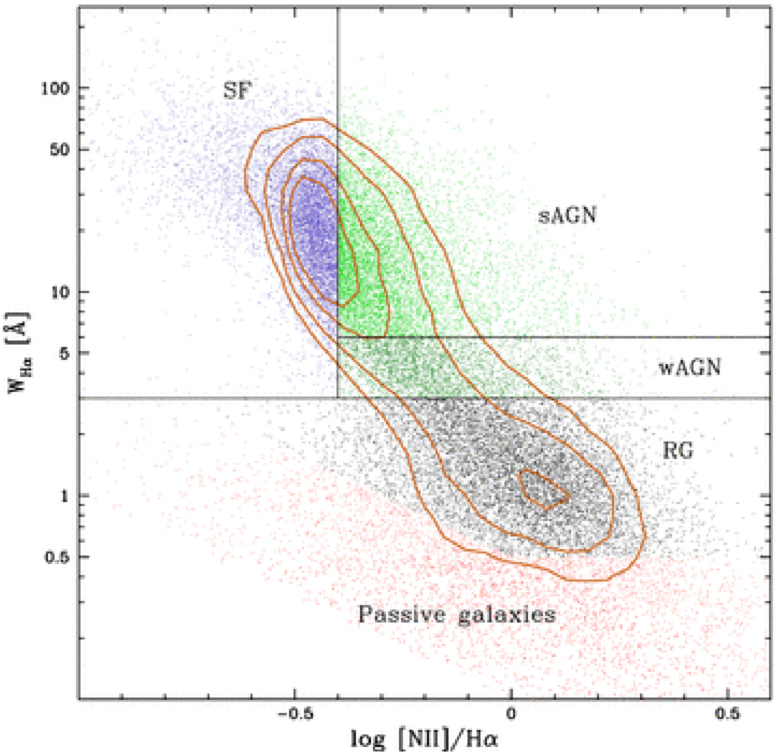

Figure (1.10) Figure from Cid Fernandes et al. (2011). The WHAN diagram with its categories: star-forming (SF), strong AGN (sAGN), weak AGN (wAGN), retired galaxies (RGs) and passive galaxies (PGs). Dots correspond to a sample of 379 330 galaxies from the SDSS DR7. Contours are drawn from a volume-limited sample of 152 749 objects, satisfying $0.04 < z < 0.095$ and $M_r < -20.43$, and represent number densities: 0.1, 0.2, 0.4, 0.6 of the peak value.

3.3 Correction for dust obscuration

Dust has to be taken into account when investigating galactic spectra. It indeed affects both the stellar continuum and the ionised gas emission. For clarity purposes, I would like to make it clear here that I will be referring to dust extinction that strictly speaking denotes the fact that starlight emitted by an embedded source becomes extinguished by a foreground dust screen and scattered out of the line of sight. In reality, the distribution of dust and stars is complex and the scattering can also be into the line of sight. In the latter case, the effect on dust is called attenuation.

Adopting a foreground dust screen, the extinction-corrected flux is computed as follows:

$$F_{\lambda,\mathrm{int}} = F_{\lambda,\mathrm{obs}}\, 10^{k(\lambda)\, \mathrm{E_s(B-V)}} \tag{1.7}$$

where F_{int} is the extinction-corrected flux, F_{obs} is the observed flux, $k(\lambda)$ is the reddening curve at the corresponding wavelength and $\mathrm{E_s(B-V)}$ is the colour excess of the stellar continuum. Different reddening curves can be used (e.g. Fitzpatrick, 1999; Calzetti, 2001). The colour excess of the stellar continuum can be obtained from the colour excess in the nebular lines, which is computed in the optical wavelength range from the Balmer decrement (Domínguez et al., 2013):

$$\mathrm{E(B-V)} = 1.97 \log_{10}\left[\frac{(\mathrm{H}\alpha/\mathrm{H}\beta)_{\mathrm{obs}}}{2.86}\right] \tag{1.8}$$

This formulation assumes an intrinsic Balmer decrement of $(\mathrm{H}\alpha/\mathrm{H}\beta)_{\mathrm{int}} = 2.86$, set by the quantum mechanics when considering a temperature $T = 10^4$K and an electron density of

$n_e = 10^2 \mathrm{cm}^{-3}$ for case B recombination (Osterbrock & Ferland, 2006).

3.4 Star formation rate indicators

Several methods have been developed to estimate the star formation rates (SFRs) in galaxies. The different parts of the electromagnetic spectrum have been studied to derive SFR estimates. One widely-used indicator is the luminosity of the emission line Hα at 6565Å. Since this luminosity originates from the gas photoionised by massive hot stars, it provides a measure of the SFR on a short timescale ($\lesssim$ 10 Myr). For a redshift $z > 2.5$, the Hα line falls beyond the near-infrared atmospheric window and therefore is not a relevant measurement for high-redshift galaxies. The calibration of SFRs from Hα is well defined but is affected by different uncertainties (Kennicutt, Jr., 1998):

- dust absorption of Lyman-continuum photons within HII regions;
- dust attenuation in the interstellar medium;
- shape of the initial mass function.

The emission line measurements can be corrected for dust extinction. The SFR is computed, for a Salpeter IMF , as follows:

$$\left(\frac{\mathrm{SFR}_{\mathrm{H}\alpha}}{M_\odot\,\mathrm{yr}^{-1}}\right) = 7.9 \times 10^{-42} \left(\frac{L_{\mathrm{H}\alpha,\mathrm{corr}}}{\mathrm{erg\,s}^{-1}}\right) \tag{1.9}$$

With the Kroupa IMF , this relation is written as:

$$\left(\frac{\mathrm{SFR}_{\mathrm{H}\alpha}}{M_\odot\,\mathrm{yr}^{-1}}\right) = 5.5 \times 10^{-42} \left(\frac{L_{\mathrm{H}\alpha,\mathrm{corr}}}{\mathrm{erg\,s}^{-1}}\right) \tag{1.10}$$

This relation is slightly different if one considers a Chabrier IMF :

$$\left(\frac{\mathrm{SFR}_{\mathrm{H}\alpha}}{M_\odot\,\mathrm{yr}^{-1}}\right) = 1.2 \times 10^{-41} \left(\frac{L_{\mathrm{H}\alpha,\mathrm{corr}}}{\mathrm{erg\,s}^{-1}}\right) \tag{1.11}$$

where $L_{\mathrm{H}\alpha,\mathrm{corr}}$ is the dust-corrected Hα luminosity. The star formation rate derived from Hα traces the radiation from young, hot stars and thus provides an estimate over the past 20 Myr. However, in the most obscured regions of a galaxy, the ionised gas emission cannot peer through the dust and therefore another star formation rate indicator is required.

The UV range is also powerful to investigate star formation in galaxies since these wavelengths trace the youngest stars. UV emission probes star formation activity over a timescale of $\approx$ 200 Myr. But, as Hα, it is affected by dust. A commonly used SFR is the one derived from the bolometric infrared luminosity ($8 - 1000\,\mu$m). This traces the stellar radiation that is absorbed by dust and re-emitted in the IR range. When not all the IR wavelength range is covered, one can use empirical calibrations at 24 μm or 70 μm. The IR-based SFR estimates suffer from uncertainty for faint galaxies, that are metal-poor, as these objects do not obscure much starlight. With a view to tracing dust-obscured and dust-unobscured star formation, SFR indicators can also mix different wavelengths (for instance FUV and IR, or Hα and IR).

3.5 Stellar population indicators

Lick indices

Lick indices consist of a set of spectral line indices for stars that enable stellar properties such as age and metallicity to be derived. They rely on measurements of spectral absorption features. A Lick index is computed through the comparison of the strength of a band centred on the line position to that of the continuum level and is expressed as a magnitude.

The 4000Å break

The 4000Å break is an additional helpful spectral feature to probe the stellar population properties, notably its age. This drop off in intensity is caused by the absorption of high-energy radiation and the lack of hot, blue -so young- stars. The spectral index D(4000), also sometimes named $D_n(4000)$, has been defined to quantify the strength of the spectral break. The D(4000) value corresponds to the ratio of the integrated flux on a redder bandwidth than 4000Åto the integrated flux on a bluer bandwidth (Bruzual A., 1983).

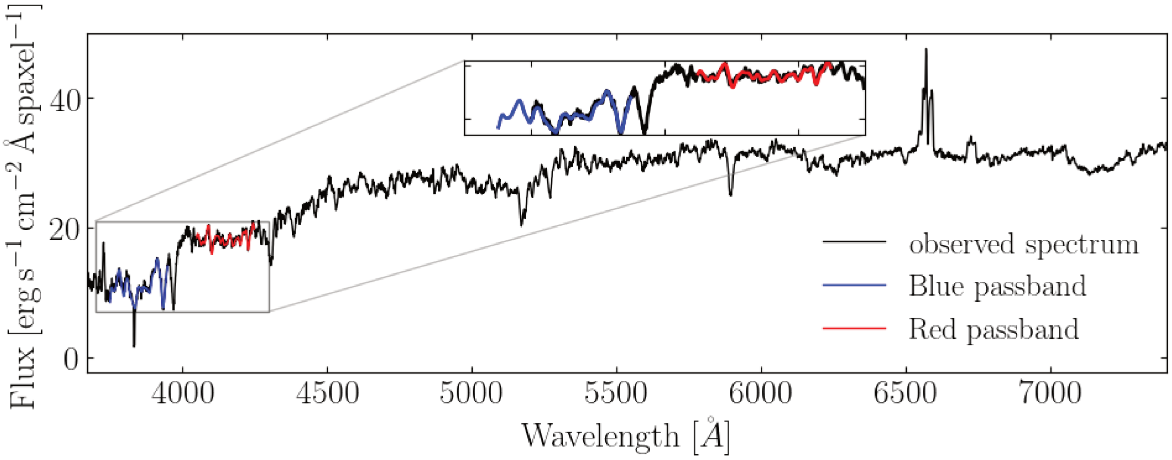

Figure (1.11) Representation of the 4000Å break in the central spectrum of a MaNGA data cube. In the definition used in the MaNGA pipeline, the D(4000) index is computed as the ratio between the flux integrated over the red passband on the one integrated over the blue part.

4 Astrophysical surveys

4.1 SDSS

The Sloan Digital Sky Survey (SDSS, York et al., 2000; Stoughton et al., 2002) provides deep multi-colour images of one third of the sky and spectra for more than three million astronomical objects. The survey uses the 2.5m telescope located at Apache Point Observatory in New Mexico. The survey has been performed in four different phases and a fifth one started in 2020, with a first data release expected in 2022. SDSS-IV published 16 data releases providing a large variety of data-products such as: images, optical spectra, infrared spectra, integral-field-unit spectra, stellar library spectra and value-added catalogue data. I use spectroscopic output data from the SDSS data release 7 (DR7, Abazajian et al., 2009). The data acquisition is made through a pair of fibre-fed spectrographs, providing a wavelength coverage from 3800Å to 9200Å and a spectral resolution in the range $R \sim 1850 - 2200$. The fibre on-sky diameter is $3''$.

4.1.1 RCSED

The value-added Reference Catalog of Spectral Energy Distributions (RCSED, Chilingarian et al., 2017) of galaxies gathers spectrophotometric data for 800,299 galaxies at low and intermediate redshift (0.007<z<0.6) taken from the Sloan Digital Sky Survey sample. The provided properties such as gas-phase metallicity, extinction, are derived from the SDSS spectra.

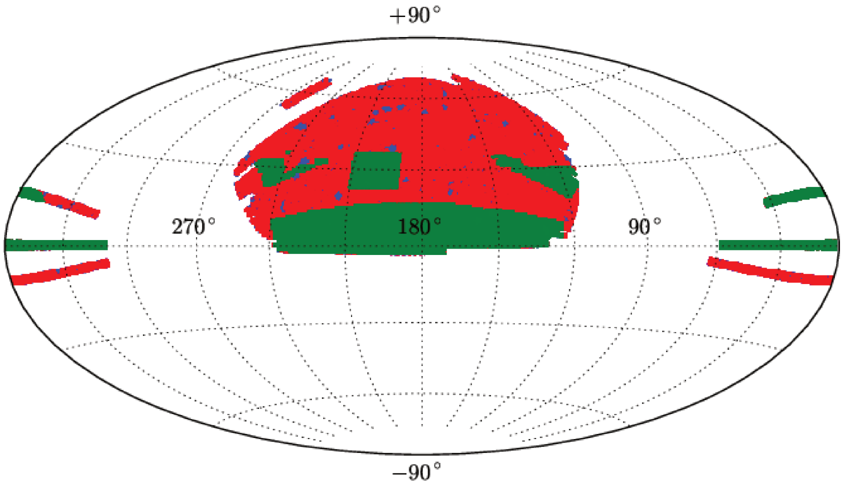

Figure (1.12) Footprint of the RCSED catalogue, taken from Chilingarian et al. (2017). Green areas stand for the availability of all three photometric datasets: SDSS, UKIDSS and GALEX; red areas denote SDSS and GALEX; and blue areas are for SDSS only.

4.2 The DECam Legacy survey

Another survey that I make use of throughout my work is the Dark Energy Camera Legacy survey (DECaLS). It is part of the DESI Legacy Imaging Surveys (Dey et al., 2019). The DECaLS provides photometry in the g, r and z bands, acquired at the Blanco 4m telescope. The pixel scale is 0.″263/pixel (Flaugher et al., 2015). Fig. 1.13 shows the footprint of the DESI surveys, with DECaLS in light-blue.

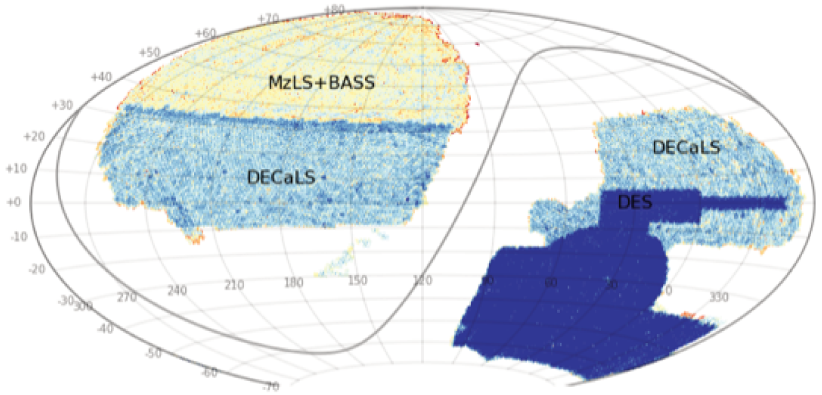

Figure (1.13) Footprint of the DESI Legacy Imaging Surveys as of Data Release 9.[1]. The colour-coding refers to depth in the r-band.

---

[1] Source: https://www.legacysurvey.org/status/

4.3 xCOLD GASS

xCOLD GASS (extended CO Legacy Database for GASS, Saintonge et al., 2017) combines observational data of two IRAM 30m large programmes. It measures CO emission in 532 nearby galaxies ($0.01 < z < 0.05$) from the SDSS and consists of a mass-selected sample (10^9-$10^{11.5}\ M_\odot$). These measurements are complemented by CO(2-1) data from IRAM 30m and APEX telescopes. It provides molecular gas measurements of objects that span the entire SFR $- M_\star$ and can be used as a reference for studies of the molecular gas content in nearby galaxies.

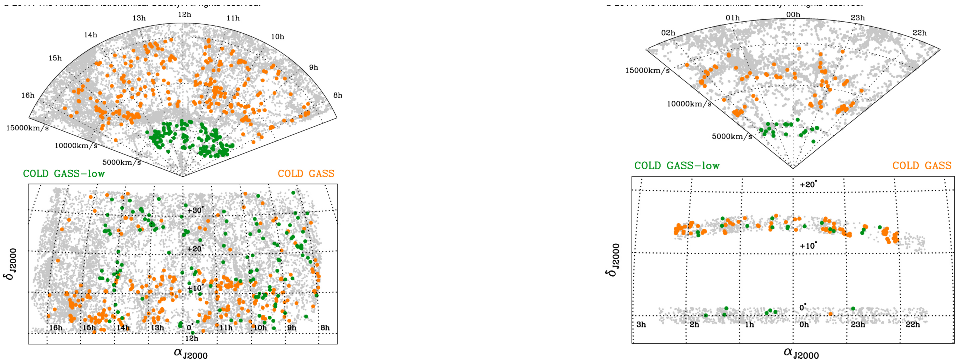

Figure (1.14) Distribution of the xCOLD GASS targets, taken from Saintonge et al. (2017). Left panels show the sample with $8\,\text{hr} < \alpha_{\text{J2000}} < 16.0\,\text{hr}$ and right panels the sample for $22\,\text{hr} < \alpha_{\text{J2000}} < 2.5\,\text{hr}$. For both, the top row displays the source distribution in the redshift-right ascension plane and the bottom row as projected on the sky.

4.4 xGASS

The extended GALEX Arecibo SDSS Survey (xGASS, Catinella et al., 2018) is the twin project of xCOLD GASS which consists of an Arecibo survey of atomic gas of 1179 nearby galaxies.

5 Need for integral field spectroscopy

The astrophysical surveys previously cited are fruitful but show limitations. Output data of a survey like SDSS consist of one spectrum per galaxy, from which spatial properties cannot be inferred. With a view to investigating spatially-resolved characteristics of the galaxies, integral field spectroscopy has emerged and has now been used for decades (e.g. VLT/MUSE Henault et al. (2003), UKIRT Image Spectrometer Wells et al. (2000), JWST/MIRI Medium Resolution Spectrometer Wells et al. (2015)). It relies on the combination of imaging and spectroscopy. The observed object is sampled in a data product called data cube, since it contains one spectral and two spatial dimensions. Therefore this technology is also called “3D spectroscopy”. Given the data structure, a slice of the data cube represents a monochromatic image while a data cube column along the spectral axis corresponds to a spectrum. Some specific terms have been created to refer to integral field spectroscopic data. The spatial element enclosing one spectrum is called *spaxel*. In comparison with long-slit spectroscopy, the integral field spectroscopy makes possible to observe the whole object and thus to represent the derived properties as 2D maps rather than 1D plots. Imaging spectroscopy can be described by three main concepts based on three kinds of instruments: the scanning spectrometers (Fabry-Perot, Fourier transform spectrometers as SITELLE, Drissen et al. (2019)), the integral field spectrographs and the energy-resolving detectors. The description in this section will on purpose not be exhaustive and I will only detail the use of integral field spectrographs, as these instruments are at the heart of my thesis work. As shown in Fig. 1.15, the integral field spectrographs are themselves divided into different classes. I will focus on the one displayed on the second row of the figure above, using fibres, since this technique is the one used for the acquisition of the data that I analyse throughout my PhD work. The fibres are arranged as a bundle located in the focal plane. This conception induces an incomplete fill factor and a non-contiguous sampling. In order to remedy this drawback, the fibre array and a lenslet array can be combined at the entrance of the integral field unit, or, like in the case of the MaNGA spectrograph, use a dithering pattern of exposures to fill in the information and flux gap. Lenslets can also be used at the output of the fibre bundle to enhance the fill factor at the spectrometer entrance. The fibre concept is illustrated in Fig. 1.16. The spectrograph then reflects light into a CCD camera. Spectroscopic data are finally reconstructed into data cubes with dimensions (right ascension, declination, λ).

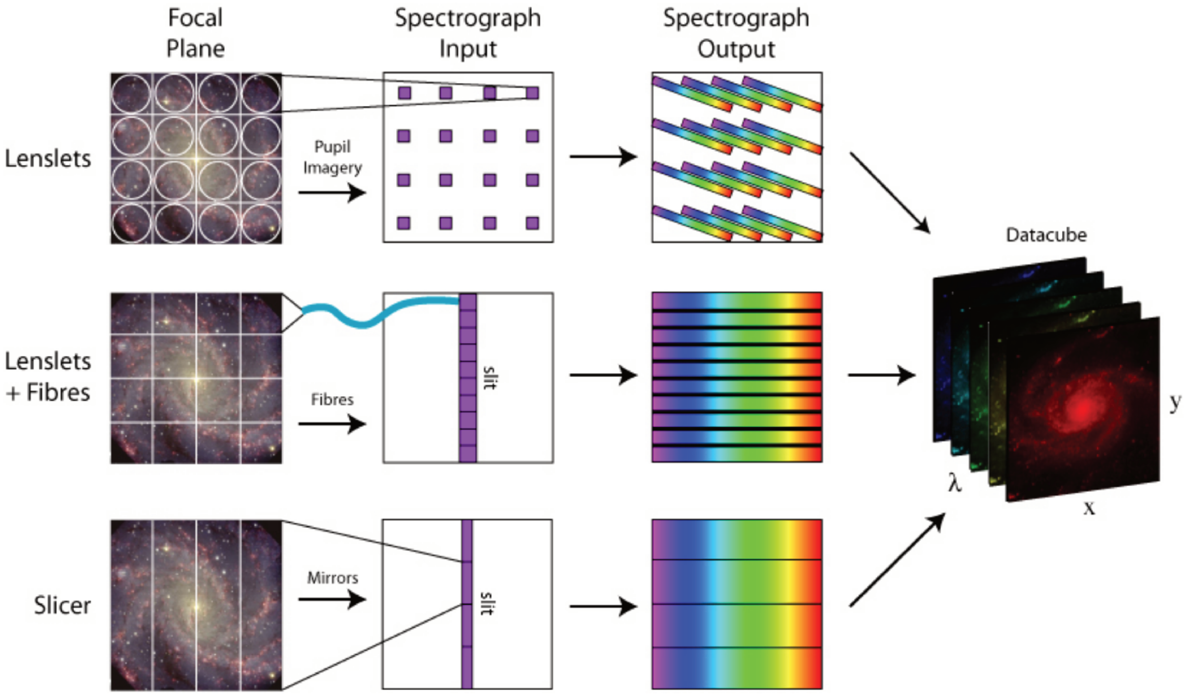

Figure (1.15) Representation of the imaging spectroscopy concept based on integral field spectrographs, taken from Westmoquette et al. (2009) (the initial version comes from Allington-Smith et al., 1998).

The great variety of high-performance instruments allowing for the simultaneous measurement of spatial and spectral information, along with the improvement of the data reduction processes of the complex collected data led to breakthroughs in observational astrophysics.

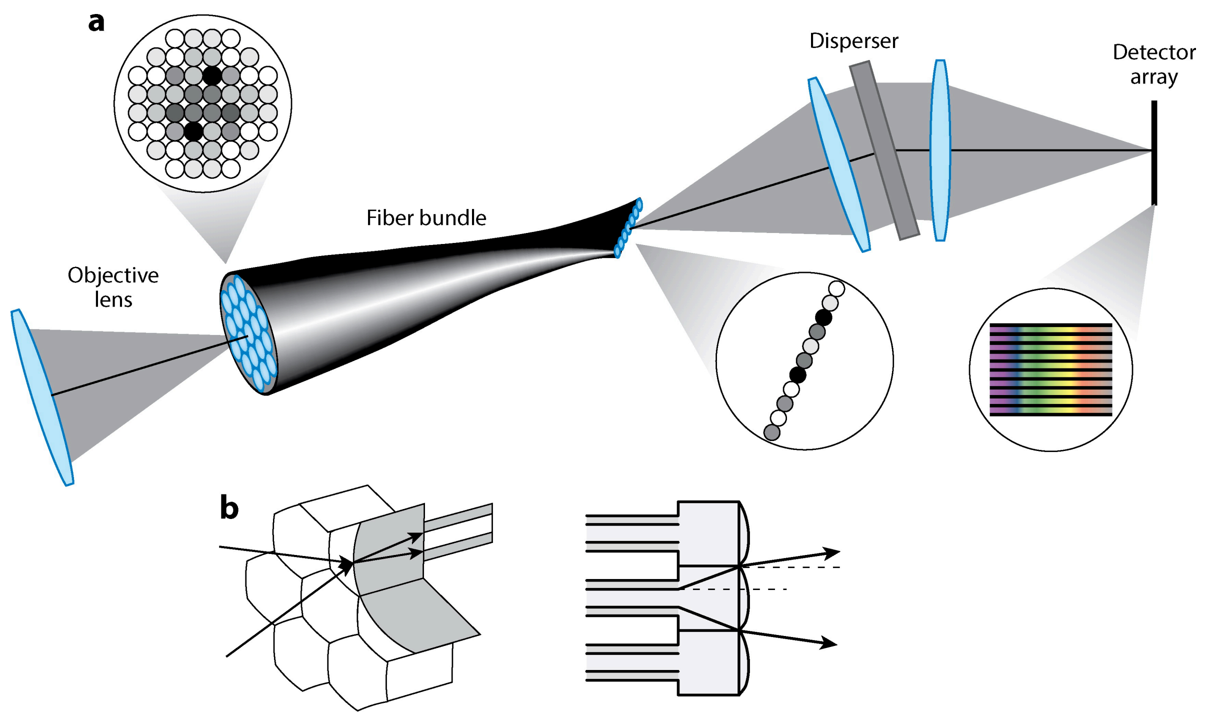

Eisenhauer F, Raab W. 2015.
Annu. Rev. Astron. Astrophys. 53:155–97

Figure (1.16) Illustration of the concept of fibre-based integral field spectrographs. From Eisenhauer & Raab (2015). **(a):** A fibre bundle is placed in the focal plane, the ends of the fibres are re-arranged and feed a long-slit spectrograph. **(b):** Lenslets can be used to increase the fill factor.

6 Outline of this thesis

This thesis aims at exploring the mechanisms that regulate and quench the star formation activity in local galaxies. The manuscript is organised into four main parts: Chapter 2 presents the description of the integral-field spectroscopic survey MANGA, as well as the selection of a 29-galaxy sample observed by this survey. Chapter 3 presents the analysis of the MaNGA data to study the morphology, the link between star formation activity and some physical properties of these galaxies. The results in this chapter are in Mazzilli Ciraulo et al. 2021, *submitted*.
In Chapter 4, I describe the innovative multi-component approach that I apply to study the ionised gas. I detail the analysis of one science case among the 29 selected galaxies, which enables us to reveal that this system consists of an interacting pair of galaxies. These results have been published in Mazzilli Ciraulo et al. 2021, A& A, 653, A47.
In Chapter 5, I address the question of the cold gas content of the 29 galaxies, by analysing the neutral and cold gas observations of the 29 galaxies.
Finally, Chapter 6 summarises the main results and conclusions of my PhD project. A description of the future perspectives and how these main findings can be developed further is given.

Observations et analyse des données MaNGA

Dans ce chapitre, je donne une description générale du relevé MaNGA, des principales données que j'ai utilisées ainsi que de l'échantillon de galaxies que j'ai étudié en détail. Ces galaxies proches, que j'appellerai galaxies à doubles pics/MaNGA (DP/MaNGA), ont été sélectionnées car elles appartiennent à la fois à un catalogue de galaxies "à doubles pics" et aux données MaNGA. Elles sont au nombre de 29, couvrent une large gamme de morphologies (spirales, S0, elliptiques, irrégulières) et un facteur de plus de 10 en termes de taux de formation d'étoiles.

Le relevé Mapping Nearby Galaxies à APO

Description du relevé

Mapping Nearby Galaxies at Apache Point Observatory (MaNGA, Bundy et al., 2014) est un relevé de spectroscopie à intégrale de champ faisant partie de la quatrième génération de SDSS. Son objectif est l'étude de la cinématique du gaz et des étoiles dans 10000 galaxies proches ($z < 0.15$) avec des masses stellaires telles que $M_\star > 10^9 M_\odot$. Les caractéristiques du relevé sont présentées dans le tableau 2.1.

Données MaNGA

La collaboration MaNGA fournit des cubes de données avec deux dimensions spatiales (ascension droite et déclinaison) et une dimension spectrale (la longueur d'onde en Å). Il existe des cubes avec un échantillonnage spectral linéaire et logarithmique. Pendant l'ajustement des spectres, deux schémas de *binning* sont réalisés : un *binning* de Voronoï avec un rapport signal sur bruit cible fixé à 10 (dans le filtre SDSS g) et un *binning* hybride pour lequel les spectres sont "binnés" pour ajuster le continuum stellaire mais les raies d'émission sont ajustées spaxel par spaxel. La figure 2.2 illustre ces deux schémas en montrant une carte de flux Hα pour chacun d'entre eux. Le schéma de Voronoï est très efficace pour les galaxies qui ont des distributions assez «lisses», mais il n'est pas optimal pour les galaxies dans lesquelles on trouve des régions concentrées et diffuses contiguës, dans la mesure où la procédure mixerait des régions aux propriétés physiques très différentes. On voit en effet sur la figure 2.2 que le schéma de Voronoï «dilue» l'émission dans la galaxie observée.

La collaboration MaNGA utilise l'outil *"penalized-PiXel Fitting routine"* (pPXF, Cappellari & Emsellem, 2004) pour ajuster le continuum stellaire. La figure 2.3 montre un exemple de spectre extrait d'un cube de données, ainsi que le meilleur modèle pour le continuum stellaire et le spectre résultant après la soustraction de ce modèle.

Catalogues à valeur ajoutée

Divers catalogues à valeur ajoutée sont disponibles et contiennent des propriétés supplémentaires sur les galaxies MaNGA. Afin d'étudier les 29 galaxies DP/MaNGA, j'ai utilisé certains d'entre eux:

Catalogues MaNGA PyMorph Photometric (MPP) et MaNGA Deep Learning Morphology (MDLM)

Ces catalogues compagnons sont complémentaires et permettent une analyse morphologique des sources observées par MaNGA. MPP fournit des mesures déduites d'ajustement de profils de luminosité 2D telles que l'indice de Sérsic. Le second contient la classification morphologique des galaxies basée sur une analyse par réseau de neurones.

Catalogue Pipe3D

Pipe3D est un pipeline d'analyse spécialement conçu pour les données de spectroscopie intégrale de champ, dont les détails sont présentés dans Sánchez et al. (2016a,b). Ce catalogue donne les propriétés intégrées, les gradients des propriétés calculées, ainsi que les propriétés spatiales, comme les taux de formation d'étoiles, les masses stellaires, la métallicité. Je suis intéressée par les cartes de masse stellaire, car elles me permettent de déduire des cartes de taux de formation d'étoiles spécifiques (sSFR=SFR/$M_\star$) et donc d'étudier cette propriété de manière spatiale.

HI-MaNGA

HI-MaNGA (Masters et al., 2019) est un programme de suivi de MaNGA qui vise à réaliser des observations HI de plus de 3000 galaxies MaNGA à $z < 0,05$ avec le Green Bank Telescope (GBT). La deuxième publication de données (Stark et al., 2021) fournit les mesures basées sur ces observations ainsi que celles issues du relevé ALFALFA (Haynes et al., 2018).

Sélection de l'échantillon

Le travail de ma thèse s'appuie sur un échantillon de 29 galaxies observées par MaNGA, sélectionnées car elles présentent des raies d'émission “à doubles pics” dans leur spectre SDSS. Un exemple d'un spectre dont les raies d'émission ont été ajustées à l'aide d'une double Gaussienne est montré sur la figure 2.4. Ces galaxies sont tirées du catalogue publié dans Maschmann et al. (2020). Pour interpréter l'origine de ces profils de raies, j'utilise les données spectroscopiques à intégrale de champ de MaNGA. Ces données me permettent d'étudier la distribution et la cinématique des différentes composantes observées dans le gaz.

2

MaNGA observations and analysis

In this Chapter, I will give a general description of the MaNGA survey, the principal delivered data products that I have used, as well as the sub-sample that I have focused on to study the mechanisms related to star formation quenching.

This sample comprises galaxies that I will name "double-peaked/MaNGA" galaxies hereafter, which have been selected using a cross-identification between a double-peaked emission-line galaxies catalogue and the MaNGA observations from the SDSS Data Release 15. This sample consists of 29 nearby galaxies, at an average redshift of z∼0.07, spanning a wide range of galaxy morphology (spirals, S0, ellipticals, objects with tidal features) and a factor of more than 10 in terms of Star Formation Rate (SFR).

1 Mapping Nearby Galaxies at Apache Point Observatory survey

1.1 Description of the survey

Mapping Nearby Galaxies at Apache Point Observatory (MaNGA, Bundy et al., 2014) is an integral field spectroscopic survey that is part of the core programs in the fourth-generation Sloan Digital Sky Survey (SDSS-IV). MaNGA aims at studying the gas and star kinematics of 10,000 nearby ($z < 0.15$) galaxies with stellar mass such that $M_\star > 10^9 M_\odot$. The observations were performed between 2014 and 2020. The data acquisition is made through purely fibre-based IFUs. These IFUs are mounted on the Sloan 2.5m telescope where the median seeing is 1.″ and feed the BOSS spectrographs (Smee et al., 2013). Spectrograph 1 (resp. 2) is fed by 709 (resp. 714) fibres. The fibre size corresponds to 2″, the spectral resolution varies with wavelength but has an average value of R∼2000. An hexagonal shape was chosen for the IFUs that are composed of 7 to 127 fibres (see Fig. 2.1), ranging in on-sky diameter from 12.5″ to 32.5″.

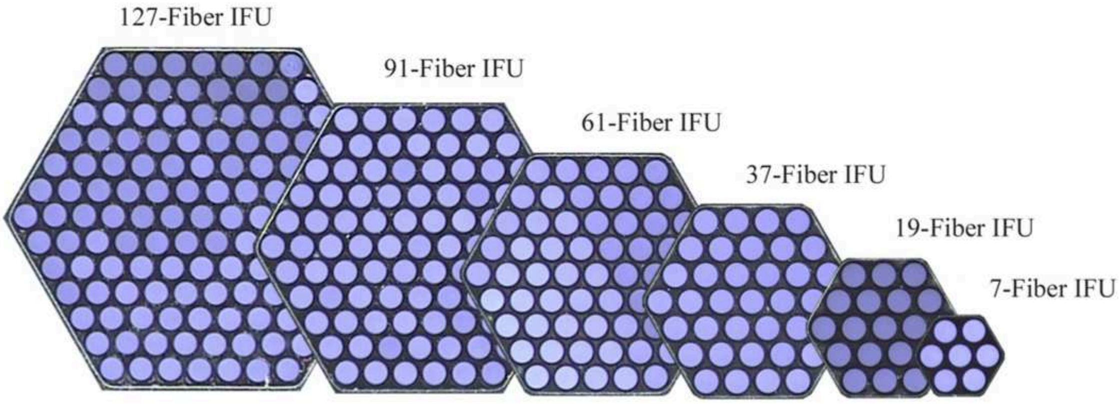

Figure (2.1) Representations of each science MaNGA IFU (from 19 to 127 fibres). Far right a seven-fibre IFU is shown, used for sky calibration. Figure from Bundy et al. (2014).

Table (2.1) Characteristics of the MaNGA IFU survey

Sample size	Selection	Redshift	Radial coverage	S/N at 1 R_e (per spatial sample)	λ range (nm)
10,000	$M_\star > 10^9 M_\odot$	0.01-0.15	1.5 R_e(P+) 2.5 R_e(S)	14-35	360-1030
$\sigma_{\text{instrument}}$ (km s^{-1})	Angular sampling (diameter)	Angular FWHM (reconstructed)	Spatial FWHM (physical)	Spatial FWHM (in R_e)	IFU fill factor
50-80	2”	2.5”	1.3-4.5kpc (P+) 2.2-5.1kpc (S)	0.2-0.6 (P+) 0.3-0.9 (S)	56%

1.2 MaNGA output products

As for any integral field spectroscopic survey, the MaNGA data products consist of data cubes with two spatial dimensions ($N \times N$, where N is the number of spaxels along the right acsension or the declination axis) and one spectral dimension (here the wavelength λ, in Å). The collaboration provides different types of data cubes: the reduced cubes contain the observed spectra, with a linear or logarithmic wavelength sampling, after calibration and reduction. The derived spectral quantities are provided in the MAPS and MODEL cubes. The former contain the measurements of spectral indices, emission-line fluxes, velocity and velocity dispersion as 2D maps, while the latter enclose the results of the stellar continuum modelling. During the fitting of the spectra, two binning schemes are performed: a Voronoi binning with a signal-to-noise ratio target set at 10 (in the broad-band SDSS g filter) and an hybrid binning for which the spectra are binned to fit the stellar continuum but the emission lines are fitted spaxel per spaxel. The Voronoi binning creates spatial bins of different sizes that reach a signal-to-noise ratio target. This procedure is very efficient for galaxies that do not have clumpy structures. Nonetheless, for objects for which emission lines do not follow the stellar continuum (strong lines but weak continuum for instance), or for which there are contiguous concentrated and diffuse regions, the Voronoi binning scheme is not optimal, as it ends up by mixing regions with no similar physical properties. One can see in Fig. 2.2 that the clumpy emission is diluted by the Voronoi binning scheme applied to the considered galaxy.

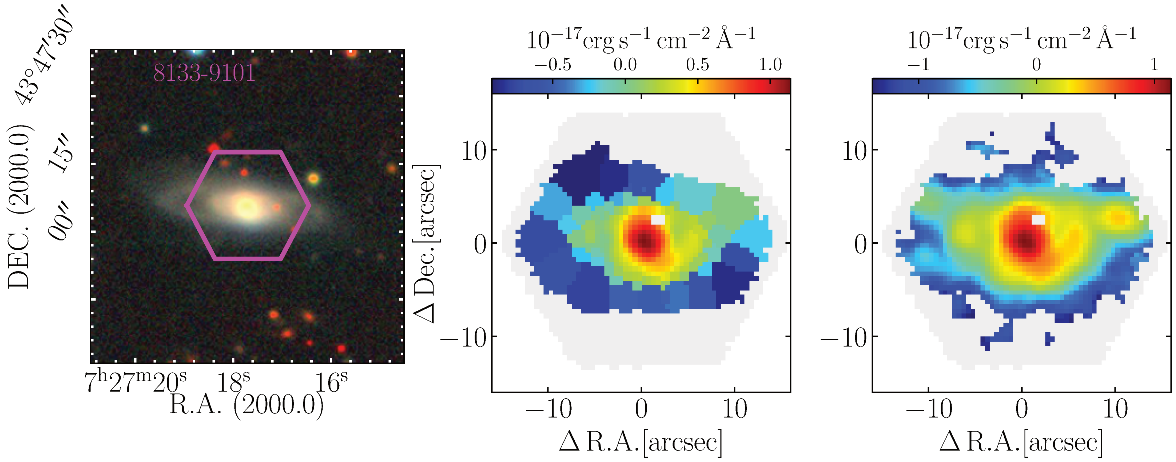

Figure (2.2) Illustration of the two available binning schemes for the MaNGA data products. The left panel shows the g, r, z snapshot from the Legacy survey, with the MaNGA footprint as a magenta hexagon. The two other panels display the MaNGA flux from the Hα line, as estimated by the Voronoi and hybrid binning, respectively.

The Data Analysis Pipeline uses the penalized-PiXel Fitting routine (pPXF, Cappellari & Emsellem, 2004). A mix of stellar templates added to a polynomial component is fitted to the stellar continuum, allowing the stellar absorption-line kinematics to be derived.

1.3 Value-added catalogues (VACs)

In addition to the spectrophotometric data, value-added catalogues are provided, that encompass complementary properties about the MANGA targets. I made use of some of them, therefore I will briefly describe the catalogues that enabled my DP/MaNGA sample study to be more complete. The exhaustive list of these value-added catalogues is available at `https://www.sdss.org/dr16/data_access/value-added-catalogs/`.

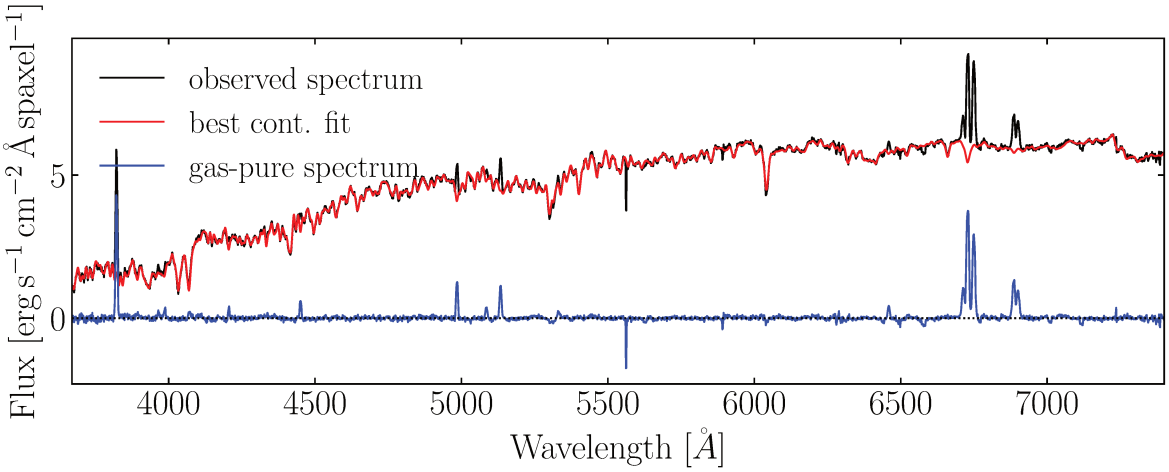

Figure (2.3) Central spectrum extracted from a MaNGA data cube, with the different stored quantities: in black, the observed spectrum; in red the best-continuum fit model; in blue the stellar-continuum-subtracted spectrum.

PyMorph Photometric (MPP-VAC) and MaNGA Deep Learning Morphology (MDLM-VAC)

These two companion catalogues are complementary and make it possible to pursue a morphological analysis of the MaNGA targets. The former provides photometric measurements derived from the 2D surface brightness profiles of the MaNGA sample. Two profiles are fitted, a Sérsic and a Sérsic+Exponential. The fitting algorithm PYMORPH[1] is used. The latter is complementary to the set of morphological parameters as it contains T-Type attributes in order to perform a morphological classification. The galaxies are classified using Deep learning models that return probability distributions for different morphological features (e.g. bar, bulge, edge-on, etc).The methodology is detailed in Domínguez Sánchez et al. (2018). The description of these catalogues is given in Fischer et al. (2019). Throughout this work, I will mainly use their estimated Sérsic index.

Pipe3D catalogue

Pipe3D is an analysis pipeline specially designed for IFU data, whose details are presented in Sánchez et al. (2016a,b). The MaNGA value-added catalogue gives integrated properties, gradients of the inferred properties, as well as spatially-resolved properties, such as star formation rates, stellar masses, oxygen abundances. I am interested in their stellar mass maps, since they enable me to infer specific star formation rate (sSFR=SFR/$M_\star$) maps and thus study this property spatially.

HI-MaNGA

HI-MaNGA (Masters et al., 2019) is a MaNGA follow-up programme that aims at conducting HI observations of more than 3000 MaNGA galaxies at $z < 0.05$ with the Green Bank Telescope (GBT). The second data release (Stark et al., 2021) provides combined HI measurements from the follow-up survey and from the ALFALFA survey (Haynes et al., 2018).

---

[1] https://pypi.org/project/pymorph/

2 Selection of the sample

To address the mechanisms of star formation quenching in local galaxies, I carried out an analysis of a particular sub-sample of galaxies. All these objects present complex spectral features, that I will hereafter call “double-peaks” (DP). This term refers to the shape of the emission lines, that is better characterised by a double-Gaussian function instead of a single one. The double-peaked features are detected by an automated selection procedure presented in Maschmann et al. (2020). This procedure consists of an emission line stacking to increase the emission line signal-to-noise ratio. Through multiple selection stages, the authors succeed in identifying genuine DP-emission-line structures. The resulting catalogue encompasses 5663 DP galaxies, corresponding to 0.8% of the parent SDSS/RCSED catalogue. The DP profiles that are detected in the SDSS spectra cannot be accounted for by rotating discs, as the authors do not find any inclination dependence. These galaxies, compared to a control sample, exhibit an excess of S0 galaxies, which cannot be explained by their environment, as they are mostly isolated galaxies. Furthermore, the authors do not detect an excess of visually-identified galaxy mergers. The DP galaxies classified as spirals show larger bulges in comparison with single-peaked counterparts. The authors argue that these galaxies with complex spectral features constitute a minor-merger sequence, that are thus not morphologically detected, but their structural properties are compatible with a gas accretion or a gas-rich minor merger scenario. To study the origin of these kinematics features in greater detail, I make use of public integral-field spectroscopic observations from the MaNGA survey. I selected the galaxies by cross-identifying the double-peaked emission line galaxies and the MaNGA catalogue of SDSS Data Release 15 (DR15, Aguado et al., 2019). I identified 29 DP galaxies which are observed with MaNGA. This sample give me the unique opportunity to study the spatial distribution of multiple gas components and to probe the underlying mechanisms responsible for double-peaked emission lines.

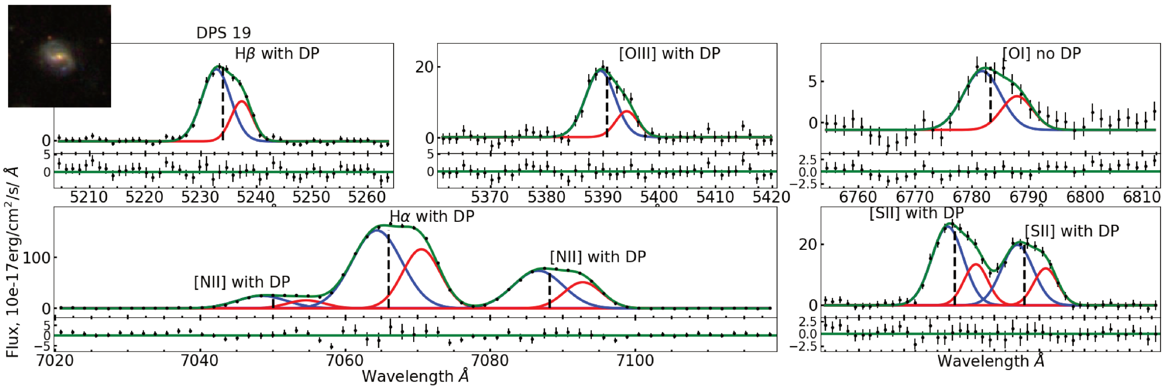

Figure (2.4) Example of an SDSS spectrum for one galaxy of my sample, fitted with the procedure from Maschmann et al. (2020). The main emission lines are shown and the validation of the double-peaked profile is displayed for each line, based on the flowchart presented in their paper. [OI] is flagged as “no DP” since this line does not meet all their criteria.

Étude de l'extinction de la formation d'étoiles à la lumière des galaxies MaNGA

Extinction de la formation stellaire dans les galaxies MaNGA à doubles pics

L'arrêt de l'activité de formation d'étoiles, communément appelé «extinction», dans les galaxies peut résulter de différents processus physiques. Ils peuvent être liés à l'évolution interne de la galaxie elle-même, par exemple en cas d'épuisement du gaz, dû à un noyau actif galactique qui expulse le réservoir de gaz, ou à des supernovæ. Des propriétés structurelles telles qu'un bulbe proéminent peuvent empêcher le gaz de s'effondrer et de former des étoiles. L'extinction de la formation d'étoiles peut également se produire à la suite d'effets environnementaux. Une galaxie qui évolue dans un amas peut subir une pression dynamique ou des forces de marée qui enlèvent son gaz. Les événements de fusion sont connus pour perturber la distribution du gaz et l'état physique (température, densité). Les fusions mineures désignent, par définition, les fusions dont les compagnons ont un faible rapport de masse, c'est-à-dire inférieur à 1:3, et ne sont donc pas les interactions de galaxies présentant les preuves observationnelles les plus évidentes. Néanmoins, leur influence peut être sondée en analysant les caractéristiques spectrales observées dans les systèmes galactiques.

Dans la section suivante, les mécanismes d'extinction de la formation d'étoiles sont étudiés à la lumière des données de spectroscopie à intégrale de champ obtenues pour 29 galaxies proches. Les observations de ces objets nous permettent d'étudier la distribution du gaz, l'excitation, ainsi que les propriétés spatiales des population stellaires.

Nous comparons l'excitation due au NAG et celle issue de la formation d'étoiles des raies d'émission du gaz ionisé avec les âges des populations stellaires, déduits des indices spectraux extraits des spectres optiques. Nous discutons ces propriétés par rapport à celles d'un échantillon de contrôle qui comprend des galaxies sans raies d'émission à doubles pics et discutons les principales différences que nous détectons. Cette analyse nous permet d'affirmer qu'une fraction plus élevée de galaxies à doubles pics se trouve dans la vallée verte, une région peuplée d'objets de couleur intermédiaire, et que cette couleur verte est causée par des populations stellaires rouges plus anciennes que 1 Ga. Nous remarquons également que la fraction d'ionisation qui peut être attribuée au NAG est corrélée avec l'âge de la population stellaire. En termes de formation d'étoiles, plus de 50% de l'activité a lieu à l'intérieur d'un rayon effectif, et elle semble plus concentrée que celle des galaxies des échantillons de contrôle. Les galaxies à doubles pis que nous étudions sont essentiellement des galaxies centrales, isolées ou en petits groupes.

À partir de ces différentes propriétés et de la façon dont elles sont réparties dans l'espace, nous classons les galaxies à doubles pics dans des groupes que nous identifions comme différents stades d'une séquence évolutive compatible avec des événements de fusion mineures. Le groupe bleu est constitué de galaxies formant activement des étoiles, avec une quantité importante de gaz et une formation d'étoiles concentrée, résultant de l'accrétion de gaz et de l'écoulement du gaz de la périphérie vers les régions intérieures. Le groupe vert représente les étapes suivantes de l'évolution : *(i)* le gaz central alimente le noyau des galaxies, déclenchant une activité nucléaire qui devient traçable par les diagnostics des raies d'émission. Cette signature est complétée par des populations stellaires plus âgées, comme le montrent les indices spectraux, et l'activité nucléaire éteint la formation d'étoiles dans un schéma «intérieur-extérieur» (*"inside-out"*) ; *(ii)* le gaz des régions extérieures alimente à nouveau les régions centrales, ce qui conduit à un épuisement du gaz dans les parties extérieures et à des disques éteints «extérieur-intérieur» *"outside-in"*.

Étude de la cinématique du gaz et des étoiles dans les galaxies MaNGA à doubles pics

Dans la section précédente, je détaille l'analyse des propriétés de formation des étoiles, les caractéristiques des populations stellaires, l'activité des AGN et je discute l'influence d'éventuelles fusions mineures. Dans de tels systèmes, nous pouvons nous attendre à des perturbations cinématiques. Les données MaNGA me permettent d'étudier ces processus en interprétant la cinématique du gaz et des étoiles.

Cinématique irrégulière

La cinématique du gaz est affectée par les interactions et les fusions (Bellocchi et al., 2013). Elle peut également être perturbée par l'activité nucléaire, par le biais d'écoulements de gaz à grande échelle dans les phases de gaz moléculaire (Cicone et al., 2014) et de gaz ionisé (Concas et al., 2019). Je représente les mesures du *pipeline* d'analyse des données pour étudier la cinématique du gaz et des étoiles. Le flux Hα, la vitesse et la dispersion de vitesse de chaque galaxie DP/MaNGA sont présentés sur les figures 3.1 et 3.2.

Afin de révéler d'éventuels mouvements irréguliers, je peux comparer la distribution radiale de la dispersion des vitesses du gaz $\sigma_{\rm gas}$ et celle des étoiles $\sigma_{\star}$, normalisée par la dispersion des vitesses stellaires dans le spaxel central du cube. Les profils radiaux correspondants sont montrés sur les figures 3.3 et 3.4. Ces diagnostics, ainsi que les cartes 2D fournies par la collaboration MaNGA, me donnent un aperçu des galaxies qui pourraient avoir des profils cinématiques irréguliers, et par conséquent sur lesquelles je pourrais appliquer une procédure d'ajustement de spectres à plusieurs composantes qui permet de sonder des caractéristiques spectrales complexes (voir les détails de l'algorithme dans la section 3).

Les résultats de cette analyse cinématique seront présentés dans Mazzilli Ciraulo et al. 2022 (en préparation).

Perspectives : comparaison avec des modèles analytiques

Comme nous l'avons vu précédemment, l'origine des profils à doubles pics peut varier et l'interprétation de ces caractéristiques souffre parfois de la résolution des données. Par conséquent, la comparaison entre les observations et les prédictions de modèles est pertinente. Nous prévoyons d'utiliser un modèle analytique simulant une distribution de vitesse sur la ligne de visée convoluée avec un élargissement instrumental.

3

Investigating star formation quenching in the light of MaNGA galaxies

1 Star formation quenching in double-peaked MaNGA galaxies

The termination of star formation activity, commonly speaking "quenching", in galaxies can result from different physical processes. They can be linked to the internal evolution of the galaxy itself, for instance when there is a gas depletion, due to an active galactic nucleus that expels the gas reservoir, or due to supernovae. Structural properties such as a prominent bulge can prevent the gas from collapsing and forming stars. Star formation quenching can also occur as a consequence of environmental effects. A galaxy that evolves in a cluster can experience ram pressure or tidal forces that stripped off its gas. Merger events are known to perturb the gas distribution and physical state (temperature, density). Minor mergers refer to, by definition, mergers whose companions have a small mass ratio, i.e. lower than 1:3, and therefore, they are not the galaxy interactions with the most obvious observational evidence. Nonetheless, their influence can be probed by analysing the spectral features observed in the galactic systems.

In the following Section, the star formation quenching mechanisms are studied in the light of integral field spectroscopic data from nearby galaxies. The observations of these objects allow us to investigate the gas distribution, excitation, as well as the stellar population properties spatially.

We compare the AGN and star-formation excitation of the ionised gas emission lines with stellar population ages, derived from spectral indices extracted from the optical spectra. We discuss these properties with respect to those of a control sample that comprises galaxies with no double-peaked emission lines and present the main differences that we detect. This analysis allows us to claim that a higher fraction of double-peaked galaxies lie in the green valley, the region populated by intermediate-colour objects, and that this green colour is caused by red stellar populations older than 1 Gyr. We also notice that the fraction of ionisation that can be attributed to AGN activity correlates with the stellar population age. In terms of star formation, more than 50% of the activity take place inside one effective radius, and it appears more concentrated than that of the galaxies of the control samples. The double-peaked galaxies that we study are central galaxies, either isolated or in small groups.

Based on these different properties and how they are spatially distributed, we classify the double-peaked galaxies in groups that we identify as different stages of an evolutionary sequence driven by minor merger events. The blue group consists of star-forming galaxies, with a significant amount of gas and concentrated star formation, resulting from gas accretion and funeling of the gas from the outskirts towards the inner regions. The green group depicts the next stages of the evolution: *(i)* the central gas feeds the central engine of the galaxies, trigger a nuclear activity that becomes traceable through emission-line diagnostics. This signature is complemented by older stellar populations, as found through spectral indices, and the nuclear activity quenches the star formation in an “inside-out scheme”; *(ii)* the gas from the outer regions fuels again the central regions, leading to a gas depletion in the outer parts and “outside-in” quenched discs.

1.1 Star formation, quenching and the connection to galaxy physical properties

The current section consists of the *submitted* Mazzilli Ciraulo et al. publication.

Astronomy & Astrophysics manuscript no. output
March 7, 2022

Resolving double-peaked emission line galaxies using MaNGA

I. Star formation, quenching and the connection to galaxy physical properties

Barbara Mazzilli Ciraulo[1], Anne-Laure Melchior[1], Françoise Combes[1,2], and Daniel Maschmann[1]

[1] LERMA, Sorbonne Université, Observatoire de Paris, Université PSL, CNRS, F-75014, Paris, France
e-mail: `Barbara.Mazzilli-Ciraulo@observatoiredeparis.psl.eu`
[2] Collège de France, 11 Place Marcelin Berthelot, 75005 Paris, France

March 7, 2022

ABSTRACT

Star formation quenching in spiral galaxies could be due to supernovae or active galaxy nuclei (AGN) feedback, but also due to the environment. To probe the influence of minor mergers, we have selected a sample of massive galaxies in the Sloan Digital Sky Survey presenting double-peaked emission lines in their centre. Within these nearby galaxies, the star formation regulation is studied together with their physical properties: morphology, environment, colour, stellar age and star formation rate versus AGN diagnostics. We want to study both the global galactic properties as well as the resolved maps tracing the gas ionisation. We therefore gather a sample of 29 star-forming galaxies from the Mapping Nearby Galaxies at APO (MaNGA) survey that exhibit central double-peaked emission lines. We define control samples of single-peaked emission line galaxies which match the same stellar mass and redshift distribution. We find that the double-peaked emission-line galaxies exhibit a higher fraction of galaxies in the green valley defined by the NUV-r colour than the control sample. This green colour is due to a contribution from old stellar populations hosted in these overall star-forming galaxies. Relying on the resolved power of MaNGA integral field spectroscopic data, we show that this sample host two types of galaxies: some have a nuclear AGN-like activity and some are inactive. This AGN excitation is correlated to the $D_n(4000)$ index tracing the age of the stellar population. We discuss that we are sampling different phases of evolution of these galaxies known to be isolated or in poor groups. Minor mergers are known to provide gas in the central regions of the merger remnant, coming in part from the companion, but also mainly from the gas reservoir of the primary galaxy's outskirts. This merging activity is acting in two phases: in the first one, the gas driven inwards triggers star formation in the centre, while the disc is replenished from the outer gas reservoir. The galaxies appear in the blue-cloud category. Then, the central gas ignites (weakly) a nuclear AGN-activity, quenching inside-out the star formation, and the galaxy enters the green valley category. In the second phase, the gas remaining in the disc converges towards the nucleus, reignites star formation, while the disc is now depleted, lacking the gas reservoir to be replenished. These green-valley galaxies appear then quenched outside-in. This scenario is compatible with other studies discussing central activities due to minor mergers.

Key words. Galaxies: star formation quenching – Methods: data analysis – Techniques: integral field spectroscopy

1. Introduction

The observation of large galaxy samples showed that galaxies in the Local Universe follow a bi-modal distribution in the colour-magnitude and colour-mass diagrams (Blanton et al. 2011; Baldry et al. 2004). The two main populations correspond to a "blue cloud" with galaxies characterised by active star formation, and a "red sequence", referring to passive galaxies; while the region lying between these two groups is called "green valley" (Salim 2014). This latter region may be defined in the UV-optical colour-magnitude diagram and is considered as a way to pinpoint transitional galaxies (Salim 2014), lying below the star-forming sequence but yet not completely passive. The bi-modality is found to depend on evolutionary stage but also on morphology (discs dominating in the blue cloud and spheroids in the red sequence), even though no specific Hubble type has been observed among the green-valley galaxies. These objects thought to be in transition are thus critical to the understanding of the paths from the active sequence to quiescence.

The termination of star formation activity, or quenching, plays a key role in this transition. However, this process remains an open question, as the mechanisms involved are numerous and complex. For instance, the environment can reduce the gas fraction in galaxy clusters, through ram-pressure stripping (Boselli et al. 2016) or strangulation (Weinmann et al. 2009). Hence, high-density environments reduce star formation and shorten the quenching timescale (e.g. Coenda et al. 2018). Other mechanisms can stop the star formation activity, such as morphological quenching (Martig et al. 2009) which corresponds to the stabilisation of the gas due to bulge growth and/or bar-driven processes, which prevents the gas from collapsing and forming stars. Saintonge et al. (2011) also showed that the molecular gas depletion time is longer at high stellar masses. They, furthermore, discuss a possible AGN contribution as one of the processes responsible for the quenching. On the one hand, Barrows et al. (2017) found a positive correlation between the specific star formation rate and AGN luminosity but on the other hand, Kaviraj et al. (2015) showed that nearby merger-triggered AGN are unlikely to provide strong regulation in the star formation process, given the different timescales involved. Gas depletion appears to be one of the most obvious mechanism leading to star formation quenching but the removal of the gas itself can be caused by different phenomena as ram-pressure stripping, viscous stripping or strangulation. The former is the most efficient in rich galaxy clusters but Rasmussen et al. (2008) showed that it is not sufficient to explain gas depletion in compact groups. The two latter are then proposed to interpret the gas depletion.

Tidal interactions and merging processes can drive the gas towards the centre of galaxies, which triggers a starburst and thus enhances central star formation on a relatively short timescale (Di Matteo et al. 2008; Patton et al. 2011). This subsequent active star formation will finally consume the gas reservoir and result in the final quenching. Identifying and studying galaxy pairs or at least interacting galaxies thus appear crucial to investigate the star formation cycle of galaxies. For spectacular systems such as the Antennae (Whitmore et al. 2014; Lahén et al. 2018), the Taffy galaxies (Condon et al. 1993) or IIZw096 (Inami et al. 2010), the merging process is obvious. In parallel, for other objects with no morphological signatures, it can be challenging to unveil an ongoing merger event, especially a minor merger. Investigating the gas kinematics is necessary. Some complex emission line profiles can be used as a tracers of galaxy interactions, such as the double-peaked (DP) emission lines. A systematic search for these features was performed in Ge et al. (2012) and more detailed works on the origin of double-peaked profiles were mostly focused on dual AGN (e.g. Comerford et al. 2012; Nevin et al. 2018).

Based on the asset that double-peaked emission lines can trace key processes of galaxy evolution, Maschmann et al. (2020) selected 5663 galaxies from the Reference Catalogue of Spectral Energy Distribution (RCSED, Chilingarian et al. 2017) exhibiting such line shapes. They developed an automated selection procedure to find DP galaxies without relying on a visual inspection of the spectra. These DP galaxies display significant differences compared to a control sample which was selected following the same stellar mass and redshift distributions: they mostly evolve in isolated environment, but show a significant excess of S0 galaxies, a large stellar velocity dispersion and an enhanced central star formation activity. No dependency on inclination is found, discarding a simple scenario of a rotating disc. The authors, thus, argue that this sample corresponds to a minor-merger sequence as suggested in Bournaud et al. (2007) (see details in Maschmann et al. 2020). More detailed studies on smaller galaxy samples, such as Comerford et al. (2018) were able to identify a past merger as the underlying process of the observed DP emission lines. Similarly, Maschmann & Melchior (2019) found different excitations in the two emission line components of DP galaxies manifesting the two progenitors of a galaxy merger. A more detailed analysis with spatially-resolved spectroscopic observations succeeded in decomposing two kinematic components (Mazzilli Ciraulo et al. 2021). They associated the two components to two galaxies in the act of merging, creating DP emission line features. However, it is still challenging to conclude on the underlying process leading to DP emission lines in large galaxy samples since many effects such as a rotating inner disc or nuclear outflows can be responsible for DP emission lines (detailed discussion in Maschmann et al. 2020, hereafter M20).

The emergence and availability of large integral field spectroscopic surveys enable the nature of the closest galaxies (at $z < 0.14$) exhibiting these DP emission line profiles to be investigated in further details. We, therefore, cross-identified the galaxies of the DP catalogue mentioned above with the targets encompassed in the summary file from the MaNGA Data Reduction Pipeline (DRP, Law et al. 2016) of the SDSS Data Release 15 (Aguado et al. 2019). We identified a sample of 29 nearby galaxies located at an average redshift of 0.0653 (D_L=254.7 Mpc) (hereafter called the DP/MaNGA sample). This paper is the first of a series of three papers dedicated to the study of this sample. As described below, the present paper is focused on the analysis of the star formation properties of this galaxy sample, with a focus on the green valley definition. The second one is based on the analysis of CO and HI observations of this sample, and will discuss the Schmidt-Kennicutt relation and the star formation efficiency. The last one is focused on the kinematic signatures and particularities of these galaxies.

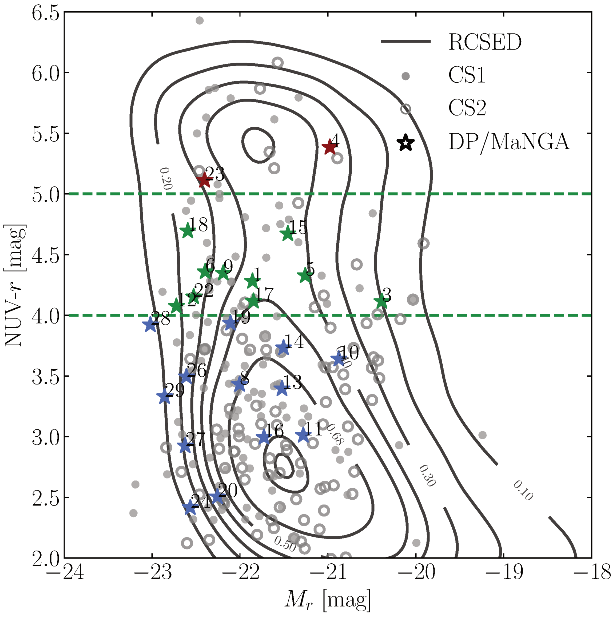

Fig. 1: Colour-magnitude diagram. The colour NUV-r is taken from the RCSED catalogue (Chilingarian et al. 2017) and is K- and dust-corrected. The M_r magnitude is the r absolute magnitude.

In Sect. 2, we describe the DP/MaNGA sample and the data gathered for the corresponding galaxies. We also define control samples of single-Gaussian-shaped emission-line galaxies that will be used for comparison. In Sect. 3, we explore the properties of these 29 DP/MaNGA galaxies in contrast to the control samples. We quantify the impact of AGN activity on the star formation and test different quenching mechanisms in Sect. 4. In Sect. 5, we discuss how these galaxies fit in the more general evolution of star formation quenching in galaxies, followed by a conclusion in Sect. 6.

A cosmology of $\Omega_m = 0.3$, $\Omega_\Lambda = 0.7$ and $H_0 = 0.7$ is assumed throughout this work.

2. Sample and data description

2.1. DP/MaNGA sample

Mapping Nearby Galaxies at APO (MaNGA, Bundy et al. 2015) is part of the fourth generation of SDSS (SDSS-IV, Blanton et al. 2017) and consists of an integral field unit survey targeting local ($0.01 < z < 0.15$) galaxies with stellar masses $M_\star \geq 10^9 M_\odot$. The observations are performed using integral field units (IFUs) of different sizes, from 19 to 127 fibres corresponding to an outer-on-sky diameter from 12.5 to 32.5″ (Drory et al. 2015). The

Table 1: The DP/MaNGA sample

ID (1)	designation (2)	z (3)	$M_\star$ $\log_{10}(M_\odot)$ (4)	SFR $M_\odot$ yr^{-1} (5)	i ° (6)	env. (7)	morph. (8)	colour-sSFR (9)
G1	J110649.16+455752.6	0.02490	10.99	1.21	32	cluster, cent.	E	GV, TZ
G2	J110704.17+454919.6	0.02521	10.85	2.07	80	cluster, sat.	LTG	*GV*
G3	J101954.80+361932.7	0.02612	10.10	2.33	76	isolated	S0	GV
G4	J074953.38+451454.6	0.03126	10.61	0.01	40	isolated	S0	red sequence
G5	J133213.69+265659.9	0.03529	10.47	2.18	65	poor group, cent.	LTG	GV
G6	J121810.50+442401.7	0.03826	11.30	1.18	46	poor group, cent.	S0	GV, TZ
G7	J080136.97+185306.6	0.03915	10.93(!)	0.80(!)	52	isolated	M	*GV, TZ*
G8	J161652.01+501655.9	0.04168	11.09	1.89	64	cluster, sat.	LTG	blue cloud, TZ
G9	J143031.19+524225.8	0.04488	11.09	0.63	51	cluster, sat.	LTG	GV, TZ
G10	J112525.63+515302.0	0.04912	10.53	2.06	77	isolated	LTG	active
G11	J075114.77+280913.0	0.05232	10.74	1.43	58	isolated	LTG	active
G12	J125448.95+440920.2	0.05432	11.36	1.50	71	isolated	LTG	GV, TZ
G13	J161552.50+440940.8	0.05484	10.93	3.69	67	isolated	LTG	blue cloud
G14	J072717.73+434705.5	0.05645	10.96	2.66	66	isolated	S0	active
G15	J161224.61+483147.6	0.05779	10.85	0.90	66	poor group, sat.	LTG	GV, TZ
G16	J041006.33-060305.9	0.05781	10.72	7.96	49	isolated	E	blue cloud
G17	J154308.66+400254.8	0.06256	10.97	6.22	54	isolated	S0	GV
G18	J015122.27+130337.3	0.06416	11.26	11.51	66	poor group, cent.	LTG	GV
G19	J120611.03+450857.1	0.06654	10.89	8.30	50	poor group, cent.	E	blue cloud
G20	J101211.76+450831.8	0.07643	11.09	10.38	46	poor group, cent.	LTG	blue cloud
G21	J080010.14+191403.6	0.07821	11.32(!)	11.43(!)	55	poor group, cent.	M	*GV*
G22	J160739.28+232500.8	0.08746	11.26	3.15	65	cluster, sat.	LTG	GV
G23	J161956.57+244440.2	0.08812	11.26	1.63	34	rich group, cent.	E	red sequence, TZ
G24	J221024.49+114247.0	0.09228	11.20	13.27	–	isolated	M(⋆)	AS
G25	J153521.83+270728.8	0.09373	10.91(!)	17.96(!)	63	poor group, cent.	LTG	*blue cloud*
G26	J154637.06+434101.2	0.10117	11.30	8.71	55	poor group, cent.	LTG	blue cloud
G27	J083635.38+230710.5	0.12522	11.33	16.75	43	isolated(Y)	M	blue cloud
G28	J145252.45+451405.3	0.13265	11.39	10.69	38	isolated(Y)	LTG	blue cloud
G29	J213002.45+002751.1	0.13506	11.32	9.06	35	isolated(Y)	LTG	blue cloud

Notes: (1) Arbitrary identifier, (2) SDSS name, (3) SDSS redshift, (4) stellar mass computed by Salim et al. (2016), except for the G7, G21 and G25 with a (!) whose stellar mass comes from Kauffmann et al. (2003a), (5) star formation rate from Salim et al. (2016), except for galaxies marked with a (!) for which SFR is from Brinchmann et al. (2004), (6) inclination angle computed using the measurements from Fischer et al. (2019), (7) galaxy environment as found in Saulder et al. (2016) except for the three last objects, with (Y), whose environment comes from Yang et al. (2007), (8) morphology classification based on the probabilities provided in the MaNGA Deep Learning DR15 Morphology catalogue, relying on the measurements from Fischer et al. (2019), except for G24 that we classify manually and that is marked with (⋆), (9) classification based on the NUV-r vs. specific Star Formation Rate (sSFR) diagram: blue cloud, green valley (GV), red sequence, transition zone (TZ).

spectra are observed in the range of 3600 to 10400 Å with an averaged spectral resolution of R∼2000 and a mean spatial resolution of 2.5″. Individual fibre spectra are re-arranged into a data cube with 0.5″ × 0.5″ spaxels. The MaNGA data are well-suited to study the ionised gas, namely its distribution, kinematics and excitation within the observed sources. Value-added catalogues are available for MaNGA galaxies and make possible to investigate the photometry measurements, morphology (MaNGA PyMorph DR15 photometric catalogue, Fischer et al. 2019), as well as stellar properties and global properties (MaNGA Pipe3D, Sánchez et al. 2016a,b) of the targets.

In order to study DP galaxies in greater detail, we cross match the DP catalogue of Maschmann et al. (2020) with the MaNGA DR15 catalogue and find 29 DP galaxies observed by MaNGA. These galaxies are listed in Table 1 and are sorted by redshift.

In Fig. 1 we show the colour-magnitude diagram for the DP/MaNGA and the control samples (see Sect. 2.2). We use dust- and K-corrected r-band and NUV magnitudes provided by the RCSED catalogue (Chilingarian et al. 2017). We compute the absolute magnitude from the apparent magnitude following Eq. (1) of Wyder et al. (2007). The contours correspond to 10^5 galaxies representative of the RCSED catalogue (Chilingarian et al. 2017). The coloured stars (resp. grey dots and solid circles) are the DP/MaNGA (resp. CS1 and CS2) galaxies discussed in Sect. 2.2. Following Salim (2014), we categorise galaxies into the red sequence characterised by colours NUV-$r > 5$, the so called green valley (GV) with $4 < \mathrm{NUV} - r < 5$ and the blue cloud at $\mathrm{NUV} - r < 4$. Beside two galaxies (G4 and G23), the majority is situated in the blue cloud and a significant fraction is found in the GV. In the following, we will adopt the colour code defined in this figure: blue for the blue cloud, green for GV galaxies and dark red for the red sequence.

2.2. Selection of the control samples

To find the particularities of the DP/MaNGA galaxies, we define two control samples of galaxies exhibiting a single-peaked emission line inside the central 3″ spectrum. Following the procedure described in Maschmann et al. (2020), we select the galaxies for

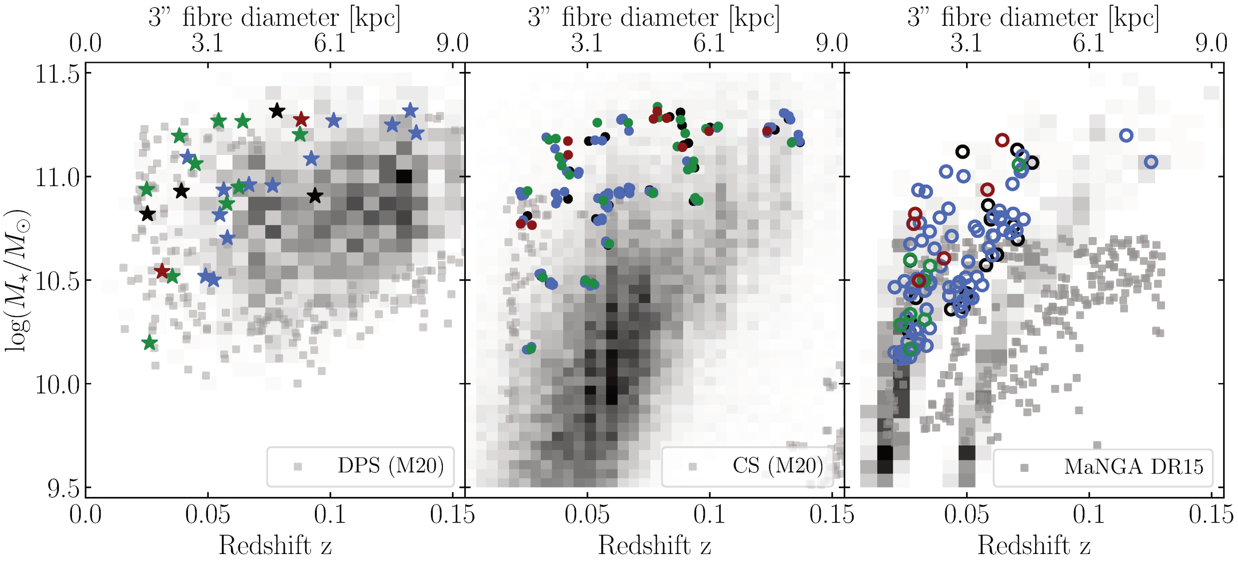

Fig. 2: Distribution in the $M_\star - z$ plane of the DP/MaNGA (colour-coded stars on left panel), CS1 (colour-coded filled circles on middle panel) and CS2 (colour-coded empty circles on right panel) galaxies. These three samples are respectively superimposed on the DPS distribution, the CS from Maschmann et al. (2020), and the whole MaNGA sample (Bundy et al. 2015). The colour-coding refers to the NUV-*r* colour: ★blue-cloud galaxies, ★green-valley galaxies; ★ red-sequence galaxies; ★ no NUV-*r* measurement available.)

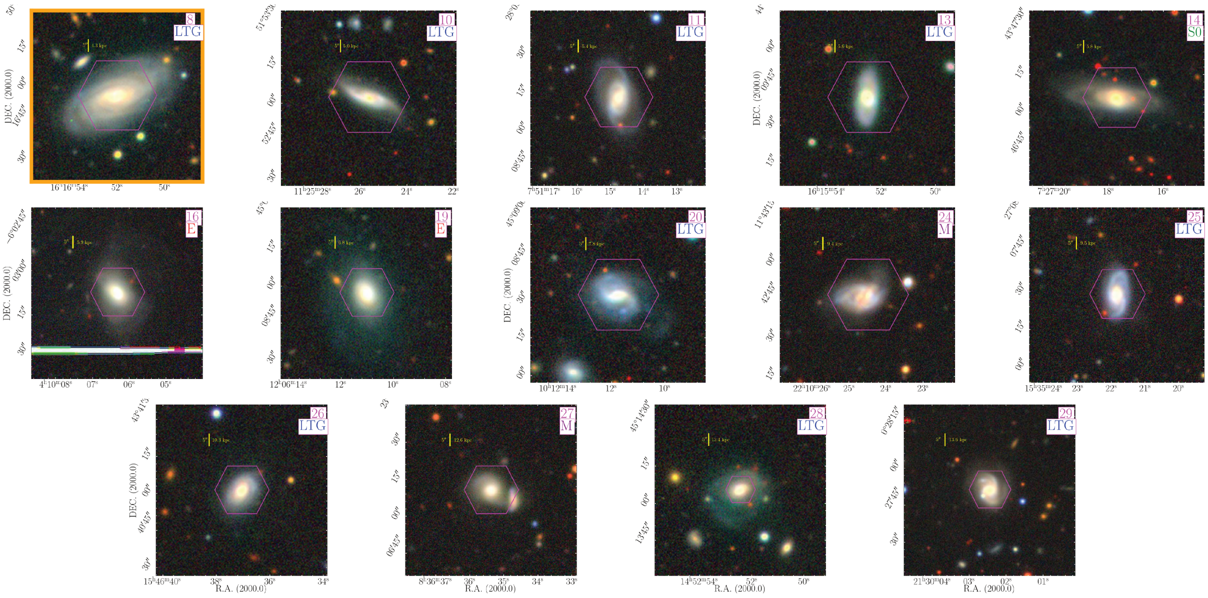

Fig. 3: 62x62″ Legacy survey snapshots of the galaxies belonging to the blue sequence, based on NUV-*r* colour, among the DP/MaNGA galaxies. The corresponding MaNGA IFU footprint in magenta and the morphological type are shown for each source. The galaxy displayed with an orange frame is the one in the transition zone in terms of sSFR ($-11.8 < \log(\mathrm{sSFR}) < -10.8$). The galaxies are sorted by redshift, from left to right, top to bottom.

our control samples following the same redshift and stellar mass $M_\star$ distribution as the DP/MaNGA sample. We start from the control sample (CS) defined by Maschmann et al. (2020) which consists of 89 412 galaxies characterised by a single-Gaussian shaped emission line in the 3″ SDSS fibre. Since the CS is dominated by galaxies with smaller stellar masses in comparison to the DP/MaNGA sample we are limited in the number of galaxies with the same redshift and stellar mass distribution.

We select a first control sample (hereafter CS1), consisting of 143 galaxies from the CS of M20, i.e. galaxies with single-Gaussian-shaped emission lines in their single SDSS spectrum. As shown in Fig. 2, the CS1 shows only small deviations in redshift and stellar mass in comparison to the DP/MaNGA. To en-

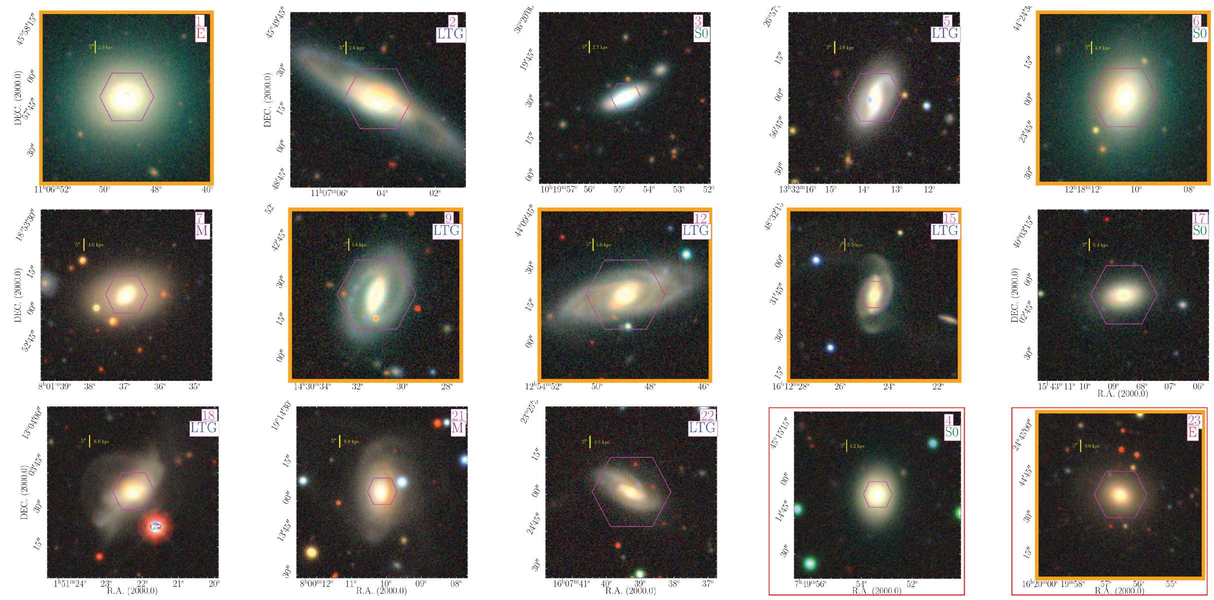

Fig. 4: Same as Fig. 3 but for the green-valley galaxies and the red galaxies (with the red frames). The panels surrounded with an orange frame are the green-valley galaxies not in the transition region.

able a comparison with MaNGA observations between galaxies exhibiting a central single- or a double-peaked emission line, we select a second control sample (hereafter CS2). Therefore, we cross-match the CS with the MaNGA DR15 catalogue and select again galaxies following the same redshift and stellar mass distribution as the DP/MaNGA sample. We finally select the CS2 consisting of 109 galaxies. As shown in Fig. 2, the CS2 comprises less massive galaxies than the CS1. This is due to the fact that at higher masses only a few galaxies with a single-peaked central emission line profile was observed by MaNGA. In order to visualise the samples selected for this work in contrast to the samples of Maschmann et al. (2020) and the MaNGA DR15 we show their stellar mass-redshift distribution in Fig. 2.

2.3. Other archival data

To discuss the physical properties of the DP/MaNGA galaxies, we make use of different catalogues.

Salim et al. (2016) analysed GALEX, SDSS and WISE data and built a catalogue from them, that encompasses stellar mass, dust attenuation, star formation rate for $\sim 7 \cdot 10^5$ galaxies. They used a Chabrier initial mass function (IMF) (Chabrier 2003). Three galaxies out of the DP/MaNGA are not included in their data set (G7, G21 and G25). For those latter three galaxies, we rely on the star formation rate estimates computed by Brinchmann et al. (2004), and available through the MPA-JHU DR7 release of spectrum measurements[1]. These latter SFR estimates are derived using a Kroupa initial mass function (Kroupa 2001), and this data set also comprises stellar mass estimates based on fits to the photometry following Kauffmann et al. (2003a). As precised in Salim et al. (2016), a -0.025 dex offset is applied when comparing these different SFR estimates, to adjust from the Kroupa to Chabrier IMF. We adopt the Salim et al. (2016) estimate as far as possible, since it is using 22μm photometry and hence minimises possible dust extinction/emission biases. We also use the $D_n(4000)$ index from MPA-JHU DR7 catalogue, to discuss the stellar ages of the galaxies.

The Reference Catalogue of Spectral Energy Distributions (RCSED, Chilingarian et al. 2017) encompasses 800 299 galaxies at low and intermediate redshift and provides for each spectrophotometric measurements from different surveys as well as value-added data such as K-correction, emission line flux measurements, gas-phase metallicity, extinction.

2.4. MaNGA data products

We aim at deriving spatially-resolved as well as global properties of the DP/MaNGA galaxies. We use the final data cubes provided by the Data Reduction Pipeline (DRP, Law et al. 2016) that are logarithmic sampled and the maps provided by the Data Analysis Pipeline (DAP, Westfall et al. 2019). Briefly, each spectrum of the 3D data is fitted using the penalized PiXel-Fitting routine (pPXF, Cappellari & Emsellem 2004; Cappellari 2017): the stellar continuum is adjusted by fitting 49 families of stellar spectra from the MILES library (Falcón-Barroso et al. 2011) and then subtracted to the observed spectrum. The nebular emission lines in the resulting spectrum are fitted using a Gaussian function. The MaNGA DAP proposes two analysis methods to derive physical quantities: the Voronoi-binned maps for which a Voronoi binning scheme has been applied and has associated the summed flux to each spaxel belonging to the same spatial bin; the hybrid maps for which a similar Voronoi binning scheme has been applied for stellar properties but for which emission line measurements are proceeded spaxel-by-spaxel. We also exploit the stellar continuum measurements and the derived stellar mass density provided in the value-added catalogue Pipe3D for MaNGA DR15 (Sánchez et al. 2016b, 2018). We aim at computing quantities like specific star-formation rate for which we make use of the stellar mass measurements of Pipe3D, whose procedure does not proceed to the same binning scheme. Therefore, we decide to work with the hybrid-scheme maps and spaxel-by-spaxel emission line measurements.

---

[1] https://wwwmpa.mpa-garching.mpg.de/SDSS/DR7/

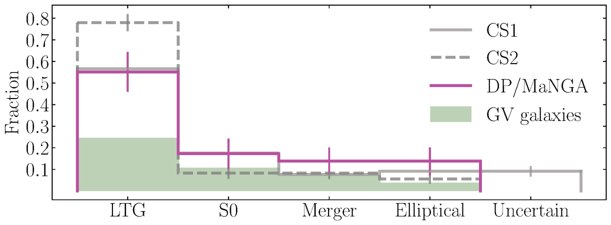

Fig. 5: Morphology distribution for the 29 DP/MaNGA galaxies (in pink), 143 CS1 galaxies (in solid grey) and 109 CS2 galaxies (in dashed grey). The filled histogram corresponds to the green valley DP/MaNGA galaxies. The error bars represent the binomial errors.

3. DP/MaNGA sample properties

3.1. Morphology

A visual inspection of the RGB images provided by the Legacy survey (Dey et al. 2019) reveals that our sample gathers a diversity of galaxy types, namely late-type galaxies (LTG), elliptical galaxies and disrupted galaxies which are most likely mergers. We display the Legacy survey snapshots in Fig. 3 and 4 and mark for each galaxy the corresponding MaNGA IFU footprint with a magenta hexagon. The two figures are sorted according to their NUV-r colour, as displayed in Fig. 1. We present the morphological classification of the DP/MaNGA sample in Table 1 and mark the morphological type of each galaxy in the top right of their snapshot in Figs. 3 and 4.

3.1.1. Methodology

Fischer et al. (2019) performed a Sérsic (as well as a Sérsic + an exponential) fit of the 2D surface brightness profiles for all MaNGA DR15 galaxies. They used the python package Pymorph[2] and added improvements compared to the fitting procedure presented in Meert et al. (2015). We use the calculated semi-minor over semi-major axis ratio (b/a) to compute the inclination angle i following:

$$\cos(i) = \sqrt{\frac{(b/a)^2 - q_0^2}{1 - q_0^2}} \tag{1}$$

where q_0 is the intrinsic axial ratio of edge-on galaxies, set to $q_0 = 0.2$ (Holmberg 1958).

We make use of the companion catalogue, MaNGA Deep Learning DR15 Morphology catalogue, which encompasses machine learning based morphological classifications (Domínguez Sánchez et al. 2018). This catalogue covers MaNGA galaxies that were not processed in former bulge-disc decomposition catalogues based on SDSS DR7 photometry. We use the following galaxy type probabilities computed by (Domínguez Sánchez et al. 2018): the T-Type to estimate the morphological type on the Hubble Sequence, P_{S0} denoting the probability to detect a S0 galaxy and P_{merg} giving the probability to detect a galaxy merger. We follow the recommended criteria to classify the galaxies of our sample as:

- Late-Type Galaxies (LTGs): T-Type > 0 ;
- Early-Type Galaxies (ETGs): T-Type ≤ 0 ;
  - S0: T-Type ≤ 0 and P_S0 > 0.5 ;
  - Ellipticals (E): T-Type ≤ 0 and P_S0 ≤ 0.5.

We also set our own criterion to define an object as a merger:

- Merger: P_merg > 0.9.

Fischer et al. (2019) precise that the given probability of merger signature indicates projected close pairs or nearby objects rather than ongoing merger events and find that 11% of the whole MaNGA sample have P_merg > 0.8. To be restrictive, we select the criterion P_merg > 0.9 to classify a source as a merger. In our sample, the three galaxies with the highest merger probabilities evolve in an isolated environment or in a poor group according to Saulder et al. (2016) and Yang et al. (2007), but the Legacy survey snapshots show projected close-by objects for galaxy 27 of the DP/MaNGA sample. Moreover, the only galaxy that is flagged by Fischer et al. (2019) because of a non-reliable fit and thus has no proper photometric measurements, is G24, whose spectroscopic analysis reveals the presence of two interacting galaxies, as described in Mazzilli Ciraulo et al. (2021). Therefore, we manually define this source as a merger.

3.1.2. Morphology of the DP/MaNGA galaxies

Figure 5 displays the morphology defined for the 29 DP/MaNGA galaxies. We observe that the sample is dominated by late-type galaxies (LTGs, more than 55%) and hosts 14% of merger-classified galaxies. We note that contrary to Maschmann et al. (2020), there is no significant excess of S0. This is due to the fact that the DP/MaNGA are relatively close galaxies (with a median redshift of 0.0577), while distant S0 galaxies can correspond to unresolved LTGs. One can observe that the morphology distribution of the DP/MaNGA is very close to the CS1 one.

In order to explore the morphological properties of these galaxies in greater detail, we compute the photometric parameters Gini and M_{20}, which is described in Appendix A. In Fig. A.1 we show the Gini-M_{20} diagram and observe that the sample is dominated by early-type galaxies with a large fraction of objects lying in the E-Sa region. However, we do not detect any significant difference with respect to the CS1. Maschmann et al. (2020) found a deficit of Sb-d galaxies in the DPS, composed of 5663 galaxies up to $z = 0.3$. We are here limited by the small statistics of the DP/MaNGA sample (7 galaxies are identified as Sb-Sd) and cannot be further categorised into more detailed Hubble types. Figures 3 and 4 illustrate that the morphologies of the blue-cloud and green-valley galaxies are quite diverse even though dominated by late-type ones, while the two galaxies of the red sequence are an elliptical and an S0 (see Fig. 4).

Last, Maschmann et al. (2020) showed that the DP feature is not related to the inclination of the main disc. The DP/MaNGA sub-sample is representative, with a mean inclination value of 53.5° and values distributed between 32° and 80°.

---

[2] https://pypi.org/project/pymorph/

3.2. Mass-size relation and Sérsic index

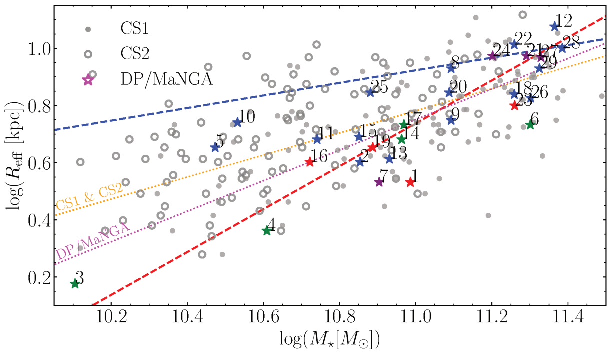

Fig. 6: Size-stellar mass distribution for the DP MaNGA galaxies. The dashed lines correspond to the low-z relations proposed by van der Wel et al. (2014) ($R \propto M_\star^{0.75}$ for ETGs in red and $R \sim M_\star^{0.22}$ for LTGs in blue). The colour-coding refers to the morphology described in Sect. 3.1: ★ ellipticals, ★ S0; ★ mergers; ★ LTGs. The dotted lines refer to the relation found for the DP/MaNGA galaxies (in magenta) and based on both control samples galaxies (in orange).

Figure 6 shows the mass-size relation for the DP/MaNGA galaxies and the control samples. The stellar masses are from Salim et al. (2016), except for G7, G21 and G25 whose estimates are taken from Kauffmann et al. (2003a). The half-light radius $R_{\rm eff}$ are from the NASA-Sloan Atlas catalogue (NSA)[3]. We superimpose the low-z relations from van der Wel et al. (2014). The trend based on the CS1 and CS2 measurements, shown as an orange dotted line, lies between these two relations. For the DP/MaNGA galaxies, we observe a large scatter with the morphological types, but, while most of these galaxies are late-type galaxies, they are closer to the early-type trend ($M_\star^{0.75}$), as presented by the fitting line in magenta. This behaviour is in line with our expectations: the E-Sa galaxies are more compact than the late-type ones, at a given mass.

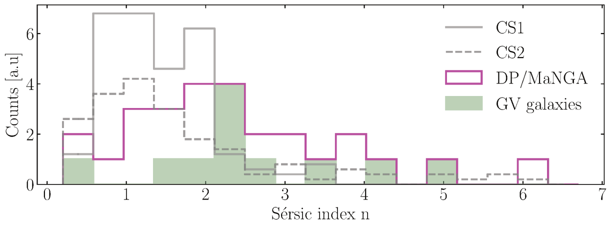

Fig. 7: Sérsic indices for the DP/MaNGA, the CS1 and the CS2 galaxies. The Sérsic indices are computed using STATMORPH for CS1 and are taken from the MaNGA PyMorph DR15 photometric catalogue for DP/MaNGA and CS2 (Fischer et al. 2019). The filled histogram corresponds to the green valley DP/MaNGA galaxies.

As discussed in Maschmann et al. (2020) for the DPS, the DP/MaNGA galaxies exhibit a higher Sérsic index than the CS1 and CS2 galaxies, as shown in Fig. 7. This further supports our finding on the mass-size relation. The DP/MaNGA galaxies are relatively compact galaxies, but this effect is not detected in the morphology.

3.3. Environment

The data sets presented in Yang et al. (2007) and in Saulder et al. (2016) provide galaxy groups and enable us to know whether a galaxy is isolated or not. To discriminate from the different environments, we use the galaxy group sizes as defined in Blanton & Moustakas (2009): a poor group holds 2 to 4 objects, a rich group 5 to 9 and a cluster 10 or more. We take the classification from Saulder et al. (2016) when available and from Yang et al. (2007) for the sources with a redshift greater than 0.11. We show the environment distribution of the DP/MaNGA, the CS1 and the CS2 galaxies in Fig. 8. The DP/MaNGA galaxies are mainly isolated and in poor groups and roughly follow the distribution of the CS1/CS2 galaxies. We note a small excess (2σ, resp. 3σ) of sources without any neighbour compared to the CS1 (resp. CS2) and (resp. slightly) less objects evolving in a rich group with respect to the CS2 (resp. CS1). This result is compatible with the findings of Maschmann et al. (2020) based on 5663 DP galaxies. The bottom panel of Fig. 8 shows that most of the DP/MaNGA galaxies correspond to central galaxies of groups or clusters with a central/satellite ratio of 4.8, and that satellite DP/MaNGA galaxies are in the green-valley (except G8 which lies in the blue cloud and is in transition). This is quite different from the CS1 which has a central/satellite ratio of 2.67, and from the CS2 with a ratio of 1.60. When one considers the DPS (resp. NBCS), 17 % (resp. 9 %) of the satellite galaxies are in the green valley, supporting the fact that this excess of green satellite galaxies is real. Lastly, we note that while the central/satellite ratio in the green valley is similar for DP/MaNGA and DPS galaxies, the global DPS central/satellite ratio is of the order 2.25 independently of the redshift range (to compare with 4.8 for the DP/MaNGA).

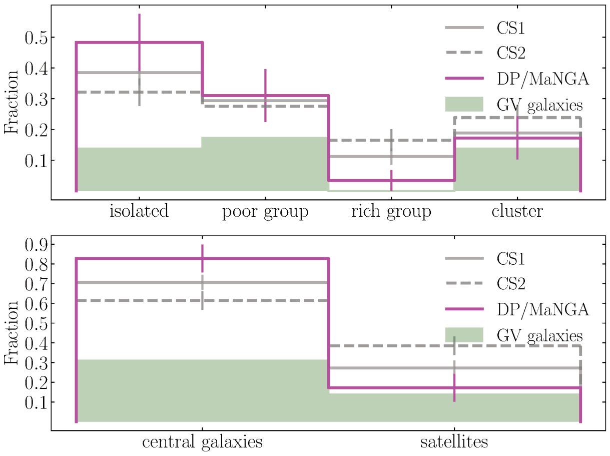

Fig. 8: **Top:** Environment distribution for the DP/MaNGA galaxies, the CS1 and the CS2 objects. The filled histogram corresponds to the green valley DP/MaNGA galaxies. The error bars show the binomial errors. **Bottom:** Distribution between central and satellite galaxies, for the DP/MaNGA, CS1 and CS2 samples. Isolated galaxies are classified as central.

---

[3] `www.nsatlas.org`

3.4. Green valley and transition

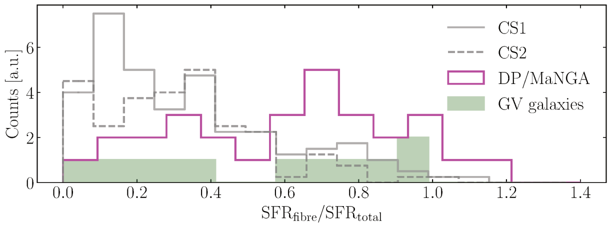

Fig. 9: Central excess of SFR (Brinchmann et al. 2004) for the DP/MaNGA, the CS1 and the CS2 galaxies.The filled histogram corresponds to the green valley DP/MaNGA galaxies.

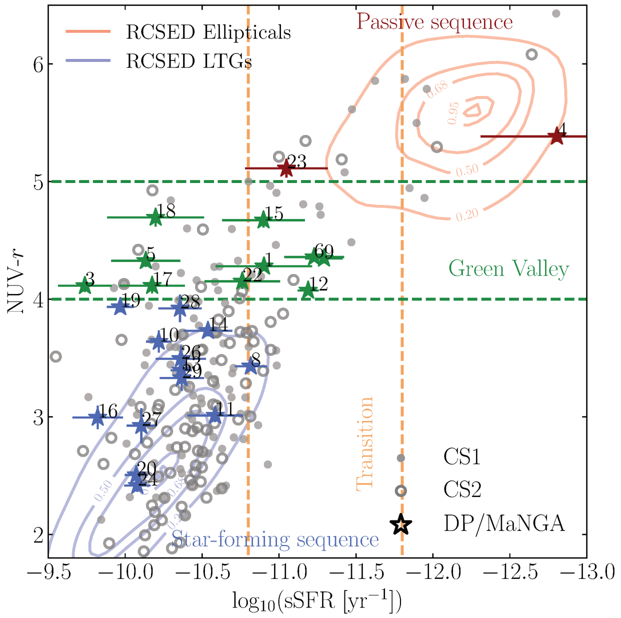

Fig. 10: NUV-r vs. sSFR diagram. The galaxies from the RCSED are shown as reference: the red (resp. blue) contour lines correspond to the elliptical (resp. late-type) galaxies, classified using the algorithm presented in Domínguez Sánchez et al. (2018). The transition zone represented by the two orange dashed lines is defined in Salim (2014). The CS1 objects are shown as grey dots while the DP/MaNGA are represented by coloured stars. The NUV-r colour, available for 25 objects, is taken from Chilingarian et al. (2017), it is dust- and k-corrected. The sSFR values are derived from SED fitting of UV and optical spectra, computed by Salim et al. (2016).

Maschmann et al. (2020) discussed that late-type DP galaxies exhibit a central enhancement of their star formation activity with respect to their control sample. We perform the same analysis by computing the ratio of the SFR computed inside the SDSS 3″ fiber $\mathrm{SFR_{fiber}}$ and the total SFR $\mathrm{SFR_{total}}$, provided by Brinchmann et al. (2004). For the DP/MaNGA sample, we do detect a global excess of central star formation enhancement as shown in Fig. 9, but it is not possible to disentangle this effect by morphological type. However, we note that the DP/MaNGA distribution seems bi-modal. In the following, we will further discuss this distribution that is limited here by the integration in the fibre.

Salim (2014) showed that the green-valley galaxies, defined with their NUV-r colour, correspond mainly to galaxies in transition with intermediate specific star formation ratio ($\mathrm{sSFR} = \mathrm{SFR}/\mathrm{M}_\star$). Figure 10 displays the NUV-r colour with respect to the sSFR for the DP/MaNGA galaxies. The NUV magnitude comes from Galaxy Evolution Explorer (GALEX, Martin et al. 2005; Morrissey et al. 2007) and the r magnitude is provided by the SDSS survey. For the sSFR, we use the estimates from Salim et al. (2016) when available, and those from Brinchmann et al. (2004), for the 3 galaxies not in S16. As discussed by Salim (2014), the NUV-r colour defines the so-called green valley, while the $u - r$ and $g - r$ colours are more ambiguous. Four DP/MaNGA objects are lacking a NUV measurement: G25 can be classified with the other colours as clearly on the blue sequence, while G2, G7 and G21 are ambiguous, and will be later discussed.

Table 2 shows, as illustrated in Fig. 10, that 48% of the DP/MaNGA objects appear to belong to the blue cloud, while 45% lie in the green valley, but only 25% of the CS1 galaxies are green-valley galaxies. Given small number statistics, these trends are in fact not significant (1.4σ and 1.3σ respectively). However, when one considers the whole DPS catalogue from Maschmann et al. (2020), as summarised in Tab. 2, there is an excess of green-valley galaxies (a factor 2) with respect to the no-bias control sample (NBCS). Interestingly, this excess disappears when one considers the galaxies in transition with respect to their sSFR, as defined by Salim (2014) ($-11.8 < \log(\mathrm{sSFR}) < -10.8$). Last, we note that while nearly half of the DP/MaNGA galaxies are in the green valley, only 17% of the DPS galaxies are in the green valley. This difference still stands if we consider the objects of the DPS with $z < 0.136$.

Table 2: Classification based on the colour-sSFR diagrams. The first (resp. second) part regards the DP/MaNGA sample compared to the CS1 (resp. the DPS compared to the NBCS from Maschmann et al. 2020).

	DP/MaNGA (29)		CS1 (143)	
NUV measurements	25	(86%)	115	(80%)
Blue cloud	14	(48%)	76	(66%)
Green valley	13	(45%)	29	(25%)
Red sequence	2	(7%)	10	(9%)
Transition zone	7	(27%)	22	(20%)
	DPS (5663)		**NBCS (5128)**	
NUV measurements	4336	(82%)	4628	(85%)
Blue cloud	3578	(63%)	3831	(75%)
Green valley	962	(17%)	410	(8%)
Red sequence	88	(2%)	95	(2%)
Transition	483	(9%)	596	(12%)

As one can notice in Fig. 10, four galaxies, namely G3, G5, G17 and G18 (and a few more discussed below), are efficiently forming stars but are situated in the GV. They are somehow reddish star-forming usually "blue" galaxies. We exclude that these galaxies are affected by undetected dust as (1) we do not see any clear excess in 22μm WISE photometry (Wide-field Infrared Survey Explorer, Wright et al. 2010), and (2) SFR estimate of Salim et al. (2016) is accounting for 22μm WISE fluxes. As we further discuss in the next section, this green feature is due to old stellar populations. However, contrarily to Belfiore et al.

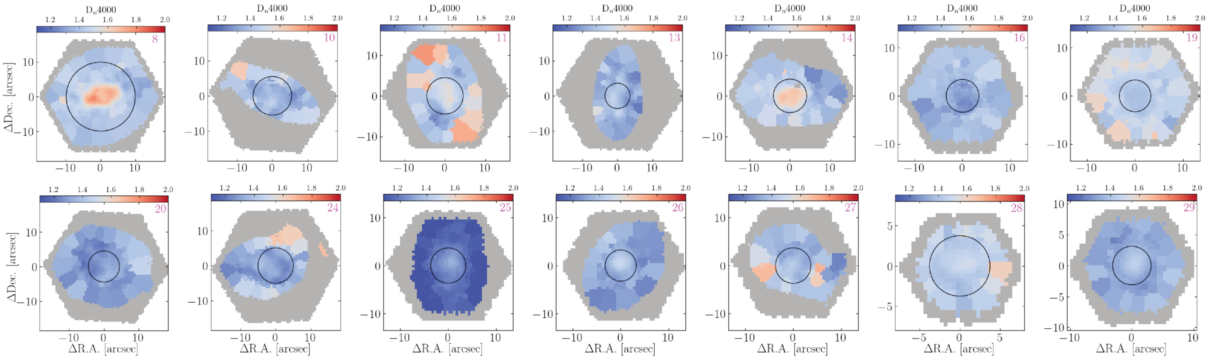

Fig. 11: D_n4000 for the DP/MaNGA galaxies of the blue cloud. The superposed circles indicate R_{eff}.

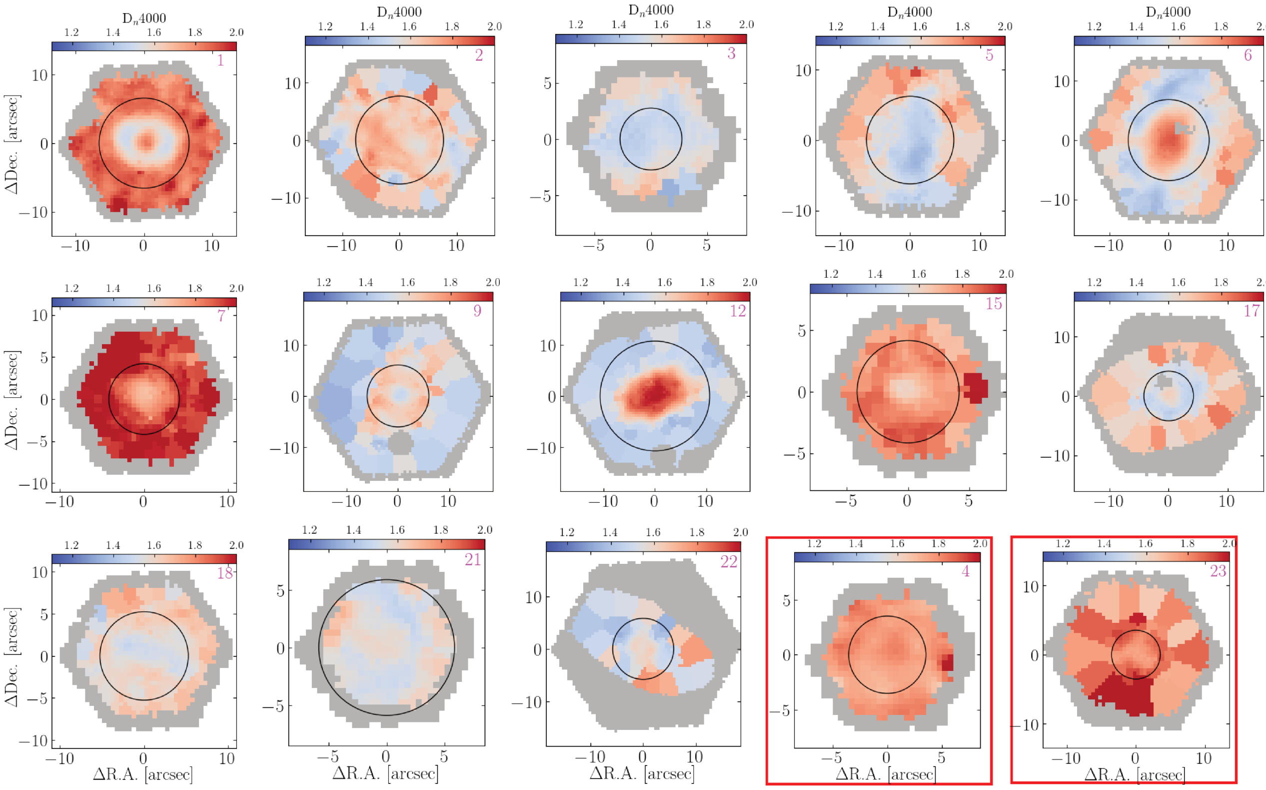

Fig. 12: Same as Fig. 11 for the green-valley and red galaxies. The red galaxies are displayed with red boxes.

(2016), these galaxies are not Low-Ionisation Emission-line Regions (LIERs) as they are actively forming stars.

3.5. Stellar indicator of age: 4000-Å break

Figures 11 and 12 display the $D_n(4000)$, discussed by Kauffmann et al. (2003b) (hereafter K03). It is defined as the ratio of the integral of the flux in the 4000 – 4100Å range divided by the integral of the flux in the 3850 – 3950Å range. This indicator quantifies the strength of the 4000-Å break, which traces a deficiency of hot, blue stars. As discussed by these authors, this index is proportional to the age of the stellar population. Stellar populations younger than 1 Gyr are characterised by an index $D_n(4000) < 1.5$. Figures 11 and 12 show that, while galaxies in the blue cloud host effectively young stellar populations (on average aged of 800 Myr, traced by an average $D_n(4000)$ value of ~ 1.4), the green-valley galaxies like those of the red sequence host old stellar populations. However, they can be observed with two different $D_n(4000)$ spatial distributions: some host old stellar populations in their centre and younger outside, while others have an opposite configuration.

This index thus makes possible to further classify the ambiguous galaxies (G2, G7, G21, G25) that have no NUV measurement (as discussed in Sect. 3.4). G25 has no NUV measurement but hosts the highest SFR and the youngest stellar population of the DP/MaNGA sample. It has been classified in the blue cloud. Alternatively, G7 hosts the oldest stellar population and a moderate SFR. It has thus been classified in the GV. Alternatively, G2 and G21 are less extreme, but we note that they have an average D$_n$(4000) larger than 1.5 and a mean Hδ_A index smaller than 4, suggesting a stellar population older than 1 Gy according to K03. Hence, we choose to classify them in the GV.

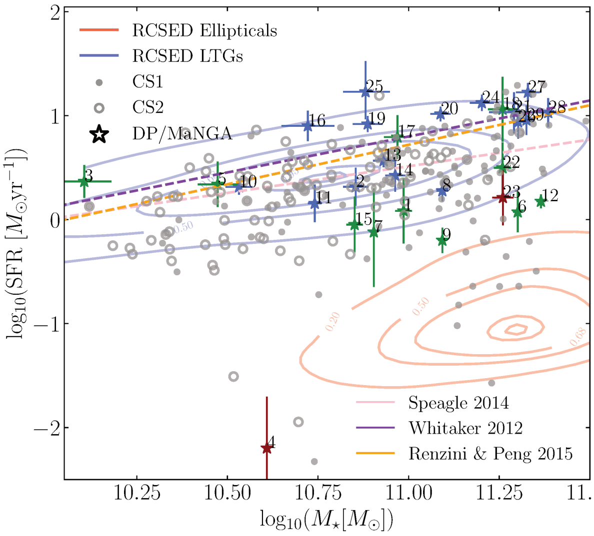

Fig. 13: SFR vs. $M_\star$ diagrams. The DP/MaNGA are represented by coloured stars. The SFR and stellar masses are based on Salim et al. (2016), except for G7, G21 and G25 (based on Brinchmann et al. 2004). The CS1 (resp. CS2) objects are shown as grey dots (resp. filled circles). The galaxies from the RCSED are shown as reference: the red (resp. blue) contour lines correspond to the elliptical (resp. late-type) galaxies, classified using the algorithm presented in Domínguez Sánchez et al. (2018).

4. Star-forming/Composite excitation and hidden AGN

In this section, we will discuss the excitation properties of the different galaxies of the DP/MaNGA sample. In Sect. 4.1, we discuss the star formation main sequence and the age of the stellar populations. In Sect. 4.2, we estimate the AGN fraction present in the DP/MaNGA galaxies. In Sect. 4.3, we study the BPT diagrams.

4.1. Star formation main sequence and stellar population age

Figure 13 displays the star-forming main sequence (SFMS, e.g. Whitaker et al. 2012; Speagle et al. 2014; Renzini & Peng 2015). The DP/MaNGA galaxies are superimposed on the RCSED distributions (80% contours) of late-type (resp. elliptical) galaxies which sample the main sequence (resp. the passive sequence). The DP/MaNGA galaxies sample the main sequence and the transition region, but exhibit a deficit of passive galaxies. The two red galaxies (as defined by their NUV-r colour) are below the SFMS, however, they are not classical quenched galaxies. On the one hand, the S0 galaxy G4 is clearly red and quenched, but shifted with respect to the location of the RCSED ellipticals in the SFR-$M_\star$ plane, due to its smaller mass. On the other hand, the elliptical galaxy G23 exhibits a star formation activity compatible with the sSFR transition zone.

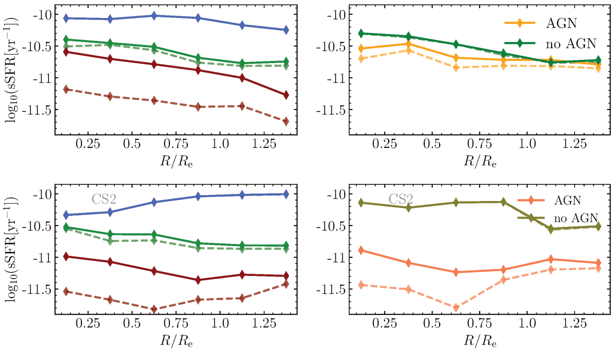

Fig. 14: Radial profiles of sSFR (SFR$_{\mathrm{H}\alpha}/M_\star$). **Top left:** Blue, green and red median of the radial profiles. **Top right:** Radial profiles for the GV galaxies for those with a (resp. no) central AGN fraction in orange (resp. in green). The panels of the **second row** display the same radial profiles but for the CS2. The dashed lines display the sSFR values corrected for extinction and AGN's contribution. The solid lines show the sSFR values corrected for extinction only.

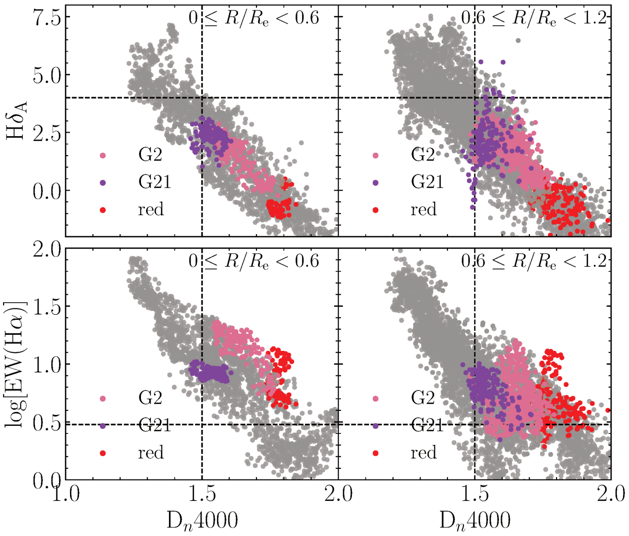

Fig. 15: Stellar age indicators for individual spaxels of the blue-cloud galaxies, represented in grey, in different radial bins. The measurements from the two red-sequence galaxies (G4 and G23) are shown as red dots. The pink (resp. violet) dots correspond to the G2 (resp. G21), ultimately classified as green-valley galaxies.

Figure 14 displays the radial behaviour of the sSFR for the blue, green and red galaxies, in the top left panel. The median profile of the galaxies belonging to the green valley is lower than that of the blue-cloud objects, and somehow less flat. This is in agreement with Belfiore et al. (2018) that found suppressed sSFR profiles for GV galaxies with respect to blue-cloud galaxies. The difference is compatible with their conclusion, as the suppression at 1.0 R_e is about 0.6 dex between the blue-cloud and the GV median profiles. The top left panel displays the radial profiles of the sSFR for the CS2 galaxies. The same overall behaviour is observed but the blue galaxies exhibit a small central deficit of sSFR. Also the red galaxies profile is closer to the green valley one for the DP/MaNGA galaxies. As discussed earlier the DP/MaNGA red galaxies are atypical, and are not well represented by the CS2 galaxies.

The right panels of Fig. 14 shows the green valley itself where we separate the radial profiles for the galaxies with or without a central AGN signature. The group with a nuclear AGN-like activity has a weaker sSFR than the one with no nuclear activity. For the DP/MaNGA galaxies, the difference is relatively small ($\sim$ 0.2 dex), while it is much larger for the CS2 galaxies ($\sim$ 1 dex). Even though we are dealing with small number statistics, such a difference is a signature that we are observing different phase of the central activity. Indeed the radial profiles of the green-valley galaxies with a central AGN activity are close to the profiles of the red galaxies.

Relying on the resolved power of the MaNGA data, we further explore the different properties of these DP/MaNGA to try to understand the quenching mechanism in the studied sources. Figure 15 displays the various stellar population age indicators for 2 radial bins for the blue and red galaxies. We display the H$\delta_{\rm A}$ index, based on the absorption line feature, and the equivalent width of Hα with respect to the D$_n$(4000) index. Following Kauffmann et al. (2003b), we consider that galaxies with an index Hδ_A < 4 and D$_n$(4000) > 1.5 host stellar populations older than 1 Gyr. We inspect the radial profiles of different properties of the blue-cloud galaxies. Their EW(Hα) values are mainly above 3 Å at all galactic radii. The D$_n$(4000) profiles are principally flat too, with low values typical typical of young stellar populations. Figure 15 shows that most of the red-sequence galaxies host stellar populations older than 1 Gyr, but with an EW(Hα) larger than 3 Å (excluding "retired" or passive stellar populations, as discussed in Cid Fernandes et al. 2011). Interestingly, in the blue galaxies, as shown in Fig. 11, the old stellar populations are present in the inner parts of galaxies G8, G11 and G14. G8 is a late-type galaxy in the sSFR transition zone (in Fig. 10), while the two other galaxies are late-type (G11) and S0 (G14) with more regular profiles. Lastly, the galaxies G2 and G21, superimposed on Fig. 15, host old stellar populations and are further classified as GV galaxies (in Fig. 17 and beyond).

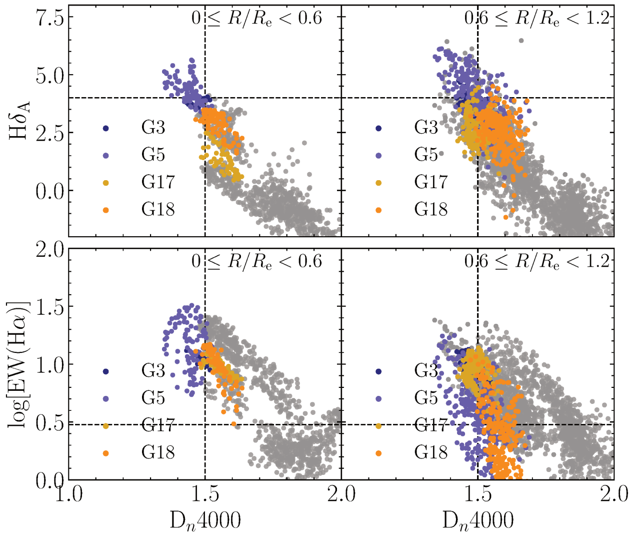

Fig. 16: Stellar age indicators for individual spaxels, of the green-valley galaxies, in different radial bins (but for G2 and G21 that are displayed in Fig. 15). The coloured points correspond to the galaxies G3, G5, G17 and G18 that have green NUV-r colour, but a high star formation activity as shown in Fig. 10.

Figure 16 displays the same stellar parameters as Fig. 15, but for the green-valley galaxies. Contrarily to the blue galaxies, these galaxies host a significant fraction of old stellar population at all scales, as displayed in Fig. 12. We highlight four green-valley galaxies in Fig. 16 which have young stellar populations in their centre and older ones in the outer parts. Among the other galaxies, three of them (G1, G7 and G15) host old stellar population in their outer parts with EW(Hα) larger than 3Å. Two galaxies (G6 and G12) host old stellar populations in their centre, with a large EW(Hα). Lastly, the galaxies G9 and G22 are intermediate galaxies with rather old stellar population and EW(Hα) larger than 3Å in their centre.

We also look at the radial profiles of the Balmer decrement, Hα/Hβ, for all the DP/MaNGA, in order to estimate the amount of dust within these galaxies. The profiles are either flat or slightly decreasing towards outer radii, without any clear discrepancy between blue, green and red galaxies.

We conclude that, besides the small size of the DP/MaNGA sample, we observe significant trends. The green valley DP/MaNGA galaxies are galaxies with a red excess in their spectra, that is due to their stellar populations. However, one part of these galaxies have a older central stellar population, and the other part has a younger central stellar population. Some blue galaxies (like G8) have a small red excess in their central part, which does not dominate their overall colour. In parallel, red galaxies (like G23) still host star formation in a transition regime. In the subsequent section, we study how this relates to the central engine. Due to their central gas content, we do not observe any LIERs (Belfiore et al. 2016).

4.2. *Resolved AGN fraction in the gas excitation*

In this Section, we study the AGN fraction per spaxel, and how this AGN fraction varies with radius for the different galaxies. This enables to classify two types of green-valley galaxies. We then recomputed the central star formation excess within the (half-)central effective radius.

AGN fraction from the ionised gas emission lines

Optical emission lines can be excited by the radiation of star forming regions, but also by AGN radiation, or through shocks. Diagnostics based on line ratios such as [NII]/Hα and [OIII]/Hβ are widely used, since independent of extinction (Baldwin et al. 1981). With MaNGA data, we can estimate the fraction of AGN-dominated excitation for each spaxel.

The Hα emission is a tracer of young, hot stars, and therefore of star-formation activity, but is also contaminated by AGN's narrow line region. The observed Hα flux is thus over-estimating the SFR. Jin et al. (2021) proposed an approach to correct for the AGN's contamination in the Hα emission that we follow. We compute the AGN fraction $f_{\rm AGN}$, based on the emission flux measurements provided by the DAP, that corresponds to the AGN's contribution to the Hα flux (Jin et al. 2021). Following the 3D diagnostic diagram presented in Ji & Yan (2020), the P_1 indicator is computed as:

$$P_1 = 0.63\log([\mathrm{NII}]/\mathrm{H}\alpha) + 0.51\log([\mathrm{SII}]/\mathrm{H}\alpha) + 0.59\log([\mathrm{OIII}]/\mathrm{H}\beta) \quad (2)$$

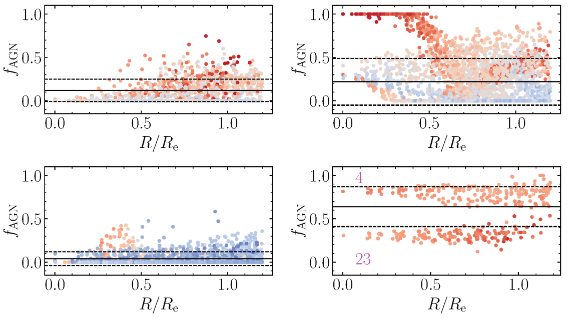

Fig. 17: Spaxel-by-spaxel radial profiles of the AGN fraction $f_{\rm AGN}$ for the DP/MaNGA galaxies. Each panel corresponds to different types of galaxies defined in the colour-sSFR diagram in Fig. 10. The top panels display the GV galaxies, the left (resp. right) panel shows the profiles of the objects without (resp. with) any important AGN fraction in their inner parts. The bottom left (resp. right) panel displays the blue (resp. red) galaxies. The dots are colour-coded with the $D_n(4000)$ values, shown on Figs 11 and 12. The full (resp. dashed) lines refer to the averaged (resp. rms) values $\langle f_{\rm AGN}\rangle$ and $\sigma_{\rm AGN}$ computed following Eq. B.1 and listed in Tab. B.1.

Then, the AGN fraction is set such that:

$$f_{\rm AGN} = \begin{cases} 0 & \text{if} P_1 \leq -0.53 \\ 0.14P_1^2 + 0.96P_1 + 0.47 & \text{if} -0.53 < P_1 \leq 0.51 \\ 1 & \text{if} P_1 \geq 0.51 \end{cases} \quad (3)$$

In this way, the AGN fraction is a number such that $0 < f_{\rm AGN} < 1$, depending on the value of P_1. This relation was applied to all spaxels where all the lines have a reliable emission (S/N > 3) in the emission lines required for the P_1 parameter computation. Figures B.1 and B.2 show the resulting 2D maps of the $f_{\rm AGN}$ value for all the DP/MaNGA galaxies. Figure 17 displays radial profiles of the $f_{\rm AGN}$ fraction of the DP/MaNGA galaxies. In the bottom panels corresponding to the blue (left) and red (right) galaxies, the radial profiles are flat, but differs by the level. As discussed in Jin et al. (2021), the blue galaxies have no significant central AGN fraction, contrarily to the red galaxies. The radial profiles of the AGN fraction $f_{\rm AGN}$ are flat for the blue galaxies (and null) but for the galaxy in transition (8), and for a few that exhibit weak $f_{\rm AGN}$ in their disc. They are also flat for the red galaxies (but at a value of about 0.8 (G4) and 0.3 (G23)). Alternatively, for the GV galaxies, we note two types of behaviours: the galaxies with a nuclear activity and those with none. The top panels of Fig. 17 display the spaxel-based resolved profiles of these two types of galaxies: the GV galaxies with no AGN fraction in their centre (G2, G3, G7, G15, G17, G18, G21), and the GV galaxies with non-zero AGN fraction in their centre (G1, G5, G6, G9, G12, G22). The former category exhibits a behaviour close to the one of the blue category. The latter shows high and medium levels of AGN fraction in their centre, but contrarily to the red galaxies the radial profiles are not flat. They seem in an multi-stage transition regime, resulting in the composite excitation observed in the BPT diagram (see below). All the four panels show a correlation between the AGN fraction $f_{\rm AGN}$ and the $D_n(4000)$ index: the AGN fraction is low for low $D_n(4000)$ values, tracing young stellar populations. Higher values of $f_{\rm AGN}$ are characterised by greater $D_n(4000)$.

Figure 17 displays the mean and scatter (rms) for each panel. This is further discussed in Appendix B. We clearly observe that the means are systematically smaller for the non-central-AGN galaxies than for the central-AGN galaxies. When this AGN fraction is used to correct the sSFR, the radial profiles displayed in Fig. 14 decrease by 0.5 dex for the red galaxies and the green-valley galaxies of the CS2, while the effect is smaller (~ 0.1 dex) for the green valley DP/MaNGA galaxies, while the green valley BPT are less filled due to small statistics.

Central star formation excess

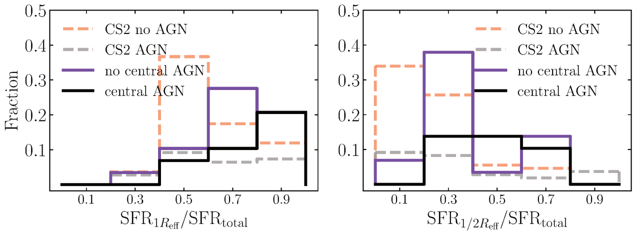

Fig. 18: Star-formation excess computed within an elliptical radius of $R_{\rm eff}$ (left) and $0.5\,R_{\rm eff}$ (right). The DP/MaNGA galaxies with and without nuclear activity are compared with their counterparts from the CS2 control sample.

Figure 18 displays the central star formation excess computed within radii of $0.5R_{\rm eff}$ and $1.0R_{\rm eff}$, for DP/MaNGA and CS2 galaxies. This excess is given as fractions for objects with and without a central AGN activity. It shows that the area over $1R_{\rm eff}$ contains at least 50% of the Hα-based star formation rate of the galaxies. The fractions are systematically lower for the CS2 sample. The right panel displays the same systematic central SF excess for the DP/MaNGA galaxies with respect to the CS2 ones but shows that the star formation activity is not restricted to the nucleus but distributed within the effective radius. In parallel, there is no clear effect between the central and satellite galaxies.

4.3. Resolved BPT diagrams

Figure 19 displays the BPT diagrams for the same categories of galaxies displayed in Fig. 17. The red galaxies lies at the border of the composite region, but mainly with the Seyfert and LINER classifications (and we discussed previously that they are not LIERs based on Fig. 15). The blue galaxies are star-forming in their centre with some spaxels from composite excitation in their outskirts (e.g. galaxy 8, which has a profile close to the upper left panel). The GV galaxies have been separated into two categories based on their AGN fraction. They mostly present a BPT diagram with spaxels along the diagonal, i.e. different from the blue galaxies. The green-valley galaxies with a central fraction of AGN have spaxels located further towards the Seyfert/LINER regions than their green with no central-AGN-fraction counterparts. The difference of the spatially-resolved BPT shape between the latter and the one of the blue-cloud objects suggests that the GV galaxies are moving from the star-formation regime to the composite one. The four emission lines used in this diagnostic diagram are required to reach a minimal signal-to-noise ratio of 3, so the lower number of detected spaxels away from the galaxy centre (displayed in red on Fig. 19) can be caused by a lack of ionised gas at the large radii. But this is also to be accounted for the spatial coverage of the MaNGA, which is either

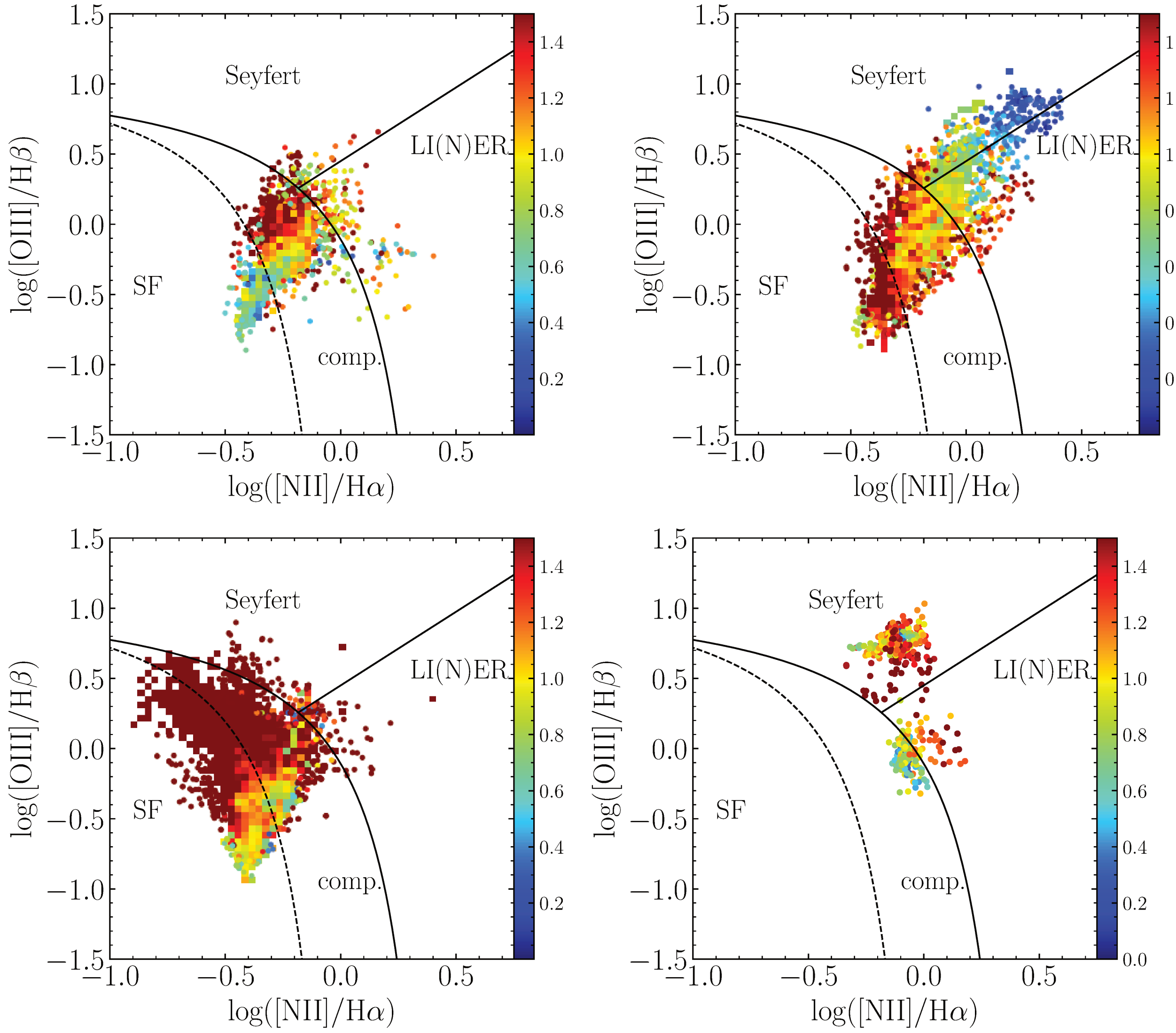

Fig. 19: BPT diagrams. **Top panels:** Green valley galaxies with a (resp. no) central AGN fraction on the right (resp. left). **Bottom-left panel:** Blue-sequence galaxies. **Bottom-right panel:** Red-sequence galaxies. The colour indicates the distance to the center, in units of R$_e$.

out to 1.5R_{eff} or 2.5$_{\mathrm{eff}}$ (Wake et al. 2017) and in our case, the majority of the blue-cloud galaxies are covered to 2.5R_{eff} while most of the green-valley objects are covered to 1.5R_{eff}. The BPT diagrams for the CS2 galaxies, following the same group division, are shown in Fig. C.1. In general, the spaxel distributions follow the same trends as for those of the DP/MaNGA galaxies, while the BPT diagrams corresponding to the green-valley galaxies are less filled due to small statistics. We also note that the CS2 red galaxies are better sampling the BPT, with a non-negligible component of star-forming regions in the outskirt.

4.4. Summary

The DP galaxies from Maschmann et al. (2020) are characterised by an excess of GV galaxies (defined with their NUV-r colour) with respect to the no-bias-control sample. We have studied the DP/MaNGA galaxies among the DP sources and found that for these sources the red-excess of the GV galaxies is due to their stellar population (with the D_n(4000) index). A fraction of these galaxies are actively star-forming, while the others are in the transition zone of star formation. We identified two types of GV galaxies, those with a high AGN fraction in their centre, and the others with no AGN fraction in their centre. The latter have a positive D_n(4000) gradient, while the former exhibit a negative one. This sample is quite peculiar in the sense that the selection has been somehow based on star-forming galaxies (i.e. with detectable emission lines) and green-valley galaxies. It thus enables to study on-going quenching mechanisms.

5. Discussion

In this section, we discuss how the DP/MaNGA galaxies fit into the more general context of galaxy quenching. In Sect. 5.1, we discuss the scenario of inside-out quenching, then in Sect. 5.2

outside-in. In Sect. 5.3, we compare the compatibility of our new findings with the scenario of minor mergers accounting for the central SFR excess and the large bulge features.

5.1. Quenching inside-out

The GV galaxies are redder that their blue counterparts as they host redder stellar populations. On the BPT, they host obvious signs of AGN-related emission in their centre for a fraction of them, clearly in transition. Those galaxies host old stellar populations in their centre, but the EW(Hα) is there larger than 3Å, excluding the LIER stage, excited only by old stars, without any young star formation, nor any nuclear activity at the origin of their excitation, described by Belfiore et al. (2017). The other part of the GV galaxies host younger stellar populations in their centre, but their location on the BPT diagram seems intermediate between the blue galaxies and the former GV galaxies, suggesting an underlying nuclear activity. This scenario would be in agreement with the results of Bluck et al. (2020a,b) based on the exploitation of spatially resolved star formation rates of MaNGA galaxies. Beside the evidence of nuclear activity, these authors also discussed that central galaxies preferentially quench inside-out, while our DP/MaNGA galaxies are mainly isolated or in small groups, they are hence mainly centrals.

Various studies have questioned the correlation between AGN and the quenching mechanism (McPartland et al. 2019; Chen et al. 2020). Our work shows that nuclear activity can be weak and escape detection. This kind of nuclear activity would certainly be undetected at high-z. Our results are in good agreement with Barrows et al. (2017), who found the AGN triggering is more probable at late-merger stages.

5.2. Quenching outside-in

Alternatively, green-valley galaxies that are actively forming stars with no-central AGN fraction and hence undetected nuclear activity host blue central stellar populations and red stellar populations in their outskirts. Some of these DP/MaNGA galaxies (including some blue ones) are quenched in their outskirts as displayed in Fig. 15 and 16. They could have quenched their outskirt star-formation activity either by environment or gas exhaustion, as discussed in Peng et al. (2010) (see also Schawinski et al. 2014).

The $D_n(4000)$ stellar population index traces the relatively young stellar populations in different massive galaxies whose masses are dominated by the old stellar population. These intermediate galaxies might host slightly less gas and star formation than the others. Could they be old galaxies having accreted gas in their centre and possibly triggering weak nuclear activity? Relying on SDSS galaxies, Kaviraj (2014) discussed that disturbed spirals also exhibit higher nuclear-accretion rates, and they interpret this with minor mergers, which can represent 40% of star formation in spirals.

Last, it is also possible that the underlying nuclear activity (detected in Fig. 19) has changed in intensity with time and generated turbulence which might impact the velocity dispersion (and the DP feature) and the star-formation. Mandal et al. (2021) studied with simulations the interaction of the interstellar medium with the radio jet. They found that the dense clouds near the central region, where the density is enhanced due to the compression, exhibit a generally higher SFR than the clouds in the outskirts, even though lower than with no-jet counterparts. This study is focused on the case where the jet lies in the disc, while there is no radio jet detection in DP/MaNGA galaxies characterised by a weak nuclear activity.

5.3. Minor mergers and other alternatives

The DP galaxies are characterised by a larger Sérsic index than the control samples matched in stellar mass and redshift, as well as by a central star formation rate excess. While classical bulges are thought to be built through mergers (e.g. Weinzirl et al. 2009), with some violent processes followed by strong relaxation (see also Mihos & Hernquist 1994), a bulge growth is also expected in the multiple sequential merger scenario proposed by Bournaud et al. (2007). The DP/MaNGA galaxies also correspond to the trend discussed in Lotz et al. (2008): post-coalescence galaxies are more concentrated in their light distribution, while tidal features vanish. In parallel, Martig et al. (2013) claimed that only a few amounts of gas can be stabilised against star formation in galaxies with massive spheroids (the so-called morphological quenching). Indeed, high surface densities can allow the gas to fragment. Moreover, interactions with other galaxies can trigger star formation, and, in these cases, some early-type galaxies are not completely quenched. This concentration can also be observed for bar-driven gas infall (e.g. Schinnerer et al. 2007; Kim & Elmegreen 2017). However, there is only a small fraction of barred objects in the DP/MaNGA sample (about 17% according to the photometric value-added catalogue) and the spatial resolution is not adapted to detect inner bars, but we cannot exclude at this stage that the DP feature is due to a decoupled inner kinematic structure.

Interestingly, Kaviraj et al. (2009) discussed that merger events onto early-type galaxies could account for red NUV-r colour. They claim that an intermediate NUV-r colour, as observed for 7 out of the 9 early-type DP/MaNGA galaxies, can result from minor mergers with smaller mass ratios than 1:6 or from mergers with higher mass ratios but more than $\sim$ 1Gyr old. On the other hand, early-types with bluer colour (NUV-r < 3.8, as galaxies G14 and G16) can originate from mergers with mass ratios between 1:4 and 1:6, involving progenitors with gas fractions greater than $\sim$ 20 percent.

Mancini et al. (2019) discussed that part of the green-valley galaxies could be quenched galaxies that are rejuvenated. This is supported by the observations of old bulges surrounded by young discs at $z \geq 0.5 - 1$, as well as local galaxies like M31 (Williams et al. 2017; Telford et al. 2019). Similarly, Sachdeva & Saha (2018) discussed that some bulges at $z < 1$ are bright and compact with 1.5-2 larger sSFR and 2.5-6 times more massive than classical and pseudo-bulges. They discussed that these bright compact bulges could correspond to rejuvenation of existing spheroids, while the majority (80%) is old and red. This could indeed account for our observations as the $D_n(4000)$ is tracing the age of the stellar populations, but does not necessary trace the mass, while the spectral flux is dominated by the young stars.

Our results are compatible with the finding of Mountrichas et al. (2021), based on X-ray measurements who discussed a scenario where AGN and star formation are both fed by cold gas, supplied by a merger event. They found that the SFR is enhanced by 40% in presence of AGN (See also Torbaniuk et al. 2021).

6. Conclusion

We have studied the star formation and AGN properties of a sample of Double-Peaked galaxies selected from the Sloan Survey, and mapped in the MaNGA (Mapping Nearby Galaxies at

APO) survey. With these resolved maps, we obtained 2D diagnostics of AGN and/or star formation excitation of the ionised gas lines, and compared with stellar population ages, deduced from $D_n(4000)$ and $H\delta_A$ indices, colours and magnitudes. This enables us to compare the possible sources of quenching, supernovae or AGN feedback, mass or environment in DP-galaxies with respect to the control sample of single-peaked ones.

Our main results are that the DP/MaNGA galaxies have:

- a higher fraction of green-valley objects
- a green colour in the GV category due to red stellar population (hence older than 1Gyr)
- an AGN fraction linked to the stellar population age
- more than 50% of the star formation activity occurs inside one effective radius, and is more concentrated than for galaxies of the control samples
- the galaxies are central galaxies mainly isolated or in small groups.

We can state that the different sub-groups defined in this analysis constitute an evolutionary sequence. The blue-cloud galaxies exhibit star-forming discs with an important gas content and a star formation concentrated in their inner parts, compatible with gas accretion through minor mergers. In these mergers, the gas may come in part from the companion, but the major part from the gas reservoir of the primary galaxy's outskirts, which is depleted and driven inwards by the interaction. After the central star formation has faded, the gas fuels the central engine of these objects, triggering a nuclear activity supposed linked to weak AGN, even though we cannot exclude intense star formation and associated feedback. AGN-like signatures are then observed, linked with old stellar populations in the central regions, and the galaxy enters the green valley. The nuclear activity of these GV galaxies is then observed to reduce the central star formation (inside-out quenching). In a possible next phase, the gas from the disc infalls and fuels again the central region, but the disc is no longer replenished from the depleted outer reservoir. The disk appears then quenched outside-in. These two transitions are mainly observed in the green-valley galaxies, which are observed in excess in the DP galaxy population.

In forthcoming papers, we will continue the investigation of the double-peaked MaNGA galaxies through other properties such as their old gas content using CO and HI observations to further explore the quenching mechanisms involved and their kinematics using a multi-component analysis to interpret their global evolution.

Acknowledgements. Funding for the Sloan Digital Sky Survey IV has been provided by the Alfred P. Sloan Foundation, the U.S. Department of Energy Office of Science, and the Participating Institutions. SDSS-IV acknowledges support and resources from the Center for High-Performance Computing at the University of Utah. The SDSS web site is www.sdss.org. SDSS-IV is managed by the Astrophysical Research Consortium for the Participating Institutions of the SDSS Collaboration including the Brazilian Participation Group, the Carnegie Institution for Science, Carnegie Mellon University, the Chilean Participation Group, the French Participation Group, Harvard-Smithsonian Center for Astrophysics, Instituto de Astrofísica de Canarias, The Johns Hopkins University, Kavli Institute for the Physics and Mathematics of the Universe (IPMU) / University of Tokyo, the Korean Participation Group, Lawrence Berkeley National Laboratory, Leibniz Institut für Astrophysik Potsdam (AIP), Max-Planck-Institut für Astronomie (MPIA Heidelberg), Max-Planck-Institut für Astrophysik (MPA Garching), Max-Planck-Institut für Extraterrestrische Physik (MPE), National Astronomical Observatories of China, New Mexico State University, New York University, University of Notre Dame, Observatário Nacional / MCTI, The Ohio State University, Pennsylvania State University, Shanghai Astronomical Observatory, United Kingdom Participation Group, Universidad Nacional Autónoma de México, University of Arizona, University of Colorado Boulder, University of Oxford, University of Portsmouth, University of Utah, University of Virginia, University of Washington, University of Wisconsin, Vanderbilt University, and Yale University.
The Legacy Surveys consist of three individual and complementary projects: the Dark Energy Camera Legacy Survey (DECaLS; Proposal ID #2014B-0404; PIs: David Schlegel and Arjun Dey), the Beijing-Arizona Sky Survey (BASS; NOAO Prop. ID #2015A-0801; PIs: Zhou Xu and Xiaohui Fan), and the Mayall z-band Legacy Survey (MzLS; Prop. ID #2016A-0453; PI: Arjun Dey). DECaLS, BASS and MzLS together include data obtained, respectively, at the Blanco telescope, Cerro Tololo Inter-American Observatory, NSF's NOIRLab; the Bok telescope, Steward Observatory, University of Arizona; and the Mayall telescope, Kitt Peak National Observatory, NOIRLab. The Legacy Surveys project is honored to be permitted to conduct astronomical research on Iolkam Du'ag (Kitt Peak), a mountain with particular significance to the Tohono O'odham Nation. This project makes use of the MaNGA-Pipe3D dataproducts. We thank the IA-UNAM MaNGA team for creating this catalogue, and the Conacyt Project CB-285080 for supporting them.

References

Aguado, D. S., Ahumada, R., Almeida, A., et al. 2019, ApJS, 240, 23
Baldry, I. K., Glazebrook, K., Brinkmann, J., et al. 2004, ApJ, 600, 681
Baldwin, J. A., Phillips, M. M., & Terlevich, R. 1981, PASP, 93, 5
Barrows, R. S., Comerford, J. M., Zakamska, N. L., & Cooper, M. C. 2017, ApJ, 850, 27
Belfiore, F., Maiolino, R., Bundy, K., et al. 2018, MNRAS, 477, 3014
Belfiore, F., Maiolino, R., Maraston, C., et al. 2017, MNRAS, 466, 2570
Belfiore, F., Maiolino, R., Maraston, C., et al. 2016, MNRAS, 461, 3111
Blanton, M. R., Bershady, M. A., Abolfathi, B., et al. 2017, AJ, 154, 28
Blanton, M. R., Kazin, E., Muna, D., Weaver, B. A., & Price-Whelan, A. 2011, AJ, 142, 31
Blanton, M. R. & Moustakas, J. 2009, ARA&A, 47, 159
Bluck, A. F. L., Maiolino, R., Piotrowska, J. M., et al. 2020a, MNRAS, 499, 230
Bluck, A. F. L., Maiolino, R., Sánchez, S. F., et al. 2020b, MNRAS, 492, 96
Boselli, A., Cuillandre, J. C., Fossati, M., et al. 2016, A&A, 587, A68
Bournaud, F., Jog, C. J., & Combes, F. 2007, A&A, 476, 1179
Brinchmann, J., Charlot, S., White, S. D. M., et al. 2004, MNRAS, 351, 1151
Bundy, K., Bershady, M. A., Law, D. R., et al. 2015, ApJ, 798, 7
Cappellari, M. 2017, MNRAS, 466, 798
Cappellari, M. & Emsellem, E. 2004, PASP, 116, 138
Chabrier, G. 2003, PASP, 115, 763
Chen, Z., Faber, S. M., Koo, D. C., et al. 2020, ApJ, 897, 102
Chilingarian, I. V., Zolotukhin, I. Y., Katkov, I. Y., et al. 2017, ApJS, 228, 14
Cid Fernandes, R., Stasińska, G., Mateus, A., & Vale Asari, N. 2011, MNRAS, 413, 1687
Coenda, V., Martínez, H. J., & Muriel, H. 2018, MNRAS, 473, 5617
Comerford, J. M., Gerke, B. F., Stern, D., et al. 2012, ApJ, 753, 42
Comerford, J. M., Nevin, R., Stemo, A., et al. 2018, ApJ, 867, 66
Condon, J. J., Helou, G., Sanders, D. B., & Soifer, B. T. 1993, AJ, 105, 1730
Dey, A., Schlegel, D. J., Lang, D., et al. 2019, AJ, 157, 168
Di Matteo, P., Bournaud, F., Martig, M., et al. 2008, A&A, 492, 31
Domínguez Sánchez, H., Huertas-Company, M., Bernardi, M., Tuccillo, D., & Fischer, J. L. 2018, MNRAS, 476, 3661
Drory, N., MacDonald, N., Bershady, M. A., et al. 2015, AJ, 149, 77
Falcón-Barroso, J., Sánchez-Blázquez, P., Vazdekis, A., et al. 2011, A&A, 532, A95
Fischer, J. L., Domínguez Sánchez, H., & Bernardi, M. 2019, MNRAS, 483, 2057
Ge, J.-Q., Hu, C., Wang, J.-M., Bai, J.-M., & Zhang, S. 2012, ApJS, 201, 31
Holmberg, E. 1958, Meddelanden fran Lunds Astronomiska Observatorium Serie II, 136, 1
Inami, H., Armus, L., Surace, J. A., et al. 2010, AJ, 140, 63
Ji, X. & Yan, R. 2020, MNRAS, 499, 5749
Jin, G., Dai, Y. S., Pan, H.-A., et al. 2021, arXiv e-prints, arXiv:2109.11084
Kauffmann, G., Heckman, T. M., White, S. D. M., et al. 2003a, MNRAS, 341, 33
Kauffmann, G., Heckman, T. M., White, S. D. M., et al. 2003b, MNRAS, 341, 54
Kaviraj, S. 2014, MNRAS, 440, 2944
Kaviraj, S., Peirani, S., Khochfar, S., Silk, J., & Kay, S. 2009, MNRAS, 394, 1713
Kaviraj, S., Shabala, S. S., Deller, A. T., & Middelberg, E. 2015, MNRAS, 452, 774
Kim, W.-T. & Elmegreen, B. G. 2017, ApJ, 841, L4
Kroupa, P. 2001, MNRAS, 322, 231
Lahén, N., Johansson, P. H., Rantala, A., Naab, T., & Frigo, M. 2018, MNRAS, 475, 3934
Law, D. R., Cherinka, B., Yan, R., et al. 2016, AJ, 152, 83
Lotz, J. M., Davis, M., Faber, S. M., et al. 2008, ApJ, 672, 177
Lotz, J. M., Primack, J., & Madau, P. 2004, AJ, 128, 163

Mancini, C., Daddi, E., Juneau, S., et al. 2019, MNRAS, 489, 1265
Mandal, A., Mukherjee, D., Federrath, C., et al. 2021, MNRAS, 508, 4738
Martig, M., Bournaud, F., Teyssier, R., & Dekel, A. 2009, ApJ, 707, 250
Martig, M., Crocker, A. F., Bournaud, F., et al. 2013, MNRAS, 432, 1914
Martin, D. C., Fanson, J., Schiminovich, D., et al. 2005, ApJ, 619, L1
Maschmann, D. & Melchior, A.-L. 2019, A&A, 627, L3
Maschmann, D., Melchior, A.-L., Mamon, G. A., Chilingarian, I. V., & Katkov, I. Y. 2020, A&A, 641, A171
Mazzilli Ciraulo, B., Melchior, A.-L., Maschmann, D., et al. 2021, A&A, 653, A47
McPartland, C., Sanders, D. B., Kewley, L. J., & Leslie, S. K. 2019, MNRAS, 482, L129
Meert, A., Vikram, V., & Bernardi, M. 2015, MNRAS, 446, 3943
Mihos, J. C. & Hernquist, L. 1994, ApJ, 431, L9
Morrissey, P., Conrow, T., Barlow, T. A., et al. 2007, ApJS, 173, 682
Mountrichas, G., Buat, V., Yang, G., et al. 2021, A&A, 653, A74
Nevin, R., Comerford, J. M., Müller-Sánchez, F., Barrows, R., & Cooper, M. C. 2018, MNRAS, 473, 2160
Patton, D. R., Ellison, S. L., Simard, L., McConnachie, A. W., & Mendel, J. T. 2011, MNRAS, 412, 591
Peng, Y.-j., Lilly, S. J., Kovač, K., et al. 2010, ApJ, 721, 193
Rasmussen, J., Ponman, T. J., Verdes-Montenegro, L., Yun, M. S., & Borthakur, S. 2008, MNRAS, 388, 1245
Renzini, A. & Peng, Y.-j. 2015, ApJ, 801, L29
Rodriguez-Gomez, V., Snyder, G. F., Lotz, J. M., et al. 2019, MNRAS, 483, 4140
Sachdeva, S. & Saha, K. 2018, MNRAS, 478, 41
Saintonge, A., Kauffmann, G., Wang, J., et al. 2011, MNRAS, 415, 61
Salim, S. 2014, Serbian Astronomical Journal, 189, 1
Salim, S., Lee, J. C., Janowiecki, S., et al. 2016, ApJS, 227, 2
Sánchez, S. F., Avila-Reese, V., Hernandez-Toledo, H., et al. 2018, Rev. Mexicana Astron. Astrofis., 54, 217
Sánchez, S. F., Pérez, E., Sánchez-Blázquez, P., et al. 2016a, Rev. Mexicana Astron. Astrofis., 52, 171
Sánchez, S. F., Pérez, E., Sánchez-Blázquez, P., et al. 2016b, Rev. Mexicana Astron. Astrofis., 52, 21
Saulder, C., van Kampen, E., Chilingarian, I. V., Mieske, S., & Zeilinger, W. W. 2016, A&A, 596, A14
Schawinski, K., Urry, C. M., Simmons, B. D., et al. 2014, MNRAS, 440, 889
Schinnerer, E., Böker, T., Emsellem, E., & Downes, D. 2007, A&A, 462, L27
Speagle, J. S., Steinhardt, C. L., Capak, P. L., & Silverman, J. D. 2014, ApJS, 214, 15
Telford, O. G., Werk, J. K., Dalcanton, J. J., & Williams, B. F. 2019, ApJ, 877, 120
Torbaniuk, O., Paolillo, M., Carrera, F., et al. 2021, MNRAS, 506, 2619
van der Wel, A., Franx, M., van Dokkum, P. G., et al. 2014, ApJ, 788, 28
Wake, D. A., Bundy, K., Diamond-Stanic, A. M., et al. 2017, AJ, 154, 86
Weinmann, S. M., Kauffmann, G., van den Bosch, F. C., et al. 2009, MNRAS, 394, 1213
Weinzirl, T., Jogee, S., Khochfar, S., Burkert, A., & Kormendy, J. 2009, ApJ, 696, 411
Westfall, K. B., Cappellari, M., Bershady, M. A., et al. 2019, AJ, 158, 231
Whitaker, K. E., van Dokkum, P. G., Brammer, G., & Franx, M. 2012, ApJ, 754, L29
Whitmore, B. C., Brogan, C., Chandar, R., et al. 2014, ApJ, 795, 156
Williams, B. F., Dolphin, A. E., Dalcanton, J. J., et al. 2017, ApJ, 846, 145
Wright, E. L., Eisenhardt, P. R. M., Mainzer, A. K., et al. 2010, AJ, 140, 1868
Wyder, T. K., Martin, D. C., Schiminovich, D., et al. 2007, ApJS, 173, 293
Yang, X., Mo, H. J., van den Bosch, F. C., et al. 2007, ApJ, 671, 153

Appendix A: Gini-M_{20} diagram

Using the python package STATMORPH[4] on the r-band Legacy survey snapshots, we calculate non-parametric morphological diagnostics (see Rodriguez-Gomez et al. 2019) in order to display our galaxies on the $G - M_{20}$ diagram (Lotz et al. 2004, 2008). This approach is based on the measurements of two parameters: the Gini coefficient G and the second-order moment of the brightest 20% of the galaxy's flux. The former can be used to quantify galaxy morphology.

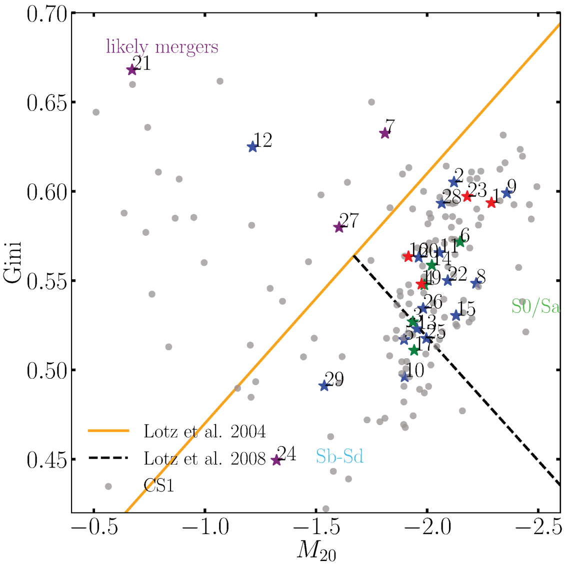

Fig. A.1: Gini vs M_{20} diagram. The CS galaxies are shown by grey dots. The orange line sets the division between merger candidates and normal Hubble types (Lotz et al. 2004). The black dotted line separates early-type (E, S0 and Sa) from late-type objects (Sb to Sd, as well as Irr) (Lotz et al. 2008). Galaxy 18 does not appear on this panel but has (-1.21,0.86) for coordinates, so falls in the "likely mergers" region.

.

In Fig. A.1, we display the so-called Gini-M_{20} diagram for the 29 DP/MaNGA galaxies, while Tab. A.1 summarises the classification of the 29 DP/MaNGA galaxies (resp. 143 CS1 galaxies) with reliable measurements.

Table A.1: Classification of the DP/MaNGA sample (coloured symbols) compared to the CS1 (grey symbols), based on the Gini-M_{20} diagram. The DP/MaNGA galaxies are colour-coded with the

	DP/MaNGA		CS	
Sb-Sd	7	(24%)	35	(24%)
S0/Sa	11	(38%)	47	(33%)
likely mergers	3	(10%)	14	(10%)

Notes: For the percentage computation, we only consider the number of galaxies that have reliable morphological measurements (see first row of the table).

Appendix B: Averaged trends depending on galaxy colours

We estimate an averaged AGN fraction $\langle f_{\rm AGN}\rangle$, an rms $\sigma_{\rm AGN}$ and an error $\epsilon_{\rm AGN}$ of this quantity for each of the four galaxy types:

$$\langle f_{\rm AGN}\rangle = \frac{\Sigma\,\phi_{\rm H\alpha} f_{\rm AGN}}{\Sigma\,\phi_{\rm H\alpha}};\, \sigma_{\rm AGN} = \sqrt{\langle {f_{\rm AGN}}^2\rangle - \langle f_{\rm AGN}\rangle^2};$$
$$\epsilon_{\rm AGN} = \frac{\sigma_{\rm AGN}}{\sqrt{N_{\rm spaxels}}} \tag{B.1}$$

where $N_{\rm spaxels}$ is the number of spaxels considered to compute the averaged value within each galaxy group. We compute these quantities for the DP/MaNGA and the CS2 galaxies, divided in different sub-groups. The errors $\epsilon_{\rm AGN}$ on the means are of order 10^{-5}: the mean values are well-defined quantities even though the scatter of the distribution is large. The statistical results are summarised in Tab. B.1. We observe an overall large scatter for each distribution and comparable values between the DP/MaNGA and the CS2 sample, but the means are systematically smaller for the non-central-AGN galaxies than for the central-AGN galaxies (in the GV and when considering all of them). Small numbers of red galaxies prevent any reliable comparison. Last, we do not detect any significant differences between the central and satellite galaxies.

Table B.1: Averaged AGN fractions weighted by the Hα fluxes and computed on all the spaxels with reliable signal (S/N > 3 for all the emission lines required for the $f_{\rm AGN}$ computation), with the rms value $\sigma_{\rm AGN}$ of each distribution. The galaxies defined as "most massive" are either isolated galaxies, or the most massive galaxies of the groups as defined in Sect. .

$\langle f_{\rm AGN}\rangle$	DP/MaNGA (29)	CS2 (108)
Blue cloud galaxies	0.04 (0.08)	0.03 (0.09)
Green valley galaxies	0.18 (0.24)	0.17 (0.26)
no-central-AGN galaxies	0.12 (0.13)	0.04 (0.08)
central-AGN galaxies	0.22 (0.27)	0.38 (0.29)
Red sequence galaxes	0.64 (0.23)	0.19 (0.32)
Transition galaxies	0.18 (0.26)	0.12 (0.22)
No-central-AGN galaxies	0.05 (0.09)	0.01 (0.05)
Central-AGN galaxies	0.23 (0.28)	0.14 (0.24)
Most massive galaxies	0.12 (0.21)	0.03 (0.11)
Satellite galaxies	0.11 (0.17)	0.06 (0.15)

Appendix C: BPT diagrams for the CS2 sample

Figure C.1 displays the BPT for the CS2 galaxies organised in four categories as defined in Sect. 4.3 and in Fig. 19.

---

[4] https://pypi.org/project/statmorph/

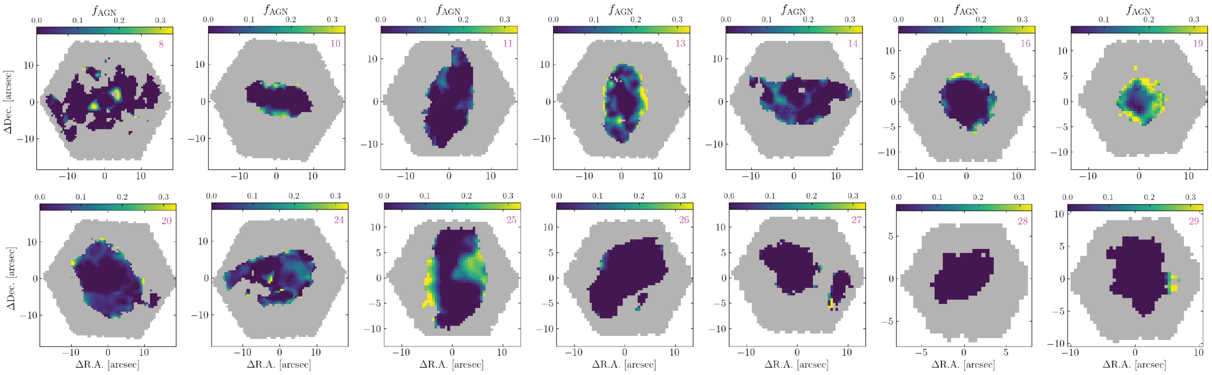

Fig. B.1: $f_{\rm AGN}$ maps for the DP/MaNGA galaxies of the blue cloud.

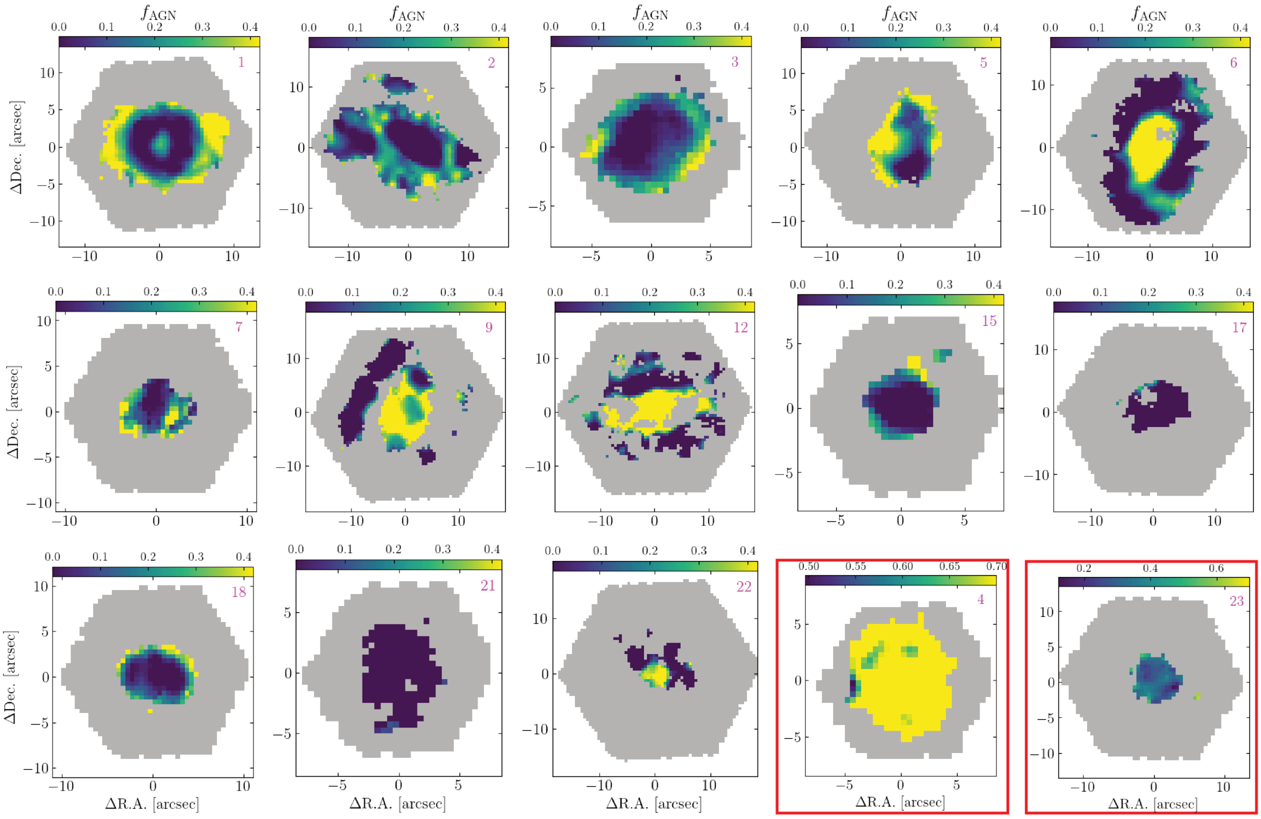

Fig. B.2: Same as Fig. B.1 but for the green-valley and red galaxies. The red galaxies are displayed with red boxes.

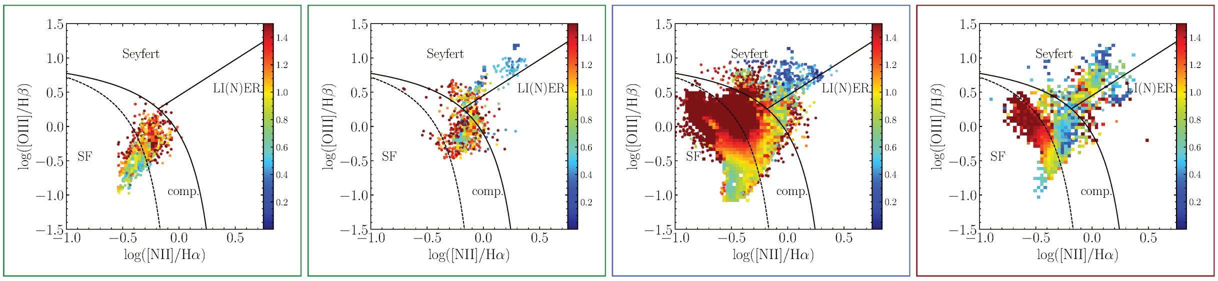

Fig. C.1: BPT diagrams for the galaxies of the CS2 sample. **Left:** GV galaxies without and with central AGN. **Right:** Blue-cloud and red-sequence galaxies. The colour indicates the distance to the centre, in units of R_e.

2 Disentangling gas and star kinematics in double-peaked MaNGA galaxies

In the previous Section, I detail the analysis of star-formation properties, stellar-population characteristics, AGN activity and probe the influence of minor mergers. In such systems, we could expect kinematics perturbations. The MaNGA data enables me to investigate these processes by interpreting the kinematics of the gas and the stars.

2.1 Perturbed kinematics

Gas kinematics is affected by interactions and mergers (Bellocchi et al., 2013). It can also be troubled by nuclear activity, through large scale gas outflows both in the molecular gas (Cicone et al., 2014) and ionised gas phases (Concas et al., 2019).

I represent the measurements of the Data Analysis Pipeline to study the gas and star kinematics. The Hα flux, velocity and velocity dispersion of each DP/MaNGA galaxy are shown in Figs. 3.1 and 3.2.

In order to reveal potential irregular motions, I can compare the radial distribution of the gas velocity dispersion σ_{gas} and that of the stars $\sigma_{\star}$, normalised by the stellar velocity dispersion in the central spaxel of the cube. The corresponding radial profiles are displayed in Figs. 3.3 and 3.4. These diagnostics along with the 2D maps from the DAP give me some insights on which galaxies could have not only regular kinematics patterns and thus, on which I could apply a multi-component fitting procedure that allows complex spectral features to be probed (see the details about the algorithm in Sect. 3).

The results of this kinematics analysis will be presented in Mazzilli Ciraulo et al. 2022 (in prep.).

2.2 Perspectives: comparison with analytical models

The origin of the double-peaked profiles, as discussed earlier, can be varied and the interpretation of such features sometimes suffers from the data resolution. Therefore, comparison between observations and model predictions is relevant. We plan to use an analytical model simulating a line-of-sight velocity distribution convolved with an instrumental broadening.

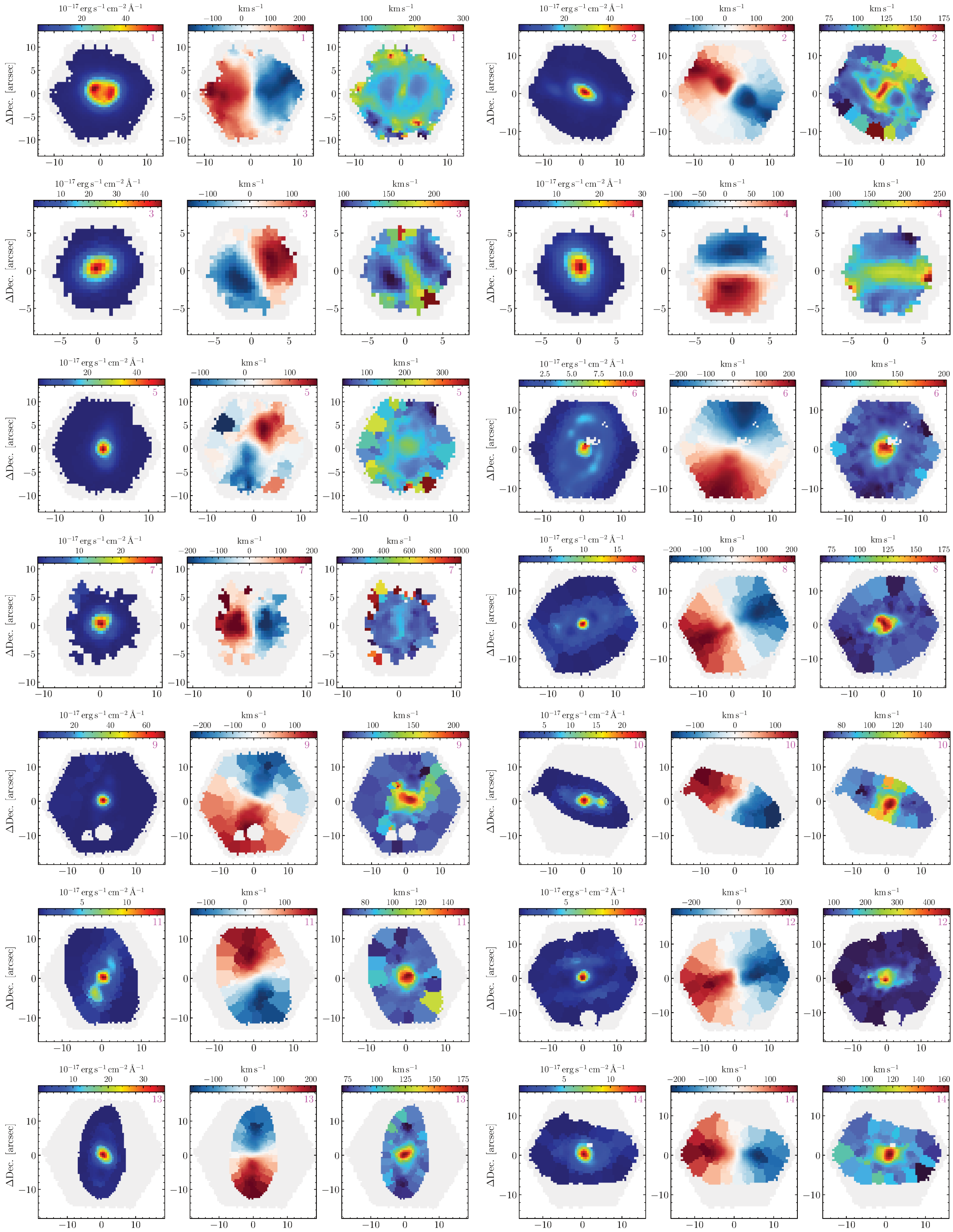

Figure (3.1) Respective Hα flux, velocity and velocity dispersion of the first 14 DP/MaNGA galaxies.

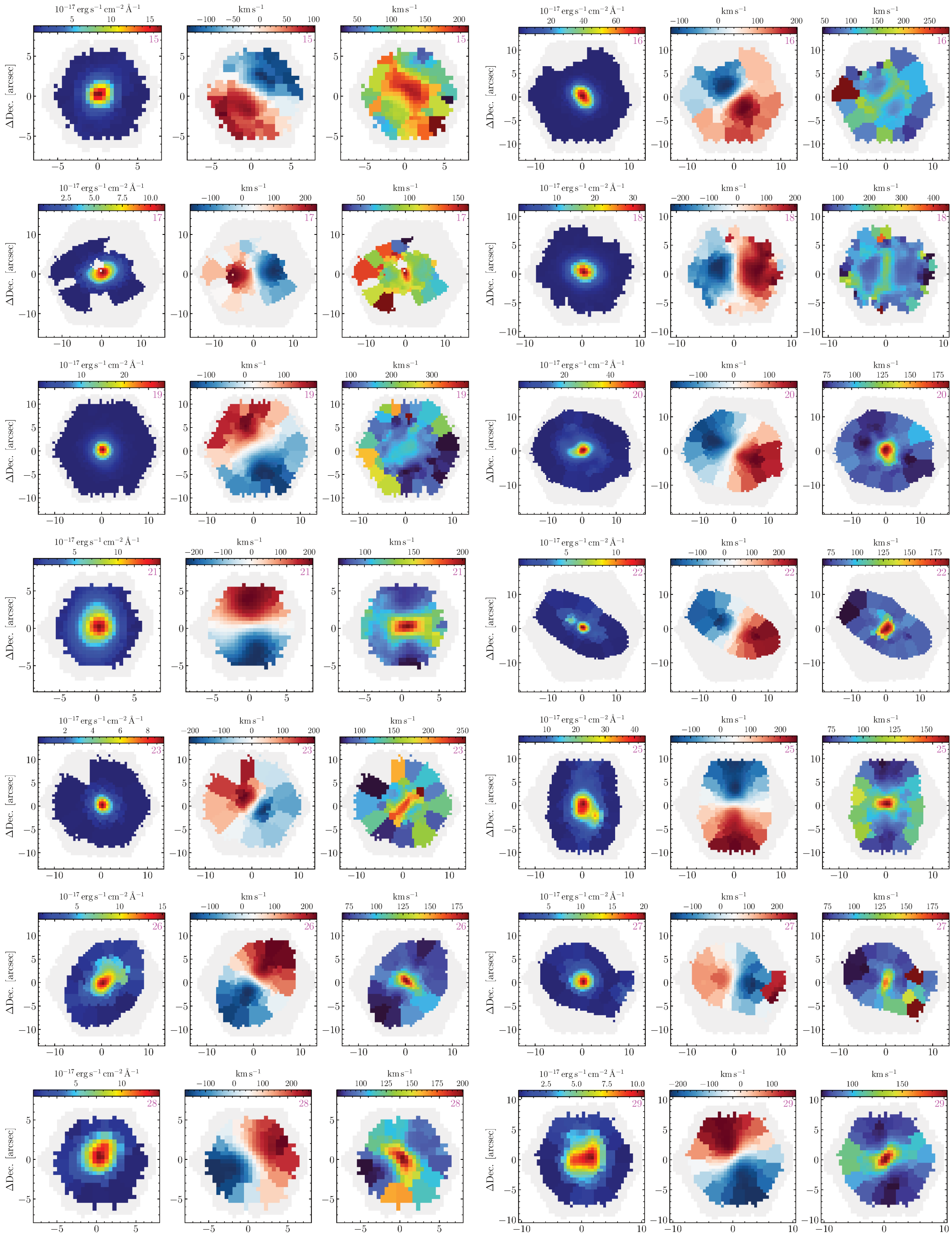

Figure (3.2) Respective Hα flux, velocity and velocity dispersion of the last 14 DP/MaNGA galaxies, except for G24 that is analysed in greater details in Chapter 4.

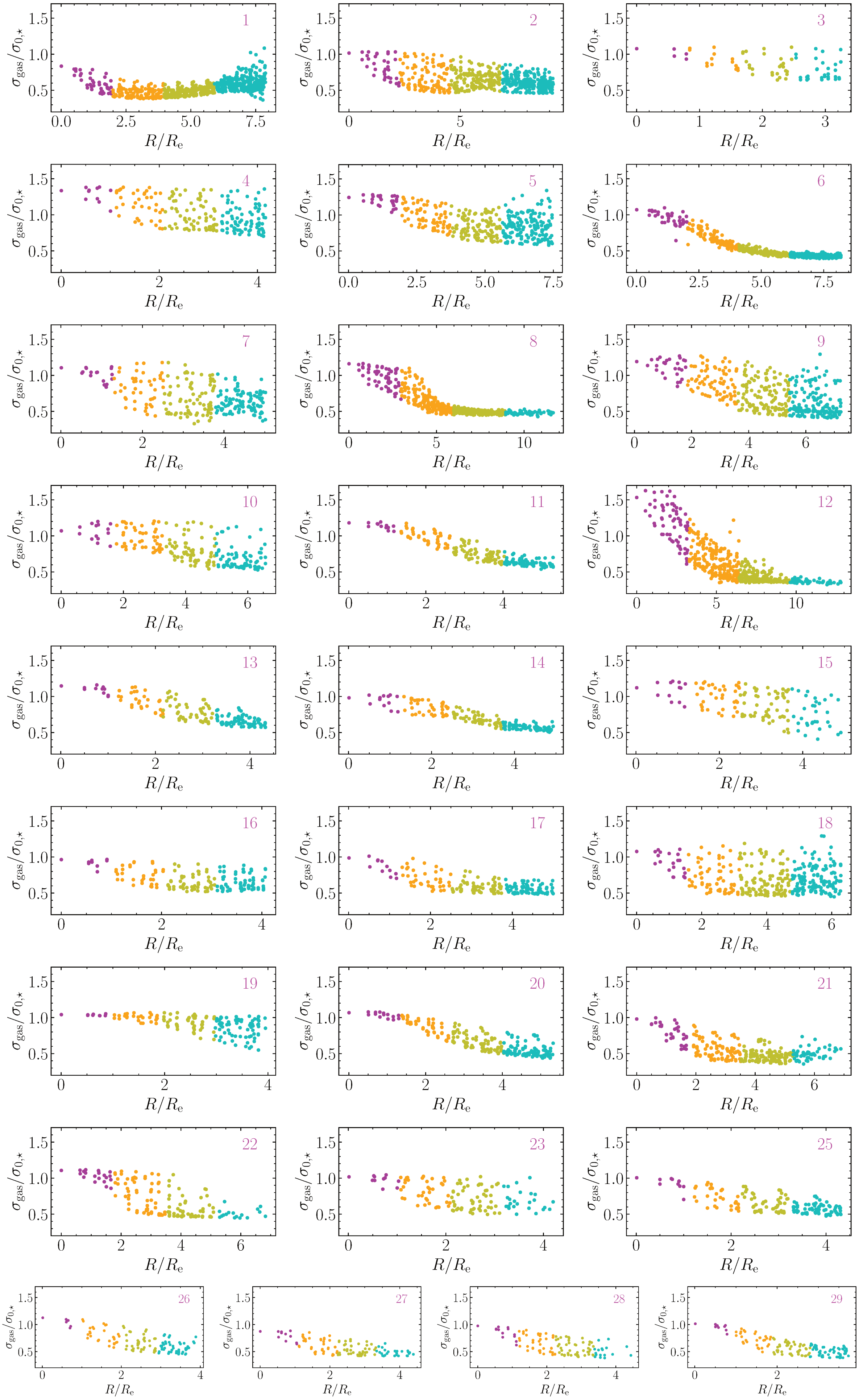

Figure (3.3) Radial profile of the Hα line velocity dispersion, normalised by the stellar velocity dispersion in the central spaxel $\sigma_{0,\star}$.

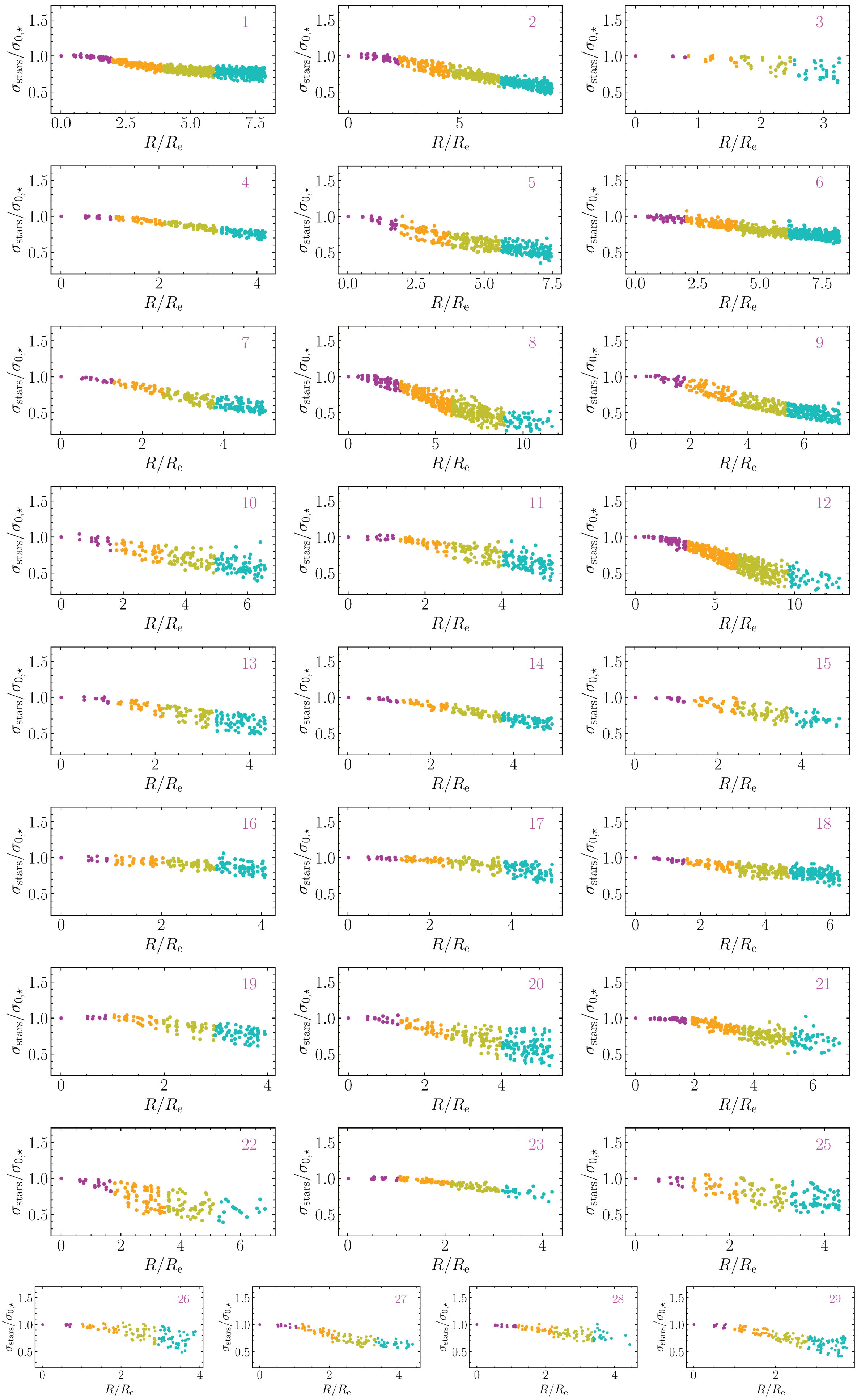

Figure (3.4) Radial profile of the stellar velocity dispersion, normalised by the stellar velocity dispersion in the central spaxel $\sigma_{0,\star}$.

Dévoiler des événements de fusion cachés grâce à l'ajustement de spectres à plusieurs composantes

Interactions et fusions de galaxies

Dans le modèle cosmologique ΛCDM, la formation des galaxies suit un processus hiérarchique. Un large halo de matière noire résulte de la fusion de progéniteurs plus petits. Dans ce contexte, les fusions et interactions de galaxies jouent un rôle majeur dans l'évolution des galaxies.

Processus de fusion et doubles pics

L'étude des interactions et fusions de galaxies est essentielle pour affiner notre compréhension de l'évolution des galaxies. En plus des signatures de fusion les plus prononcées telles que les queues de marée, ou des structures plus fines comme les coquilles, les événements de fusion peuvent être détectés par analyse spectroscopique. Historiquement, la recherche de raies d'émission à doubles pics est motivée par la chasse aux NAGs binaires (par exemple Comerford et al., 2012; Koss et al., 2012; Rubinur et al., 2019). Un trou noir binaire peut en effet se former au centre du vestige d'une fusion si les deux galaxies progénitrices contiennent un trou noir supermassif (par exemple Begelman et al., 1980). Les simulations numériques montrent qu'un double pic dans la distribution des vitesses moyennes est une caractéristique commune (Lahén et al., 2018). Fu et al. (2012) ont effectué une analyse de l'imagerie à haute résolution de la raie [OIII] dans le but d'identifier les NAGs binaires. Ils ont finalement affirmé que les NAGs simples peuvent être indiscernables des NAGs doubles et représentent au moins 70 % des NAGs présentant une raie [OIII] à doubles pics. Comerford et al. (2018) ont étudié les raies d'émission étroites des NAGs à doubles pics par le biais d'une analyse cinématique et ont conclu que ces caractéristiques spectrales sont observées deux fois plus souvent dans les fusions de galaxies que les raies d'émission à pic unique.

Algorithme d'ajustement de spectres à plusieurs composantes

La collaboration MaNGA fournit des cubes de données réduits incluant les spectres observés ainsi que les résultats de l'ajustement du continuum stellaire et des raies d'émission du gaz. Néanmoins, ces raies sont approximées par une fonctionne gaussienne. Afin d'interpréter la nature des profils à doubles pics observés dans les spectres des 29 galaxies étudiées, nous avons développé une procédure innovante qui permet d'ajuster le profil des raies d'émission avec plusieurs composantes cinématiques. Nous avons ajusté une double gaussienne à chaque raie des spectres. Les étapes de notre procédure peuvent être résumées ainsi:

- J'extrais les spectres des *bins* de Voronoï auxquels le continuum stellaire a été soustrait.
- Toutes les raies d'émission sont ajustées simultanément par une double gaussienne qui peut être modélisée telle que dans l'équation 2. Les amplitudes des gaussiennes sont des paramètres libres pour chaque raie, tandis que les moyennes et largeurs sont identiques à toutes les raies. L'ajustement est fait par un algorithme effectuant une régression χ^2. Les largeurs de raies sont corrigées de l'élargissement instrumental (voir équation 2).
- Le *spaxel* ayant le plus haut rapport signal-sur-bruit est ajusté en premier. Nous fournissons des limites aux paramètres ajustés. Une fois le premier *bin* traité, la procédure considère le *bin* le plus proche. Pour garantir des résultats cohérents d'un point de vue physique, les paramètres obtenus contraignent les paramètres du nouveau *bin* à ajuster.

Nous pouvons choisir les variations maximales permises sur chaque paramètre pendant la procédure d'ajustement. La figure 4.3 illustre l'exemple d'un *bin* ajusté, pour lequel je montre les différentes raies d'émision ainsi que la position dudit *bin* dans le champ de vue de MaNGA.

Deux galaxies en interaction se cachant comme une seule, révélées par MaNGA

Cette section est constituée de la publication Mazzilli Ciraulo et al. (2021), publiée dans `Astronomy & Astrophysics` en 2021.

4

Unveiling hidden merger events through multi-component fitting

1 Galaxy interactions and mergers

In the current widely accepted cosmological model, the so-called ΛCDM, dark matter halos follow a hierarchical formation process: a large halo is the result of the merging of smaller progenitors. In this framework, galaxies undergo interactions with one another and thus, galaxy interactions and mergers are crucial in galaxy evolution. The outcomes of galaxy mergers can be very different depending on the properties of the progenitors. Mergers that involve gas-poor galaxies, the so-called 'dry' mergers, are thought to be at the origin of the increase of mass and size of the early-type galaxies (van Dokkum et al., 2010). In the contrary, 'wet' mergers that involve gas-rich companions are thought to be responsible for triggering starbursts (Patton et al., 2011) and AGN activity (Barnes & Hernquist, 1991).

1.1 Merging processes and double peaks

As discussed in Sect. 1, galaxy interactions and mergers are a powerful tool for our understanding of galaxy evolution. In addition to the most pronounced merging signatures such as tidal tails, or finer structures as shells or ripples, merger events can be detected through spectroscopic analysis. Historically, the search for double-peaked emission lines is motivated for the hunt for dual AGN (e.g. Comerford et al., 2012; Koss et al., 2012; Rubinur et al., 2019). A binary black hole may indeed form at the centre of the merger remnant if both progenitors contain a supermassive black hole (e.g. Begelman et al., 1980). Numerical simulations show that a double maximum feature in the mean velocity distribution is a common characteristic (Lahén et al., 2018). Fu et al. (2012) performed an analysis of high-resolution imaging of the [OIII] line with a view to identify binary AGN. They finally claimed that single AGN can be indistinguishable from dual ones and account for at least 70% of the double-peaked [OIII] AGN. Comerford et al. (2018) studied double-peaked narrow AGN emission lines through a kinematic analysis and concluded that such spectral features are observed twice as often in galaxy mergers than are single-peaked emission lines.

2 Mass-metallicity relation

Galaxy evolution is partly ruled by the co-action of gas inflows, metal production and outflows that make up the baryonic cycle. These processes do not act on the same timescales. The gas-phase metallicity in galaxies result from these gas flows and star formation. For ISM studies, the word 'metallicity" denotes the gas-phase oxygen abundance, measured in units of 12+log(O/H). In these units, solar metallicity is 8.69 (Allende Prieto et al., 2001). A relation between galaxy stellar mass and gas metallicity has first been established some decades ago (Lequeux et al., 1979), on irregular and blue compact galaxies. The advent of large surveys and accurate stellar mass measurements led to the demonstration of a tight correlation between stellar mass and metallicity from tens of thousands of galaxies (Tremonti et al., 2004). They fitted a polynomial function to this relationship, valid for stellar masses such that $8.5 < \log M_\star < 11.5$, of the form:

$$12 + \log(\mathrm{O/H}) = \alpha + \beta\,(\log M_\star) + \gamma\,(\log M_\star)^2 \tag{4.1}$$

Other studies found consistent scatter and slope when extending this relation to supplementary galaxies. Nonetheless, it appears that galaxies with high SFRs show a systematic offset to lower metallicities (Ellison et al., 2008). Mannucci et al. (2010) defined the fundamental metallicity relation up to $z = 2.5$ by accounting for SFR. They introduced a quantity $\mu_{0.32} = \log M_\star - 0.32\log(\mathrm{SFR})$ and gave the following relation:

$$12 + \log(\mathrm{O/H}) = \begin{cases} 8.90 + 0.47\,x, & \text{if } \mu_{0.32} < 10.2 \\ 9.07 & \text{if } \mu_{0.32} > 10.5 \end{cases} \tag{4.2}$$

with $x = \mu_{0.32} - 10$. The value 0.32 enables the minimisation of the scatter. This M$_\star$-Z-SFR relation is not redshift-dependent up to z∼2.5 but presents a turnover at the highest stellar masses (M$_\star$ $\sim 10^{10.5} M_\odot$). Andrews & Martini (2013) studied the mass-metallicity relation by measuring the metallicities of hundreds of thousand SDSS star-forming galaxies through the auroral lines [OIII]λ4363 and [OII]$\lambda\lambda$7320,7330 measurements. Since these temperature-sensitive lines are weak, they stacked the SDSS spectra by stellar-mass bins in order to enhance the signal-to-noise ratio and be able to detect [OIII] up to log($M_\star$)=9.4 and [OII] doublet up to log($M_\star$)=10.5. They found a large dependence on SFR with respect to stellar mass. Since the scaling relation between stellar mass, metallicity and SFR does not show any strong redshift-dependency, it is sometimes referred to as the “fundamental metallicity relation” (FMR).

Gas metallicity calibrators

Several ratios of strong emission lines provide metallicity calibrators. Here I will give some of the most common metallicity diagnostics. For all presented calibrations, the emission line fluxes refer to the measurements corrected for dust extinction. The R23 index was first defined by Pagel et al. (1979):

$$\mathrm{R23} = ([\mathrm{OII}]\lambda3727 + [\mathrm{OIII}]4960, 5008)/\mathrm{H}\beta \tag{4.3}$$

This consists of the calibrator used by Tremonti et al. (2004) to compute gas-phase oxygen abundance. Another diagnostic is the O3N2 index:

$$\mathrm{O3N2} = ([\mathrm{OIII}]\lambda5008/\mathrm{H}\beta)/([\mathrm{NII}]\lambda6585/\mathrm{H}\alpha) \tag{4.4}$$

This presents the advantage to consider ratio of lines that are close in terms of wavelength, and thus, their ratios are not too sensitive to dust. The latter index is used by Pettini & Pagel (2004), which calibrated the relationship between 12+log(O/H) and O3N2 for star-forming galaxies. These works established their relation based on photoionisation models. The inferred abundances are impacted by the metholodogy that is used. Kewley & Ellison (2008) noticed up to 0.7 dex higher values for metallicities derived from photoionisation models compared to those predicted by determing the electron temperature of the nebula (T_e method). Thus, Curti et al. (2020) revised the FMR using exclusively the T_e method and compared their parametrisation to those of the literature.

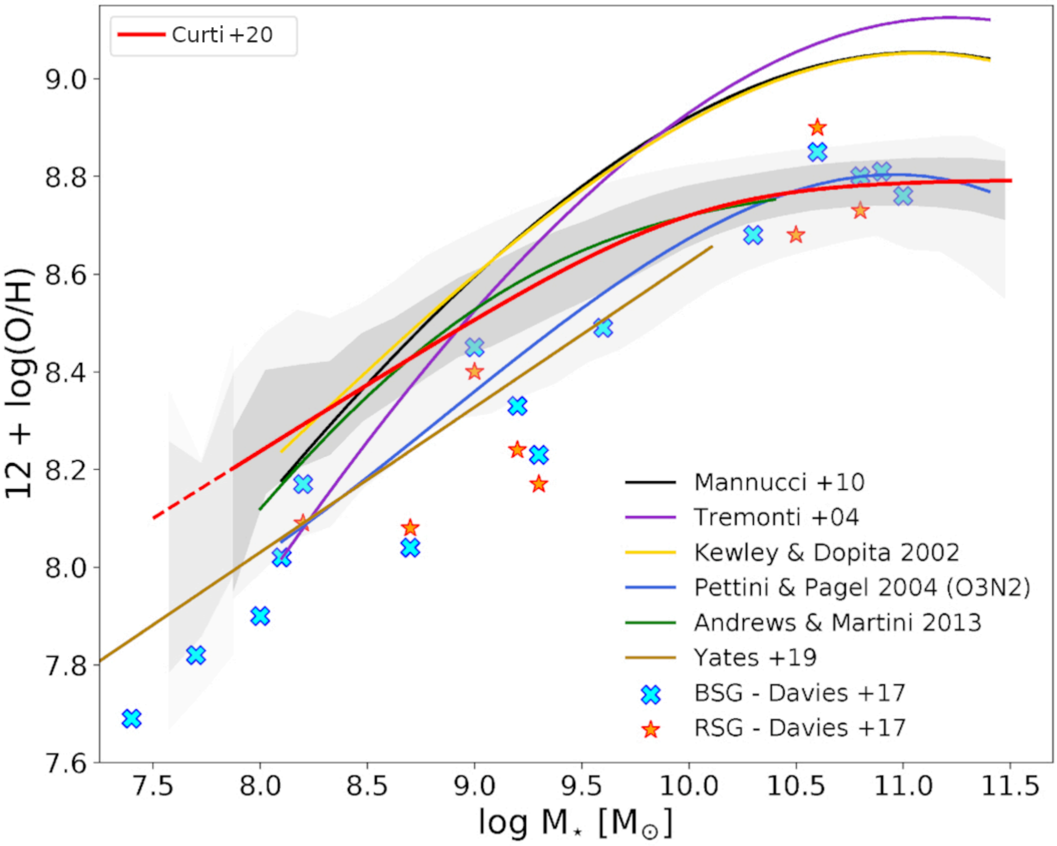

Figure (4.1) Comparison of different mass-metallicity relations described in the literature. From Curti et al. (2020).

3 Multi-component fitting algorithm

The MaNGA data analysis pipeline extracts emission line fluxes and stellar population indices from the MaNGA data through a spectral fitting procedure, which models both the stellar continuum and the nebular emission lines. Nonetheless, for each spectrum, one Gaussian function is fitted to each emission line and thus information related to a multi-component spectral feature can be lost. With the aim of disentangling the nature of the double-peaked profiles in the emission lines of the studied galaxies, I perform a customised multi-component fitting procedure. The steps of this procedure are the following:

1. I extract the stellar-continuum-subtracted Voronoi-binned MaNGA spectra. These spectra are provided after having been fitted with a set of single stellar population models using pPXF. They consist of continuum-subtracted spectra, where the emission lines are preserved.

2. For each bin the emission lines are simultaneously fitted by a double Gaussian function. I considered the following emission lines: Hβ, [OIII]$\lambda\lambda$4960,5008, [OI]λ6301, Hα, [NII]$\lambda\lambda$6550,6585, [SII]$\lambda\lambda$6718,6733. The modelled function is:

$$g(v) = A_1 \exp\left(\frac{(v-\mu_1)^2}{2\sigma_1^2}\right) + A_2 \exp\left(\frac{(v-\mu_2)^2}{2\sigma_2^2}\right) \tag{4.5}$$

where A_1, A_2 refer to the amplitudes, μ_1, μ_2 to the means, and σ_1, σ_2 to the standard deviations of each Gaussian component. v corresponds to the expected line velocity with respect to the redshift of the source.

$\mu_{1,2}$ and $\sigma_{1,2}$ are the same for all the lines and $A_{1,2}$ are free parameters for each fitted emission line. This approach enables similar kinematic features to be retrieved for each emission line and thus provides a coherent analysis of the two components. For the emission line doublets [OIII]$\lambda\lambda$4659,5007 and [NII]$\lambda\lambda$6548,6583, their amplitude ratios are fixed to the theoretical values, respectively [OIII]5007/[OIII]4959 = 3.01 and [NII]6583/[NII]6548 = 2.92 (Acker et al., 1989). The fitting procedure is based on the iminuit library [1] and performs a χ^2 regression. Since the model is fitted to the MaNGA spectra at their native resolution, the measured linewidths, or velocity dispersions, have to be corrected for the instrumental broadening σ_{inst}. This is done following:

$$\sigma^2_{\text{gas}} = \sigma^2_{\text{obs}} - \sigma^2_{\text{inst}} \tag{4.6}$$

where σ_{gas} is the true astrophysical emission line velocity dispersion.

3. In details, the central spaxel of the cube is fitted first. Usually it corresponds to the bin where the lines have the highest signal-to-noise ratio. The set of initial guesses for the fit parameters are:

- $v_{\text{init},1} = v_{\text{line}} - 200$ [km s^{-1}]
  $v_{\text{init},2} = v_{\text{line}} + 200$ [km s^{-1}] where v_{line} is the velocity provided by the Data Analysis Pipeline of MaNGA.

- $A_{\text{init},1} = A_{\text{init},2} = A_{\text{line}}$ where A_{line} is the amplitude provided by the Data Analysis Pipeline of MaNGA.

- $\sigma_{\text{init},1} = \sigma_{\text{init},2} = 100$ [km s^{-1}].

By default, the parameters are restricted by providing some bounds: $[v_{\text{line}} - 1000; v_{\text{line}} + 1000]$ for the velocities, $[0, 1000\,\text{km}\,\text{s}^{-1}]$ for the velocity dispersions, $[0, 1.5\,A_{\text{line}}]$ for the amplitudes. The emission lines are isolated by selecting 60Å-wide regions around them (30Å on each side of the position given by the DAP).

Once the first bin is fitted, the procedure estimates the distance to the other Voronoi bins and the closest one is fitted next. If there are more than one, one of the closest neighbouring Voronoi bins is arbitrarily chosen. In order to obtain a physically-coherent gas distribution, the new fit parameters are constrained using the best fit parameters found for the already-fitted bin.

---

[1] https://pypi.org/project/iminuit/

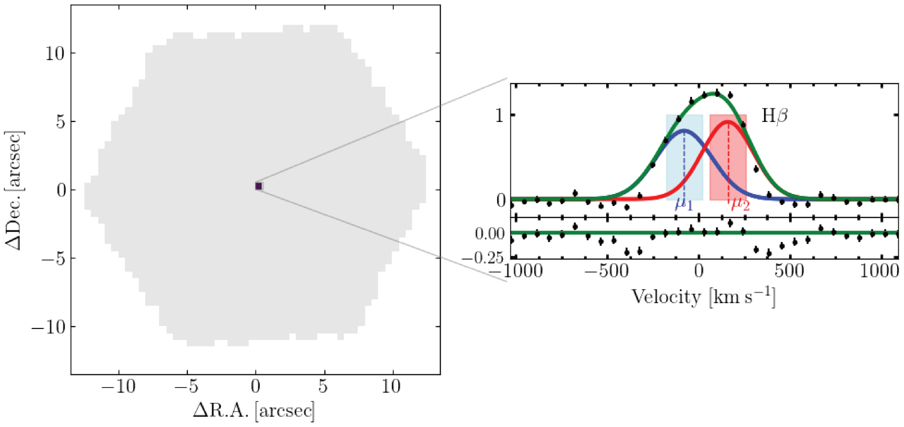

Figure (4.2) Illustration of the beginning of the fitting procedure. The central bin has been fitted (here Hβ line is shown) and the returned fit parameters define the bounds for the parameters of the next bin.

One can choose the maximal variations allowed on each free parameter during the fitting procedure. Here below is an example of a fitted bin, for which I am showing the different emision lines as well as the position of the bin within the MaNGA field of view.

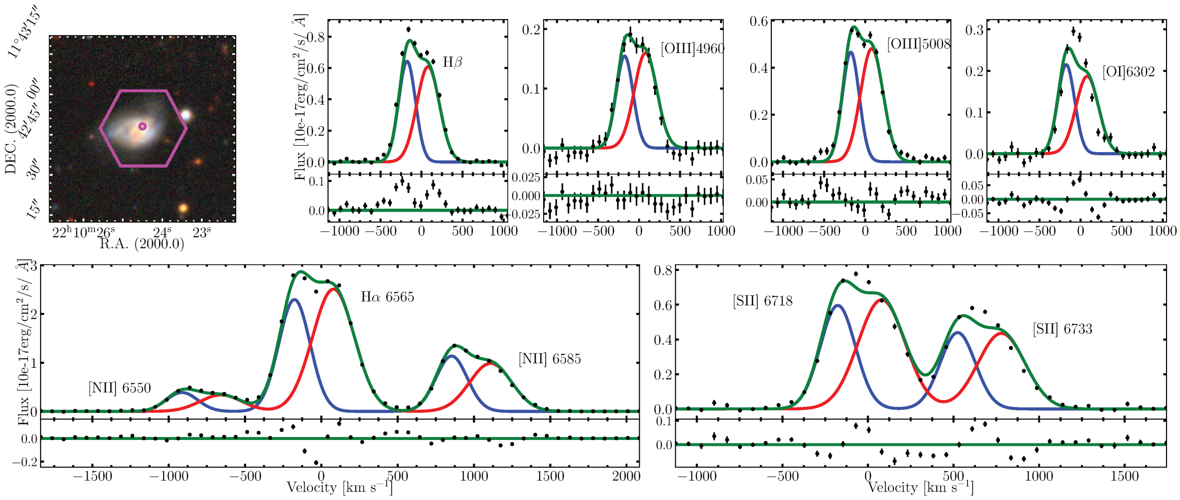

Figure (4.3) Double-Gaussian fitting results for each emission line in the spectrum extracted from bin 0, in the data cube of the merging system studied in Sect. 5. The top-left snapshot is the Legacy survey image, with the MaNGA footprint superimposed in magenta. The circle depicts the position of the bin under consideration. The other panels show regions of the optical spectrum where I fit the emission lines.

The same process is applied until all the bins are fitted.

3.1 Selection criteria for double-peaked emission lines

In this section, I emphasise the choices that I made to confirm the detection of two components in the gas component. Since multiple gas components can be only detectable in restricted regions within the MaNGA field of view, I need to decide whether two components are reliably detected or not. Therefore, I established the following criteria:

- Each fitted peak must have a signal-to-noise ratio greater than 3. This avoids to consider spectral features that are fitted but that do not have an emission well above the spectrum noise level.

- The velocity difference between both peaks must be greater than 180 $\mathrm{km\,s^{-1}}$. This criterion is motivated by the spectral resolution of the MaNGA data, which is about 60 $\mathrm{km\,s^{-1}}$. It ensures that the double-peaked profile is not due to resolution effect.

- The amplitude ratio between both peaks must verify $1/3 < A_1/A_2 < 3$. This ensures that the selected bins are those for which the detected peaks are representative of a reliable physical signal.

- The double-Gaussian fit must model the data better than the single-Gaussian one, which is quantified through an F-test. This test guarantees that the $\chi^2_{\rm double}$ is significantly smaller relative to the increase of the number of degrees of freedom $\mathrm{Ndof_{double}}$, compared to the single-Gaussian fit. The test is more restrictive than a basic χ^2 comparison. The F-statistic is computed as follows (see Mendenhall & Sincich, 2012):

  $$f_{\rm stat} = \frac{(\chi^2_{\rm single} - \chi^2_{\rm double})/(\mathrm{Ndof_{single}} - \mathrm{Ndof_{double}})}{\chi^2_{\rm double}/\mathrm{Ndof_{double}}} \tag{4.7}$$

  where $\mathrm{Ndof_{single}}$ and $\mathrm{Ndof_{double}}$ are the respective number of degrees of freedom for the single and the double Gaussian models. The Fischer distribution F computes the probability that the double-Gaussian fit represents the data better than the single-Gaussian fit. I, thus, reject the single Gaussian model with a probability of less than 5% by using the cumulative distribution:

  $$F_{\rm cd}(f_{\rm stat}|\mathrm{Ndof_{single}} - \mathrm{Ndof_{double}}, \mathrm{Ndof_{double}}) > 0.95 \tag{4.8}$$

In the case of the source studied in Sect. 5, the amplitude variation can vary up to 100% betwen two adjacent bins, the velocity of each peak can vary up to a difference of 40 $\mathrm{km\,s^{1}}$ and the velocity dispersion up to a difference of 100 $\mathrm{km\,s^{1}}$. I decided to use these variations after different tests that show that this set of variations adjusts well the spectral features observed in the MaNGA data.

4 Full-spectral fitting to confirm two stellar contributions

The procedure described in the paper presented in Sect. 3 is an efficient approach to reveal the contribution of multiple components in the observed spectral line features. In order to confirm the presence of two galaxies, the investigation of the stellar continuum is of paramount importance. The paper in Sect. 5 highlights a multi-component approach that we used to disentangle both components in the stellar contribution. This procedure is inspired from the one used for the study of galaxies that host counter-rotating stellar dics (Katkov et al., 2013, 2016). Here I am going to precise our method.

4.1 NBursts fitting

Our analysis workflow is based on the NBursts full spectral fitting technique (Chilingarian et al., 2006a) that relies on the fitting of high-resolution PEGASE.HR (Le Borgne et al., 2004) simple stellar population (SSP) models to the MaNGA spectra. The minimisation technique is based on a χ^2 computation corresponding to (see Eq. 2.1 of Chilingarian et al., 2006b):

$$\chi^2 = \sum_{N_\lambda} \frac{(F_i - P_{1p}(T_i(\mathrm{SFH}) \otimes \mathcal{L}(\mathrm{v}, \sigma, \mathrm{h}_3, \mathrm{h}_4) + \mathrm{P}_{2\mathrm{q}}))^2}{\Delta F_i^2} \tag{4.9}$$

where F_i and ΔF_i are the observed flux and its uncertainty; T_i(SFH) is the flux of a synthetic spectrum; P_{1p} and P_{2q} are polynomials of respective order p and q to correct the continuum; v, σ, h_3 and h_4 are the radial velocity, velocity dispersion, Gauss-Hermite coefficients of the line-of-sight velocity distribution (LOSVD) respectively. The two latters measure deviations of the line profile from a Gaussian: h_3 refers to asymmetric deviations and h_4 to symmetric deviations. The emission lines are excluded from the fit by masking 20Å-wide regions around them.
This analysis, applied to the galaxy MaNGA 1-114955, reveals a line-of-sight velocity distribution with a complex shape, that is probed using a non-parametric recovery technique.

4.2 Non-parametric LOSVD recovery

The template spectrum used here is an SSP model, created from the code PEGASE.HR that is based on the empirical stellar library ELODIE3.1 (Prugniel et al., 2007). These spectra have a resolution of $R = 10000$, which is much higher than the resolution of the MaNGA spectra. In order to take into account the instrumental resolution, the stellar population spectra are convolved with the MaNGA line-spread function (LSF). In that way, “correct” values are obtained, meaning that the observed broadening during the fit can be attributed to the internal velocity dispersion of the object. By performing this approach, we recover a non-parametric LOSVD to all the Voronoi bins with S/N $\geq$ 20, then we perform a modelling of it, and we highlight kinematically separated stellar populations. Fig. 4.4 shows the results of our modelling of the non-parametric recovered LOSVD. For each panel, the x-axis corresponds to the number of spatial bins that we consider (namely 374) and the y-axis refers to the number of velocity bins in the LOSVD (51 here). As one can see on Fig. 4.4, the shape of the recovered stellar LOSVD

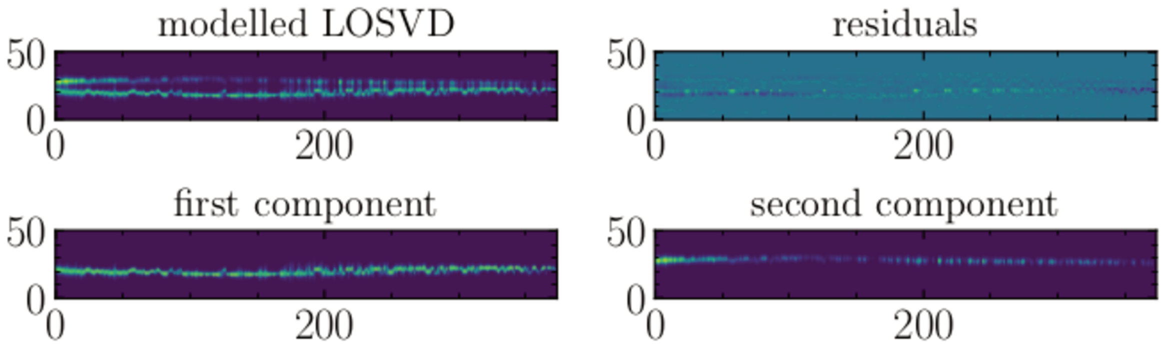

Figure (4.4) Representation of the double-peaked structure detected in the stellar LOSVD. **Top-left:** Modelled LOSVD. It shows a clear double-peaked structure in most of the spatial bins. **Top-right:** Residuals between the recovered LOSVD normalised by spectrum continuum and the model. **Bottom-left:** First component used in the model. **Bottom-right:** Second component used in the model.

clearly demonstrates the double-peaked structure (in some spatial bins) in stellar component.

4.3 Two-component decomposition

We decompose the recovered non-parametric stellar LOSVD into two Gaussians in order to derive the velocity and the velocity dispersion of each component. As initial guesses for these kinematical parameters, we use the corresponding values obtained from the analysis of the non-parametric stellar LOSVD. This improves the stability of the modelling.

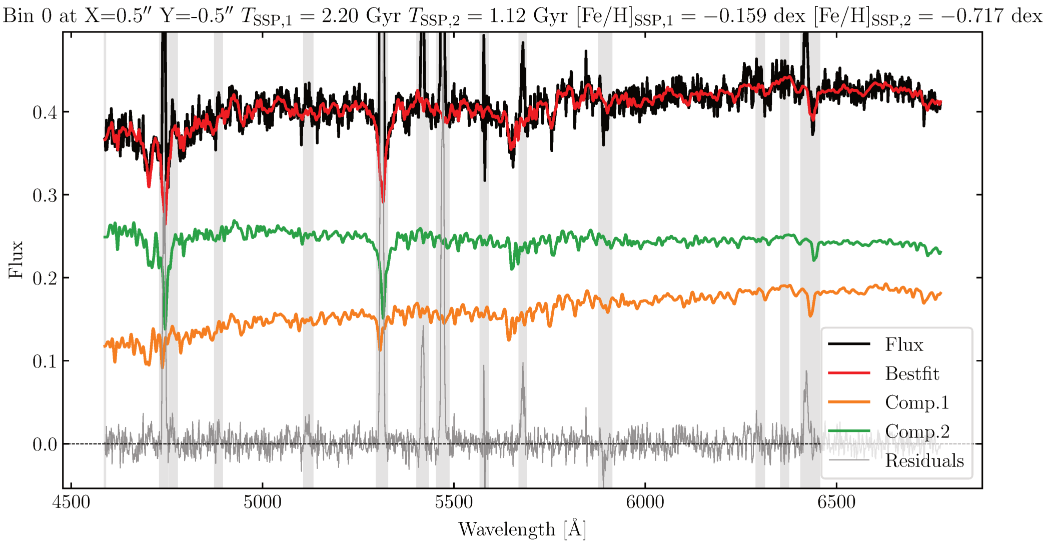

Figure (4.5) Example of a spectrum fitted using NBURSTS. The observed spectrum appears in black, the best fit is shown in red and the components inferred from the two-component decomposition are displayed in orange and green. The residuals are shown in grey. The bin number, its position with respect to the galaxy centre, as well as the derived properties (age and metallicity, SSP-equivalent) for each stellar population are given in the figure title.

This step allows us to obtain SSP-equivalent properties such as age and metallicity for both components. The SSP model that we use is indeed a model spectrum for a given age T_{SSP} and metallicity [Fe/H], assuming that all stars formed instantaneously T yeas ago and have a metallicity [Fe/H]. For each spaxel where we recover a LOSVD that adjust the observed spectrum, we thus find optimal values for T and [Fe/H]. This bin-by-bin procedure provides age and metallicity, SSP equivalent, for individual spaxels. Nonetheless, the estimates of these properties suffer from internal degeneracies and model parameters, so they could be uncertain. We thus decide to trust the averaged values of the SSP-equivalent age and metallicity maps that are recovered by fixing the velocity and velocity dispersion of both components to that of the LOSVD.

4.4 Modelling details

Evaluating the contribution of both components is a tricky task because the decomposition of the double-peaked structure in the LOSVD suffers from low signal-to-noise ratio in some spatial bins.

One method to address this issue is to simultaneously model an entire recovered LOSVD over the full field of view instead of fitting individual spaxels. So, contrary to the analysis detailed in the previous section, that we perfomed for individual spaxels, the following step is made on the whole MaNGA field of view and help reconstruct a full-coverage model. This enables us to get better constraints on total light contribution. For this analysis, the initial data are the non-parametrically recovered stellar LOSVD for all the spatial bins. We simultaneously model all spaxels. This model consists of two components, represented each by a thin exponential disc whose characteristics are detailed below. The flux distribution is given by:

$$F(R) = F_0 \cdot \exp\left(-\frac{R}{f_\mathrm{h}}\right) \tag{4.10}$$

The velocity distribution is:

$$v(R) = v_\mathrm{sys} + v_\mathrm{rot}(R) \cdot \sin(i) \cdot \cos(\theta) \tag{4.11}$$

where v_sys is the systemic velocity of the galaxy, $v_\mathrm{rot}(R)$ is the rotational velocity and θ is the azimuthal angle in the galaxy plane. At the given radius R, the azimuthal velocity in the disc is parametrised through:

$$v_\phi(R) = V_r \cdot \left(\tanh\left(\frac{R}{R_0 \pi}\right) + c\,\frac{R}{R_0}\right) \tag{4.12}$$

where ϕ is the azimuthal angle in the sky plane, V_r is the amplitude of rotation, R_0 is the radius where v_ϕ reaches V_r and c is a parameter to reproduce declining or increasing rotation curves. The velocity dispersion distribution can be written as:

$$\sigma(R) = \sigma_0 \cdot \exp\left(-\frac{R}{\sigma_\mathrm{h}}\right) + \sigma_\mathrm{c} \tag{4.13}$$

where R is the radius in the plane of the galaxy.

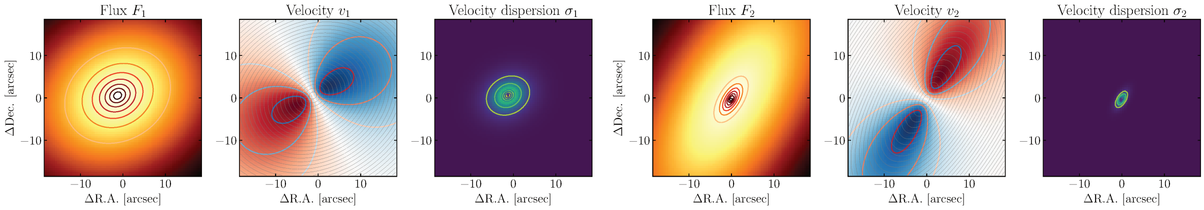

Figure (4.6) Representation of the modeled components. For each, the flux, velocity and velocity dispersion are displayed, respectively.

With a view to compute the stellar mass ratio between both interacting galaxies, we then estimate the light fraction of both stellar components.

4.5 Light and stellar mass ratio estimates

The best value of the light ratio between both components is given using the de-projected surface brightnesses F_1 and F_2 as well as the exponential scales f_{h_1} and f_{h_2}, with a correction for inclination:

$$\frac{\mathrm{disc}_1}{\mathrm{disc}_2} = \frac{F_1}{F_2} \cdot \left(\frac{f_{\mathrm{h}_1}}{f_{\mathrm{h}_2}}\right)^2 \cdot \left(\frac{\cos(i_1)}{\cos(i_2)}\right) \tag{4.14}$$

With the best fit parameters that we obtain with our analysis, this gives us a light ratio of 6.16.

In order to check the consistency of this analytical value, we produce extended high-resolution maps beyond the MaNGA field of view. The light ratio computed from the numerical integration of these maps equals 6.16. Mass-to-light ratios in various bands are output products of the PEGASE.2 code (Fioc & Rocca-Volmerange, 1997), based on BaSeL synthetic stellar library (Lejeune et al., 1997). By using the averaged stellar populations properties that we found, we obtain the mass-to-light ratios for both components, that we called M/L_1 and M/L_2. The stellar mass ratio is finally expressed as:

$$\frac{M_{\star,1}}{M_{\star,2}} = 6.16 \cdot \frac{M/L_1}{M/L_2} = 6.16 \cdot \frac{0.63}{0.43} \sim 9 \tag{4.15}$$

At the end, we conclude that the galaxies detected in the MaNGA data correspond to a merging system with a mass ratio 9:1.

5 Two interacting galaxies hiding as one, revealed by MaNGA

The current section consists of the article Mazzilli Ciraulo et al. (2021) published in `Astronomy & Astrophysics` in 2021. This paper presents the unveiling of an interacting system through the analysis of the MaNGA spectroscopic data.

A&A 653, A47 (2021)
https://doi.org/10.1051/0004-6361/202141319

Astronomy & Astrophysics

Two interacting galaxies hiding as one, revealed by MaNGA

Barbara Mazzilli Ciraulo[1], Anne-Laure Melchior[1], Daniel Maschmann[1], Ivan Yu. Katkov[2,3,4], Anaëlle Halle[1], Françoise Combes[1,5], Joseph D. Gelfand[2,3,6], and Aisha Al Yazeedi[2,3]

[1] Observatoire de Paris, PSL University, Sorbonne Université, CNRS, LERMA, 75014 Paris, France
e-mail: `Barbara.Mazzilli-Ciraulo@observatoiredeparis.psl.eu`
[2] New York University Abu Dhabi, Saadiyat Island, PO Box 129188, Abu Dhabi, UAE
[3] Center for Astro, Particle, and Planetary Physics, NYU Abu Dhabi, PO Box 129188, Abu Dhabi, UAE
[4] Sternberg Astronomical Institute, M.V. Lomonosov Moscow State University, 13 Universitetsky Prospect, Moscow 119991, Russia
[5] Collège de France, 11 Place Marcelin Berthelot, 75005 Paris, France
[6] Center for Cosmology and Particle Physics, New York University, 726 Broadway, New York, NY 10003, USA

Received 15 May 2021 / Accepted 10 June 2021

ABSTRACT

Given their prominent role in galaxy evolution, it is of paramount importance to unveil galaxy interactions and merger events and to investigate the underlying mechanisms. The use of high-resolution data makes it easier to identify merging systems, but it can still be challenging when the morphology does not show any clear galaxy pair or gas bridge. Characterising the origin of puzzling kinematic features can help reveal complicated systems. Here, we present a merging galaxy, MaNGA 1-114955, in which we highlighted the superimposition of two distinct rotating discs along the line of sight. These counter-rotating objects both lie on the star-forming main sequence but display perturbed stellar velocity dispersions. The main galaxy presents off-centred star formation as well as off-centred high-metallicity regions, supporting the scenario of recent starbursts, while the secondary galaxy hosts a central starburst that coincides with an extended radio emission, in excess with respect to star formation expectations. Stellar mass as well as dynamical mass estimates agree towards a mass ratio within the visible radius of 9:1 for these interacting galaxies. We suggest that we are observing a pre-coalescence stage of a merger. The primary galaxy accreted gas through a past first pericentre passage about 1 Gyr ago and more recently from the secondary gas-rich galaxy, which exhibits an underlying active galactic nucleus. Our results demonstrate how a galaxy can hide another one and the relevance of a multi-component approach for studying ambiguous systems. We anticipate that our method will be efficient at unveiling the mechanisms taking place in a sub-sample of galaxies observed by the Mapping Nearby Galaxies at Apache Point Observatory (MaNGA) survey, all of which exhibit kinematic features of a puzzling origin in their gas emission lines.

Key words. Galaxy: evolution – Galaxy: kinematics and dynamics – galaxies: interactions – techniques: spectroscopic – methods: data analysis

1. Introduction

The importance of galaxy interactions and merger events is nowadays beyond dispute as hierarchical galaxy evolution is widely adopted and multiple observational as well as theoretical works have been carried out to investigate the various mechanisms related to the evolution of interacting galaxies (e.g. van Dokkum et al. 2015; Cappellari 2016). The improvement in data resolution has made it possible to highlight various observational signatures of mergers, such as colour change (Alonso et al. 2012), morphological disruption (Ellison et al. 2010; Casteels et al. 2013), star formation enhancement (Patton et al. 2013), and merger-induced nuclear activity at low redshift for optical and mid-IR active galactic nuclei (AGNs; Ellison et al. 2019). The presence of double nuclei (such as in NGC 3526; Sakamoto et al. 2014) is a clear signature of mergers as the existence of tidal tails (Mesa et al. 2014) and, alternatively, spectral features, such as double-peaked profiles in molecular gas emission lines, have also been interpreted as merger signatures (e.g. Greve et al. 2005; Weiß et al. 2005). While the timescales of the merging are well monitored statistically through numerical simulations (e.g. Somerville & Davé 2015; Nevin et al. 2019) and for individual objects (e.g. Lahén et al. 2018), dating the epochs of these observed processes remains a challenge. Lastly, some important questions remain unanswered regarding the possible impact of AGNs on the merging stage (e.g. Alonso et al. 2007; McAlpine et al. 2020; Shah et al. 2020; Sharma et al. 2021) and whether the quenching is related to the merging (e.g. Ellison et al. 2018; Hani et al. 2020; Das et al. 2021).

In this article we present a multi-wavelength analysis of a galaxy merger (J221024.49+114247.0) at $z = 0.09$, identified through the detection of double-peaked emission-line profiles in the central spectrum of the Sloan Digital Sky Survey (SDSS; Strauss et al. 2002). Two gas and stellar counter-rotating components have been identified and analysed. In Sect. 2 we discuss how we extract properties from the Mapping Nearby Galaxies at Apache Point Observatory (MaNGA; Bundy et al. 2015) data cube to identify the two components. In Sect. 3 we discuss the molecular gas data, as well as other archives (Very Large Array) and properties used from value-added catalogues. In Sect. 4 we analyse the properties of this merger. In Sect. 5 we discuss our results. We adopt throughout this work a Λ cold dark matter (CDM) cosmology with parameters $\Omega_\Lambda = 0.7$, $\Omega_M = 0.3$, and $H_0 = 70\,\mathrm{km\,s^{-1}\,Mpc^{-1}}$.

2. MaNGA data analysis

The galaxy J221024.49+114247.0 is one optical merger identified in a sub-sample (Mazzilli Ciraulo et al., in prep.) obtained by cross-matching the summary file from the MaNGA

Table 1. Information about MaNGA ID 1−114955.

RA (J2000)	Dec (J2000)	Redshift	Morphology	Inclination (°)	$M_\star$ ($M_\odot$)	$\mathrm{SFR_{SED}}$ ($M_\odot\,\mathrm{yr^{-1}}$)	SFR ($M_\odot\,\mathrm{yr^{-1}}$)
22h 10m 24.5s	+11d 42m 47s	0.09228	Interacting	44	1.59×10^{11}	13.3	10.6

Notes. The coordinates and redshift come from the NASA-Sloan Atlas catalogue, while the morphology is determined by visual inspection (this object is classified as uncertain in Galaxy Zoo). The inclination is derived using the measurements from Domínguez Sánchez et al. (2018). The stellar mass and the star formation rate (SFR) value are derived from SED fitting based on optical and UV spectra (Salim et al. 2016). The last column gives the SFR estimate outlined in Brinchmann et al. (2004).

Data Reduction Pipeline (DRP; SDSS Data Release DR14, Abolfathi et al. 2018) and a double-peak galaxy catalogue produced by Maschmann et al. (2020), relying on the Reference Catalogue of Spectral Energy Distributions (RCSED) from Chilingarian et al. (2017). The basic properties of this source, provided by different value-added catalogues, are given in Table 1. The Legacy survey (Dey et al. 2019) reveals a disrupted object, and the integrated spectrum within the 3 arcsec SDSS fibre shows double-peaked emission lines. The effective point spread function (PSF) of the MaNGA data is about 2.5 arcsec and corresponds to a spatial resolution of 4.3 kpc at the redshift of the source (z = 0.09228), and the data are gridded on 0.5×0.5″ spaxels.

We produced 2D maps based on the derived properties from the MaNGA Data Analysis Pipeline (DAP; SDSS-IV, Westfall et al. 2019). The main emission lines peak in a compact central region. The velocity field does not display any standard rotating motion and appears to be strongly irregular, with values covering a very wide range ($-525\,\mathrm{km\,s^{-1}} < V_{\mathrm{gas}} < 445\,\mathrm{km\,s^{-1}}$). As displayed in Fig. 1, the velocity dispersion is also remarkable, with spaxels exhibiting values greater than 400 km s^{-1} and not centred. The double-peak features of these spaxels are not well fitted by the single component fit, and some of them are masked during the data processing. In order to further investigate this complex system, we developed an optimised multi-component analysis.

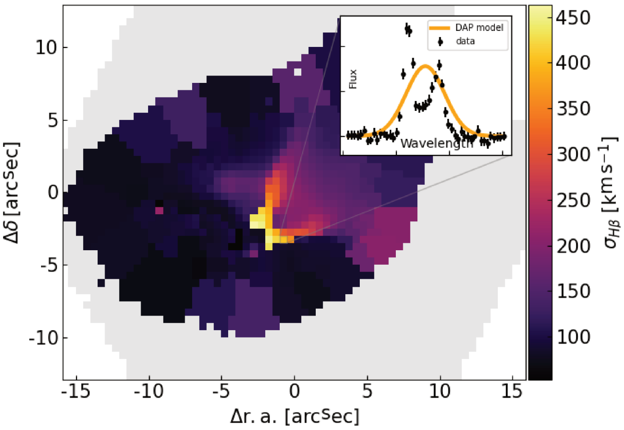

Fig. 1. Velocity dispersion of the Hβ emission line derived by the MaNGA DAP. The MaNGA field of view is represented as a grey footprint. The included panel shows a portion of the continuum-subtracted spectrum from one spaxel where the model (in orange) does not manage to fit the spectral features.

2.1. Gas kinematics derived from the multi-component approach

We developed a fitting procedure, adjusting two components for the selected emission lines. We ran and applied it to the Voronoi binned continuum-subtracted spectra and fitted Hβ, [OIII] doublet, Hα, and [NII] doublet lines. As in the MaNGA DAP, we assigned the same velocity and velocity dispersion to all these lines. We were able to highlight the presence of two components along the line of sight. We first selected reliable spaxels, relying on a signal-to-noise ratio (S/N) threshold of 3. When the S/N criterion is not met by the two fitted components, we kept the single-Gaussian results and associated them with the main galaxy. For the secondary component, we based our spaxel selection on an F-test (Mendenhall & Sincich 2011) to ensure that the double-Gaussian fit was better than the single Gaussian one, that a velocity difference between both peaks was significantly greater than the MaNGA data spectral resolution, and that there was an amplitude ratio between 1/3 and 3 between both peaks to guarantee that one of them was not completely suppressed.

We display the derived properties for each of them on the 2D maps shown in Figs. 2 and 3. Figure 2 displays the extinction-corrected Hα line fluxes, the extinction derived from the Balmer decrement, and the gas metallicity using the O_3N_2 calibrator, while Fig. 3 exhibits the gas kinematics of the two components with their velocity and velocity dispersion. The spatially resolved maps confirm the contribution of two separate components: The first is related to a galaxy with a fairly regular velocity field, whereas the second is detected in a smaller region of the field of view, shows a slightly stronger Hα line flux, and shows a velocity field counter-rotating with respect to the main object.

2.2. Multi-component analysis of the stellar kinematics

To explore whether the double-peaked structure in the emission lines has associated counterparts in the stellar kinematics, we applied an analysis workflow used for the study of galaxies that host counter-rotating stellar discs (Katkov et al. 2013, 2016). Firstly, we fitted spectra using a full spectral fitting technique, NBursts (Chilingarian et al. 2007a,b), in the basic mode, where a spectrum is approximated by a single simple stellar population (SSP) model. Secondly, we recovered a non-parametric stellar line-of-sight velocity distribution (LOSVD) using an un-broadened stellar population model template from the first step (see method details in Kasparova et al. 2020). The non-parametrical stellar LOSVD reveals a clearly separated double-peaked structure, on which we adjusted a double-Gaussian function to derive kinematics parameters of individual components. We hence spotlight two stellar population components: One is regular, and the second is less prominent but is detected in the region where we see a second gas component as well. We used quality filters based on the uncertainties of the parameters and a sufficient relative flux for the second component to show relevant 2D maps.

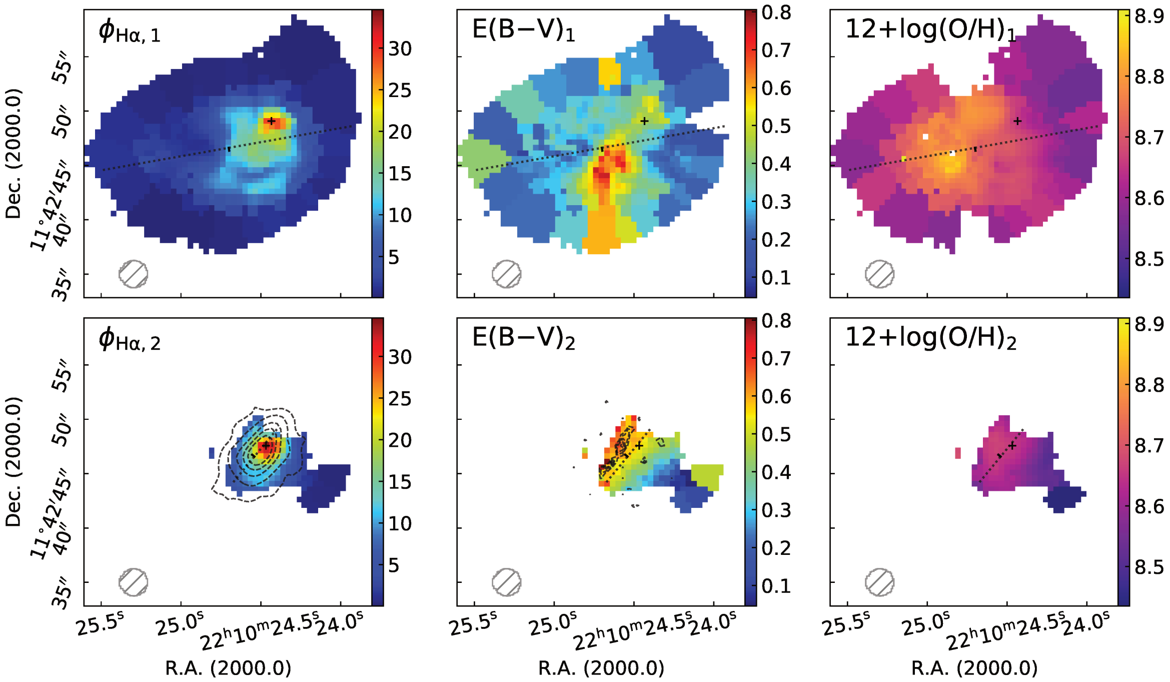

Fig. 2. Gas properties derived from our multi-component approach. *First* and *second rows*: maps for the first and second components detected in MaNGA data, respectively. *First column*: Hα extinction-corrected flux (in erg s^{-1} Å^{-1} cm^{-2} per spaxel), *second column*: extinction computed from the Balmer decrement, and *last column*: oxygen gas-phase abundance derived using the O$_3$N$_2$ calibrator. The black crosses indicate the position of the extinction-corrected Hα flux peak for the represented component. The MaNGA PSF is displayed as a hatched grey circle in the bottom-left corner of the panels.

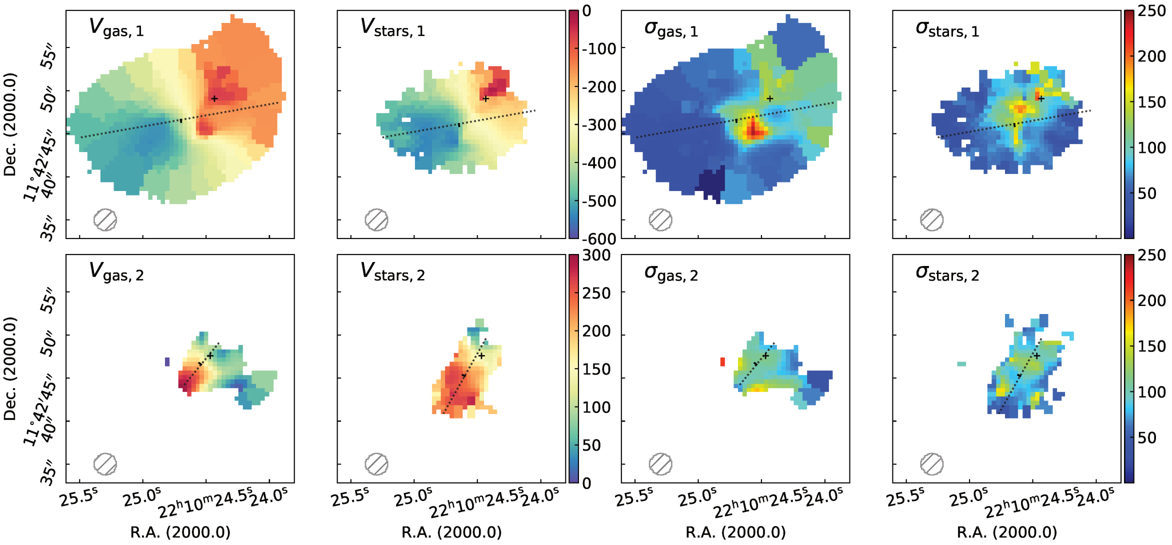

Fig. 3. Gas and star kinematics. *First row*: maps for the first component, and *second row*: second component detected in MaNGA data. *First* and *second columns*: respective ionised gas and stellar velocity fields (in km s^{-1}). The dotted black lines refer to the computed position angles. *Third* and *fourth columns*: respective velocity dispersion fields (in km s^{-1}) for the gas and the stars. As in Fig. 2, the black crosses indicate the position of the extinction-corrected Hα flux peak for the represented component.

The second and fourth columns of Fig. 3 display the stellar velocity and stellar velocity dispersion fields, respectively, for each component. Finally, we re-fitted spectra with NBursts, using a two-component approach in which both components have individual and independent kinematics. We considered velocity and dispersion estimates from the previous step as initial guesses. This analysis suggests that both components have similar but slightly different (SSP-equivalent) averaged stellar ages of $T_1 \approx 1.70$ Gyr and $T_2 \approx 1.42$ Gyr and metallicities of $[\mathrm{Fe/H}]_1 \approx -0.24$ dex and $[\mathrm{Fe/H}]_2 \approx -0.82$ dex.

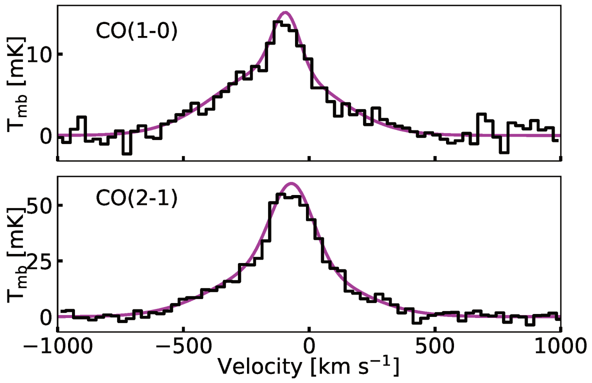

Fig. 4. Molecular gas. We show the CO(1−0) and CO (2−1) lines observed with the IRAM 30 m telescope in units of main beam temperature, $T_{\rm mb}$.

Table 2. Fit parameters for CO(1−0) and CO(2−1) spectra.

	V_0 (km s^{-1})	$T_{\rm mb}$ (mK)	$\sigma_{\rm noise}$ (mK)	$FWHM_v$ (km s^{-1})	$I_{\rm CO}$ (K km s^{-1})
CO(1−0)	−139 ± 14	8	0.7	537	4.46 ± 0.29
	−92 ± 8	7	0.7	127	0.89 ± 0.24
CO(2−1)	−102 ± 9	23	1.5	571	13.83 ± 0.75
	−69 ± 3	34	1.5	196	7.01 ± 0.72

3. Analysis of other data

3.1. Molecular gas content

IRAM 30 m telescope observations were carried out in December 2019 with the Eight MIxer Receiver (EMIR) and the symmetrical wobbler switching mode, in which the secondary mirror switches up to a maximum of ±120 arcsec in azimuth. We operated in dual-sideband mode, and these sidebands were connected to two spectroscopic back ends, WILMA and FTS. J221024.49+114247.0 was integrated for 2.0 h in the E090 band and 2.8 h in the E230 band, enabling the detection of CO(1−0) emission in the former and CO(2−1) emission in the latter, as displayed in Fig. 4. We fitted linear baselines and subtracted them from the spectra. The spectral lines exhibit wide tails and are better adjusted with two Gaussian functions of different widths (see Fig. 4 and the parameters in Table 2) than with a single Gaussian function fit. Firstly, we calculated the CO line luminosity, in K km s^{-1} pc^2, as defined in Solomon et al. (1997):

$$L_{\rm CO} = 3.25 \times 10^7 \, S_{\rm CO} \, \Delta V \, \nu_{\rm obs}^{-2} \, D_{\rm L}^2 \, (1+z)^{-3} \tag{1}$$

where $S_{\rm CO} = 5\, I_{\rm CO}$ is the integrated flux in Jy km s^{-1}, $I_{\rm CO}$ is the line area given in Table 2 in K km s^{-1} (we considered the sum of both $I_{\rm CO}$ in order to integrate the whole flux), $\nu_{\rm obs}$ is the line frequency in GHz, and $D_{\rm L}$ = 422 Mpc is the luminosity distance to the galaxy. Secondly, we derived the mass of molecular gas using $M_{\rm H_2} = \alpha L_{\rm CO}$, where α is the CO-to-H$_2$ conversion factor, estimated following Freundlich et al. (2019). We hence derived a CO-to-H$_2$ conversion factor of $\alpha = 4\, M_\odot/({\rm K\,km\,s^{-1}\,pc^2})$ and finally found a total molecular gas mass of $M_{\rm H_2} = 3.29 \times 10^{10}\, M_\odot$, which corresponds to 21% of the total stellar mass. Table 2 gives the properties of the reduced CO spectra.

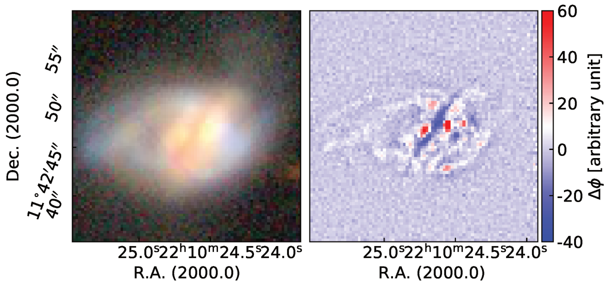

Fig. 5. Morphology. *Left*: composite image (g, r, z bands) from the Legacy survey (Dey et al. 2019). *Right*: difference between the MegaCam r-band filter image and its smoothed version.

3.2. Faint structures detected in the r-band MegaPipe/CFHT image

We also used the publicly available r-band stacked image from MegaCam, a wide-field imager mounted on the Canada-France-Hawaii Telescope (CFHT), with very precise astrometric and photometric calibrations, respectively accurate to within 0.15″ and 0.03 mag. By smoothing the image from the MegaCam Image Stacking Pipeline (MegaPipe; Gwyn 2008) using a Gaussian kernel and then subtracting the result from the original image, we spotlight the presence of an obscured dust lane across the galaxy (see the right panel of Fig. 5) and some irregular arms of stars around the core of the system.

3.3. Radio continuum VLA archives

J221024.49+114247.0 was observed with the Very Large Array (VLA) on 2016 September 30 in A configuration in both frequencies 1.5 GHz and 2.5 GHz (which respectively correspond to the L and the S band), with a 1.3 × 1.3″ resolution for the former and a 0.65 × 0.65″ resolution for the latter (P.I.: J. D. Gelfand). The corresponding fluxes are respectively 8.2 mJy and 3.1 mJy. In parallel, we collected the following integrated fluxes from archival data: 7.4 ± 0.3 mJy at 1.4 GHz from the Faint Images of the Radio Sky at Twenty-Centimeters (FIRST) survey (Becker et al. 1994; Helfand et al. 2015) and 3.1 ± 0.5 mJy at 3 GHz from the Very Large Array Sky Survey (VLASS; Lacy et al. 2020). We derived a synchrotron spectral index of −1.3 and a rest-frame 1.4 GHz luminosity of 1.3×10^{23} W Hz^{-1} (Condon et al. 2019). As displayed in the bottom-left panel of Fig. 2, the 1.5 GHz peak coincides with the second Hα component.

4. Results: Properties of the merger

4.1. Kinematics and geometry

4.1.1. Two stellar and gaseous discs

We highlight the superposition of two components along the line of sight in MaNGA data and interpret these spectral features as the two progenitors of an on-going merger event. This interaction involves one galaxy whose gas kinematics appears fairly regular and a second galaxy that is counter-rotating with respect to the first one. As displayed in Fig. 3, the stellar velocity motions for both components are consistent with the velocity fields of the gas. The position angles (PA) of the gas and stellar velocity fields, computed using the algorithms described in Krajnović et al. (2006) (see `FIT_KINEMATIC_PA` in

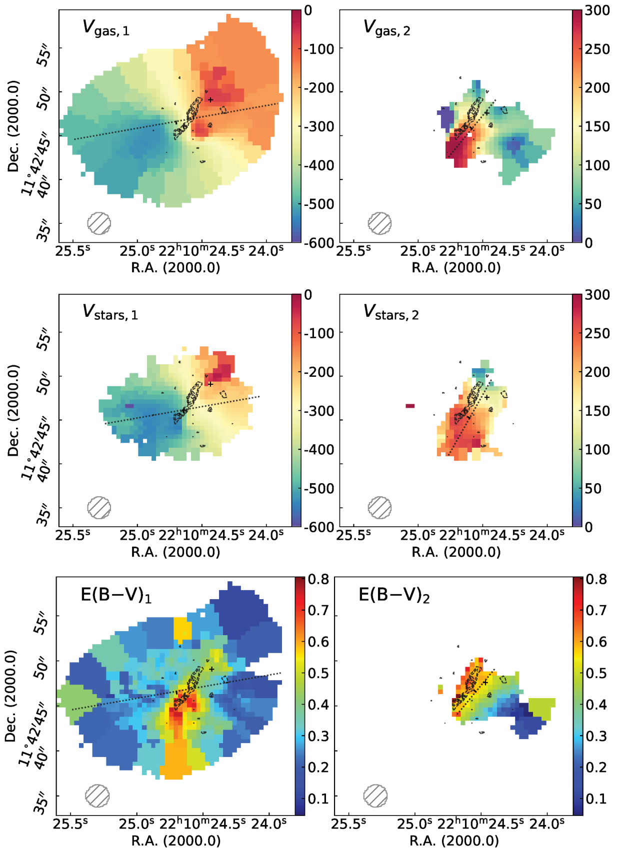

Fig. 6. Superimposition of the dust lane on the gas velocity maps (*top*), the stellar velocity maps (*middle*), and the extinction maps (*bottom*) derived from Balmer decrement computation.

Cappellari 2017), are similar: $\mathrm{PA}_{\mathrm{gas},1} = 280.0 \pm 0.5^\circ$ and $\mathrm{PA}_{\mathrm{stars},1} = 280.0 \pm 0.5^\circ$ for the first component, and $\mathrm{PA}_{\mathrm{gas},2} = 140.5 \pm 2.5^\circ$ and $\mathrm{PA}_{\mathrm{stars},2} = 150.5 \pm 2.0^\circ$ for the second component. Using the axes found for the gas kinematics, we estimated lengths of the major and minor axes of, respectively, 41 kpc and 27 kpc for the main galaxy, and of 13 kpc and 9 kpc for the second galaxy.

For the main galaxy, we derived an inclination of $i_1 = 49^\circ$, assuming a negligible disc thickness (e.g. Hubble 1926) of up to 53° with the correction proposed by Aaronson et al. (1980). For the second component, we derived an inclination $i_2 = 46^\circ$ using the basic formula and $i_2 = 50^\circ$ when applying the correction for disc thickness.

4.1.2. Dust lane

The dust lane displayed in the right panel of Fig. 5 extends from the south-east to the north-west over approximately 11 kpc. We estimated a position angle ($\mathrm{PA}_{\mathrm{dl}} = 147^\circ$) consistent with the position angle derived from the velocity field of the second MaNGA component. As displayed in Fig. 6, this dust lane is compatible with the extinction computed with the Balmer decrement for the second component, with the same inclination, while it is somehow detected in the extinction measured for the first component, supporting the view that the second component lies in front of the system. When compared with the stellar and gaseous component (middle and top panels), it exhibits the same position angle as the velocities but shifted to the north, and hence compatible with an inclination of about 50°.

4.2. Star formation activity

4.2.1. Hα-based SFR

We derive an extinction-corrected star formation rate (SFR) for each component based on the measurements from the double-component decomposition. We corrected the Hα luminosity following Calzetti (2001): $L_{\mathrm{int}}(\mathrm{H}\alpha) = L_{\mathrm{obs}}(\mathrm{H}\alpha)10^{0.4k(\mathrm{H}\alpha)E(B-V)}$, where L_{int} is the intrinsic luminosity, L_{obs} is the observed luminosity, $k(\mathrm{H}\alpha)$ is the reddening curve at the Hα wavelength, and $E(B-V)$ is the dust extinction. To compute this last value, we used the Hα/Hβ ratio and assumed an intrinsic value of 2.86 (corresponding to a temperature of $T = 10^4$ K and an electron density $n_{\mathrm{e}} = 10^2\,\mathrm{cm}^{-3}$ for a case B recombination; Osterbrock & Ferland 2006). Our derived values based on the MaNGA data, $\mathrm{SFR}_{\mathrm{H}\alpha,1} = 7.9\,M_\odot\,\mathrm{yr}^{-1}$ and $\mathrm{SFR}_{\mathrm{H}\alpha,2} = 2.3\,M_\odot\,\mathrm{yr}^{-1}$, are consistent with the different estimates of the SFR, namely from Brinchmann et al. (2004) and from a spectral energy distribution (SED) fitting based on UV and optical spectra performed by Salim et al. (2016), which agree towards a total value above $10\,M_\odot\,\mathrm{yr}^{-1}$.

4.2.2. WISE-based SFR

The SFR derived from Wide-field Infrared Survey Explorer (WISE) data provides $10.57\,M_\odot\,\mathrm{yr}^{-1}$ (Salim et al. 2016). It is in excellent agreement with the previous Hα-based estimate, supporting the assumption that there is no significant underestimation of the star formation activity. As discussed later in Sect. 4.2.5, the two galaxies lie on the star formation main sequence.

4.2.3. Radio-based SFR

Following Condon et al. (2019) and assuming the radio flux is due to star formation only, we also derived a radio-based SFR that could be as large as $160\,M_\odot\,\mathrm{yr}^{-1}$. As mentioned in Sect. 3.3, the slope computed from the four flux densities (FIRST, both bands of VLA, and VLASS) is very steep. Although this value of −1.3 is not sufficient to assess whether the emission originates from AGNs or star formation, it is typical of a synchrotron emission rather than a free-free one. The discrepancy between the optical-based and the radio-based SFR estimates is due to either a severe underestimation of the extinction in the optical estimate or a hidden AGN or Low-Ionisation Nuclear Emission-line Region (LINER) contributing to the radio flux. However, the good agreement between the optical Hα-based SFR and the infrared WISE-based SFR discussed above rules out the first hypothesis.

As displayed in the bottom-left panel of Fig. 2, the peak at 1.5 GHz (as well as the peak at 2.5 GHz) is coincident with the second component Hα flux. Given the large SFR observed for the main galaxy, the radio flux due to star formation would be expected to peak on this galaxy. The fact that the radio flux is centred on the second component is a strong argument in favour of a hidden AGN and supports the notion that most of this radio flux (more than 90%) is not due to star formation.

4.2.4. Off-centred star formation

For the main galaxy, the peak of star formation detected in Hα is off-centred with respect to the kinematic centre. The velocity dispersion peaks at the centre of the rotation pattern, but some

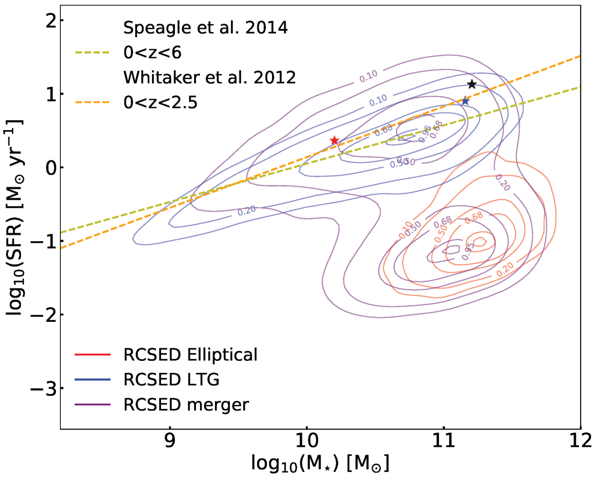

Fig. 7. SFR vs. stellar mass plot. The black star corresponds to the total system, relying on the values provided by Salim et al. (2016) for J221024.49+114247.0. The blue and red stars refer to the main and secondary component, respectively, based on our SFR and stellar mass computations. The contours correspond to representative galaxies of the RCSED sample (Chilingarian et al. 2017), classified using Domínguez Sánchez et al. (2018).

large gas velocity dispersions are detected in the north-west part of the disc. Indeed, while the stellar velocities are in good agreement with gas velocities, the stellar velocity dispersions are shifted with respect to those observed for the gas. Moreover, we cannot exclude that the extinction correction of Hα emission is not sufficient to trace the actual ionised gas emission in the centre of the main galaxy. We might thus miss star formation at its centre. The stellar velocity dispersion might also be affected by an important amount of dust in the centre, which would explain why we detect high values in the north-west region of the galaxy where there is less dust. The presence of clumps and filament-like structures, observed in the dust extinction maps (Fig. 2) and in the velocity dispersion map of the primary galaxy (Fig. 3), also suggests the presence of underlying velocity gradients due to recent gas accretion triggered by the interaction.

4.2.5. Two main-sequence galaxies

Figure 7 summarises the main star-forming properties of the two galaxies. They have a regular star-forming activity as both lie on the main sequence. For comparison, we display the contours based on galaxies taken from the RCSED (Chilingarian et al. 2017). This catalogue encompasses 800 299 low- and intermediate-redshift galaxies ($0.007 < z < 0.6$) and provides multi-wavelength spectrophotometric measurements from various surveys (GALEX, SDSS, and UKIDSS) as well as value-added data (k corrections, star and gas kinematics, and extinction estimates) for each object. Globally, the two detected components currently do not exhibit any excess of star formation. This result is compatible with the molecular gas detection discussed in Sect. 4.5. Lastly, the excitation diagram explored next also supports the star-forming and composite excitations for most regions of these two galaxies.

4.3. BPT excitation diagram

When considering the Baldwin, Phillips & Telervich diagnostic diagram (introduced in Baldwin et al. 1981) for each peak separately (cf. Fig. 8), most of the spaxels lie in the composite and star-forming regions for both peaks, but the second peak displays a systematically higher [OIII]/Hβ ratio than the first one. This supports our two-component analysis and is in line with the fact that the redshifted component has a smaller mass (and lower metallicity; e.g. Kewley et al. 2019; Curti et al. 2020). While the two discs are mostly star forming, the BPT maps (Fig. 8) display very localised LINER-type emission.

Based on the [OIII]λ5008 emission, it appears that the double-peaked profile for this line is reliably detected in a wider part of the MaNGA field of view. The spaxels identified as the secondary component do not seem to be associated with the main velocity gradient (their velocity is below 0 km s^{-1}) and show a higher excitation compared to the other spaxels related to this galaxy. This is reflected in their position on the BPT diagram, slightly shifted with respect to the main distribution of the other points and clearly belonging to the composite region (or even to the LINER region for three of them). The integrated [OIII]λ5008 luminosities for each component within an area equivalent to the PSF (a circular region of about 2.5″) around the respective emission peak are $L_{\rm [OIII],1} = 1.1 \times 10^7\,L_\odot$ and $L_{\rm [OIII],2} = 8.3 \times 10^6\,L_\odot$. Even though we applied an extinction correction to derive these values, this might not be sufficient to trace the total [OIII]λ5008 emission in these inner parts of the galaxies. The values we find are higher than $10^{6.5}\,L_\odot$, the limit between weak and powerful AGNs considered by Alonso et al. (2007), which is consistent with their conclusion that most of the AGNs in pairs show an [OIII] luminosity above this threshold.

In Fig. 9 we also study stacked histograms of [OIII] and Hβ fluxes. We both stacked the spectra of all spaxels and stacked the models of the blue and red components. Interestingly, we find some high velocity residuals that escaped the adjustment. They typically correspond to expected velocity fields in the outskirts of both discs, where the S/N is weak.

4.4. Possible evidence of a radio jet

Above we stated that the radio flux seems to be associated with the smaller galaxy. The radio emission from VLA observations is extended: We computed an integrated flux, called $F_{\rm int}$ hereafter, by summing up the emission over an area of 30×30 pixels around the flux peak and divided the derived value by the beam surface. We finally find $F_{\rm int}/F_{\rm peak} = 8.7$ (respectively 5.1) at 2.5 GHz (respectively 1.5 GHz) with a 0.65″ (respectively 1.3″) resolution. Given the radio flux excess with respect to the expected SFR, we could argue that this is a weak radio jet.

4.5. Molecular gas content

The single-dish CO observations reveal an important reservoir of molecular gas within the system, both in CO(1−0) and CO(2−1). The inferred total H$_2$ mass represents 21% of the stellar mass of the system. The Kennicutt–Schmidt relation shows that the system is located on the main sequence.

When we discriminate the flux below 0 km s^{-1} from the one above this value, as for the optical data, we find that the galaxy detected in the negative velocities has a higher CO(1−0)/CO(2−1) ratio than the secondary component. The beam sizes are different for both transitions, but since the CO(2−1) beam covers ~23 kpc, we consider that we do not miss any significant emission outside the beam coverage. Thus, we can associate this ratio discrepancy with different excitations.

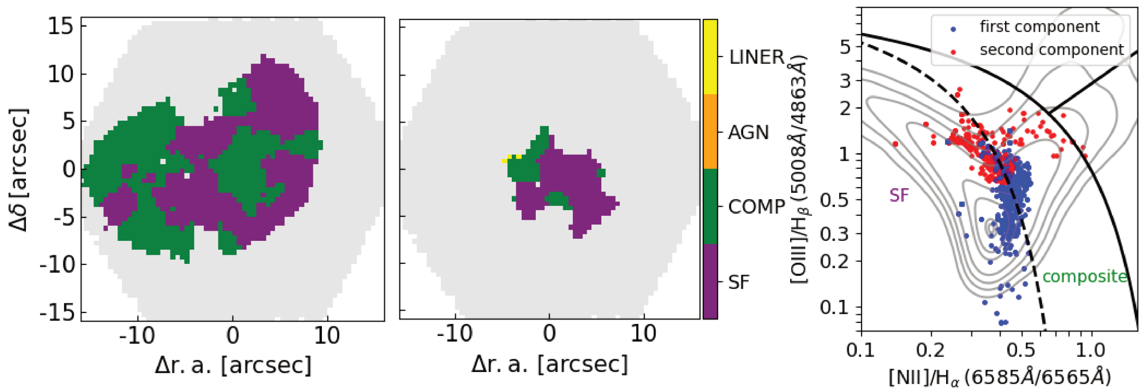

Fig. 8. Ionisation properties of the gas for the two components of J221024.49+114247.0. *Left* and *middle panels*: BPT (Baldwin et al. 1981) maps for both fitted components. *Right panel*: BPT diagram showing the position of the spaxels. The S/N threshold is set at 3. The spaxels where the S/N of at least one emission line is below the corresponding threshold are masked. Moreover, for the redshifted component, the masks described in Sect. 2.1 are applied. The *last panel* displays the LINER, AGN, composite, and star-forming excitation regions as defined by Kewley et al. (2001), Kauffmann et al. (2003), and Schawinski et al. (2007). The grey contours refer to galaxies representative of the RCSED sample.

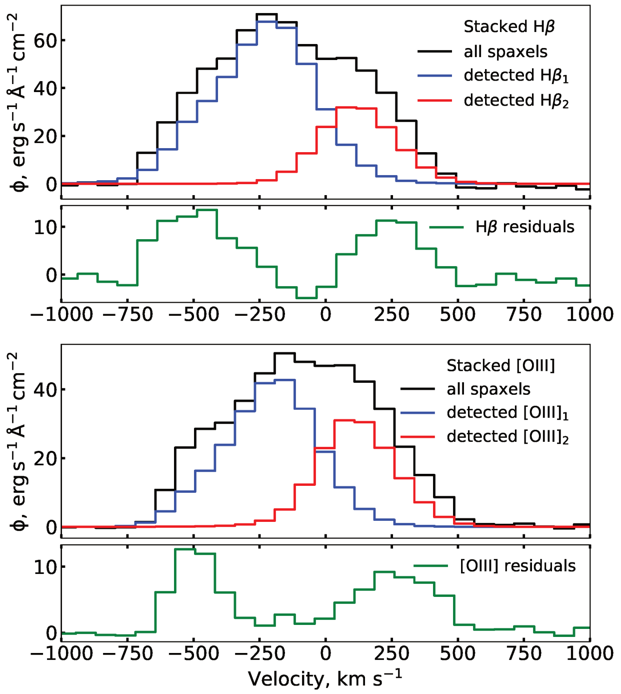

Fig. 9. Stacked ionised-gas lines. *Top* and *bottom panels*: stacked Hβ and [OIII]λ5008 emission lines, respectively, from all MaNGA spaxels in black. We show with blue and red the stacked blueshifted and redshifted components of our fitted model, only including spaxels with detected lines. Below the stacked emission lines, we show the residuals that exhibit excesses at large velocities.

4.6. Gas metallicity and post-starburst signature

The maps of the gas metallicity are shown in the right panels of Fig. 2. The smaller component appears to have a lower gas-phase oxygen abundance than the main galaxy, but this is not so clear when one computes averaged metallicities $12 + \log(\mathrm{O/H})_1 = 8.65$ and $12 + \log(\mathrm{O/H})_2 = 8.58$. However, the spatial distribution is very different. While the small component has a metallicity gradient roughly centered on the kinematic centre, the main galaxy exhibits a large gas metallicity region east of the star formation peak. This disordered metallicity gradient can be related to the gas accretion from the low-metallicity. The main galaxy follows the mass-metallicity relation when we consider this off-centred area, while it exhibits a lower-than-expected metallicity in the central parts, as explained in Sect. 4.7.4 and shown in Fig. 10. Moreover, the galaxy spectra in these off-centred regions exhibit a significant Balmer absorption line that is attributed to a stellar population of ~1 Gyr (e.g. Pawlik et al. 2018), typical of post-starburst regions. On the contrary, the spectra extracted from the regions where the computed gas-phase oxygen abundance is below the solar metallicity do not show such an important Balmer absorption line. Typical spectra extracted from these two different types of regions are displayed in Fig. B.1. Unlike in Goto (2007), the galaxies are still forming stars. Also, the starburst is quite old (1 Gyr) compared to the systems observed in, for example, Poggianti & Wu (2000).

However, we do not see explicit or strong signs of a recently formed stellar population in the optical spectrum, but the S/N of the data makes it difficult to provide definitive conclusions based on individual bins. Ultraviolet data with a good spatial resolution would help us conduct a qualitative analysis of these regions.

The irregular metallicity distribution can be compared with other merging systems, such as NGC 4038/4039. This system was studied by Gunawardhana et al. (2020), who detected star-forming regions with gas more enriched than the rest of the galaxy.

4.7. Mass ratio estimates

4.7.1. Stellar mass ratio

To determine the light fraction between both detected stellar components, we performed a modelling of the stellar LOSVD. The recovered LOSVD (see Sect. 2.2) is approximated in each spatial bin by two Gaussian components. Each of these components is represented by a thin inclined exponential disc. We used arbitrary initial guesses for the different characteristics of these profiles and eventually found an optimal set of parameters to reproduce the modelled LOSVD. We obtain a light fraction of 6.1 between the main component and the secondary one. Using stellar ages and metallicities derived with

NBursts, as mentioned in Sect. 2.2, we determined the mass-to-light (M/L) ratios for the r-band filter: $M/L_{r,1} = 0.63$ and $M/L_{r,2} = 0.43$. Given that the light fraction is 6.1, the stellar mass fraction is as follows: $6.1\ (M/L_{r,1})/(M/L_{r,2}) = 9$. This mass ratio enabled us to infer stellar masses for each of the detected component: According to Salim et al. (2016), the total stellar mass of the system is $1.59 \times 10^{11}\ M_{\odot}$, which, when considering the stellar mass ratio described above, gives: $M_{\star,1} = 1.43 \times 10^{11}\ M_{\odot}$ and $M_{\star,2} = 1.59 \times 10^{10}\ M_{\odot}$.

4.7.2. Dynamical mass ratio

For each galaxy, the inclination angle computed in Sect. 4.1 can be used to calculate the respective rotation velocity as in Cortese et al. (2014) and Aquino-Ortíz et al. (2018) following $V_{\rm rot} = W/2\ \sin(i)$, where W is defined as the difference between the 90th and 10th percentile points of the velocity histogram. We derive a rotation velocity of $V_{\rm rot,1} = 236\ {\rm km\,s^{-1}}$ for the main galaxy and $V_{\rm rot,2} = 140\ {\rm km\,s^{-1}}$ for the secondary one. Then we computed the dynamical mass corresponding to the first MaNGA component as follows: $M_{\rm dyn,1} = V^2_{\rm rot,1}\ R_1/G$, where R_1 is the maximal radius where Hα emission is detected. We find $M_{\rm dyn,1} = 2.65 \times 10^{11}\ M_{\odot}$. Similarly, the dynamical mass of the second component is defined as: $M_{\rm dyn,2} = V^2_{\rm rot,2}\ R_2/G$. We derive $M_{\rm dyn,2} = 2.93 \times 10^{10}\ M_{\odot}$. These results give a mass ratio of $M_{\rm dyn,1}/M_{\rm dyn,2} \sim 9$.

4.7.3. Uncertainties

To evaluate the robustness of the previous estimate of the merger mass ratio, we varied the parameters used in the computations of the stellar and the dynamical masses. As the interaction between both objects certainly perturbs both galaxies, we can consider that it is relevant to include the contribution of the velocity dispersion $\sigma_{\rm gas}$ in the dynamical mass estimate. Based on the $S_{0.5}$ parameter defined and discussed in Aquino-Ortíz et al. (2018), we calculated the dynamical mass using the proxy they introduce as $M_{\rm dyn} = \eta R S^2_{0.5}/G$. The inferred dynamical masses are $M_{\rm dyn,1} = 6.98 \times 10^{11}\ M_{\odot}$ and $M_{\rm dyn,2} = 5.80 \times 10^{10}\ M_{\odot}$, corresponding to a mass ratio $M_{\rm dyn,1}/M_{\rm dyn,2}$ of 12. In parallel, for the stellar masses, we can force both inclinations of the modelled exponential disc profiles based on the inclination angles computed using the gas velocity fields. This leads to a light fraction of 7.3. Relying on the mass-to-light ratios given in Sect. 4.7.1, the corresponding stellar mass ratio is ∼10. Lastly, one can note that considering a large inclination angle for the secondary galaxy provides a dynamical mass similar to the stellar mass, constraining an inclination smaller than 80°.

Finally, all the approaches converge on a mass ratio within the visible radius of about 9:1 for MaNGA 1−114955.

4.7.4. Mass-metallicity relation

In order to determine if the metallicities of these two galaxies, which both lie on the star formation main sequence, are perturbed, we tried to position them on the stellar mass-SFR-gas metallicity relation proposed by Curti et al. (2020) (based on Mannucci et al. 2010). Figure 10 shows the mass-metallicity relations for different SFR bins as described in Curti et al. (2020). It should be noted that the gas metallicity computed here corresponds to the gas metallicity computed in the SDSS 3 arcsec (central) fibre. We used the calibration defined in this work to compute the metallicity, based on the O_3N_2 calibrator, within circular regions with a diameter of 3 arcsec. On the one hand, the second galaxy lies almost on the curve parametrised for objects with a similar SFR. On the other hand, the properties of the first galaxy are consistent with the relation only if we compute the metallicity over the off-centred region with high gas-phase oxygen abundance values (see the top-right panel of Fig. 2). If we compute the metallicity around the kinematic centre or the star formation peak, the value is too low compared to the mass of the galaxy and thus does not follow the relation. We can argue that this primary galaxy has probably accreted metal-poor gas in its centre through the interaction.

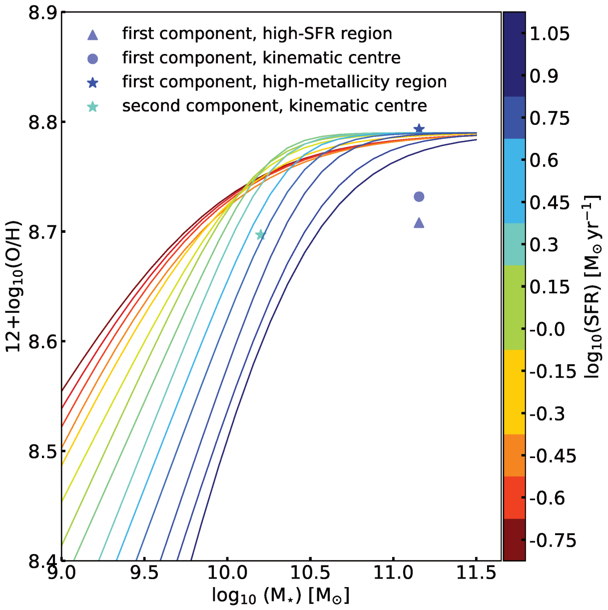

Fig. 10. Mass-metallicity relations for different values of total SFR, as defined in Curti et al. (2020). The SFRs of both components are the ones computed from our two-component analysis and given in Sect. 4.2.1. The markers are colour-coded with the SFR of the corresponding host galaxies. For the primary galaxy, different 3 arcsec circular apertures have been considered, as discussed in Sect. 4.7.4.

5. Discussion

5.1. Pre-coalescence merger

We identify J221024.49+114247.0 as a merging system caught in action. We observe two distinct counter-rotating discs, aligned along the line of sight, with a line-of-sight velocity difference of $\Delta V = 450\ {\rm km\,s^{-1}}$. We find one main galaxy with an inclination of $i_1 = 49°$ and a second galaxy of $i_2 = 46°$ as a smaller counterpart. Using high-resolution imaging from the Megacam-CFHT footprint, we identified a dust lane that is aligned with the stellar component of the smaller galaxy and is associated with measured extinction in the main galaxy, suggesting a scenario where the small galaxy is positioned in front of the main galaxy along the line of sight, as shown in Fig. 11. These two disc components are both detected in the ionised gas and in the stellar continuum emission, and they have not yet been destroyed by the interaction. We estimated a mass ratio of 9:1 using the stellar masses and dynamical masses. For both galaxies, we find off-centred peaks in stellar velocity dispersion, reminiscent of

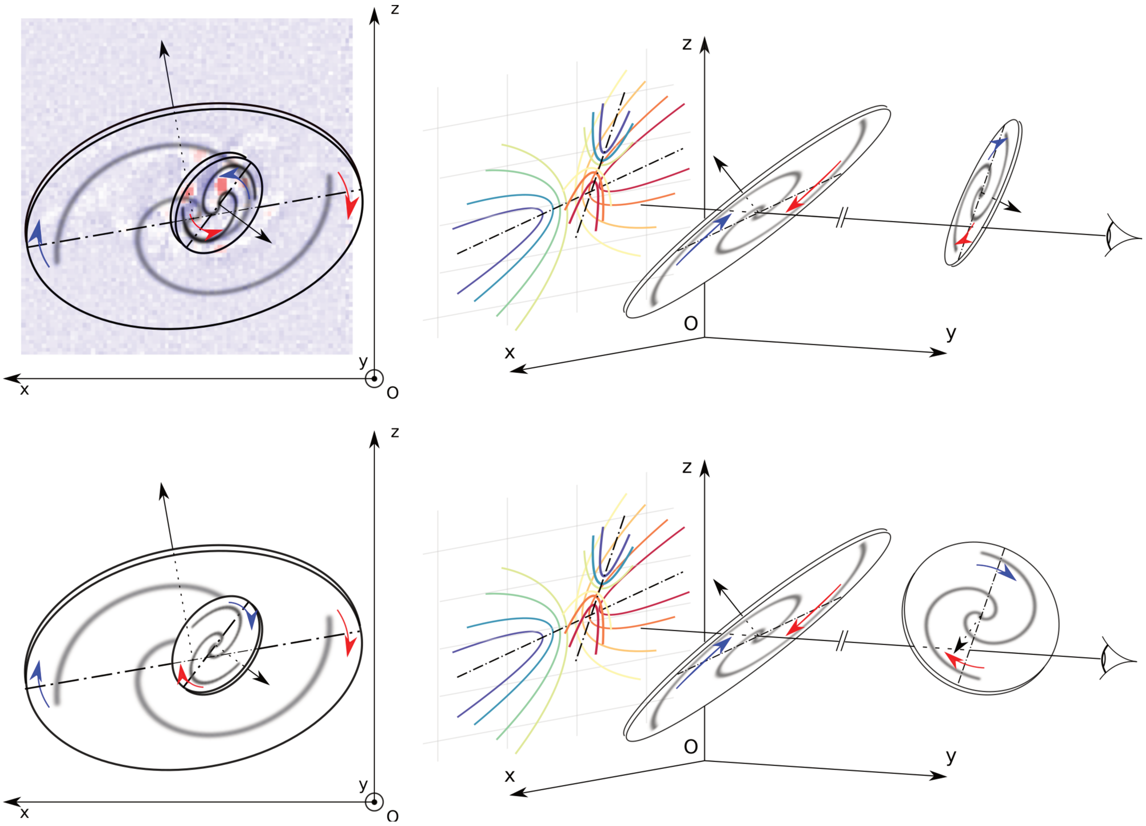

Fig. 11. Schematic illustration of the revealed merging system. *Top*: configuration where the near side of the secondary galaxy is on the north side. *Bottom*: configuration where the near side is on the south side of the major axis. *Left panels*: discs as projected on the sky. *Right panels*: a '3D view', with a different viewing angle, for which discs can be represented with no superposition. *Top-left panel*: highlighting of a potential dust lane in Fig. 5.

possible accretion onto the disc and an underlying filamentary structure.

We show schematic representations of two possible configurations of the observed objects in Fig. 11: Each row of the figure shows one of these configurations, viewed as projected on the sky (left panels) or with a viewing angle (the same for the two rows) for which the discs can be represented with no superposition (right panels, '3D views'). The line of sight along which the system is observed with MaNGA is parallel to the (Oy) axis (the MaNGA observer is symbolised with the eye to the right). The disc on the left of the 3D views represents the primary galaxy, and the one on the right, the secondary. The rotation of each disc is shown with a spin (black arrow) and corresponding schematic trailing spiral arms. The coloured arrows represent the line-of-sight velocity for the MaNGA observer (blue- or red-shifted with respect to each kinematic centre), and the MaNGA velocity maps are schematically represented on the (Oxz) plane of the right panels (with different colours corresponding to each kinematic centre, as in Fig. 3). We note that the distance between the two galaxies is unknown (hence the break in the line of sight). For a given disc inclination, part of one side of the major axis of the projection of the disc on the sky is either farther away than this major axis or closer to it (near side). We can determine the near side of the primary galaxy with the help of its spiral arms, seen in Fig. 5. We assumed that these spiral arms are trailing, which gives the sense of rotation on the sky. Combined with the line-of-sight velocities, this determines the inclination of the disc plane, with a near side north-east of the major axis. The near side of the secondary galaxy is harder to determine. The presence of the dust lane parallel to the kinematic axis but shifted to the north could support an argument that the near side is on the north side, as in the top panel of Fig. 11. Alternatively, the bottom panel shows a configuration compatible with the observation of an ionisation cone north-east of the major axis of the secondary disc, which would mean that the near side is on the south side of the major axis.

5.2. Possible outflows driven by central activity

The interaction might also have triggered gas accretion on the supermassive black hole (SMBH) and a hidden AGN detected in radio. This is compatible with the discussion in Shah et al. (2020) regarding the possibility of low-level AGN enhancement in galaxy interactions. Using BPT diagrams, we find that the two galaxies are located in different regions, associated with different states of ionisation. On the one hand, the star-forming and composite excitation occupies different regions, probably due to the different galaxy masses, while the second galaxy shows some regions with LINER excitation, suggesting a different mechanism that is potentially linked to the radio flux found to be associated with this galaxy. This might indicate that the merger process can induce different mechanisms, shifting the two components on the BPT diagram, as discussed in Maschmann & Melchior (2019).

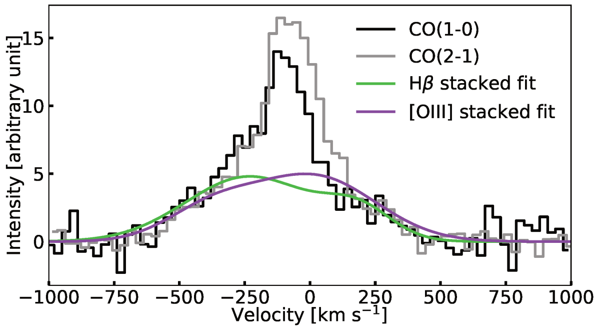

Fig. 12. Re-scaled CO spectra and fits of the stacked Hβ and [OIII] lines that display a similar range of velocities.

The molecular gas spectra obtained for both galaxies exhibit a large range of velocities of about 1000 km s^{-1}. By comparing these spectra to the stacked Hβ and [OIII] emission lines from the optical spectra in Fig. 12, we observe that the wide wings of CO emission coincide with the wings observed in the ionised gas. This accounts for the rotation patterns of the two discs. In parallel, we detect, in the velocity range −100 to 0 km s^{-1}, a relative excess of molecular gas corresponding to the peak of star formation activities. To understand how the molecular gas behaves in the vicinity of the possible AGN identified in radio, higher-resolution observations of molecular gas with the NOrthern Extended Millimeter Array (NOEMA) are needed.

The wide range of velocities detected in both molecular and ionised gas might correspond to a gaseous outflow, either due to the star formation triggered by the interaction or to the feedback due to the AGN in the small galaxy. It has been shown that radio jets, even when compact, can create major turmoil in galaxies, enhancing the velocity width (Venturi et al. 2021). Figure 9 reveals that the wide wings are not detected in individual spectra, but appear only by stacking. This turbulent or outflowing gas must be spread over some diffuse regions and only at low intensity.

5.3. Evidence of two pericentre passages

The total SFR of the entire system is estimated to be 13.3 $M_\odot$ yr^{-1} (Salim et al. 2016). Radio observations suggest a much higher SFR of more than 80 $M_\odot$ yr^{-1}, which is probably biased by a contribution of an obscured AGN. Using the extinction-corrected Hα emission line, we located a concentration of ongoing star formation in the main galaxy, which is off-centred with respect to the kinematic centre by about 5 kpc in projection. The smaller galaxy exhibits a strong peak in star formation, located at its kinematic centre, and is associated with an extended radio emission.

It seems that the external gas of the smaller companion has been stripped by the main galaxy, which has probably accreted this gas onto its disc. It is hence probable that the progenitor of the smaller galaxy was originally more massive. The ignition of the AGN, somehow related to the gas present in the central starburst, is due either to accretion of gas (from the primary) or to the original central distribution of gas, and is not necessary related to the harassment. We also observe a peak in the gas-phase metallicity of the main galaxy located to the east of its main star formation region. This high-metallicity region, located more than 6 kpc away from the kinematic centre, is associated with significant Balmer absorption lines imprinted in the galaxy spectrum (see Fig. B.1). This feature could trace past starburst events not older than 1 Gyr (e.g. Pawlik et al. 2018). Indeed, this clearly asymmetric metallicity distribution is not expected in a relaxed system. We argue that this could be the signature of a first pericentre passage, while the current star formation (in the north-west part of the main galaxy) could be associated with a recent pericentre passage. Star formation induced by the interaction of galaxies varies significantly (in terms of highest SFR, duration of high SFR periods, and integrated star formation on the duration of the merger) as a function of the orbital parameters and the inclination of the discs of the progenitors (e.g. Di Matteo et al. 2008). It is thus difficult to infer the geometry of the interaction (prograde or retrograde orientation of the spins of the galaxies) from the observed star formation.

5.4. Comparison with other merging systems

The interacting galaxies presented in this work can be compared to the less massive system Mrk 739, which hosts a double AGN (Tubín et al. 2021). In this case, two AGNs have been identified in X-ray (Koss et al. 2011). Interestingly, in this source the ionised gas distribution clearly peaks at the position of the two AGNs. The gas is concentrated in the centre, which explains the ignition of both AGNs. As the system is more face-on with a projected nuclear separation of 3.4 kpc, it is not obvious if there are two rotating distinct discs, such as those we observe for J221024.49+114247.0. The authors noted that the progenitors were a star-forming galaxy and an old elliptical.

In our case, the main galaxy has a larger SFR than its companion, but this is probably triggered by accretion of the stripped gas. Interestingly, this gas did not reach the galaxy centre and was not able to fuel the SMBH. Using a simulation of NGC 2623, Prieto et al. (2021) explained that the first passage can trigger extended star formation, such as we observed here. He et al. (2020) discussed the two galaxies in Arp 240 with a projected distance of about 40 kpc. They claim that the low depletion time (100 Myr) is an argument for a late-stage merger. In the case of J221024.49+114247.0, the global depletion time (3.3 Gyr) is typical of normal star-forming galaxies (e.g. Saintonge et al. 2011).

6. Conclusions

We have presented a multi-wavelength analysis of a pre-coalescence merger, J221024.49+114247.0, at $z = 0.09$. Originally identified with a double-peaked feature in the SDSS fibre and a disrupted merger morphology, this galaxy has been observed with MaNGA. We developed a fitting procedure based on a double-Gaussian function and applied it throughout the MaNGA field of view. We have been able to highlight the presence of two counter-rotating discs along the line of sight in gas as well as in stars. The difference of their systemic velocity is 450 km s^{-1}, and they are aligned along the line of sight. A modelling of the stellar LOSVD enables us to derive a stellar mass ratio between the main and the secondary component of ~9, relying on the mass-to-light ratio estimates. The mass ratio based on dynamical mass estimates is in good agreement with that derived from the stellar distribution analysis.

The main galaxy exhibits off-centred regions of star formation. A large region (at ~6 kpc from the kinematic centre) exhibits a large gas metallicity and a Balmer absorption line in the galaxy spectra, possibly reminiscent of a 1 Gyr old starburst, while the current SFR detected in Hα is also off-centred with respect to the kinematic centre. We argue that this is due to two different pericentric passages. This more massive galaxy is probably more gas rich than its companion, but the gas has not collapsed in the centre. The minor galaxy exhibits an excess of extended radio flux centred on its kinematic centre with respect to the expected SFR. Its kinematic centre corresponds to a standard velocity dispersion and metallicity gradient. We argue that its external gas has been stripped. Large molecular gas velocities are compatible with the ionised gas rotation velocities, and we cannot conclude on the possibility of an outflow.

We propose to extend this work with NOEMA/IRAM interferometric observations in order to study the molecular gas distribution and the sub-millimetre continuum distribution.

Acknowledgements. We are most grateful to the IRAM-30 m team who supported us for these observations. IK acknowledges the support from the Russian Scientific Foundation grant 19-12-00281 and the Interdisciplinary Scientific and Educational School of Moscow University “Fundamental and Applied Space Research”. We thank the anonymous referee for constructive comments. Funding for the Sloan Digital Sky Survey IV has been provided by the Alfred P. Sloan Foundation, the US Department of Energy Office of Science, and the Participating Institutions. SDSS-IV acknowledges support and resources from the Center for High-Performance Computing at the University of Utah. The SDSS website is `www.sdss.org`. SDSS-IV is managed by the Astrophysical Research Consortium for the Participating Institutions of the SDSS Collaboration including the Brazilian Participation Group, the Carnegie Institution for Science, Carnegie Mellon University, the Chilean Participation Group, the French Participation Group, Harvard-Smithsonian Center for Astrophysics, Instituto de Astrofísica de Canarias, The Johns Hopkins University, Kavli Institute for the Physics and Mathematics of the Universe (IPMU)/University of Tokyo, the Korean Participation Group, Lawrence Berkeley National Laboratory, Leibniz Institut für Astrophysik Potsdam (AIP), Max-Planck-Institut für Astronomie (MPIA Heidelberg), Max-Planck-Institut für Astrophysik (MPA Garching), Max-Planck-Institut für Extraterrestrische Physik (MPE), National Astronomical Observatories of China, New Mexico State University, New York University, University of Notre Dame, Observatário Nacional/MCTI, The Ohio State University, Pennsylvania State University, Shanghai Astronomical Observatory, United Kingdom Participation Group, Universidad Nacional Autónoma de México, University of Arizona, University of Colorado Boulder, University of Oxford, University of Portsmouth, University of Utah, University of Virginia, University of Washington, University of Wisconsin, Vanderbilt University, and Yale University. The Legacy Surveys consist of three individual and complementary projects: the Dark Energy Camera Legacy Survey (DECaLS; Proposal ID #2014B-0404; PIs: David Schlegel and Arjun Dey), the Beijing-Arizona Sky Survey (BASS; NOAO Prop. ID #2015A-0801; PIs: Zhou Xu and Xiaohui Fan), and the Mayall *z*-band Legacy Survey (MzLS; Prop. ID #2016A-0453; PI: Arjun Dey). DECaLS, BASS and MzLS together include data obtained, respectively, at the Blanco telescope, Cerro Tololo Inter-American Observatory, NSF’s NOIRLab; the Bok telescope, Steward Observatory, University of Arizona; and the Mayall telescope, Kitt Peak National Observatory, NOIRLab. The Legacy Surveys project is honored to be permitted to conduct astronomical research on Iolkam Du’ag (Kitt Peak), a mountain with particular significance to the Tohono O’odham Nation. This research used the facilities of the Canadian Astronomy Data Centre operated by the National Research Council of Canada with the support of the Canadian Space Agency.

References

Aaronson, M., Mould, J., & Huchra, J. 1980, ApJ, 237, 655
Abolfathi, B., Aguado, D. S., Aguilar, G., et al. 2018, ApJS, 235, 42
Alonso, M. S., Lambas, D. G., Tissera, P., & Coldwell, G. 2007, MNRAS, 375, 1017
Alonso, S., Mesa, V., Padilla, N., & Lambas, D. G. 2012, A&A, 539, A46
Aquino-Ortíz, E., Valenzuela, O., Sánchez, S. F., et al. 2018, MNRAS, 479, 2133
Baldwin, J. A., Phillips, M. M., & Terlevich, R. 1981, PASP, 93, 5
Becker, R. H., White, R. L., & Helfand, D. J. 1994, in Astronomical Data Analysis Software and Systems III, eds. D. R. Crabtree, R. J. Hanisch, & J. Barnes, ASP Conf. Ser., 61, 165
Brinchmann, J., Charlot, S., White, S. D. M., et al. 2004, MNRAS, 351, 1151
Bundy, K., Bershady, M. A., Law, D. R., et al. 2015, ApJ, 798, 7
Calzetti, D. 2001, PASP, 113, 1449
Cappellari, M. 2016, ARA&A, 54, 597
Cappellari, M. 2017, MNRAS, 466, 798
Casteels, K. R. V., Bamford, S. P., Skibba, R. A., et al. 2013, MNRAS, 429, 1051
Chilingarian, I., Prugniel, P., Sil’Chenko, O., & Koleva, M. 2007a, in Stellar Populations as Building Blocks of Galaxies, eds. A. Vazdekis, & R. Peletier, 241, 175
Chilingarian, I. V., Prugniel, P., Sil’Chenko, O. K., & Afanasiev, V. L. 2007b, MNRAS, 376, 1033
Chilingarian, I. V., Zolotukhin, I. Y., Katkov, I. Y., et al. 2017, ApJS, 228, 14
Condon, J. J., Matthews, A. M., & Broderick, J. J. 2019, ApJ, 872, 148
Cortese, L., Fogarty, L. M. R., Ho, I. T., et al. 2014, ApJ, 795, L37
Curti, M., Mannucci, F., Cresci, G., & Maiolino, R. 2020, MNRAS, 491, 944
Das, A., Pandey, B., & Sarkar, S. 2021, JCAP, 06, 045
Dey, A., Schlegel, D. J., Lang, D., et al. 2019, AJ, 157, 168
Di Matteo, P., Bournaud, F., Martig, M., et al. 2008, A&A, 492, 31
Domínguez Sánchez, H., Huertas-Company, M., Bernardi, M., Tuccillo, D., & Fischer, J. L. 2018, MNRAS, 476, 3661
Ellison, S. L., Patton, D. R., Simard, L., et al. 2010, MNRAS, 407, 1514
Ellison, S. L., Catinella, B., & Cortese, L. 2018, MNRAS, 478, 3447
Ellison, S. L., Viswanathan, A., Patton, D. R., et al. 2019, MNRAS, 487, 2491
Freundlich, J., Combes, F., Tacconi, L. J., et al. 2019, A&A, 622, A105
Goto, T. 2007, MNRAS, 377, 1222
Greve, T. R., Bertoldi, F., Smail, I., et al. 2005, MNRAS, 359, 1165
Gunawardhana, M. L. P., Brinchmann, J., Weilbacher, P. M., et al. 2020, MNRAS, 497, 3860
Gwyn, S. D. J. 2008, PASP, 120, 212
Hani, M. H., Gosain, H., Ellison, S. L., Patton, D. R., & Torrey, P. 2020, MNRAS, 493, 3716
He, H., Wilson, C. D., Sliwa, K., Iono, D., & Saito, T. 2020, MNRAS, 496, 5243
Helfand, D. J., White, R. L., & Becker, R. H. 2015, ApJ, 801, 26
Hubble, E. P. 1926, ApJ, 64, 321
Kasparova, A. V., Katkov, I. Y., & Chilingarian, I. V. 2020, MNRAS, 493, 5464
Katkov, I. Y., Sil’chenko, O. K., & Afanasiev, V. L. 2013, ApJ, 769, 105
Katkov, I. Y., Sil’chenko, O. K., Chilingarian, I. V., Uklein, R. I., & Egorov, O. V. 2016, MNRAS, 461, 2068
Kauffmann, G., Heckman, T. M., Tremonti, C., et al. 2003, MNRAS, 346, 1055
Kewley, L. J., Dopita, M. A., Sutherland, R. S., Heisler, C. A., & Trevena, J. 2001, ApJ, 556, 121
Kewley, L. J., Nicholls, D. C., & Sutherland, R. S. 2019, ARA&A, 57, 511
Koss, M., Mushotzky, R., Treister, E., et al. 2011, ApJ, 735, L42
Krajnović, D., Cappellari, M., de Zeeuw, P. T., & Copin, Y. 2006, MNRAS, 366, 787
Lacy, M., Baum, S. A., Chandler, C. J., et al. 2020, PASP, 132, 035001
Lahén, N., Johansson, P. H., Rantala, A., Naab, T., & Frigo, M. 2018, MNRAS, 475, 3934
Mannucci, F., Cresci, G., Maiolino, R., Marconi, A., & Gnerucci, A. 2010, MNRAS, 408, 2115
Maschmann, D., & Melchior, A.-L. 2019, A&A, 627, L3
Maschmann, D., Melchior, A.-L., Mamon, G. A., Chilingarian, I. V., & Katkov, I. Y. 2020, A&A, 641, A171
McAlpine, S., Harrison, C. M., Rosario, D. J., et al. 2020, MNRAS, 494, 5713
Mendenhall, W., & Sincich, T. 2011, A Second Course in Statistics Regression Analysis (Pearson Education)
Mesa, V., Duplancic, F., Alonso, S., Coldwell, G., & Lambas, D. G. 2014, MNRAS, 438, 1784
Nevin, R., Blecha, L., Comerford, J., & Greene, J. 2019, ApJ, 872, 76
Osterbrock, D. E., & Ferland, G. J. 2006, Astrophysics of Gaseous Nebulae and Active Galactic Nuclei (Sausalito, CA: University Science Books)
Patton, D. R., Torrey, P., Ellison, S. L., Mendel, J. T., & Scudder, J. M. 2013, MNRAS, 433, L59
Pawlik, M. M., Taj Aldeen, L., Wild, V., et al. 2018, MNRAS, 477, 1708
Poggianti, B. M., & Wu, H. 2000, ApJ, 529, 157
Prieto, J., Escala, A., Privon, G., & d’Etigny, J. 2021, ArXiv e-prints [arXiv:`2101.09407`]
Saintonge, A., Kauffmann, G., Wang, J., et al. 2011, MNRAS, 415, 61
Sakamoto, K., Aalto, S., Combes, F., Evans, A., & Peck, A. 2014, ApJ, 797, 90
Salim, S., Lee, J. C., Janowiecki, S., et al. 2016, ApJS, 227, 2
Schawinski, K., Thomas, D., Sarzi, M., et al. 2007, MNRAS, 382, 1415
Shah, E. A., Kartaltepe, J. S., Magagnoli, C. T., et al. 2020, ApJ, 904, 107
Sharma, R. S., Choi, E., Somerville, R. S., et al. 2021, ArXiv e-prints [arXiv:`2101.01729`]
Solomon, P. M., Downes, D., Radford, S. J. E., & Barrett, J. W. 1997, ApJ, 478, 144
Somerville, R. S., & Davé, R. 2015, ARA&A, 53, 51
Strauss, M. A., Weinberg, D. H., Lupton, R. H., et al. 2002, AJ, 124, 1810
Tubín, D., Treister, E., D’Ago, G., et al. 2021, ApJ, 911, 100
van Dokkum, P. G., Nelson, E. J., Franx, M., et al. 2015, ApJ, 813, 23
Venturi, G., Cresci, G., Marconi, A., et al. 2021, A&A, 648, A17
Weiß, A., Downes, D., Walter, F., & Henkel, C. 2005, A&A, 440, L45
Westfall, K. B., Cappellari, M., Bershady, M. A., et al. 2019, AJ, 158, 231

Appendix A: Gas spatial properties obtained through our fitting procedure

A.1. Flux maps

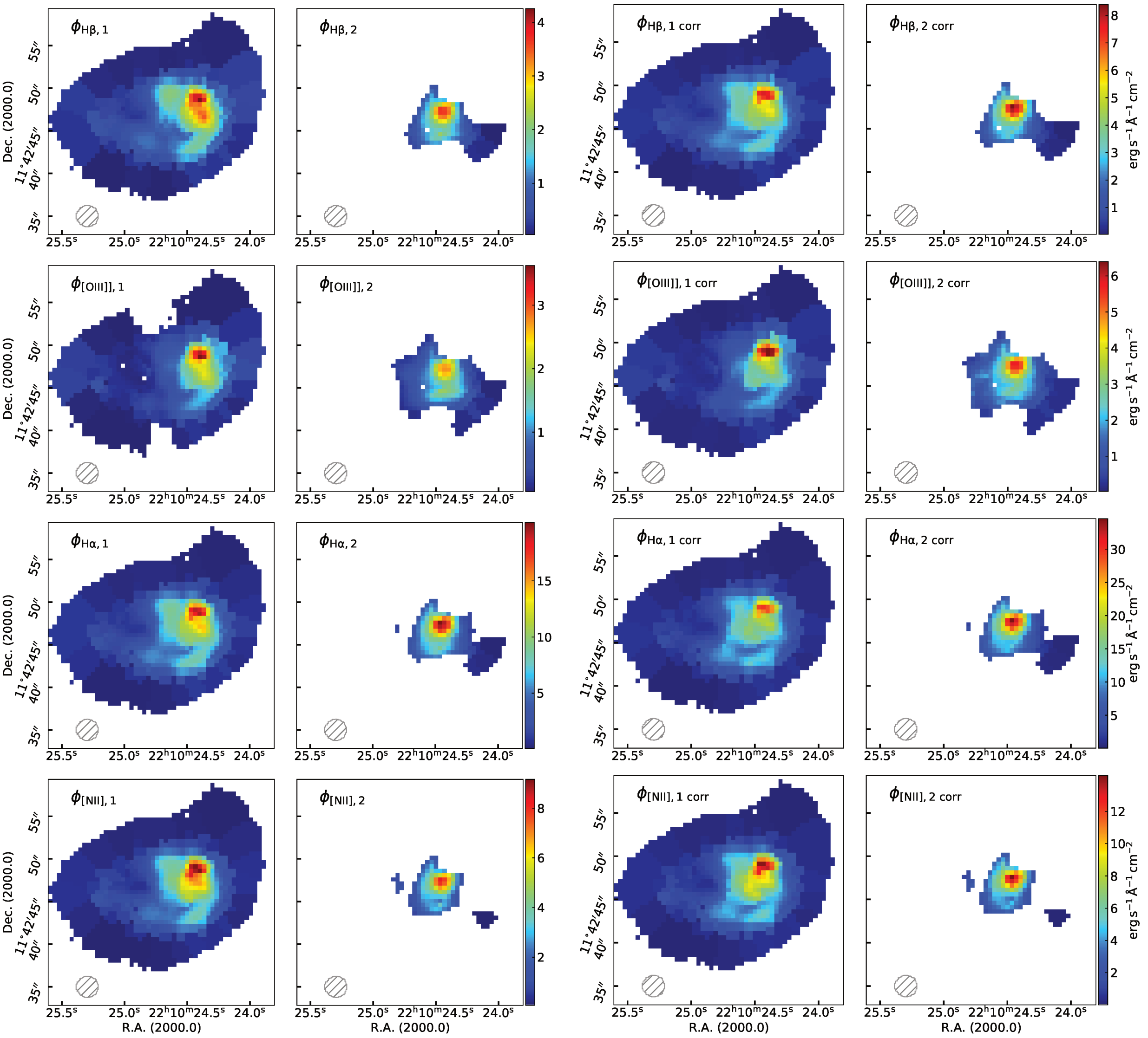

Fig. A.1. Respective Hβ, [OIII]λ5007, Hα, and [NII]λ6585 flux maps for both fitted components. The S/N threshold is set at 3 (spaxels with S/N below this value are masked). Moreover, for the second component, all the spaxels that do not meet the criteria defined in Sect. 2.1 are masked. The maps shown in the right column are the respective fluxes but corrected for extinction.

Appendix B: Spectra from regions with different extreme metallicities

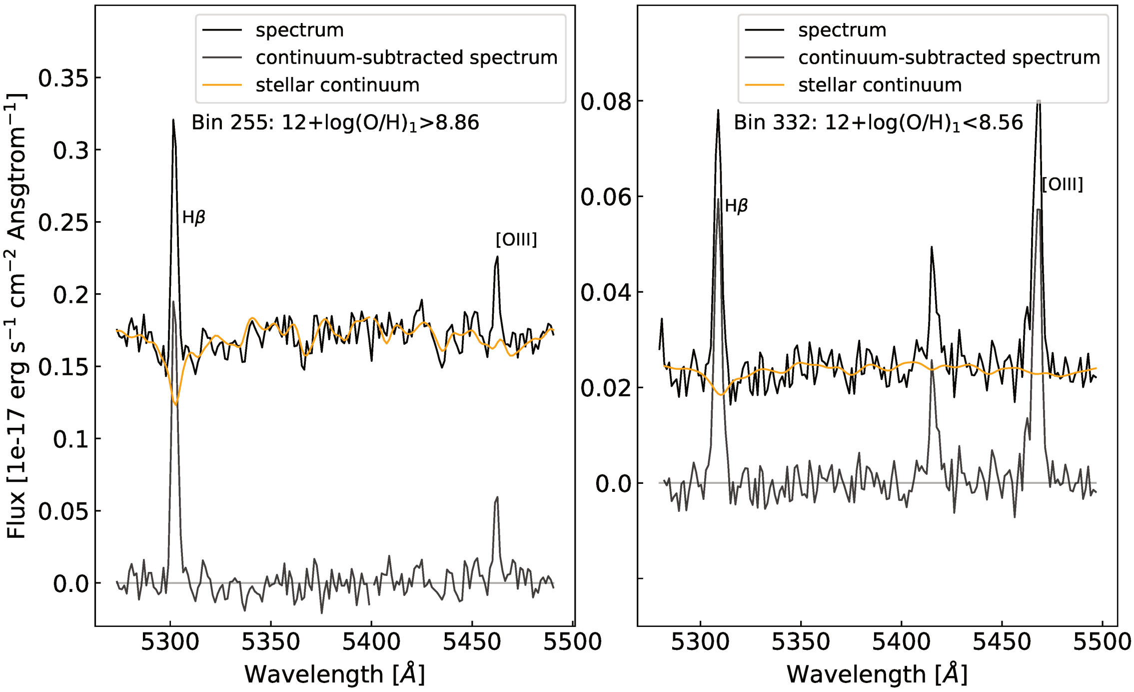

Fig. B.1. Different extracted spectra and their corresponding fits. *Left panel*: spectrum of a bin with a high gas-phase oxygen abundance, and *right panel*: a bin where the computed gas-phase oxygen abundance is low. *Left panel*: an important Balmer absorption line below Hβ can be seen.

Exploration du contenu en gaz froid des galaxies DP/MaNGA

Gaz moléculaire

Dans les conditions typiques du milieu interstellaire, la molécule H_2 n'est pas directement observable car son absence de moment dipolaire électrique rend la probabilité d'une transition rotationelle énergétique très faible.Il est donc nécessaire d'observer d'autres molécules et de contraindre l'abondance de la molécule observée et avec celle de H_2. La molécule la plus communément utilisée pour tracer H_2 est le monoxyde de carbone, CO. Les transitions rotationnelles CO(1-0) et CO(2-1) sont largement étudiées et ont pour fréquences au repos respectives $\nu_{1-0} = 115.271\,\mathrm{GHz}$ et $\nu_{2-1} = 230.538\,\mathrm{GHz}$.

Facteur de conversion CO/H_2

Calibrer la relation entre l'intensité observée de CO et la masse de gaz H_2 est crucial pour interpréter la quantité de gaz susceptible de former des étoiles. Une relation répandue est:

$$M_{\mathrm{mol}} = \alpha_{\mathrm{CO}}\, L\mathrm{CO} \tag{4.16}$$

où M_{mol} est exprimée en masses solaires $M_\odot$ et $L\mathrm{CO}$ en $\mathrm{K\,km\,s}{-1}\,\mathrm{pc}^2$. α_{CO} est alors un rapport masse-lumière. Ce rapport dépend de différents paramètres, tels que la densité du gaz, la température et la métallicité. La valeur de $\alpha = 4,36 \pm 0,9\,\mathrm{M}_\odot/(\mathrm{K\,km\,s}^{-1}\,\mathrm{pc}^2$, qui tient compte de la quantité d'Helium, est souvent utilisée pour la Voie Lactée, les galaxies proches et celles à faible métallicité (par ex. Bolatto et al., 2008; Schinnerer et al., 2010). Une valeur de ce facteur qui tient compte de la métallicité est discutée dans divers travaux (Genzel et al., 2015; Tacconi et al., 2018).

Observations à l'IRAM 30m

Afin d'estimer le contenu en gaz moléculaire des galaxies DP/MaNGA et de mesurer leur efficacité à former des étoiles, nous avons observé ces 29 sources avec le télescope 30m de l'Institut de Radio Astronomie Millimétrique (IRAM). La luminosité du CO est donnée par l'équation 5.4 et la masse totale de gaz moléculaire est obtenue avec l'équation 5.5. J'ai appliqué une correction d'ouverture pour les galaxies étendues au-delà de la taille du faisceau primaire ($22''$ à la fréquence de la transition CO(1-0)), afin de tenir compte du gaz moléculaire présent dans les régions non couvertes par les observations. Pour ce faire, j'ai suivi la procédure détaillée dans Lisenfeld et al. (2011).

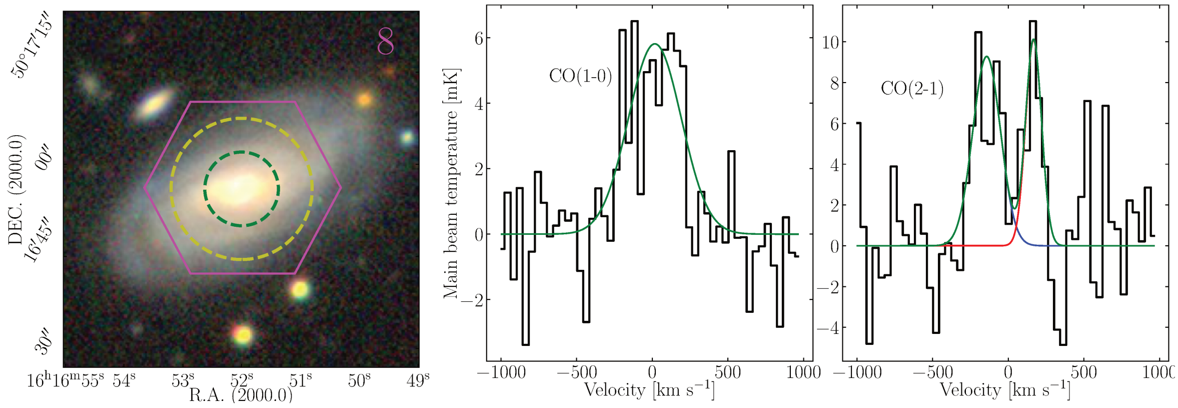

Figure (4.7) Exemple de spectres des transitions CO(1-0) et CO(2-1) obtenus à l'IRAM 30 m. La vignette montre l'image du relevé Legacy, avec le champ de vue MaNGA en magenta et les largeurs des faisceaux de l'IRAM en jaune (resp. vert) à 3 mm (resp. 1 mm). Les deux spectres montrent la raie CO(1-0) ajustée avec une gaussienne et la raie CO(2-1) ajustée avec une double gaussienne.

Observations avec NOEMA

Pour être en mesure d'étudier la distribution et la cinématique du gaz moléculaire dans le système de galaxies en interaction décrit dans Mazzilli Ciraulo et al. (2021), j'ai demandé à observer ce système avec l'interféromètre NOEMA. J'ai obtenu un cube de données correspondant à la transition CO(1-0) et une analyse préliminaire des données suggère que la distribution de gaz moléculaire est irrégulière et semble cohérente avec celle du gaz ionisé (cartes préliminaire sur la figure 5.7).

Gaz atomique

Les atomes d'hydrogène neutre (HI) peuvent être détectés et il est d'une importance capitale d'estimer le contenu en gaz froid d'une galaxie, puisqu'il constitue le réservoir pour la formation d'étoiles. De nombreuses relations d'échelle montrent une corrélation entre le contenu en HI et les propriétés des galaxies telles que la masse stellaire, la densité massique de surface ou la couleur et les magnitudes.

Observations avec le radio-télescope de Nançay

Les 16 galaxies DP/MaNGA les plus proches ($z < 0.06$) ont été observées durant le second semestre de 2020 par le radio-télescope de Nançay dans le but de détecter la raie HI à 21 cm. Ces observations nous permettront d'estimer la masse totale de gaz atomique dans les galaxies détectées et d'établir une relation de Kennicutt-Schmidt en utilisant la masse totale de gaz froid (moléculaire et atomique).

5

Exploring the cold gas content of the DP/MaNGA galaxies

In this chapter, I present the observations I conducted at the IRAM 30m telescope and at the Nançay Radio Telescope to respectively obtain molecular and atomic gas content within the DP/MaNGA sources. First I give brief introductions to what can be inferred from cold gas observations, then I describe the setups of the observations and finally I present the results and analyse them in the light of other surveys of nearby galaxies.

1 Molecular gas phase

In the typical conditions within the interstellar medium, the H_2 molecule cannot be observed directly because of very small rotational transition probabilities and thus weak line emission, due to its lack of an electric dipole moment. Thus it is necessary to use other molecules in order to trace H_2 by making assumptions on the relation between the abundance of the observed molecule and the one of H_2. The most commonly tracer of H_2 is the carbon monoxyde CO. This molecule becomes excited through collisions with the H_2 molecule and its de-excitation results in the emission of photons in observable wavelength regions. The most studied CO rotational transitions are CO($J\,1 \rightarrow 0$) and CO($J\,2 \rightarrow 1$) that are at the heart of various molecular gas surveys and that are commonly referred to as CO(1-0) and CO(2-1). Their respective rest-frame frequencies are $\nu_{\mathrm{CO}(1-0)} = 115.271\,\mathrm{GHz}$ and $\nu_{\mathrm{CO}(2-1)} = 230.538\,\mathrm{GHz}$.

1.1 CO-to-H_2 conversion factor

Calibrating the relation between the observed CO intensity and the total H_2 gas mass is crucial to interpret the amount of gas that is likely to form stars. A standard methodology gives:

$$\mathrm{N(H_2)} = X_{\mathrm{CO}}\, I_{\mathrm{CO}} \tag{5.1}$$

where $\mathrm{N(H_2)}$ is the dihydrogen column density in $\mathrm{cm^{-2}}$ and I_{CO} is the observed CO integrated line intensity in $\mathrm{K\,km\,s^{-1}}$. The factor X_{CO} is thus given in $\mathrm{cm^{-2}/(K\,km\,s^{-1})}$. By integrating over the emitting area and correcting by the mass contribution of heavier elements, another relation is adopted:

$$M_{\mathrm{mol}} = \alpha_{\mathrm{CO}}\, L_{\mathrm{CO}} \tag{5.2}$$

where M_{mol} is given in units of $M_\odot$ and L_{CO} in $\mathrm{K\,km\,s^{-1}\,pc^2}$. With this definition, α_{CO} is a mass-to-light ratio. One refers to "CO-to-H_2 conversion factor" for both X_{CO} and α_{CO}. This factor depends on different environmental parameters such as the gas density, temperature and metallicity. In the Milky Way, as well as in nearby star-forming and low-metallicity galaxies, a value of $\alpha = 4.36 \pm 0.9 M_\odot/(\mathrm{K\,km\,s^{-1}\,pc^2})$ accounting for helium has been found using different estimate methods (e.g. Dame et al., 2001; Bolatto et al., 2008; Schinnerer et al., 2010; Leroy et al., 2011). At higher redshift, the metallicity dependence of the factor can be taken into account through (as in Genzel et al., 2015; Tacconi et al., 2018):

$$\alpha_{\mathrm{CO}} = \alpha\,\sqrt{0.67 \times \exp(0.36 \cdot 10^{8.67-\log \mathrm{Z}}) \times 10^{-1.27\cdot(\log \mathrm{Z}-8.67)}} \tag{5.3}$$

where α is the factor given above and where log Z=12+log(O/H), the gas-phase metallicity based on the Pettini & Pagel (2004) calibration.

2 Observations at IRAM 30m

We aimed at measuring the molecular gas content of the DP/MaNGA galaxies in order to estimate their star formation efficiency and study the process of quenching within these systems. We observed all objects with the IRAM 30m telescope at Pico Veleta in Spain.

2.1 Data acquisition and reduction

We used the spectral line receiver Eight MIxer Receiver (EMIR) in the configuration E0/2, which enables us to simultaneously operate in the 3 and 1.3 mm windows. The EMIR bands were connected to two backends: the Fast Fourier Transform Spectrometers (FTS) and the Wideband Line Multiple Autocorrelator (WILMA), allowing us to obtain measurements with a resolution of 0.195 MHz and 2 MHz, respectively. We used the symmetrical wobbler switching mode, in which the secondary mirror moves up to ±120 arcsec in azimuth. Since the telescope are performed with the on-off mode enabled by the rapid motion of the secondary mirror, the on and off positions are shifted along the azimuthal axis and therefore the airmass does not vary between both scans. The provided baselines are thus better than in the position switching mode for instance. Scans of 6 min duration were performed and encompassed on-source and off-source sub-scans of 30 s duration each. Pointing calibrations were taken on a nearby planet or bright quasar. Telescope focusing was regularly carried out. Integrations were repeated until a signal was detected and a reasonable signal-to-noise ratio of the line was reached. Multiple integrations were combined in the dedicated software package CLASS. Usually, baselines were calculated in line-free regions using a linear fit, except for some cases in which we evaluated that higher order polynomials were required, based on visual inspection. Scans from September 1st, 2019, were discarded as the weather conditions were bad on this day. The averaged spectra were smoothed by binning the velocity channels to a velocity resolution of $\sim 64\,\mathrm{km\,s^{-1}}$. The reduced spectra are displayed in Figs. 5.1 and 5.2, with the Legacy survey snapshot to see the MaNGA coverage as well as the IRAM 30m telescope beam-widths.

2.2 Molecular gas analysis

The CO luminosity is expressed as:

$$\left(\frac{L_{\mathrm{CO}}}{\mathrm{K\,km\,s^{-1}\,pc^{-2}}}\right) = \frac{3.25\times10^{7}}{(1+z)}\left(\frac{F_{\mathrm{CO}}}{\mathrm{Jy\,km\,s^{-1}}}\right)\left(\frac{\nu_{\mathrm{rest}}}{\mathrm{GHz}}\right)^{-2}\left(\frac{D_{\mathrm{L}}}{\mathrm{Mpc}}\right)^{2} \tag{5.4}$$

where F_{CO} is the velocity-integrated flux, ν_{rest} is the rest-frame frequency and D_{L} the luminosity distance. For all detected galaxies, we compute the molecular gas mass $M_{\mathrm{H_2}}$ following:

$$M_{\mathrm{H_2}} = \alpha_{\mathrm{CO}}\, L_{\mathrm{CO}} \tag{5.5}$$

where α_{CO} is the estimated CO-to-$\mathrm{H_2}$ conversion factor. For the galaxies which are extended over a region broader than the beam size ($22''$ at the frequency of CO(1-0)), an aperture correction has to be applied in order to account for the molecular gas in the non-covered regions. I follow the procedure explained in Lisenfeld et al. (2011). An exponential distribution is assumed for CO (CO maps have shown that such distributions describe the CO emission well, e.g. Nishiyama et al., 2001; Regan et al., 2001; Leroy et al., 2008). I consider the optical radius at the 25 mag isophote, r_{25}, by dividing the optical diameter at the 25 mag isophote extracted from the NASA/IPAC Extragalactic Database (NED)[1]. We can assume $r_e/r_{25} = 0.2$ where r_e is the CO scale length (Lisenfeld et al., 2011). I measure the galaxy inclination using the minor-to-major axial ratio b/a given in the MaNGA PyMorph photometric value-added catalogue. The ratio is estimated based on a 2D surface brightness fit, either with a Sérsic profile or with a

---

[1] https://ned.ipac.caltech.edu/

Sérsic+Exponential profile (Fischer et al., 2019). I compute the inclination i as:

$$\cos i = \sqrt{\frac{(b/a)^2 - q_0^2}{1 - q_0^2}}, \tag{5.6}$$

where q_0 describes the intrinsic axial ratio of an edge-on observation and is set to $q_0 = 0.2$ (Holmberg, 1958, see also e.g. Tully et al. (2009)). Following Lisenfeld et al. (2011), I estimate the correction factor:

$$f_\mathrm{a} = \pi r_e^2 \left\{ \int_0^\infty dx \int_0^\infty dy \exp\left(-\ln(2)\left[\left(\frac{2\,x}{\Theta_\mathrm{B}}\right)^2 + \left(\frac{2\,y\cos(i)}{\Theta_\mathrm{B}}\right)^2\right]\right) \exp\left(-\frac{\sqrt{x^2+y^2}}{r_e}\right)\right\}^{-1}, \tag{5.7}$$

where Θ_B is the FWHM of the telescope beam, at the observed frequency. The integration of Eq. 5.7 is carried out numerically. The correction factor depends on the scale length of the CO emission, the beam size and the inclination of the galaxy. The correction factors obtained for the DP/MaNGA galaxies are such that $f_\mathrm{a} \leq 2$.

ID	r_{25}	i	corr. factor	α_{CO}	M_{H_2}	μ_{H_2}	log(SFE)	t_{depl}
		°		$M_{\odot}/(\mathrm{K\ km\ s^{-}1\ pc^2})$	$10^9\ M_{\odot}$		yr^{-1}	Gyr
G1	30.495	33	1.81	3.9	1.3	-1.8	-9.1	1.3
G2	45.505	67	2.00	3.9	2.3	-1.3	-9.3	2.1
G3	14.56	75	1.13	3.8	0.3	-1.6	-8.9	0.9
G4	15.415	41	1.23	3.8	0.6	-1.7	-9.4	2.6
G5	18.935	66	1.24	3.8	5.5	-0.9	-9.3	2.0
G6	27.495	46	1.59	4.2	3.2	-1.6	-9.1	1.3
G7	21.78	0.0	1.52	3.9	1.0	-1.8	-9.4	2.4
G8	29.765	63	1.53	4.0	3.7	-1.3	-9.0	1.1
G9	24.685	53	1.45	4.0	4.1	-1.5	-9.3	1.9
G10	17.01	76	1.17	3.8	4.4	-0.9	-9.3	1.8
G11	17.265	58	1.22	3.8	2.1	-1.3	-8.9	0.8
G12	38.99	71	1.73	4.2	4.4	-1.5	-9.3	2.1
G13	14.955	67	1.15	3.9	6.1	-1.1	-8.8	0.6
G14	22.19	56	1.36	3.9	3.1	-1.4	-8.8	0.7
G15	14.665	66	1.15	3.8	3.3	-1.4	-8.4	0.3
G16	18.765	44	1.31	3.8	1.5	-1.5	-9.4	2.3
G17	16.29	55	1.21	3.9	3.5	-1.4	-9.0	0.9
G18	20.76	47	1.36	4.1	10.6	-1.1	-9.4	2.5
G19	17.265	49	1.25	3.8	7.5	-1.1	-9.3	1.9
G20	14.085	48	1.18	3.9	9.9	-1.1	-8.6	0.4
G21	20.33	0.0	1.46	4.1	13.9	-0.9	-9.4	2.7
G22	17.88	65	1.22	4.1	11.8	-0.9	-9.8	5.8
G23	13.69	35	1.20	4.1	9.7	-1.0	-9.8	6.9
G24	13.74	0.0	1.23	4.0	43.0	-0.6	-9.4	2.8
G25	13.71	60	1.14	3.8	17.2	-0.9	-8.7	0.5
G26	12.01	53	1.12	4.1	30.0	-0.6	-9.6	4.2
G27	10.895	0.0	1.15	4.1	13.2	-1.0	-9.1	1.4
G28	13.875	39	1.19	4.1	32.4	-0.6	-9.7	4.7
G29	8.81	32	1.09	4.0	31.8	-0.7	-9.1	1.1

Table (5.1) Relevant properties of the DP/MaNGA galaxies to explore their molecular gas content. THe first column gives an arbitrary identifier to each galaxy; columns 2 to 4 display the radius at the 25 mag isophote, the inclination and the correction factor for aperture effect. Columns 5 to 9 refer to inferred quantities from the CO observations: the CO-to-H_2 conversion factor, the H_2 mass, the H_2 fraction, the logarithmic star formation efficiency and the depletion time.

I compute the conversion factor α_{CO} following Eq. 5.3. The mean conversion factor for the 29-galaxy sample is 3.9 with a standard deviation of 0.1.

Star-formation main sequence

I am able to investigate how some properties derived from the CO observations vary across the SFMS. To do this and to get homogeneous values with current CO surveys on MaNGA galaxies, I make use of the measurements found in Salim et al. (2016), if available, otherwise in Brinchmann et al. (2004). I define the molecular gas fraction $\mu_{\rm H_2} = M_{\rm H_2}/M_\star$. I measure a median molecular gas fraction for the DP/MaNGA sample of $\mu_{\rm H_2} = 0.07$, computed with the detected sources. I also estimate the star formation efficiency $\rm SFE = SFR/M_{H_2}$, expressed in $\rm yr^{-1}$, and the depletion time $t_{\rm depl}$ which is the inverse of SFE. The latter quantity is an indicator of the necessary time to convert all the available molecular gas into stars at the current star formation rate. The median star formation efficiency is $\log(\rm SFE/yr^{-1}) = -9.3$. Figure 5.3 shows the offset with respect to the star-formation main sequence defined by Whitaker et al. (2012), for the 29 DP/MaNGA galaxies. I colour-coded them according to the classification detailed in 1.1. The left panel of Fig. 5.4 shows the galaxies in the SFR-$M_\star$ plane, with a colour-coding referring to the molecular gas fraction. The right panel displays the SFE as colour-coding.

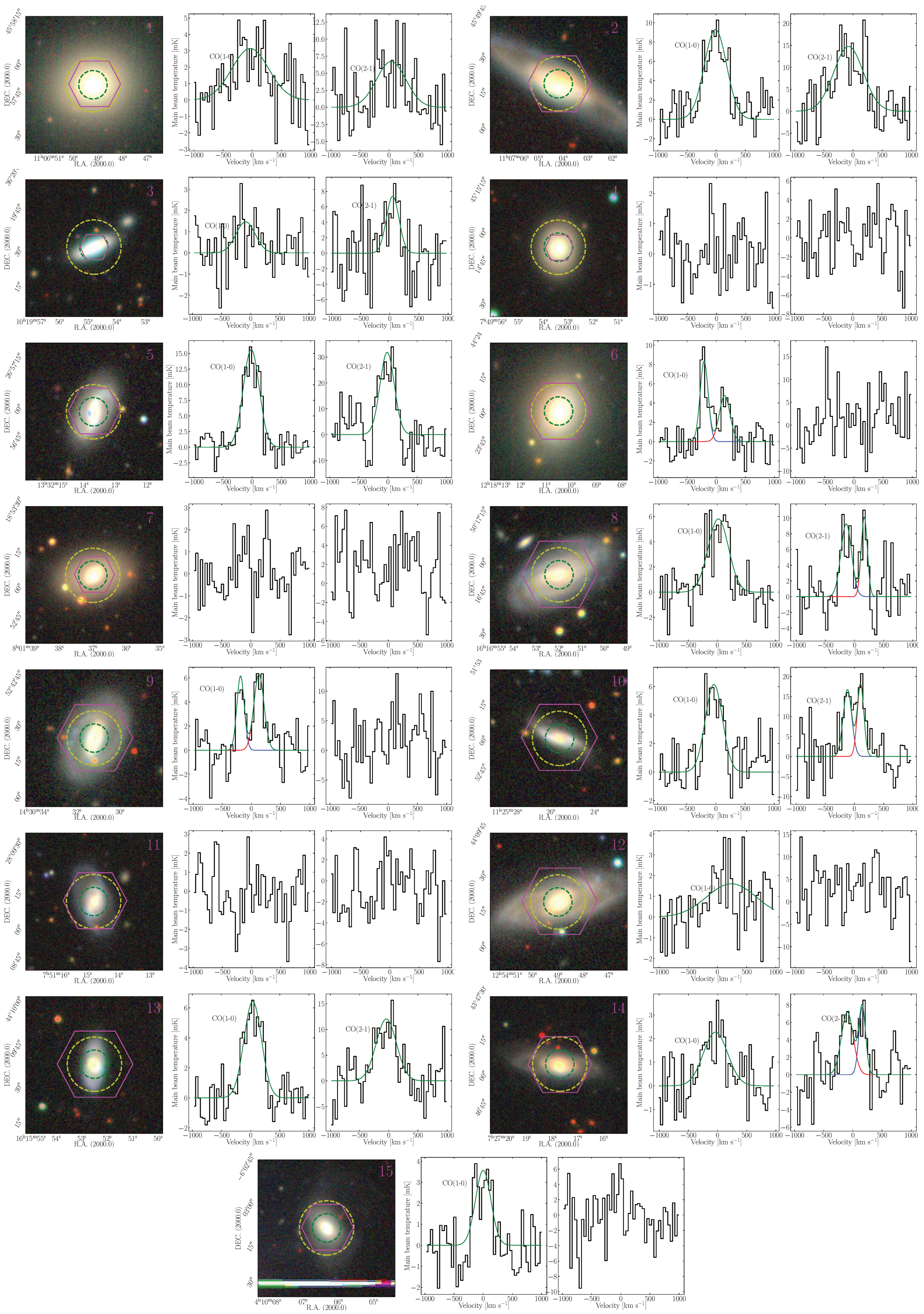

Figure (5.1) Spectra of the molecular gas obtained at the IRAM 30 m telescope. The MaNGA footprint is shown as a magenta hexagon, the CO(1-0) beam-width as a yellow dashed circle and the CO(2-1) beam width as a green dashed circle.

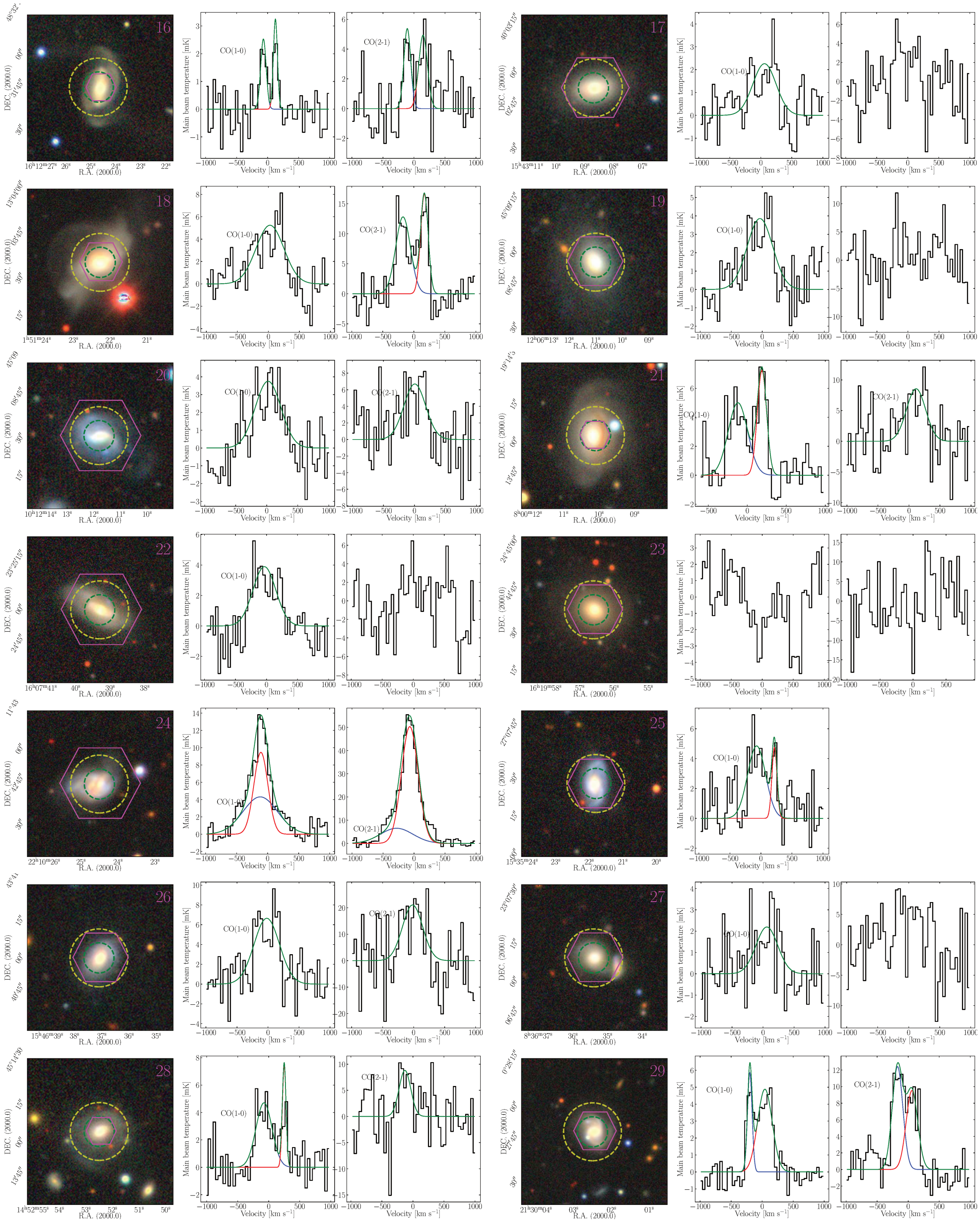

Figure (5.2) Same as Fig. 5.1

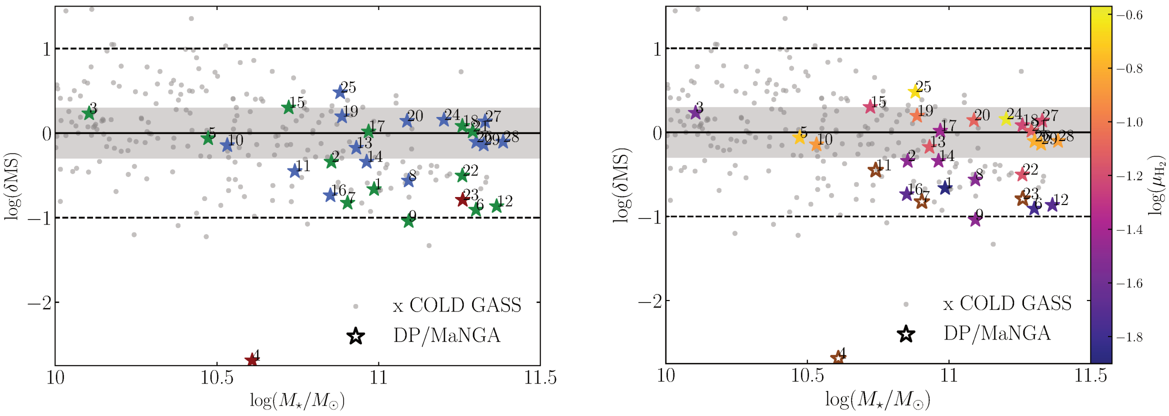

Figure (5.3) δMS as a function of the stellar mass, with $\delta\,\mathrm{MS} = \mathrm{SFR}/\mathrm{SFR}_{\mathrm{MS}}$ and the star-formation sequence of Whitaker et al. (2012). **Left:** The colour-coding refers to the blue cloud, green valley, or red sequence, as dicussed in Sect. 1.1. **Right:** The colour-coding refers to the molecular gas fraction. The undetected galaxies are displayed as empty brown stars.

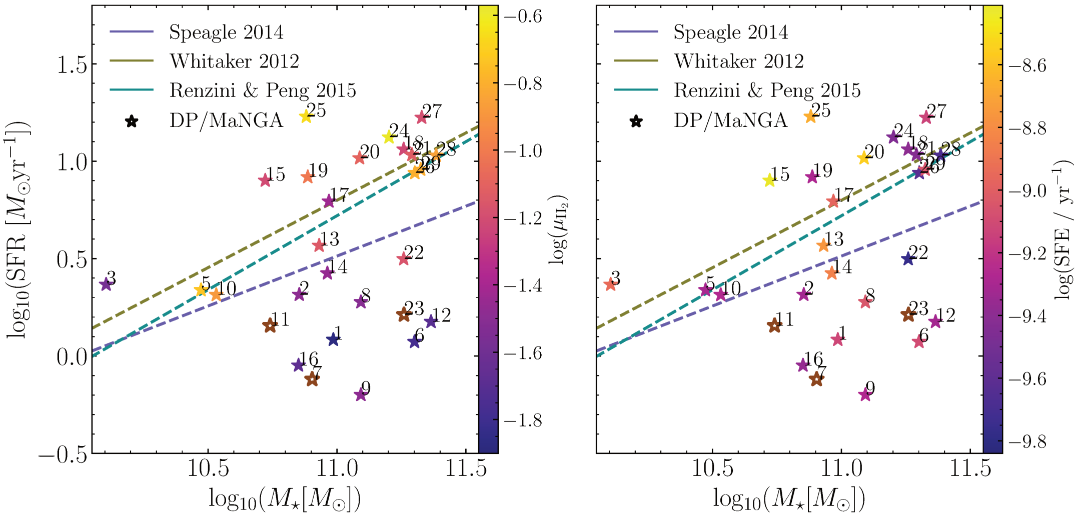

Figure (5.4) SFR-$M_\star$ relation for the DP/MaNGA galaxies. The empty brown stars correspond to the undetected sources. The galaxy identified as G4 does not appear on the panels because its coordinates are (10.6;-2.2). **Left:** The colour coding refers to the logarithmic molecular gas fraction. **Right:** The colour coding refers to the logarithmic SFE.

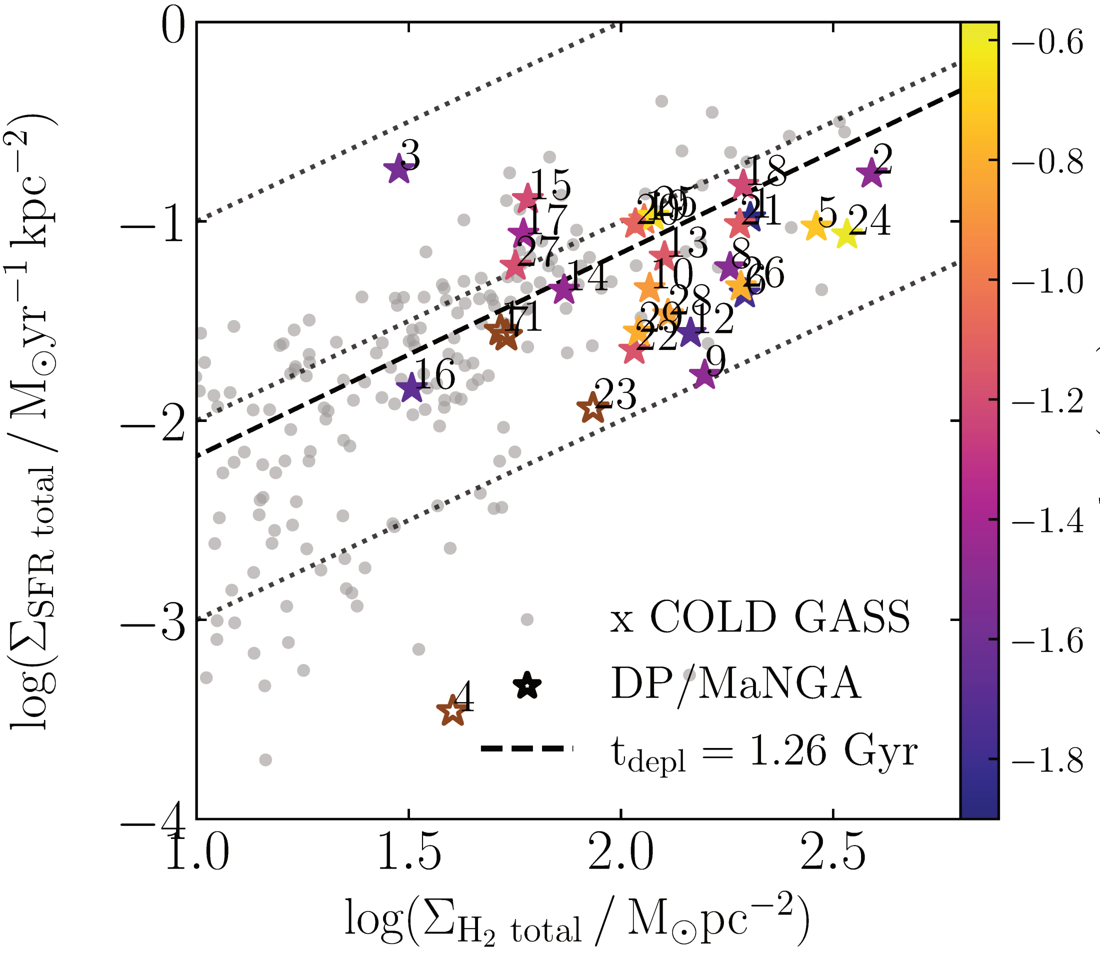

Figure (5.5) Kennicutt-Schmidt relation for the DP/MaNGA galaxies. The surface densities are computed using the total molecular gas mass (for the x-axis) and the star formation rate of the entire galaxy (for the y-axis), normalised using the half-light radius of each galaxy. The x COLD GASS galaxies are shown as grey dots. The undetected DP/MaNGA galaxies are displayed as empty brown stars. The colour-coding refers to the H_2 fraction. The three dotted lines represent constant depletion times of 0.1, 1 and 10 Gyr. The dashed line denotes the relation for a depletion time of 1.26 Gyr, computed for the mean redshift and stellar mass of the DP/MaNGA sample, as in Tacconi et al. (2018).

3 Observations with NOEMA

3.1 Interferometry concepts

The angular resolution of a telescope is physically limited by diffraction. It is given by:

$$\theta \sim 1.22\,\frac{\lambda}{D} \tag{5.8}$$

where λ is the observed wavelength and D is the telescope diameter. The larger the wavelength, the more extended the telescope has to be to achieve a good resolution. So as to reach sub-arcsecond resolution at radio wavelengths, one would need a single-dish with an impossible large diameter (not to mention the pointing and tracking accuracy issue for large antennae). To tackle this observational constraint, high-resolution observations are based on the interferometry technique. It consists of simultaneously using N antennae to observe a source.
The simplest interferometer consists of a pair of radio telescopes, and more generally an interferometer composed of N antennae can be treated as $N(N-1)/2$ independent two-element interferometers.

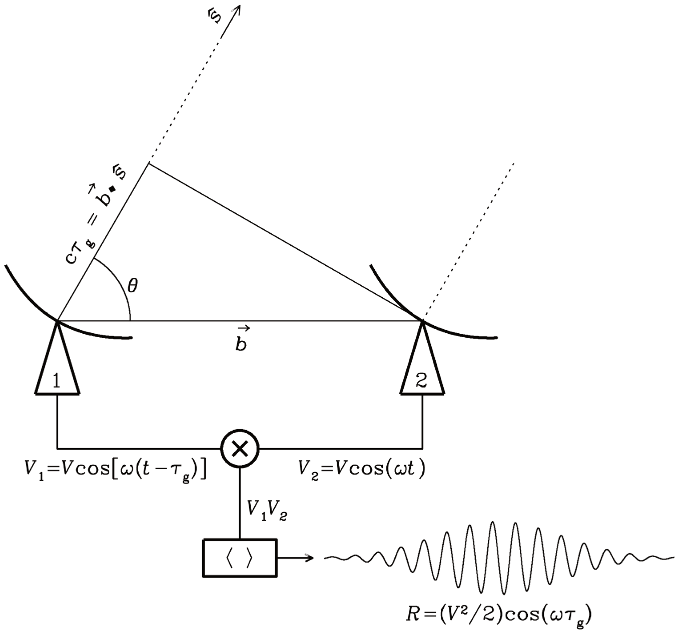

Figure (5.6) Schematic illustration of a two-antenna interferometer.

Here above is the representation of a two-antenna interferometer, also called a short dipole antenna. This system allows to depict the most fundamental aspects of interferometry. Let a pair of antennae at respective locations $\mathbf{P_1}$ and $\mathbf{P_1}$. The baseline between these two can be defined as $\mathbf{b} = \mathbf{P_2} - \mathbf{P_1}$.
In interferometry, the coordinate system (u, v, w) is used to describe the antenna positions and baselines. It is usually oriented such that the antennae lie on a plane corresponding to $w = 0$. The baseline is then expressed in the (u, v, w) system as $\mathbf{b} = (\lambda\, u, \lambda\, v)$. In the example presented in Fig. 5.6, both antennae are oriented towards the same source in direction $\mathbf{s}$ in the sky. The wavefront incident to both antennae reaches antenna 2 first and then antenna 1, with a delay of $\tau_g = \frac{\mathbf{b}\cdot\mathbf{s}}{c}$. At a frequency $\nu = \frac{w}{2\,\pi}$, the output tensions of the antennae are:

$$V_1 = V\cos(w\,(t-\tau_g));\, V_2 = V\cos(w\,t) \tag{5.9}$$

Through the correlator, these signals are then multiplied and time averaged. The resulting output signal is:

$$R_c = \frac{V^2}{2}\cos(w\,\tau_g) \tag{5.10}$$

As an even function, the correlator only detects the even part of the brightness distribution of the observed source. It is possible to introduce a second correlator which adds a $\pi/2$ phase delay to the output of one of the antennae. The second correlator has then as output signal: $R_s = \frac{V^2}{2}\sin(w\,\tau_g)$. Both correlators can be combined into a complex value, that is referred to as a *visibility V(u,v)*:

$$V(u,v) = R_c - i\,R_s = \int I(\mathbf{s})\,\mathrm{e}^{-2\,\pi\,\mathrm{i}\,\nu\,\frac{\mathbf{u}\cdot\mathbf{s}}{c}}\,\mathrm{ds} \tag{5.11}$$

where I is the spatial sky brightness distribution. An interferometer thus gives a measure of the two dimensional Fourier transform of the spatial sky surface brightness distribution I. This distribution is retrieved by applying an inverse Fourier transform on the measured visibilities. The more antennae composing the interferometer, the better the (u, v) plane is sampled.

3.2 Proposed project

The merging system MaNGA ID 1-114955 that we describe in the previous chapter presents a peculiar stage of pre-coalescence merger with strong kinematic disturbances. As we detected a large reservoir of molecular gas in this system with the IRAM 30m telescope, this system probably gained a large part of its gas mass through the merging process. By mapping this galaxy with the NOEMA telescope, we will be able to spatially resolve the molecular gas and to conclude on its dynamics. We will be able to disentangle the molecular gas content corresponding to the stellar components of both galaxies. The mapping of both CO transitions will enable us to investigate the excitation and the density of the gas, using the CO(2-1)/CO(1-0) ratio. In addition, we expect a continuum flux of 30 μ Jy and 12 μ Jy at 3 mm and 1 mm respectively and a high resolution map might provide new arguments on the relation between the radio continuum flux and the star formation in a complex system, and possibly the presence of a hidden AGN. We will distinguish possible point sources at the centre of each galaxy, and separate them from diffuse emission.

We already have measurements of the CO(1-0) and CO(2-1) gas content with the IRAM 30m telescope within a beam of $23''$ and $12''$ in diameter respectively. The respective measured velocity-integrated flux and linewidth are $F_{\mathrm{CO(1-0)}} = 27\mathrm{Jy\,km\,s^{-1}}$, $\mathrm{FWHM_{CO(1-0)}} = 624\mathrm{km\,s^{-1}}$ and $F_{\mathrm{CO(1-0)}} = 117\mathrm{Jy\,km\,s^{-1}}$, $\mathrm{FWHM_{CO(2-1)}} = 897\mathrm{km\,s^{-1}}$. Since the molecular gas in galaxies is not equally distributed, we expect the signal to be dispatched into clumps and streams. We thus assume only N_{clumps} ($\sim$ 20 to 50) to contain a signal given the NOEMA $2'' \times 2''$ synthesised beam. Since we will measure smaller regions of the two superimposed galaxies, we will also expect to probe only a fraction, σ_{v}, of the global velocity gradient. These local velocity dispersions are expected to be about $30\mathrm{km\,s^{-1}}$ for the studied galaxy. We thus expect to find a signal strength of approximately $F/(N_{\mathrm{clumps}} \times \sigma_{\mathrm{v}})$ in each beam. In Tab. 5.2, we give the estimated signal in each beam for the proposed observations. We furthermore show the expected noise $\mathrm{RMS^{exp}}$ computed with the IRAM sensitivity estimator. We also plan to search for the continuum flux (expected at 30μJy and 12μJy respectively in the $2'' \times 2''$ synthesised beam) which might be associated to the VLA flux. We finally find for a telescope time of 4h for each CO line an estimated signal strong enough to map the molecular gas with high spatial and spectral resolution. This project,

Galaxy name	N_{clumps}	σ_{v}	$\frac{F_{\text{CO(1-0)}}}{N_{clumps}\times\sigma_{\text{v}}}$	$\text{RMS}^{\text{exp}}_{\text{CO(1-0)}}$	$\frac{F_{\text{CO(2-1)}}}{N_{clumps}\times\sigma_{\text{v}}}$	$\text{RMS}^{\text{exp}}_{\text{CO(2-1)}}$
		km/s	mJy	mJy	mJy	mJy
J221024.49+114247.0	20-50	30	18-46	1.0	78-196	3.8

Table (5.2) Sensitivity estimates for the proposed merger.

proposed for semester 2021B, has been accepted and we were noticed early December that the observations were done.

3.3 First look on the data

The CO(1-0) observations are completed and I proceeded to a first look on the different moment maps.

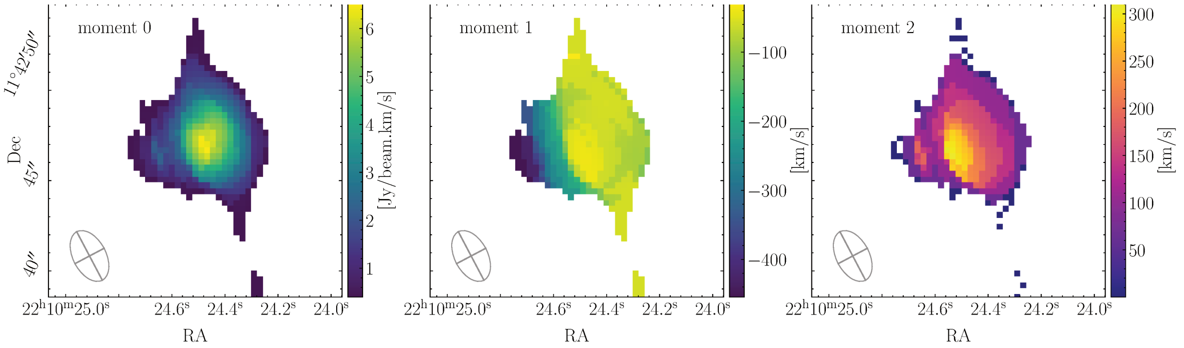

Figure (5.7) Maps obtained with the NOEMA observations of the CO(1-0) transition.

4 Atomic gas phase

In the interstellar medium, the most abundant element is hydrogen but as said before, the H_2 molecule does not emit any spectral line. On the contrary, neutral atoms (HI) are detectable. When the relative spins of the electron and the proton change from parallel to antiparallel, a photon is emitted and thus detectable at $\lambda \sim 21\,\text{cm}$ ($\nu \sim 1420.40575\text{MHz}$). The HI content is related to the galaxy environment as effects in high-density environments such as ram-pressure stripping and tidal interactions can remove HI from the discs. Hence, more HI-deficient spirals have been observed in denser environments. Investigating the total cold gas content within a galaxy is of paramount importance since it sets up the reservoir for star formation. HI is more present in the outskirts of the galaxy as it is condensed and transformed into CO gas in the most inner regions. HI can also trace whether the galaxy is interacting or not. Given the high fraction of HI with respect to the total galaxy mass and the extended radius of the neutral gas, it is a good indicator for galaxy-galaxy interactions or gas accretion. Multiple studies focus on the atomic gas and how it is related to the galaxy evolution stage. Deg et al. (2020) examine the HI asymmetric profiles and propose a new method to quantify these asymmetries which is less sensitive to viewing angles as the previous measurements. They develop a 1-D asymmetry calculation, sensitive to perturbations within a given velocity channel. Numerous scaling relations show correlation between HI content and galaxy properties such as stellar mass, surface mass density or colour and magnitudes.

5 Observations at NRT

5.1 Data acquisition and reduction

We observed the 16 lowest-redshifted DP/MaNGA galaxies with the Nançay Radio Telescope (NRT), located in France. The radio telescope is composed of a rotating plane mirror that reflects the waves towards the spherical mirror which sends them to the focal carriage in the centre, where they are collected by cooled receivers. At 21 cm, the half power beam widths are 4′(R.A.)× 22′(Dec.). The radio telescope is composed of a plane mirror that reflects the waves towards the spherical mirror which sends them to the focal carriage in the centre, where they are collected by cooled receivers. We used the Low Frequency system which is optimised for the HI 21 cm line and recorded four polarisations simultaneously.

Figure (5.8) **Left panel:** Photography of the NRT. **Right panel:** Photography of the focal carriage and schematic representation of the wave path.

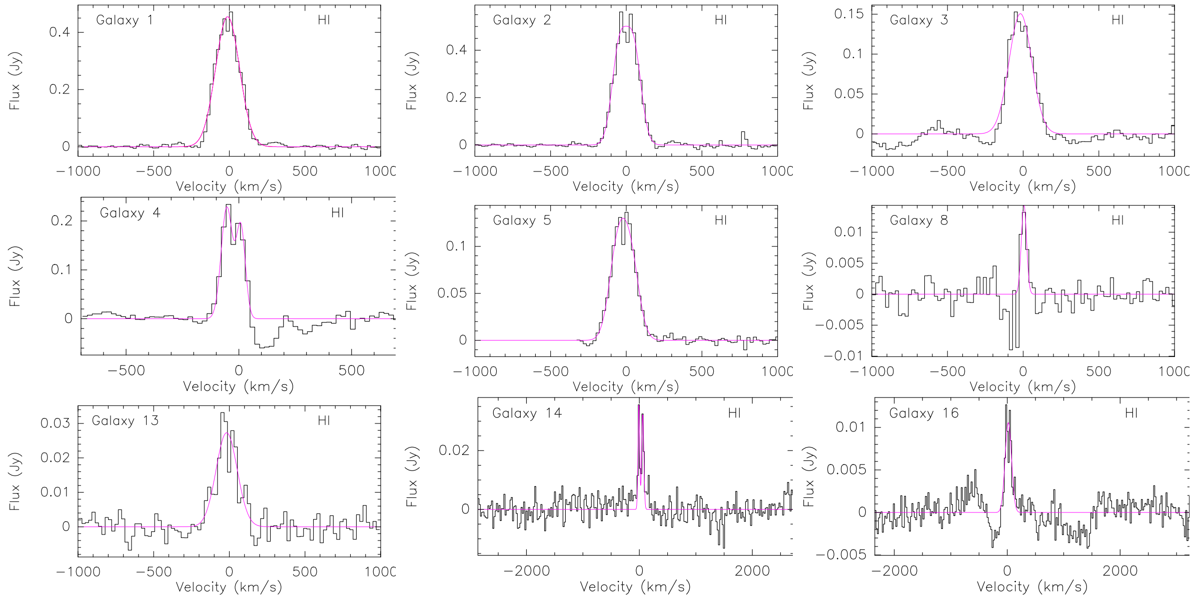

Figure (5.9) Atomic gas spectra for the detected DP/MaNGA galaxies.

5.2 Atomic gas analysis

For all detected galaxies, we compute the atomic gas mass using:

$$\left(\frac{M_{\mathrm{HI}}}{M_{\odot}}\right) = \frac{2.356 \times 10^{5}}{(1+z)} \left(\frac{D_{\mathrm{L}}}{\mathrm{Mpc}}\right)^{2} \left(\frac{F_{\mathrm{HI}}}{\mathrm{Jy\,km\,s^{-1}}}\right) \tag{5.12}$$

where D_{L} is the luminosity distance of the source and F_{HI} is the velocity-integrated flux (Giovanelli & Haynes, 2016).

We have started computing the HI masses and upper limits for the galaxies that we observed. We will be able to compare our results with the measurements from HI-MaNGA (Masters et al., 2019; Stark et al., 2021) and ALFALFA surveys, when available.

5.3 Perspectives

Combining both the CO and the HI data will allow me to infer the cold gas content of 16 of the DP/MaNGA galaxies. I will be able to derive a Kennicutt-Schmidt relation based on both the molecular and atomic gas.

Conclusion

Ce travail porte sur les mécanismes responsables de l'arrêt de la formation d'étoiles dans les galaxies proches, à travers l'étude de la morphologie, de la cinématique et de l'excitation du gaz ionisé. Afin de connaître le contenu en gaz froid, constituant le réservoir de formation d'étoiles, au sein de ces galaxies locales, la quantité de gaz moléculaire et atomique est également estimée. En utilisant le relevé Mapping Nearby Galaxies at APO (MaNGA), nous avons effectué une analyse des propriétés résolues spatialement d'un échantillon de 29 galaxies proches. Dans ce travail, nous nous concentrons sur l'étude d'objets qui présentent tous la même particularité : des caractéristiques spectrales complexes sont détectées dans leur spectre intégré dans les $3''$ centrales, qui sont bien ajustées par une approche d'ajustement à plusieurs composantes.
Nous avons étudié différentes raies d'émission de gaz ionisé (notamment Hβ, [OIII], Hα, [NII]) afin d'étudier les processus de formation et d'extinction des étoiles. Nous avons inspecté certains indices spectraux, afin de déduire les propriétés des populations stellaires des 29 galaxies que nous avons analysées. Nous avons également commencé à étudier la cinématique du gaz et des étoiles au sein de ces galaxies, afin de sonder les mécanismes sous-jacents responsables des caractéristiques spectrales complexes que nous observons. Pour estimer l'efficacité de la formation d'étoiles, nous avons réalisé des observations du gaz moléculaire à l'IRAM 30 m et calculé la masse totale d'hydrogène moléculaire. Dans le but de sonder le contenu global en gaz froid de ces galaxies, nous avons également commencé à évaluer leur masse de gaz atomique, sur la base de nos observations au radio-télescope Nançay pour 16 galaxies.
Les principaux résultats concernant ces 29 galaxies sont résumés ci-dessous:

Grâce à l'analyse des données MaNGA, nous avons remarqué que les 29 galaxies DP/MaNGA montrent un excès de formation d'étoiles dans un rayon effectif. En étudiant les traceurs de l'âge des populations stellaires ainsi que la source de l'excitation du gaz ionisé, nous avons établi que ces galaxies constituent une séquence évolutive, compatible avec un scénario de fusions mineures. Les galaxies appartenant au «nuage bleu» sont des galaxies qui présentent une formation d'étoiles active et des populations stellaires jeunes à tous les rayons galactiques, et qui ont une grande quantité de gaz, probablement due à une accrétion de gaz. Les galaxies de la «vallée verte» que nous observons doivent leur couleur à des populations stellaires rouges et présentent deux types de distributions spatiales: certaines galaxies ont une excitation de type AGN dans leurs régions centrales, ainsi que des populations stellaires âgées. Elles pourraient correspondre à des galaxies dont l'activité nucléaire a été déclenchée par des flux de gaz vers le centre, éteignant la formation d'étoiles "de l'intérieur vers l'extérieur". D'autres galaxies ne montrent pas de claire évidence d'excitation type AGN en leur centre et possèdent de vieilles populations stellaires dans leurs régions périphériques. Nous affirmons que le gaz dans ces galaxies a été entraîné des parties extérieures vers le noyau et que l'épuisement du gaz extérieur entraîne une extinction de la formation d'étoiles "de l'extérieur vers l'intérieur".

Dans l'une de ces 29 galaxies, notre propre procédure d'ajustement, basée sur une approche à plusieurs composantes, a révélé la présence de deux objets sur la ligne de visée. Nous avons associé chaque composante cinématique à une galaxie individuelle et estimé un rapport de masse de 1:9 pour ce système en interaction. De plus, nous avons remarqué une émission radio étendue superposée au compagnon le plus petit, et avons détecté une métallicité du gaz élevée et une région de formation d'étoiles excentrée dans la galaxie principale. Ces caractéristiques peuvent résulter d'échanges de gaz pendant le processus de fusion et, afin de comparer la cinématique du gaz ionisé avec celle du gaz moléculaire, nous avons demandé des observations à haute résolution du gaz CO avec l'interféromètre NOrthern Extended Millimetre Array. La première inspection des données indique une distribution irrégulière du gaz moléculaire.

L'analyse effectuée sur cette galaxie s'est avérée efficace pour dévoiler les mécanismes sous-jacents responsables des caractéristiques spectrales que nous avons détectées. Par la suite, nous utiliserons donc cette analyse à plusieurs composantes pour étudier et interpréter la cinématique des autres galaxies à doubles-pics/MaNGA.

Des analyses innovantes telles que celle que nous avons appliquée aideront à obtenir une compréhension satisfaisante des processus qui déclenchent, régulent et éteignent la formation d'étoiles, et par conséquent, à résoudre certaines des questions restantes sur l'évolution des galaxies.

6

Conclusion

This work addresses the mechanisms responsible for star formation quenching in nearby galaxies, through the study of the morphology, the kinematics and the excitation of the ionised gas. In order to inquire the cold gas content, constituting the star formation reservoir, within these local galaxies, the amount of molecular and atomic gas is also estimated.

Using the Mapping Nearby Galaxies at APO –MaNGA– survey, we have performed an analysis of the spatially-resolved properties of a sample of 29 nearby galaxies. In this work, we focus on the study of objects that all show the same peculiarity: they present complex spectral features in their central $3''$ spectrum, which are well recovered by a multi-component fitting approach.

We investigated different ionised-gas emision lines (notably Hβ, [OIII], Hα, [NII]) to study star formation and termination processes. We inspected some spectral indices, in order to infer stellar population properties of the 29 galaxies that we analysed. We have also started to investigate the kinematics of gas and stars within these galaxies, so as to probe the underlying mechanisms reponsible for the complex spectral features that we observe. To estimate the star formation efficiency, we have performed molecular gas observations at IRAM 30 m and computed the total mass of molecular hydrogen. Aiming at probing the global cold gas content of these galaxies, we have started evaluating their atomic gas mass as well, based on our observations at the Nançay Radio Telescope for 16 galaxies.

The main conclusions about these 29 galaxies are summarised below:

Through the analysis of the spatially-resolved data, we showed that the star formation excess, in these 29 galaxies, is located within one effective radius. By classifying them according to the AGN activity evidence, as well as their stellar population age, we established that these galaxies constitute an evolutionary sequence, compatible with a minor merger scenario. The blue group gathers galaxies that exhibit star formation and young stellar populations at all radii, that have a large amount of gas possibly due to gas accretion. The green objects that we observe owe their colour to red stellar populations and present two types of spatial distributions. Some galaxies have an important AGN contribution in their inner parts, which correlates with a lack of young stars. They might correspond to galaxies whose nuclear activity has been triggered by gas fueling towards the centre, quenching star formation "inside-out". Some others do not show any strong AGN evidence at their centre and host old stellar populations in their outskirts. We state that the gas in these galaxies is funneled from the outer parts into the core and the outer gas depletion results in an “outside-in” quenching.

In one of these 29 galaxies, our own fitting procedure, based on a multi-component approach, revealed the presence of two objects in the line of sight. We associated each kinematics component to an individual galaxy and estimated a mass ratio of 1:9 for this interacting system. Furthermore, we noticed an extended radio emission superimposed on the smaller companion, and detected off-centered high gas-phase metallicity and star formation in the main component. These characteristics can result from gas exchanges during the merging process and so as to compare the ionised gas kinematics with that of the molecular gas, we applied for high-resolution CO gas observations with the NOrthern Extended Millimetre Array. The first inspection of the data indicates an irregular distribution of the molecular gas.

The analysis performed on this galaxy proved to be efficient at unveiling the underlying mechanisms responsible for the spectral features that we detected. Next, we will thus make use of this multi-component analysis to study and interpret the kinematics of the other double-peaked/MaNGA galaxies.

Innovative analyses such as the one that we applied will help obtain a satisfactory understanding of the processes that trigger, regulate and quench star formation, and consequently, solve some of the remaining questions about galaxy evolution.

7

Appendices

1 Workshop and conference participations

1.1 Workshops and conferences

- February 2021 (online)
  Double-peak emission line galaxies workshop, organising: committee member "Morpho-kinematic transformations in an interacting local galaxy in the light of MaNGA",
  oral presentation

- 2019 & 2020 (online)
  European Astronomical Society Annual Meeting Lyon: "Morpho-kinematic transformation observed in double-peak emission-line MaNGA galaxies",
  poster presentation

- May 2019 (Québec, Canada)
  SIGNALS survey workshop: "Asymmetric kinematics features within galaxies at z=0.06 as revealed by MaNGA",
  oral presentation.

- October 2019 (Paris)
  Participation in organising committees :
  "First Galaxies, First Structures"
  "Paris Observatory Joint Galaxies and Cosmology Seminar"

2 Poster

Interacting galaxies hiding into one, revealed by MaNGA

LERMA l'Observatoire de Paris | PSL★

Barbara Mazzilli Ciraulo, Anne-Laure Melchior, Daniel Maschmann, Ivan Yu. Katkov, Anaëlle Hallé,
Françoise Combes, Joseph D. Gelfand and Aisha Al Yazeedi

SF2A

Using IFU data from the MaNGA survey and a multi-component fitting approach, we highlight the superimposition of two distinct rotating discs in one peculiar target. We interpret the resulting 2D maps as the identification of a pre-coalescence minor-merger.

Selection of the target

This galaxy merger at z = 0.09 belongs to a sub-sample (Mazzilli Ciraulo et al., in prep.) created by cross-identifying the MaNGA data release (SDSS DR15, Aguado et al. 2019) and a catalogue gathering sources with detected double-peaked emission-line profiles in their central SDSS spectrum (Maschmann et al. 2020).
This galaxy exhibits a disrupted morphology.

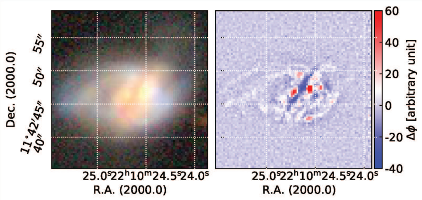

Left: Composite image (g, r, z bands) from the Legacy survey (Dey et al. 2019). **Right:** Difference between the MegaCam r band filter image and its smoothed version.

Gas kinematics from the multi-component approach

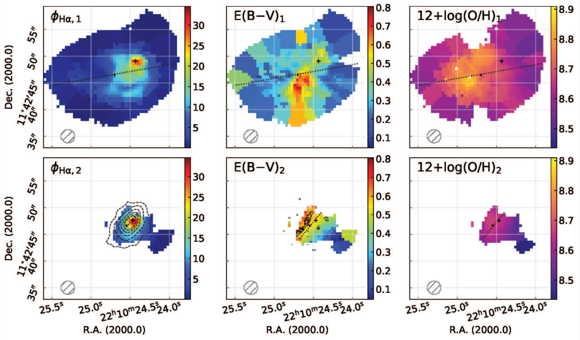

Gas properties derived from our multi-component approach:
Hα extinction-corrected flux, extinction and gas-phase oxygen abundance maps.

Fitting procedure adjusting two components to each emission line.

- Hα emission peaks in different locations
- Extinction of the second component consistent with the dust-lane on the composite image
- Off-centred metallicity peak for the first component
- $M_{dyn,1}/M_{dyn,2} \sim 9$

Consistent gas and star kinematics

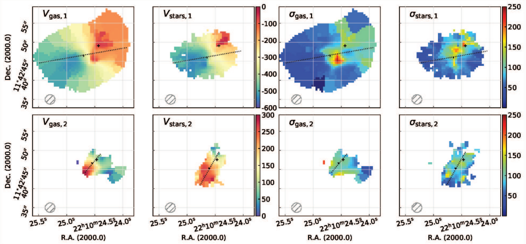

Gas and star kinematics:
Velocity and velocity dispersion maps.

Recovery of a non-parametric stellar line of sight velocity distribution
Decomposition of this LOSVD into two Gaussian components

- Consistent position angles (P.A.s) between gas and stars
- Consistent P.A. between the stellar component of the second component and the dust-lane
- Off-centred velocity dispersion peak for the first component, with respect to the flux emission peak
- $M_{\star,1}/M_{\star,2} \sim 9$

Pre-coaslescence merger

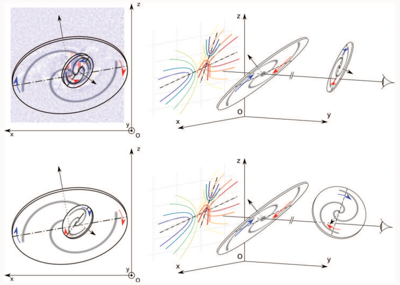

Schematic illustration of the revealed merging system.

Conclusions and remaining questions

- Two detected components along the line of sight
- Radio emission superimposed on the second component
- Hα-based SFR under-estimated with respect to the one expected from the radio luminosity
- Gas excitation of composite origin within the system
- Inferred H_2 mass corresponding to 27% of the total stellar mass
- Need for high-resolution CO observations to get the kinematics of the molecular gas.

These results are presented in a paper in revision before publication in A&A.

References

• Aguado, D. S. et al.: 2019, ApJS, 240, 23. • Dey, A. et al.: 2019, AJ, 157, 168. • Maschmann, D. et al.: 2020, A&A, 641, A171.

e-mail `Barbara.Mazzilli-Ciraulo@observatoiredeparis.psl.eu`

LaTeX TikZposter

Bibliography

Aalto S., et al., 2020, Astronomy & Astrophysics, 640, A104 15

Abazajian K. N., et al., 2009, The Astrophysical Journal Supplement Series, 182, 543 14, 21

Acker A., Köppen J., Samland M., Stenholm B., 1989, The Messenger, 58, 44 71

Aguado D. S., et al., 2019, The Astrophysical Journal Supplement Series, 240, 23 33

Allende Prieto C., Lambert D. L., Asplund M., 2001, The Astrophysical Journal, 556, L63 68

Allington-Smith J. R., Content R., Haynes R., 1998, in D'Odorico S., ed., Vol. 3355, Optical Astronomical Instrumentation. pp 196–205, doi:10.1117/12.316743, `http://proceedings.spiedigitallibrary.org/proceeding.aspx?articleid=946194` 24

Andrews B. H., Martini P., 2013, The Astrophysical Journal, 765, 140 69

Baldry I. K., Glazebrook K., Brinkmann J., Ivezić Ž., Lupton R. H., Nichol R. C., Szalay A. S., 2004, The Astrophysical Journal, 600, 681 13

Baldwin J. A., Phillips M. M., Terlevich R., 1981, Publications of the Astronomical Society of the Pacific, 93, 5 4, 17

Barnes J. E., Hernquist L. E., 1991, The Astrophysical Journal, 370, L65 68

Begelman M. C., Blandford R. D., Rees M. J., 1980, Nature, 287, 307 65, 68

Bellocchi E., Arribas S., Colina L., Miralles-Caballero D., 2013, Astronomy & Astrophysics, 557, A59 36, 59

Best P. N., Heckman T. M., 2012, Monthly Notices of the Royal Astronomical Society, 421, 1569 15

Bigiel F., Leroy A., Walter F., Brinks E., de Blok W. J. G., Madore B., Thornley M. D., 2008, The Astronomical Journal, 136, 2846 12

Blanton M. R., Roweis S., 2007, The Astronomical Journal, 133, 734 10

Bolatto A. D., Leroy A. K., Rosolowsky E., Walter F., Blitz L., 2008, Proceedings of the International Astronomical Union, 4, 274 91, 94

Boselli A., et al., 2016, Astronomy & Astrophysics, 587, A68 15

Brinchmann J., Charlot S., White S. D. M., Tremonti C., Kauffmann G., Heckman T., Brinkmann J., 2004, Monthly Notices of the Royal Astronomical Society, 351, 1151 98

Bruzual A. G., 1983, The Astrophysical Journal, 273, 105 21

Bundy K., et al., 2014, The Astrophysical Journal, 798, 7 27, 30

Calzetti D., 2001, Publications of the Astronomical Society of the Pacific, 113, 1449 19

Cappellari M., Emsellem E., 2004, Publications of the Astronomical Society of the Pacific, 116, 138 27, 31

Catinella B., et al., 2018, Monthly Notices of the Royal Astronomical Society, 476, 875 23

Chabrier G., 2003, Publications of the Astronomical Society of the Pacific, 115, 763 13

Charmandaris V., Combes F., van der Hulst J. M., 2000, Astronomy and Astrophysics, 356, 1 15

Chilingarian I., Prugniel P., Sil'chenko O., Koleva M., 2006a, Proceedings of the International Astronomical Union, 2, 175 73

Chilingarian I., Prugniel P., Sil'chenko O., Koleva M., 2006b, Proceedings of the International Astronomical Union, 2, 175 74

Chilingarian I. V., Melchior A.-L., Zolotukhin I. Y., 2010, Monthly Notices of the Royal Astronomical Society, 405, no 10

Chilingarian I. V., Zolotukhin I. Y., Katkov I. Y., Melchior A.-L., Rubtsov E. V., Grishin K. A., 2017, The Astrophysical Journal Supplement Series, 228, 14 22

Chung A., van Gorkom J. H., Kenney J. D. P., Vollmer B., 2007, The Astrophysical Journal, 659, L115 15

Cicone C., et al., 2014, Astronomy & Astrophysics, 562, A21 15, 36, 59

Cid Fernandes R., Stasińska G., Mateus A., Vale Asari N., 2011, Monthly Notices of the Royal Astronomical Society, 413, 1687 4, 18, 19

Combes F., 2017, Frontiers in Astronomy and Space Sciences, 4, 1 15

Comerford J. M., Gerke B. F., Stern D., Cooper M. C., Weiner B. J., Newman J. A., Madsen K., Barrows R. S., 2012, The Astrophysical Journal, 753, 42 65, 68

Comerford J. M., Nevin R., Stemo A., Müller-Sánchez F., Barrows R. S., Cooper M. C., Newman J. A., 2018, The Astrophysical Journal, 867, 66 65, 68

Concas A., Popesso P., Brusa M., Mainieri V., Thomas D., 2019, Astronomy & Astrophysics, 622, A188 36, 59

Curti M., Mannucci F., Cresci G., Maiolino R., 2020, Monthly Notices of the Royal Astronomical Society, 491, 944 69, 70

Dame T. M., Hartmann D., Thaddeus P., 2001, The Astrophysical Journal, 547, 792 94

De Vaucouleurs G., 1959, in , Handbuch der Physik. pp 275–310, doi:10.1007/978-3-642-45932-0_7, `http://link.springer.com/10.1007/978-3-642-45932-0{_}7` 1, 8

Deg N., Blyth S.-L., Hank N., Kruger S., Carignan C., 2020, Monthly Notices of the Royal Astronomical Society, 495, 1984 105

Dey A., et al., 2019, The Astronomical Journal, 157, 168 22

Domínguez Sánchez H., Huertas-Company M., Bernardi M., Tuccillo D., Fischer J. L., 2018, Monthly Notices of the Royal Astronomical Society, 476, 3661 32

Domínguez A., et al., 2013, The Astrophysical Journal, 763, 145 19

Drissen L., et al., 2019, Monthly Notices of the Royal Astronomical Society, 485, 3930 23

Eisenhauer F., Raab W., 2015, Annual Review of Astronomy and Astrophysics, 53, 155 25

Ellison S. L., Patton D. R., Simard L., McConnachie A. W., 2008, The Astronomical Journal, 135, 1877 69

Fioc M., Rocca-Volmerange B., 1997, Astronomy and Astrophysics, 326, 950 77

Fischer J.-L., Domínguez Sánchez H., Bernardi M., 2019, Monthly Notices of the Royal Astronomical Society, 483, 2057 32, 96

Fitzpatrick E. L., 1999, Publications of the Astronomical Society of the Pacific, 111, 63 19

Flaugher B., et al., 2015, The Astronomical Journal, 150, 150 22

Fu H., Yan L., Myers A. D., Stockton A., Djorgovski S. G., Aldering G., Rich J. A., 2012, The Astrophysical Journal, 745, 67 65, 68

Fukugita M., Ichikawa T., Gunn J. E., Doi M., Shimasaku K., Schneider D. P., 1996, The Astronomical Journal, 111, 1748 9

Genzel R., et al., 2015, The Astrophysical Journal, 800, 20 91, 94

Giovanelli R., Haynes M. P., 2016, The Astronomy and Astrophysics Review, 24, 1 107

Haynes M. P., et al., 2018, The Astrophysical Journal, 861, 49 28, 32

Heckman T. M., 1980, Astronomy and Astrophysics, 500, 187 17

Heckman T. M., Best P. N., 2014, Annual Review of Astronomy and Astrophysics, 52, 589 15

Henault F., et al., 2003, in Iye M., Moorwood A. F. M., eds, Vol. 4841, Instrument Design and Performance for Optical/Infrared Ground-based Telescopes. p. 1096, doi:10.1117/12.462334, `http://proceedings.spiedigitallibrary.org/proceeding.aspx?doi=10.1117/12.462334` 23

Holmberg E., 1958, Meddelanden fran Lunds Astronomiska Observatorium Serie II, 136, 1 96

Hubble E. P., 1936, Realm of the Nebulae 1, 7

Ivison R. J., et al., 2012, Monthly Notices of the Royal Astronomical Society, 425, 1320 15

Kannappan S. J., Guie J. M., Baker A. J., 2009, The Astronomical Journal, 138, 579 13

Katkov I. Y., Sil'chenko O. K., Afanasiev V. L., 2013, The Astrophysical Journal, 769, 105 73

Katkov I. Y., Sil'chenko O. K., Chilingarian I. V., Uklein R. I., Egorov O. V., 2016, Monthly Notices of the Royal Astronomical Society, 461, 2068 73

Kauffmann G., et al., 2003, Monthly Notices of the Royal Astronomical Society, 346, 1055 18

Kennicutt R. C., Evans N. J., 2012, Annual Review of Astronomy and Astrophysics, 50, 531 12

Kennicutt, Jr. R. C., 1998, The Astrophysical Journal, 498, 541 2, 12, 20

Kewley L. J., Ellison S. L., 2008, The Astrophysical Journal, 681, 1183 69

Kewley L. J., Dopita M. A., Sutherland R. S., Heisler C. A., Trevena J., 2001, The Astrophysical Journal, 556, 121 18

Koss M., Mushotzky R., Treister E., Veilleux S., Vasudevan R., Trippe M., 2012, The Astrophysical Journal, 746, L22 65, 68

Kroupa P., 2001, Monthly Notices of the Royal Astronomical Society, 322, 231 13

Lahén N., Johansson P. H., Rantala A., Naab T., Frigo M., 2018, Monthly Notices of the Royal Astronomical Society, 475, 3934 65, 68

Le Borgne D., Rocca-Volmerange B., Prugniel P., Lançon A., Fioc M., Soubiran C., 2004, Astronomy & Astrophysics, 425, 881 73

Leavitt H. S., Pickering E. C., 1912, Harvard College Observatory Circular, 173, 1 7

Lejeune T., Cuisinier F., Buser R., 1997, Astronomy and Astrophysics Supplement Series, 125, 229 77

Lequeux J., Peimbert M., Rayo J. F., Serrano A., Torres-Peimbert S., 1979, Astronomy and Astrophysics, 500, 145 68

Leroy A. K., Walter F., Brinks E., Bigiel F., de Blok W. J. G., Madore B., Thornley M. D., 2008, The Astronomical Journal, 136, 2782 95

Leroy A. K., et al., 2011, The Astrophysical Journal, 737, 12 94

Lisenfeld U., et al., 2011, Astronomy & Astrophysics, 534, A102 92, 95, 96

Mannucci F., Cresci G., Maiolino R., Marconi A., Gnerucci A., 2010, Monthly Notices of the Royal Astronomical Society, 408, 2115 69

Marleau F. R., Clancy D., Bianconi M., 2013, Monthly Notices of the Royal Astronomical Society, 435, 3085 15

Martig M., Bournaud F., Teyssier R., Dekel A., 2009, The Astrophysical Journal, 707, 250 15

Maschmann D., Melchior A.-L., Mamon G. A., Chilingarian I. V., Katkov I. Y., 2020, Astronomy & Astrophysics, 641, A171 28, 33

Masters K. L., et al., 2019, Monthly Notices of the Royal Astronomical Society, 488, 3396 28, 32, 107

Mazzilli Ciraulo B., Melchior A.-L., Maschmann D., Katkov I. Y., Halle A., Combes F., Gelfand J. D., Al Yazeedi A., 2021, Astronomy & Astrophysics, 653, A47 66, 77, 92

Mendenhall W., Sincich T. T., 2012, A Second Course in Statistics : regression analysis 73

Nishiyama K., Nakai N., Kuno N., 2001, Publications of the Astronomical Society of Japan, 53, 757 95

Oke J. B., Sandage A., 1968, The Astrophysical Journal, 154, 21 9

Osterbrock D. E., Ferland G., 2006, `https://ui.adsabs.harvard.edu/abs/2006agna.book.....O` 20

Pagel B. E. J., Edmunds M. G., Blackwell D. E., Chun M. S., Smith G., 1979, Monthly Notices of the Royal Astronomical Society, 189, 95 69

Patton D. R., Ellison S. L., Simard L., McConnachie A. W., Mendel J. T., 2011, Monthly Notices of the Royal Astronomical Society, 412, 591 68

Pearson W. J., et al., 2018, Astronomy & Astrophysics, 615, A146 3, 14

Peng Y., Maiolino R., Cochrane R., 2015, Nature, 521, 192 15

Pettini M., Pagel B. E. J., 2004, Monthly Notices of the Royal Astronomical Society, 348, L59 69, 94

Poggianti B. M., et al., 2016, The Astronomical Journal, 151, 78 15

Prugniel P., Soubiran C., Koleva M., Borgne D. L., 2007, pp 1–8 74

Regan M. W., Thornley M. D., Helfer T. T., Sheth K., Wong T., Vogel S. N., Blitz L., Bock D. C., 2001, The Astrophysical Journal, 561, 218 95

Renzini A., Peng Y.-j., 2015, The Astrophysical Journal, 801, L29 3, 14

Rubinur K., Das M., Kharb P., 2019, Monthly Notices of the Royal Astronomical Society, 484, 4933 65, 68

Saintonge A., et al., 2017, The Astrophysical Journal Supplement Series, 233, 22 23

Salim S., 2014, Serbian Astronomical Journal, 1, 1 3, 13, 14

Salim S., et al., 2007, The Astrophysical Journal Supplement Series, 173, 267 14

Salim S., et al., 2016, The Astrophysical Journal Supplement Series, 227, 2 97

Salpeter E. E., 1955, The Astrophysical Journal, 121, 161 12

Sánchez S. F., et al., 2016a, Revista Mexicana de Astronomia y Astrofisica, 52, 21 28, 32

Sánchez S. F., et al., 2016b, Revista Mexicana de Astronomia y Astrofisica, 52, 171 28, 32

Schawinski K., Thomas D., Sarzi M., Maraston C., Kaviraj S., Joo S.-J., Yi S. K., Silk J., 2007, Monthly Notices of the Royal Astronomical Society, 382, 1415 18

Schawinski K., et al., 2014, Monthly Notices of the Royal Astronomical Society, 440, 889 13, 14

Schinnerer E., Weiß A., Aalto S., Scoville N. Z., 2010, The Astrophysical Journal, 719, 1588 91, 94

Schmidt M., 1959, The Astrophysical Journal, 129, 243 2, 12

Seyfert C. K., 1943, The Astrophysical Journal, 97, 28 17

Smee S. A., et al., 2013, The Astronomical Journal, 146, 32 30

Smith J. A., et al., 2002, The Astronomical Journal, 123, 2121 9

Smith R. J., et al., 2010, Monthly Notices of the Royal Astronomical Society, 408, 1417 15

Speagle J. S., Steinhardt C. L., Capak P. L., Silverman J. D., 2014, Astrophysical Journal, Supplement Series, 214 3, 14

Stark D. V., et al., 2021, Monthly Notices of the Royal Astronomical Society, 503, 1345 28, 32, 107

Stoughton C., et al., 2002, pp 485–548 9, 21

Strateva I., et al., 2001, The Astronomical Journal, 122, 1861 13

Tacconi L. J., et al., 2018, The Astrophysical Journal, 853, 179 12, 91, 94, 102

Tomczak A. R., et al., 2016, The Astrophysical Journal, 817, 118 3, 15

Tremonti C. A., et al., 2004, The Astrophysical Journal, 613, 898 68, 69

Tully R. B., Rizzi L., Shaya E. J., Courtois H. M., Makarov D. I., Jacobs B. A., 2009, The Astronomical Journal, 138, 323 96

Vincenzo F., Matteucci F., Belfiore F., Maiolino R., 2016, Monthly Notices of the Royal Astronomical Society, 455, 4183 13

Wells M., Hastings P. R., Ramsay-Howat S. K., 2000, in Iye M., Moorwood A. F. M., eds, Vol. 4008, Optical and IR Telescope Instrumentation and Detectors. p. 1215, doi:10.1117/12.395440, `http://proceedings.spiedigitallibrary.org/proceeding.aspx?doi=10.1117/12.395440` 23

Wells M., et al., 2015, Publications of the Astronomical Society of the Pacific, 127, 646 23

Westmoquette M. S., Exter K. M., Christensen L., Maier M., Lemoine-Busserolle M., Turner J., Marquart T., 2009, pp 1–5 24

Whitaker K. E., van Dokkum P. G., Brammer G., Franx M., 2012, The Astrophysical Journal, 754, L29 3, 14, 98, 101

Williams R. J., Quadri R. F., Franx M., van Dokkum P., Labbé I., 2009, The Astrophysical Journal, 691, 1879 13

Wyder T. K., et al., 2007, The Astrophysical Journal Supplement Series, 173, 293 13

York D. G., et al., 2000, The Astronomical Journal, 120, 1579 9, 14, 21

van Dokkum P. G., et al., 2010, The Astrophysical Journal, 709, 1018 68

RÉSUMÉ

Les données astronomiques deviennent de plus en plus précises et permettent d'affiner notre compréhension des processus qui régissent l'évolution des galaxies, mais nous ne disposons toujours pas d'un paradigme global pour expliquer certains mécanismes physiques. En particulier, le déclenchement et la régulation de l'extinction de la formation stellaire ne sont pas compris en détail étant donné les nombreux processus dont elle peut résulter et les différentes échelles de temps qui sont impliquées.

Le but de ce projet de thèse est d'étudier le contenu en gaz, l'activité de formation d'étoiles et l'extinction des étoiles dans les galaxies en utilisant les données spectroscopiques de l'étude SDSS-IV MaNGA, ainsi que des observations de gaz moléculaire et atomique.

Tout d'abord, je décris l'échantillon de galaxies proches sur lequel j'ai décidé de me concentrer. Il s'agit de 29 galaxies proches qui présentent des caractéristiques cinématiques complexes dans leurs spectres dans le domaine visible. Dans la deuxième partie, je présente une analyse de cet échantillon en termes de paramètres structurels des galaxies et d'activité de formation d'étoiles. Je conclus que ces objets nous permettent d'échantillonner différentes phases de l'évolution des galaxies, qui résultent d'événements de fusions mineures. Dans la troisième partie, je détaille les résultats que j'ai obtenus en appliquant une procédure d'ajustement de spectres innovante aux données d'une galaxie MaNGA particulière. Cette approche permet de mettre en évidence une fusion mineure en décomposant les caractéristiques spectrales optiques, à la fois dans les raies d'émission du gaz et dans le continuum stellaire. Dans la quatrième partie, je me concentre sur l'analyse du contenu en gaz froid à travers des observations de gaz moléculaire et atomique. Je déduis les masses de gaz moléculaire ainsi qu'une relation de Kennicutt-Schmidt afin d'estimer l'efficacité de la formation d'étoiles des galaxies étudiées.

MOTS CLÉS

Evolution des galaxies; Raies d'émission; Cinématique; Spectroscopie à intégrale de champ; Gaz moléculaire; Gaz atomique.

ABSTRACT

Astronomical data become more and more precise and help the refining of our understanding of the processes that drive galaxy evolution, but we still do not have a global paradigm to explain some physical mechanisms. Especially, the triggering and regulation of star formation quenching are not understood in detail given the numerous processes that it can be resulting from and the different timescales that are involved.

The aim of this thesis project is to study gas content, star formation activity and quenching within galaxies using intregral field spectroscopic data from the SDSS-IV MaNGA survey, as well as single-dish observations of molecular and atomic gas.

First, I describe the sample of nearby galaxies that I decided to focus on. It consists of 29 nearby galaxies that show complex kinematic features in their optical spectra. In the second part, I present an analysis of this sample in terms of galaxy structural parameters and star formation activity. I concluded that these objects enable us to sample different phases of galaxy evolution, that act as the following of minor-merger events. In the third part, I detail the results that I obtained by applying an innovative fitting procedure to the data from one peculiar MaNGA galaxy. This approach helps reveal a minor-merger event by disentangling the optical spectral features, both in gas and stellar components. In the fourth I focus on the analysis of cold gas content through molecular and atomic gas observations. I infer the molecular and atomic gas masses as well as a Kennicutt-Schmidt relation so as to estimate the star formation efficiency of the studied galaxies.

KEYWORDS

Galaxy evolution; Emission lines; Kinematics; Integral field spectroscopy; Molecular gas; Atomic gas.